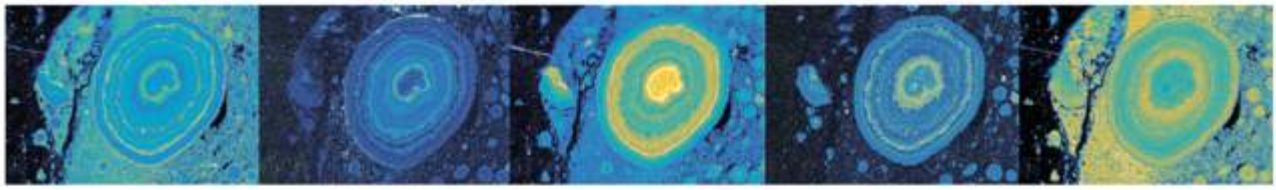

Università degli Studi di Genova

Dipartimento di Scienze della Terra, dell'Ambiente e della Vita

Scuola di Dottorato in Scienze e Tecnologie per l'Ambiente e il Territorio

Ciclo XXX

Faulting, fluid - rock interaction and hydrothermal mineralisation in ultramafic rocks (Voltri Massif, Ligurian Alps)

Marco Scarsi

Tutor: Prof.ssa L. Crispini

Co-tutors: Prof. P.S. Garofalo, Prof. G. Capponi

Coordinatore del dottorato: Prof. M. Firpo

Anni Accademici: 2014-2017

Settore scientifico-disciplinare di afferenza: GEO/03

Università degli Studi di Genova

Dipartimento di Scienze della Terra dell'Ambiente e della Vita

Corso di Dottorato in Scienze e Tecnologie per l'Ambiente e il Territorio

Ciclo XXX

Faulting, fluid-rock interaction and hydrothermal mineralisation in ultramafic rocks (Voltri Massif, Ligurian Alps).

Fenomeni di faglia, interazione fluido-roccia e mineralizzazioni idrotermali in rocce ultramafiche (Massiccio di Voltri, Alpi Liguri).

Marco Scarsi

Tutor: Prof.ssa L. **Crispini**

Co-tutors: Prof. P. S. **Garofalo,** Prof. G. **Capponi**

Coordinatore del dottorato: Prof. M. Firpo

Anni Accademici: 2014-2017

Settore scientifico-disciplinare di afferenza: GEO/03

Abstract

This study deals with reverse faults within intensely carbonated meta-lherzolites, with related gold mineralisations, from the Voltri Massif, and in particular within the Lavagnina Lakes area, in the Gorzente Valley. This area is located in northwest Italy among the municipalities of Casaleggio Boiro, Lerma, Mornese, and Bosio (Alessandria, Italy; GPS coordinates WGS84, 44.600685° N, 8.784286° E).

The Voltri Massif is a metaophiolitic complex, which occurs within the Eastern edges of the Ligurian Alps. It is made up of of metaophiolitic rocks associated with metasediments and slices of subcontinental lithospheric mantle. These rocks underwent a complex Alpine tectono-metamorphic evolution, with blueschist- to eclogite- facies peak metamorphism with variable retrogressive overprints.

For this study the analysed structures are the upper crustal deformational events (UDC), from late- to post-orogenic linked to the collisional events. These deformational events are linked to different structural regimes, and developed during the late-Alpine to early-Appenine events.

The Lavagnina Lakes area is mainly characterised by outcrops of serpentinites, lherzolites, metabasites, metagabbros, lenses of metasediments, and listvenites (in decreasing order of volumetric extension). From a structural point of view, this area is characterised by brittle to brittle-ductile systems of shear zones, with associated carbonates and chalcedony-quartz veins associated with local gold mineralisations.

Hydrothermal, carbon-rich fluids permeated the rocks and sustained these deformation stages producing widespread and intense carbonate-rich alteration zones, exclusive meso- and microstructures within carbonates fault zones, called fault pearls, chalcedony shear veins along fault surfaces, widespread quartz-chalcedony and carbonates veining, and leading to local gold mineralisation.

The geological survey allowed identifying four main structures (Chapter 5) that I studied in detail. In particular I studied the Bisciarelle Creek thrust fault for the occurrence of meso- and microstructures never reported in literature, called fault pearls. Their compositional and textural characteristics, described in chapter 5.3.4, make the fault core of the Bisciarelle fault a peculiar geological object.

The data shown in chapter 7 provide constraints on the chemical properties of the fluid that generate the intense carbonation along the Bisciarelle fault. Through the mass transfer profiles was possible to identify and quantify those elements transferred from the fluid to the rock and *vice versa*.

The morphometric image analysis results (Described in chapter 5.3.5) show that the fault pearls have circular shape irrespective to the direction of observation (parallel and orthogonal to the slickenlines), with values that indicate a nearly perfect circular shape. These values are in line with the roundness values, hence the fault pearls in three-dimensions can be considered as nearly perfect spheres or as very spherical textures.

Single-spot SEM-EDS (Chapter 8) analyses show that ferroan dolomite makes the pearl bands (CaO: 29.13±2.33 wt%; MgO: 19.03±4.86 wt%; FeO: 1.77±0.87 wt%) and that minor compositional variations across large and thin bands exist, and that silica makes most of the chalcedony veins (SiO_2: 97.97±3.23 wt%).

Elemental imaging by LA-ICPTOFMS (Chapter 8) provides a detailed account of the distribution of chemical elements within pearls, matrix, and chalcedony shear veins. Mineral paragenesis and elemental imaging by LA-ICP-TOFMS confirm the hypothesis of hydrothermal derivation of the fault rock. This is best evaluated by comparing the concentration ranges of the key trace elements As, Sb, In, Ga, Ag, Zn, and Cu of fault pearls levels and chalcedony with those of the same elements in the average upper crust. Such comparison clearly shows that the peak concentrations of these elements are 5 (Cu, Zn) to 50 (Sb, In) times higher than those of the upper crust, demonstrating that the Bisciarelle fault fluid was capable to transport and deposit a suite of ore elements.

These evidences are fundamental to discuss the possible origin of the fluids that developed the carbonation and the fluid-rock interactions along the Bisciarelle thrust fault and along the main fault of the Lavagnina Lakes area.

On the basis of all the constraints described, the fault pearl features are compatible with a genesis from a process called “transient” boiling in microfluidics. This process occurs within cavities when a liquid is instantaneously overheated and a vapour phase nucleates and expands up to explosive boiling, and so generates a myriad of vapour bubbles. Such process, which occurred during mixed mode fracturing in the fault, implies that pearls might reflect the liquid-vapour

fractionation of chemical elements in a boiling hydrothermal fluid during seismic failure.

The close association of fault pearls with seismic-related structures such as sub-micron carbonates coating of slip surfaces, quartz microtexture related to silica gel deposition, syn-kinematic filamentous phase, injection veins with similar characteristics and overpressure with respect to seismic pseudotachylites along slip zone supports the hypothesis that fault pearls developed during shear events at seismic rates, and hence are considerable as paleo-seismic events indicators.

Moreover I discuss the tectonic evolution of the Lavagnina Lakes area linked to the syn-kynematic fluid rock interaction, the origin of the fluids and the gold mineralisations of the area. The occurrence of syn-tectonic fluid flow and consequent fluid-rock interaction (e.g. carbonation) along the two systems of Reverse Shear Zones (RSZ1-RSZ2), is testified by: metasomatic alteration (ALT-1, ALT-2, and ALT-3), at least three main systems of veins (V1, V2, and V3), and hydraulic and cockade breccias. The evidence that the carbonation took place along these structures, in particular along the RSZs systems, and within their damage zones, highlights how these structures acted as important fluid pathways and played a major control in the distribution of the ore deposits.

Finally, I stress out further consideration about the comparison between the gold mineralisations of the area with the gold mineralisations of the whole Voltri Massif.

1 – Introduction

1.1 Aim of the present study

Understanding the development and the evolution of fault zones has always attracted the interest of many geoscientists. All this interest is due to their complex interplay with a wide spectrum of other geological processes; they often change the chemical, physical, and mechanical properties of rocks (like porosity and permeability characteristics), becoming preferential pathways or barriers for fluids circulation, depending on the former properties. When the porosity and the permeability rise up near the fault and along the fault damage zone, the zone becomes like a conduit for the fluids, also enhancing and speeding up the fluid-rock interactions. Field evidence and theoretical considerations indicate that reverse faults and thrust faults could have experienced stages of fault-valve behaviour (Sibson, 1977; Sibson et al., 1988; Sibson, 1992; Shelly et al., 2015; Japas et al., 2016), similar to the stick-slip movement, which consisted in cycles of fluid pressure builds-up, fault opening, fluid flushing, leading to intense fluid-rock interaction and host-rock alteration, possibly with ore mineralisations during the seismic failure of the faults.

This study deals with reverse faults within intensely carbonated meta-lherzolites, with related gold mineralisations, from the Voltri Massif, and in particular within the Lavagnina Lakes area, in the Gorzente Valley. In this area I investigated structures that are possibly related to paleo-seismic events, i.e. micro textures associated to recrystallization over silica gel, carbonates nano-grains coating along slip surfaces, and a novel meso- and microtextures called fault-pearls.

The Voltri Massif is one of the ophiolitic massifs of the Western Alps, and is located at the eastern edge of the Ligurian Alps. The Units of the Voltri Massif experienced a complex Alpine tectono-metamorphic history, evolving from ductile to brittle deformations (Capponi and Crispini, 1997, 2002) and from high-pressure metamorphic conditions to variable retrogressive overprints (Cimmino and Messiga, 1979; Capponi and Crispini, 1997; Desmons et al., 1999; Piana et al 2006). The Oligocene to Present Alpine history, mainly developed under brittle-ductile to brittle conditions, and can be related to polyphasic upper crustal deformations

(Spagnolo, 2004; Spagnolo et al., 2007). Hydrothermal, carbon-rich fluids accompained late- metamorphic deformation stages, characterised by thrust fault, leading to local gold enrichment.

Knowledge of gold occurrences in central Liguria comes from literature. Gold deposits are described in many units, e.g. in the Sestri-Voltaggio Zone and in the ophiolitic rocks belonging to the Internal Ligurian Units, but they are widely developed only in the Voltri Massif and specially in the Gorzente Valley. Most important works about gold occurrences in the Voltri Massif and in the Lavagnina Lake – Gorzente Valley area are due to Buisson and Leblanc (1985a, 1985b) and to Pipino (1976, 1978, 1980, 1982, 2000, 2001, 2003).

The Lavagnina Lakes area is mainly characterised by outcrops of serpentinites, lherzolites, metabasites, metagabbros, and lenses of metasediments s.l. (in decreasing order of areal extension). From a structural point of view, this area is characterised by brittle to brittle-ductile systems of shear zones, with associated carbonates and chalcedony-quartz veins associated with local gold mineralisations.

Hydrothermal, carbon-rich fluids permeated the rocks and sustained these deformation stages producing widespread and intense carbonate-rich alteration zones, exclusive meso- and microstructures within carbonates fault zones, called fault pearls, chalcedony shear veins along fault surfaces, widespread quartz-chalcedony and carbonates veining, and leading to local gold mineralisation.

Since these structures, their superposition, and their interactions with fluids have led to complex multiple generations of fault rocks, to widespread carbonate-rich alteration zones, and to local gold mineralisations the aims of this work are:

- analyse the systems of reverse shear zones that characterise the area;
- investigate the development and the evolution of these systems;
- investigate the seismic behaviour of these faults;
- investigate and quantify the fluid-rock interaction that took place within these faults;
- investigate the structures, and microstructures possibly related to paleo-seismic events;
- investigate the development, the evolution, the chemistry and mineral chemistry, and the seismic behaviour of the novel meso- and microstructures called fault pearls;

- Understand the late- to post-orogenic evolution of the Lavagnina lakes area and Gorzente Valley.

1.2 Milestone of this study

The researches direct to investigate the complex fluid-rock interactions of the Lavagnina Lakes area included several stages:

- field survey, in order to identify the major structures affected by intense fluid-rock interactions;
- representative sampling of the host- and fault rocks;
- production of a geo-referenced map;
- image analyses of fault pearls samples;
- X-Ray Powder Diffraction (XRPD) analysis for preliminary qualitative identification of the mineral assemblages;
- petrographic study of the collected samples, aiming at the definition of their metasomatic processes using transmitted light and scanning electronic microscope (SEM); SEM has also been used for the definition of textural relationships among the minerals and mineral composition;
- high-resolution (10 μm), large-format (1 cm^2) images of the major-, minor-, and trace-element distributions by Laser Ablation Inductively Coupled Plasma Time-of-Flight Mass Spectrometry (LA-ICP-TOFMS) to determine the chemical properties of fault core rocks;
- bulk-rock chemical analyses, necessary to realize the next step;
- mass-transfer calculation necessary to realize the mass-transfer profiles, to monitor chemical exchanges that took place between hydrothermal fluids flowing within the fault, at the time of its slip, and the host lherzolite.

2– Fault related processes

2.1 Introduction

Faults are complex and compound structures found in many geological settings in the upper crust. They are in general mechanically weak, prone to be reactivated during stress build-up, though with rare documented exceptions (e.g. Tavarnelli, 1997). Faults systems control a wide range of crustal processes. Although faults occupy only a small volume of the crust, they have a controlling influence on the crust's mechanical and fluid flow properties (Sibson, 1977; Sibson et al., 1988; Sibson, 1992, 2000, 2001; Faulkner et al., 2010). Fault zones are lithologically heterogeneous, anisotropic and discontinuous. Individual fault zones commonly show significant variation in complexity along strike or down dip, even over relatively short distances (Schulz and Evans, 1998, 2000; Shipton and Cowie, 2001; Kirkpatrick et al., 2008, Lunn et al., 2008; Faulkner et al., 2010). In particular, it is well known that the damage zones, consisting of subsidiary structures through relatively large volume of rock surrounding the fault core, are associated with fault initiation, propagation and termination as well as its long-term evolution (Rawling et al., 2001; Shipton and Cowie, 2001, Faulkner et al., 2003; Faulkner et al., 2010). Damage zones are regarded as a key factor in a variety of geologic fields, such as the deformation processes associated with faulting (e.g. Chester et al., 1993; Schulz and Evans, 1998, 2000; Wilson et al., 2003), strain distribution and deformation history in a region (e.g. Scholz and Cowie, 1990; Walsh et al., 1991; Marrett and Allmendinger, 1992; Schulz and Evans, 2000; Choi et al., 2012, 2016), earthquake rupture propagation and related seismic hazards (e.g. Sibson et al., 1988; Sibson, 2001; Kim and Sanderson, 2008; Choi et al., 2012), and fluid permeability in the crust (Brodsky et al., 2009; Caine and Forster, 2009; Caine et al., 2010; Faulkner et al., 2010; Choi et al., 2016 and reference therein). The last one is particularly important as it is used in practical applications to ground water (e.g. Lopez and Smith, 1995; Bense et al., 2008, 2013; Rotevant and Fossen, 2011 Welch et al., 2014; Cilona et al., 2015), hydrocarbon reservoirs and ore-deposits (e.g. Aydin, 2000; Brogi, 2011), and the underground storage of CO_2 (e.g. Shipton et al., 2004; Kelemen and Matter, 2008; Dockrill and Shipton, 2010; Kelemen et al., 2011; Van Noort et al., 2013).

Fault zone structure, mechanics and permeability can vary strongly both over geological time (e.g. Eichhubl et al., 2009 and reference therein) and at timescales relevant to a variety of industrial applications.

Faults play an important role in controlling the migration of crustal fluids (e.g. hydrothermal fluids or hydrocarbon; Dilles and Einaudi, 1992; Cox et al., 2001; Garofalo, 2004a, b; Cox, 2005; Faulkner et al., 2010; Garofalo et al., 2014 and reference therein). Ore deposits are also commonly related to fault zones due to episodic, localised hydrothermal flows that occur during and immediately after periods of fault movement (e.g. Sibson et al., 1988; Cox et al., 2001; Sibson, 2001; Garofalo, 2004a, b; Cox, 2005; Micklethwaite, 2009; Garofalo et al., 2014).

The structure, the mechanics and the fluid flow properties of the fault zone, are three inextricably coupled, and must recent research reflects efforts to understand the nature and processes behind this coupling (Dilles and Einaudi, 1992; Caine and Forster, 1999; Cox et al., 2001; Cox, 2005; Bense et al., 2008; Caine et al., 2010; Faulkner et al., 2010; Bense et al., 2013). For instance, fault rocks are commonly altered, and are not simply the result of the comminution of their protolith (Kaneko et al., 2017). In fact, in the upper crust, many fault rocks may be viewed as low- to medium-grade metamorphic rocks, with authigenic growth of clay minerals and other minerals (Tembe et al., 2010; Kaneko et al., 2017 and reference therein). A close relation coupling exists between deformation, mechanics and fluid flow in fault zones by deformation- and reaction-driven changes in porosity and permeability, and fluids causing changes in deformation mechanisms through fluid-rock interaction in fault zones (e.g. Schulz and Evans, 1998; Eichubl et al., 2005; Holyoke and Tullis, 2006; Eichhubl et al., 2009; Faulkner et al., 2010; Shelly et al., 2015). The impact on fault rheology, such as by fluid-enhanced reaction softening, may be considerable (Jefferies et al., 2006; Faulkner and Rutter, 2003; Faber et al., 2014).

2.2 Hydrothermal/metasomatic processes

Faults deeply affect the patterns and rates of fluid flow in both modern and paleo-flow systems found in the upper crust. Meteoric water and deep-level fluids may penetrate and influence rocks at depths as deep as 15-20 km and in flow regimes operating on scales ranging from the microscale to basins tens of

kilometres wide (Evans et al., 1997, Wibberley and Shimamoto, 2003; Farough et al., 2016). In fact, faults may act as barriers, conduits, or as fault-valve (Sibson, 1992; Faleiros et al., 2014; Shelly et al., 2015; Japas et al., 2016) that is a mixed conduit/barrier system.

Faults could enhance the rock permeability, through variable degree of fracturing, acting as preferential pathways for fluid migration. Furthermore, the fracturing of the host-rock enhances the reactive surface speeding up the fluid-rock interactions. Moreover the fluids are important features in hydrothermal/metasomatic alterations, and the fluid flow and its interactions with heterogeneous permeability structures in a fault zone can control and influence the seismicity in the upper crust (Lopez and Smith, 1995; Caine and Forster, 1999; Gudmundsson et al., 2010; Evans et al., 2014; Welch and Allen, 2014; Choi et al., 2016).

Hydrothermal/metasomatic alterations developed along faults are example of fluid-rock interactions, and can control the location, emplacement, and evolution of economic mineral deposits and geothermal systems (Sibson, 2001; Micklethwaite, 2009; Groves et al., 2000; Caine et al., 2010; Garofalo et al., 2014; Groves and Santhos, 2016). These alterations are mainly related to the: lithology, fault scale, fault type, deformation style and history, fluid chemistry, and P-T metamorphic conditions (Reed, 1997; Caine and Forster, 1999; Caine et al., 2010; Schandl and Gorton, 2012).

Metasomatic processes, linked to the circulation of CO_2 rich fluids along faults into ultramafic rocks (e.g. peridotites, serpentinites), are exothermal processes (Matter and Kelemen, 2009; Dockrill and Shipton, 2010; Kelemen et al., 2011, Van Noort et al., 2013), which leads to carbonation of the host rocks. Since peridotites and serpentinites are the two main lithologies cropping out in the study area, and the analysed structures are linked to similar processes, the reactions for the carbonation will be briefly described for these two lithologies.

Peridotite is a rock composed of >40% by olivine. Typical residual mantle peridotite exposed on the seafloor and in ophiolites is composed of 70-80% by olivine. Carbonation of olivine occurs together with hydration via simplified reactions (Matter and Kelemen, 2009; Kelemen et al., 2011):

$$4Mg_2SiO_4 + 4H_2O + 2CO_2 = 2Mg_3Si_2O_5(OH)_4 + 2MgCO_3(magnesite) \qquad (1a)$$

$$4Mg_2SiO_4 + 4H_2O + 5CO_2 = 2Mg_3Si_4O_{10}(OH)_2(talc) + 5MgCO_3, \quad and \qquad (1b)$$

$$4Mg_2SiO_4 + 8CO_2 = 4SiO_2 + 8MgCO_3 \qquad (1c)$$

After hydration, carbonation occurs via the simplified reactions (Matter and Kelemen, 2009; Kelemen et al., 2011):

$$4Mg_2SiO_4 + 6H_2O = 2Mg_3Si_2O_5(OH)_4 + 2Mg(OH)_2(brucite) \qquad (1d)$$

$$products\ of\ 1d + 2CO_2 = 2Mg_3Si_2O_5(OH)_4 + 2MgCO_3 + 2H_2O \qquad (1e)$$

$$products\ of\ 1e + 3CO_2 = Mg_3Si_4O_{10}(OH)_2 + 5MgCO_3 + 5H_2O \qquad (1f)$$

$$products\ of\ 1f + 3CO_2 = 8MgCO_3 + 4SiO_2 + 6H_2O \qquad (1g)$$

The second and third most abundant minerals in peridotite are Ca-poor pyroxenes (often termed orthopyroxenes, with Mg-end-member enstatite $Mg_2Si_2O_6$) and Ca-rich pyroxenes (often termed clinopyroxenes, with Mg-end-member diopside, $CaMgSi_2O_6$); hence, it is important to add the simplified reaction (Kelemen and Matter, 2008; Matter and Kelemen, 2009; Kelemen et al., 2011):

$$4Mg_2SiO_4 + CaMgSi_2O_6 + 7H_2O + CO_2 = 3Mg_3Si_2O_5(OH)_4 + Ca^{2+}_{(aq)} + 2OH^- \qquad (1h)$$

$$Ca^{2+}_{(aq)} + 2OH^- + CO_2 = CaCO_3 + H_2O \qquad (1i)$$

But, these reactions may generally be formulated as described by Kelemen and Matter (2008):

$$Mg_2SiO_4 + CaMgSi_2O_6 + 2H_2O + 2CO_2 = Mg_3Si_2O_5(OH)_4 + (Ca, Mg)(CO_3)_2 \qquad (1l)$$

The carbonation over serpentinites occur via the simplified reactions (Kelemen and Matter, 2008; Matter and Kelemen, 2009; Kelemen et al., 2011):

$$4Mg_2SiO_4 + 6H_2O = 2Mg_3Si_2O_5(OH)_4 + 2Mg(OH)_2(brucite) \quad (2a)$$

$$products\ of\ 1 + 2CO_2 = 2Mg_3Si_2O_5(OH)_4 + 2MgCO_3 + 2H_2O \quad (2b)$$

$$products\ of\ 2 + 3CO_2 = Mg_3Si_4O_{10}(OH)_2 + 5MgCO_3 + 5H_2O \quad (2c)$$

$$products\ of\ 3 + 3CO_2 = 8MgCO_3 + 4SiO_2 + 6H_2O \quad (2d)$$

These reactions are written without other components than H_2O and CO_2 in fluids; however, they can change when other components, such as aqueous silica, Ca^{2+}, H_2, and sulphur species, are considered to be transported in fluids. However, the silica produced by the carbonation, visible in equation 1g and 2d, is released into the fluids, and generally deposits as chalcedony (Boschi et al., 2009).

Infiltration of such fluids in ultramafic rocks results in significant amounts and a broad-spectrum of metasomatic rocks (Hansen et al., 2005; Kelemen and Matter, 2008; Matter and Kelemen, 2009; Kelemen et al., 2011; Van Noort et al., 2013; Ulrich et al., 2014; Peuble et al., 2017). For example the hydrothermal/metasomatic process occurring along fault inside serpentinites produces variously carbonated rocks for example: listvenites (quartz-carbonate-chromium mica association), quartz-carbonate rocks (silica- carbonate association), carbonate-rich rocks, serpentine- talc- (chlorite)- carbonate rocks, talc-carbonate rocks and talc-silica-carbonate rocks are examples of products of hydrothermal/metasomatic alteration (Hans et al., 2005; Akbulut et al., 2006; Van Noort et al., 2013; Ulrich et al., 2014). These kind of carbonated rocks, and in particular listvenites are genetically linked to gold mineralisation.

Moreover, these processes incorporate carbon dioxide into stable mineral carbonate phases trapping safely CO_2 over geological times (Kelemen and Matter, 2008; Boschi et al., 2009; Matter and Kelemen, 2009; Dockrill and Shipton, 2010; Kelemen et al., 2011 and references therein); it represents the natural analogue of in situ CO_2 mineral sequestration. The in situ CO_2 mineral sequestration was proposed by Seifritz (1990) and it is an induced industrial exothermic alteration of

metal-rich non- carbonate minerals (i.e., Mg_2SiO_4 olivine, $Mg_3Si_2O_5(OH)_4$ serpentine, $Mg_2Si_2O_6$ enstatite, $CaMgSi_2O_6$ diopside) to geologically and thermodynamically stable mineral carbonates (i.e., $MgCO_3$ magnesite, $(Ca,Mg)(CO_3)_2$ dolomite, $CaCO_3$ calcite, $FeCO_3$ siderite; Boschi et al., 2009) in order to reduce the anthropogenic carbon dioxide pollution.

Moreover, the carbonation of ultramafic rocks along fault is an important geological process, with implications that include formation of ore deposits. For example many mesothermal gold-quartz deposits are localized along high-angle reverse or reverse-oblique shear zones within ultramafic rocks.

2.3 Earthquake-related deformational processes

Particularly in the last decades, exhumed fault zones represent an engaging geological topic, since they may offer, among others, insights into earthquake-related deformational processes, the main issue being the distinction between seismic and aseismic slip (Boutareaud et al., 2008, 2010; Smith et al., 2011; Viganò et al., 2011; Fondriest et al., 2012; Rowe and Griffith, 2015; Viti et al., 2016; Chen et al., 2017).

For a long time, identifying unambiguous seismic slip in a rock record relied on the recognition of tectonic pseudotachylites (Billi et al., 2008; Kirkpatrick and Rowe, 2013; Rowe and Griffith, 2015), which have become a sort of holy grail for geologist interested in studying seismic processes (Kirkpatrick and Rowe, 2013; Rowe and Griffith, 2015). Pseudotachylites, however, are rare in comparison to the seismic activity in the Earth's crust (Kirkpatrick and Rowe, 2013; Rowe and Griffith, 2015), they develop only in crystalline rock and hence are basically absent in fault-zones hosted in carbonate-bearing rocks (e.g. Billi et al., 2008). In carbonate-bearing rocks, in contrast, fault rock assemblages such as pulverized rocks or fluidized gouges occur rather frequently. In fact, many authors suggest that during seismic slip along faults in carbonate-bearing rocks, thermal decomposition of carbonates produce slip weakening (e.g. Novellino et al., 2015), before to reach necessary conditions for the development of pseudotachylites. However, Viganò et al. (2011) described fault- and injection-veins with carbonate-rich matrix and their data suggest that this matrix represent the result of an undercooled carbonate melt-bearing assemblages.

Actually, pseudotachylites are no longer the unique unequivocal record of paleo-seismic fault. Many processes possibly linked to seismic events, other than shear-related melting, have been investigated, like the processes which lead to fault strength reduction as flash heating (Rice et al., 2006; Goldsby and Tullis, 2011; Weatherley and Allen, 2014; Hayward et al., 2016), nanograins coating along slip surfaces (Schleicher et al., 2010; Siman-Tov et al., 2013) thermal decomposition of carbonates (Han et al., 2007; Sulem and Famin, 2009; Collettini et al., 2013; Novellino et al., 2015), silica gel formation (Kirkpatrick et al., 2013; Faber et al., 2014; Prokofiev et al., 2017).

Thermal decomposition of carbonates during seismic slip may be recorded, even when peak temperature does not exceed the local fault rock solidus (Rowe and Griffith, 2015). In particular, hydrous and carbonate minerals have been shown to thermally dissociate during fast slip. Dissociation leaves volatiles and amorphous or nano crystalline materials that are potentially reactive with fluids and surrounding minerals, and unstable over geologic time (e.g. CaO, Han et al., 2007). The recrystallization of these products may occur immediately post-seismically, or after the fault has cooled. In the former case, the new minerals may record higher than ambient temperatures, or in the latter, the pre-seismic mineralogy may be reproduced by back-reaction of the dissociation products.

High-velocity friction experiments have shown an almost complete loss of strength associated with silica gel formation on slip surfaces. The identification of frictional silica gel products in paleo-seismic faults is, however, problematic, because there are multiple natural sources of silica gel and recrystallization of gel to quartz complicates preservation.

In addition, many other structures have been proposed as potentially seismic indicators, for example: mirror-like slip surfaces (Siman-Tov et al., 2013; Evans et al., 2014; Rowe and Griffith, 2015; Viti et al., 2016), and clast-cortex aggregates (Boutareaud et al., 2008, 2010; Smith et al., 2011; Rempe et al., 2014; Rowe and Griffith, 2015), even if no general *consesu* still exists on their interpretation.

3 – Geological framework of the area

3.1 – The Western Alps

The Alps are a double vergent orogen that developed since the Cretaceous, as the result of the convergence between Europe and Adria (Vanossi, 1984; Vanossi et al., 1986; Polino et al., 1990, 1995; Beltrando et al., 2010; Malusà et al., 2005, 2016 and references therein) which is alternatively considered as a promontory of Africa or as an independent micro-plate (Dewey et al., 1989; Rosenbaum et al., 2002; Beltrando et al., 2010). The convergent evolution involved the continental margins, of these plates, and the western Tethys, i.e. the Jurassic Ligurian-Piedmontese ocean, lying in between; slices of continental mantle were also involved (i.e. in the Lanzo Massif; Nicolas et al., 1972; and in the Voltri Massif; Piccardo et al., 1988). Convergence was accommodated by the E-SE dipping subduction (e.g. Polino et al., 1990, 1995; Stampfli et al., 1998) of the Ligurian–Piedmont oceanic lithosphere below the Adriatic plate, and then evolved to continental collision with the arrival at the subduction hinge of the European lithosphere during the middle Eocene.

The following exhumation occurred at the Eocene-Oligocene boundary (Carrapa et al., 2016), in different sectors of the Western Alps through different mechanisms, such as crustal thickening (e.g. for the Briançonnais units, Maino et al., 2012), by mass transfer in a low viscosity subduction channel (e.g. the Ligurian-Piedmontese units, Federico et al., 2005, 2007), or such as crustal thickening (Schwartz et al., 2017). The emplacement of the exhumed rock bodies with a vergence towards paleo-Europe built up the Alpine belt, which resulted from the structural stack of several units, heterogeneous from both the point of view of the paleogeographic derivation and the structural-metamorphic evolution (Capponi et al., 2016).

The ongoing convergence of the European and Apulian plates was then accommodated by a W directed subduction (i.e. “Apenninic” subduction) which later resulted in the Apennine orogenic phase (Elter & Pertusati, 1973; Molli et al., 2010). The transition from an E-SE dipping subduction (i.e. “Alpine” subduction) to a W directed subduction (i.e. “Apenninic” subduction) is a matter of debate. A twist in the direction of subduction (e.g. Doglioni et al., 1998; Handy et al., 2010) is the

most usual explanation, but many other geodynamic models have also been proposed for the Alps- Apennine transition (e.g. Hoogerduijn Strating, 1990, 1991, 1994; Faccenna et al., 2004; Vignaroli et al., 2008); however, an in-depth discussion of this topic is beyond the scope of this work.

The Alps may be subdivided into two belts of differing size, age and geological meaning: 1) the Europe-vergent belt, a thick collisional wedge of Cretaceous-Neogene age, consisting of continental and minor oceanic units radially displaced towards the Molasse foredeep and European foreland; 2) the Southern Alps, a minor, shallower (non-metamorphic) and younger (Neogene) thrust-and-fold belt displaced to the south (Adria-vergent), which developed within the Alpine hinterland of the Adria upper plate, far from the oceanic suture (Dal Piaz and Gosso, 1994; Dal Piaz, 1999, 2001; Dal Piaz et al., 2003). These belts are separated by the Periadriatic (Insubric) lineament, a major fault system of Oligocene-Neogene age (Dal Piaz and Gosso, 1994; Dal Piaz, 1999, 2001; Dal Piaz et al., 2003).

From top to bottom and from the internal to the external side, the principal Europe-vergent tectonic domains are are (Fig. 1): *i*) the Austroalpine composite nappe system, derived from the distal part of the Adriatic passive continental margin, which mainly developed during the Cretaceous (Eoalpine) orogeny; *ii*) the Penninic zone, a stack of metamorphic nappes, scraped off the subducting oceanic lithosphere and European passive continental margin, mainly accreted during the Paleogene; and *iii*) the Helvetic zone, consisting of shallower basement slices and detached cover units derived from the proximal part of the European margin, mainly imbricated from the Oligocene onwards (Dal Piaz and Gosso, 1994; Dal Piaz, 1999, 2001; Dal Piaz et al., 2003).

The deep anatomy of the Alps has been explored by the deep seismic experiments, identifying two distinct Moho surfaces, i.e., the Adriatic and the deeper European Moho, gently bending from the Alpine foreland to the deep base of the collisional wedge (Dal Piaz and Gosso, 1994; Dal Piaz, 1999, 2001; Dal Piaz et al., 2003). This means that the overall setting of the Alps is asymmetric: the orogen was dominated by Europe-vergent displacements, and the antithetic Southalpine belt is only a superficial feature within the Adriatic upper plate. Integrating the surface geology with the interpretation of seismic images, the Europe-vergent belt is a mantle- free crustal wedge which tapers to the north, floats on top the European lower plate and is indented, to the south, by the present

Adriatic (Southern Alps) lithosphere (Dal Piaz et al., 2003).

Both continental plate margins originally extended into the Penninic-Helvetic and Austroalpine domains are presently incorporated into the collisional belt. This wedge may be subdivided into two diachronous parts: *i*) the internal older part (Austroalpine-Penninic), which forms now the axial zone of the Alps (Dal Piaz and Gosso, 1994; Dal Piaz, 1999, 2001; Dal Piaz et al., 2003); it is a exhumed subduction complex which includes the Adria/Europe collisional zone, and it is marked by one or more ophiolitic units (in different areas). It displays polyphase metamorphism evolving from blueschist or eclogite facies imprint (Cretaceous-Eocene subduction), locally coesite-bearing, to a Barrovian overprint (mature collision, slab break-off) of Late Eocene-Early Oligocene age (Frey et al., 1999). *ii*) The outer, younger part (Helvetic), which is made up of shallower basement thrust-sheets and by detached cover units derived from the proximal European margin, that escaped the low-T subduction regime and that, from the Oligocene, were accreted in front of the exhumed Austroalpine-Penninic wedge (Dal Piaz and Gosso, 1994; Dal Piaz, 1999, 2001; Dal Piaz et al., 2003).

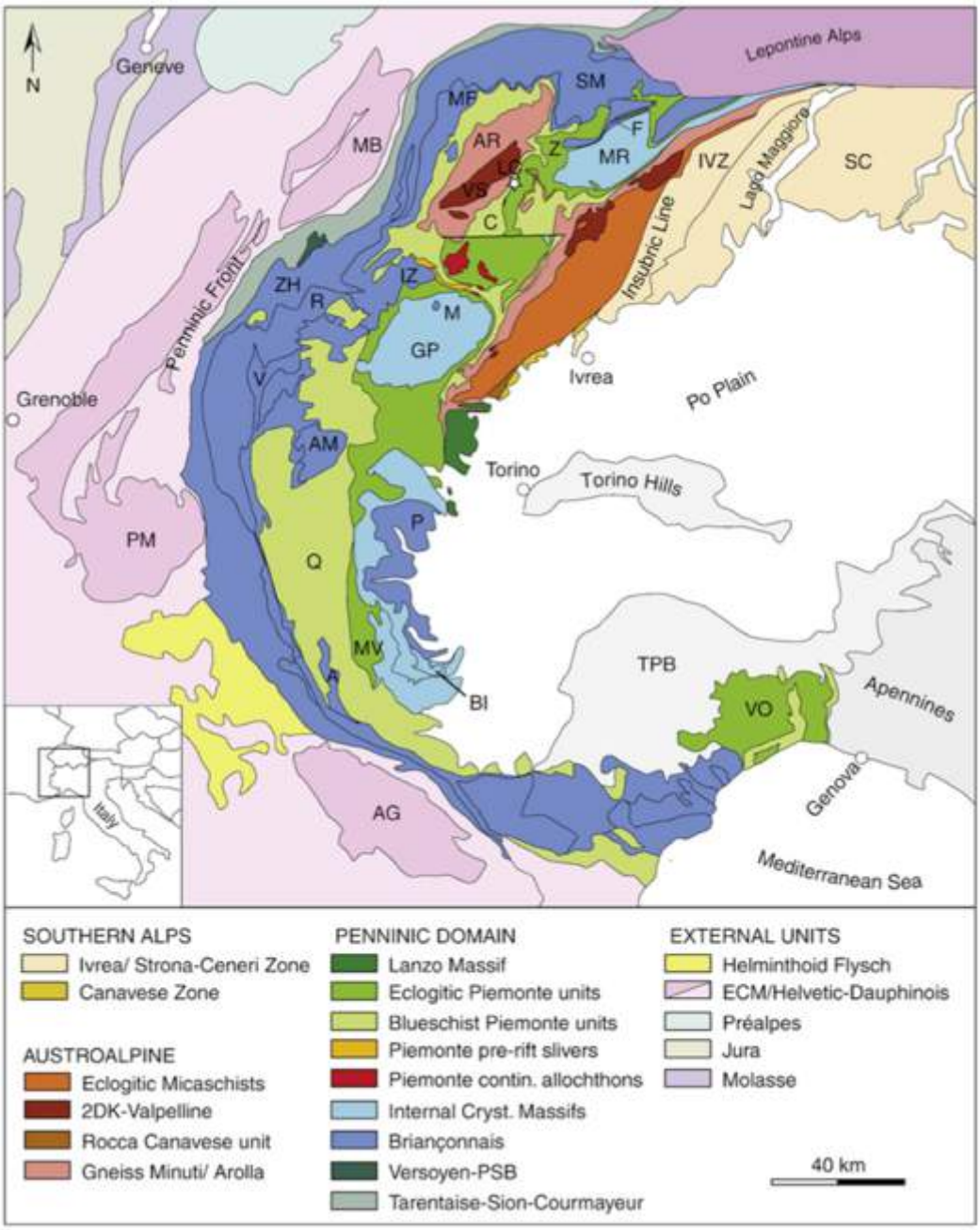

Figure 1: Tectonic map of the Western Alps (Redrawn by Beltrando et al., 2010) A: Acceglio Zone; AG: Argentera Massif; AM: Ambin Massif; AR: Arolla Series; BI: Brossasco–Isasca UHP Unit; C: Combin Zone; ECM: External Crystalline Massifs; F: Furgg Zone; GP: Gran Paradiso Massif; IVZ: Ivrea Zone; IZ: Internal Zone; LC: Lago di Cignana UHP Unit; M: Money Unit; MB: Mont Blanc Massif; MF: Mont Fort Unit; MR: Monte Rosa Massif; MV: Monviso Massif; P: Pinerolo Unit; PM: Pelvoux Massif; Q: Queyras Schistes Lustrés; R: Rutor Massif; SL: Serie dei Laghi; SM: Siviez–Mischabel; TPB: Tertiary Piemonte Basin; VA: Vanoise; VO: Voltri Massif; VS: Valpelline Series; ZH: Zone Houillère; ZS: Zermatt–Saas Zone. Star indicates location of the UHP Lago di Cignana Unit.

3.2 – Exhumation and late orogenic tectonics

Since this work deals with the study of the late- to post orogenic deformations, this topic will be dealt with more detail.

The axial domain of the north-western Alps is characterised by polyphase metamorphic history and superposed and penetrative ductile deformation, and also by brittle deformation (i.e. brittle faulting). The importance of the brittle faulting has been underestimated for a long time (Bistacchi and Massaroni, 2000; Bistacchi et al., 2000, 2001 and reference therein), Only recently, following several examples from other orogens, an increasing interest has been addressed to the late-collisional tectonics in shaping the present-day Alps (Bucher et al., 2003; Bertrand and Sue, 2017).

According to the literature, the final exhumation of the Penninic-Austroalpine nappe stack was accomplished, from the Oligocene to the Present, could be summarized through the following steps:

(a) Oligocene extension coupled with the Periadriatic magmatism and emplacement of gold-bearing quartz veins (Dal Piaz et al., 1979; Venturelli et al., 1984; Diamond, 1990, 1993; Dal Piaz and Gosso, 1994, Dal Piaz et al., 2003).

(b) Differential exhumation at the Oligocene-Miocene boundary evidenced by thermochronological data (Hurford et al., 1991; Hunziker et al., 1992) and characterised by increasing exhumation rates toward the north (Malusà et al., 2005, 2016). Such differential exhumation was accommodated in the northern portion of the belt thanks to reverse motion along the Internal Houiller Fault, which occurred in a convergent transcurrent framework. To the south, it was accommodated instead by normal reactivation of the Briançonnais Front and by activity of the Longitudinal Fault System, which occurred in a divergent transcurrent framework (Malusà et al., 2005, 2016 and reference therein). This event is generally considered to be a consequence of back-thrusting and back-folding, which were in turn generated by the counterclockwise rotation of the Corsica-Sardinia block (Schmid et al., 1989; Polino et al., 1990; Giglia et al., 1996, Maino et al., 2013).

(c) Rapid exhumation of the western sector of the Lepontine dome (Simplon sub-dome, *Auct.*) from 18 to at least 3 Ma, accommodated by

normal displacement along the Simplon fault (Mancktelow, 1997 and references therein) and coupled with SW-ward gravitational lateral extrusion of the Pennine-Graian Alps block bounded by other major faults (Bistacchi et al., 2000).

Moreover, in literature (Mancktelow 1985, Schmid et al. 1989, Laubscher 1992, 1996; Steck and Hunziker 1994, Eva and Solarino, 1998; Bistacchi et al., 2000; Bucher et al., 2003), the Neogene tectonic evolution of the Western Alps is described as dominated by discontinuous deformation which causes the subdivision of the pre-Neogene orogenic wedge into a number of blocks which accumulated a relative low-amount of strain (*low-strain block concept*, Perrello et al. 2004 and quoted references), separated by late- to post-metamorphic high-strain fault zones.

In the last years, different kinematic interpretations have been proposed for the Miocene-Present evolution of the Alpine belt, mainly for the inner portion of the north-western Alps:

Eva and Solarino (1998) suggested a major role of extensional collapse perpendicular to the belt axis, and this is supported by seismotectonic and geological data for the southern portion of the Western Alps (Eva and Solarino 1998; Sue and Tricart 2003). A NW–SE striking right-lateral fault system, which follows the general curvature of the arc and controls the overall morphology of the area, dominates the regional-scale fault network. A second fault set strikes N–S and is mainly represented by normal faults which accommodate orogen-parallel extension. Structural analysis and paleostress tensors derived from inversion of fault-slip data reveal a complex pattern of deformation involving extensional and strike-slip deformation events. Bucher et al., (2003) show that the orogen-parallel extension is combined with right-lateral strike- slip deformation that increases in intensity towards the south-west.

The opening of the Ligurian basin during the early-middle Miocene could be the free boundary necessary for such a large-scale orogen-parallel extension in the north-western Alps. This lateral extrusion event is no longer active. From Pliocene to Present an orogen-perpendicular extension (reminiscent of the “orogenic collapse” model) leads to the current state of stress in the Alpine belt as indicated by fan-like extension directions at high-angle with respect to the strike of the Alpine arc.

The predominance of dextral strike-slips and their radially changing orientation in a fan-like pattern has led some authors to consider rotation, rather than sideways extrusion as an alternative large-scale process at the NW tip of the Adriatic indenter (Pavoni 1991, Pfiffner et al., 2000; Collombet et al., 2002; Pfiffner, 2016; Favaro et al., 2017). Rotation models are supported by geomagnetic data that documented large anticlockwise vertical axis rotation of up to 90° and more, increasing southward along the arc of the Western Alps (Collombet et al., 2002). Intermediate models with anticlockwise rotation and lateral expulsion of a large block, belonging to the European margin, were envisaged by Vialon et al. (1989) to accommodate the Adria plate north-western indentation and to explain the dextral transcurrence along the Rhone-Chamonix system by means of main horizontal movement, disregarding gravitational effects.

A major role of maximum horizontal compression and models with a double lateral escape and a central indenter have been proposed by Giglia et al. (1996): they envisaged a seismotectonic model in which the frontal Penninic thrust and the basal surface of the accretionary wedge corresponding to the Penninic sole thrust are reactivated during Miocene to Present evolution. Activity along the frontal thrust increases the arcuate shape of the Western Alps and disengages them from the Central and the Ligurian Alps along the tear faults of the Simplon-Centovalli-Tonale system (main dextral transcurrence) and the Stura "couloir" (main sinistral transcurrence) respectively.

3.3 – The Ligurian Alps

The Ligurian Alps are the south-eastern sector of the Western Alps (Fig. 1) and, for their geologic and geographic position, represent a link between the Alpine belt and the Northern Apennine (Cortesogno et al., 1979; Cortesogno and Haccard, 1979, 1984; Hoogerdujn Strating, 1991; Molli, 2008; Molli et al., 2010). The present-day architecture of the Ligurian Alps is currently a topic of debate, but for many authors, the present architecture is the result of the relative movements of three main plates (Africa, Adria and Europe) and the closure of an interposed

oceanic basin, which led to the formation of the Alpine belt (Scrocca et al., 2003; Molli et al., 2010 and reference therein).

The Ligurian Alps are made up of a nappe pile, from the top to the bottom, constituted namely by: the Ligurian-Piedmontese, Piedmontese/Pre-Piedmontese and Briançonnais tectonic units, all stacked onto the Duphinois domains (Vanossi, 1984; Vanossi et al., 1986; Stampfli 1993; Dal Piaz, 1999, Seno et al., 2005; Molli et al., 2010; Decarlis et al., 2013).

The units of the Ligurian Alps are overlain by the late- to post-orogenic clastic sediments of the (Upper Eocene)- Oligocene to Miocene Tertiary Piedmont Basin (TPB) that is a syn-tectonic Neo Alpine-Apennine Basin (Lorenz, 1968; Gelati and Gnaccolini, 1988; Mutti et al., 1995; Gelati and Gnaccolini, 1998; Federico et al., 2004; Maino et al., 2013).

During the same period, the opening of the Ligurian-Provençal Basin caused the counterclockwise rotation of the Corsica-Sardinia block, and the related torsion of the Western Alps. The result was that the Ligurian Alps was rotated by tens of degrees to the present WNW-ESE structural trend (e.g. Vanossi, 1984; Maffione et al., 2008; Decarlis et al., 2014), contrasting with the N-S to NNE-SSW trend of most of the Western Alps. This tectonic event resulted in a top-to-the E-NE backthrusting of the involved units, including the TPB, which partially acted as a piggy-back basin (Mosca et al., 2010; Maino et al., 2013), and affected their internal structural architecture, with thrust faults, strike-slip faults and folds that accommodated a SW-NE shortening (Crispini et al., 2009; Federico et al., 2009, 2014).

3.4 – The Voltri Massif

The Voltri Massif (Fig. 2) crops out at the easter termination of the Ligurian Alps. It is part of the Penninc ophiolites, which represent the dismembered Jurassic Piedmont-Ligurian Ocean; it is a metaophiolitic massif associated with metasediments that were involved in the Alpine orogenic events and experienced a complex tectono- metamorphic evolution, with blueschist- to eclogite- facies peak metamorphism with variable retrogressive overprints (Chiesa et al., 1975; Capponi, 1987, 1991; Capponi et al,. 1994, 2016; L. Crispini, unpub. Ph.D. thesis, Univ. degli

Studi di Genova, 1996; Capponi and Crispini, 2002, 2008; Federico et al., 2007; Malatesta et al., 2012; Scarsi et al., 2017).

Consequently, these units show several superimposed deformations, evolving from syn-metamorphic, ductile regime to brittle- ductile and brittle regime (Capponi, 1987; Capponi et al., 1999).

Hereafter the terms Voltri unit and Palmaro-Caffarella Unit (Fig. 2) will be used in the sense of Capponi et al. (2008). The term "Voltri Massif" is maintained as a general term that includes both the Palmaro-Caffarella and the Voltri units.

For a review of the interpretations of the Voltri Massif see Capponi et al. (2016).

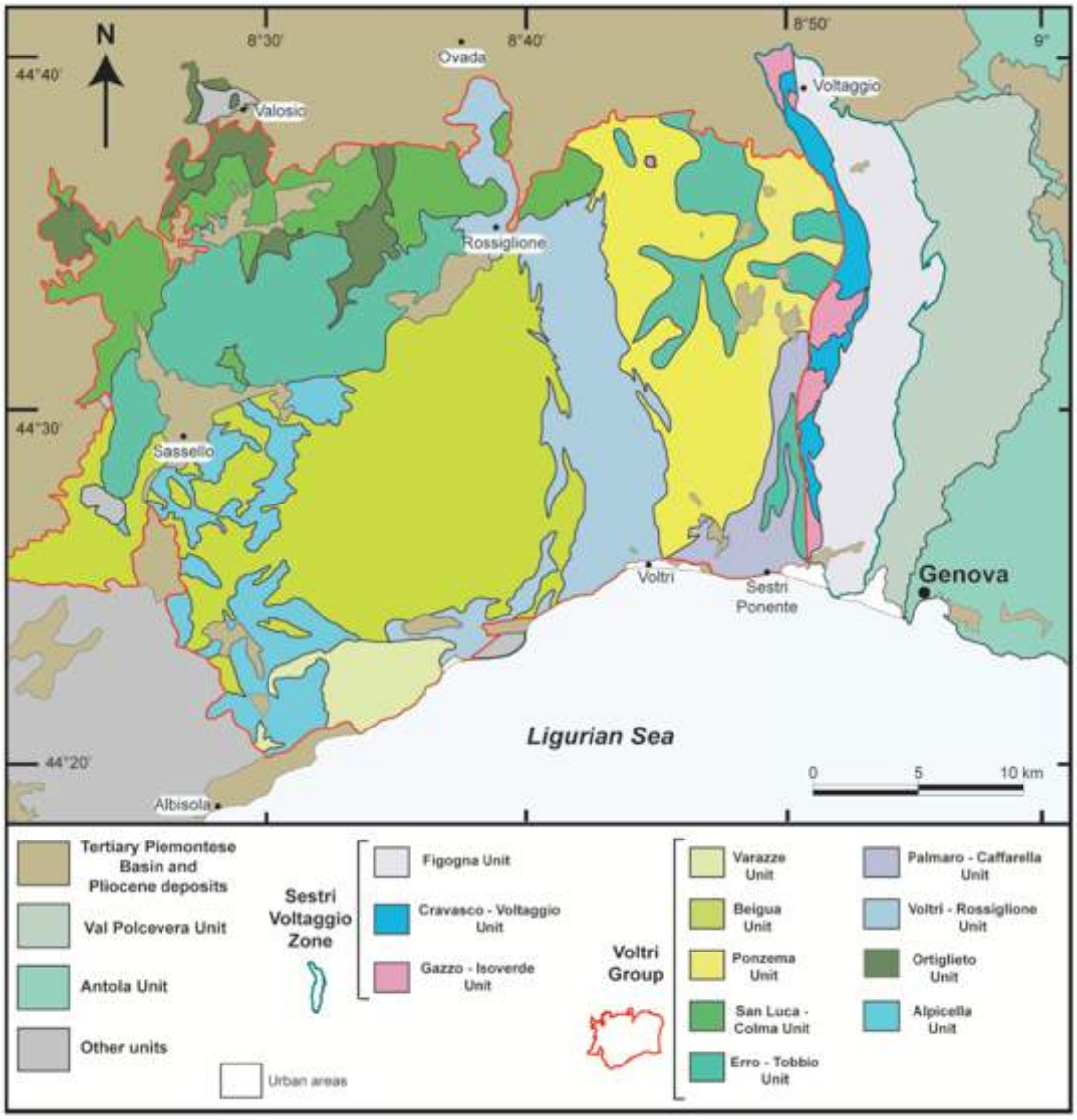

Figure 2: Tectonic sketch map of the eastern Ligurian Alps (Capponi et al., 2016), with the units of the Voltri Group (after Chiesa et al., 1975) and the Sestri Voltaggio Zone (Cortesogno and Haccard, 1984).

3.5 – The boundaries of the Voltri Massif

In the north, the Voltri Massif, is bordered by the Tertiary Piedmont Basin and by the Valosio Massif, in the east by the Palmaro-Caffarella Unit, and by the Sestri-Voltaggio zone, in the south by the Arenzano Massif and by the coastline, and finally in the west by the Savona Massif and by the Montenotte nappe.

The Tertiary Piedmont Basin (TPB) consists of late- to post- orogenic deposits outcropping in the northern part of the Voltri Unit and in some isolated outcrops in the southern part. These deposits unconformably overlie the Alpine and Apennine Units and have been involved in the late-orogenic deformational events (Gelati and Gnaccolini, 1988, 1998; Federico et al., 2004; Rossi et al., 2009; Maino et al., 2013).

The Valosio Massif consists slices of paragneiss, orthogneiss, garnet-mica-schists, amphibolites, and silicate-bearing marbles outcropping in the northwestern boundary of the Voltri Unit. These rocks record poli-metamorphic pre-Alpine events and Alpine deformational events and metamorphism in eclogite facies (Messiga et al., 1992). The Voltri Unit overthrusting onto the Valosio Massif has been referred to the mesoalpine tectonics and partially to the later brittle tectonics (Forcella et al., 1973; Cabella et al., 1991; Piana et al., 1997).

The Palmaro-Caffarella Unit consists of metasediments, metabasalts, metagabbros, and serpentinites. It occupies a peculiar position, since it is intermediate between the eclogitic Voltri Unit and the blueschist units of the Sestri-Voltaggio zone (Federico et al., 2004). The Palmaro-Caffarella Unit record blueschist conditions with high temperatures, with no evidences of an eclogitic event (Cortesogno et al., 1977; Cabella et al., 1994). Malatesta et al. (2012) recently provided a pseudosection study for a Palmaro-Caffarella metagabbro, indicating blueschist facies peak metamorphic conditions of $10<P$ (kbar)<15 and $450<T$ (°C)<500; no eclogite relics occur in the metagabbro.

To the east two blueschist facies units bound the Voltri Unit: the Cravasco-Voltaggio Unit and the Gazzo-Isoverde Unit, which together with the low grade Monte Figogna Unit have usually been referred as the "Sestri-Voltaggio Zone" (Cortesogno and Haccard, 1984).

These units have been involved in the Alpine subduction-related deformational events and underwent metamorphic re-equilibration under different metamorphic peak conditions (Federico et al., 2004):

- the Cravasco-Voltaggio Unit crops out along a N-S elongated band; the Figogna and the Palmaro-Caffarella Unit bound it. The Cravasco-Voltaggio Unit consists of metaophiolite and related metasediment, equilibrated in LT blueschist facies metamorphic peak conditions (Cabella et al., 1994) with a following metamorphic imprint at lower pressure;

- the Figogna tectono-metamorphic unit crops out along a N-S elongated band, which follows the Sestri-Voltaggio zone. The Figogna Unit consists of metaperidotitic basement and relatively metasedimentary covers, characterised by pumpellyite-actinolite facies, in the lawsonite stability field (Cortesogno and Haccard, 1984);

- the Gazzo-Isoverde Unit is characterised by metasedimentary slices, made up of dolostone with evaporate horizons, limestone and schists, with Piedmont affinity (Cortesogno and Haccard, 1979).

The Arenzano Massif consists of pre-alpine gneisses, amphibolites, and metasedimentary covers probably belonging to the Briançonnais domain (Cortesogno and Forcella, 1978). These rocks crop out along the coast between Arenzano and Cogoleto villages. The Arenzano Massif has been involved in the Alpine tectonics recorded by local high strain shear zones, and experienced high-pressure metamorphism. The tectonic limit between the Arenzano and the Voltri Unit is represented by E-W oriented faults, steeply dipping to the South (Cortesogno and Forcella, 1978).

The Savona Massif is made up by basement slices of gneisses, amphibolites and granitic rocks, that can be ascribed to the Briançonnais domain (Vanossi, 1984). These rocks outcrop at the southwestern limit of the Voltri Unit, and experienced poliphasic pre-alpine syn-metamorphic deformation, locally overprinted by an alpine blueschist facies event.

The Montenotte nappe crops out along the southwestern margin of the Voltri Unit; it encompasses a metamorphosed ophiolitic succession, made up of predominant metagabbro (both Fe-and Ti-oxide-rich and Mg-rich varieties), metabasalt and serpentinite, plus the metamorphosed sedimentary cover comprising metachert, meta-limestone and phylladic schist (Capponi et al., 2016,

Malatesta et al., 2017). The Montenotte unit record a blueschist facies peak metamorphic condition (Capponi et al., 2013), locally overprinted by greenschist-facies metamorphic conditions.

3.6 – Voltri Massif Structural evolution

The Voltri Massif units underwent a complex Alpine structural and metamorphic evolution, from the Alpine orogenesis, to subduction-related events to uplift- and exhumation-related events.

During subduction the Voltri Unit reached depth of 50-70 km, and was re-equilibrated under metamorphic conditions from eclogite to blueschist facies (T=450-500°C and P=13-20 kbar; Messiga et al., 1983; Messiga, 1987; Messiga and Scambelluri, 1991; Desmons et al., 1999); the Palmaro-Caffarella Unit was re-equilibrated under blueschist facies without evidences of an eclogitic event (T=400°C and P=13 kbar; Cortesogno et al., 1977; Cabella et al., 1994). The tectonic stacking of eclogite and blueschist unit has been related to the early stages of the exhumation processes (Federico et al., 2004).

During the subsequent uplift, these units have been re-equilibrated under greenschist and sub greenschist facies (Cimmino and Messiga, 1979; Capponi and Crispini, 2002).

The structural evolution of these units is recorded by several superposed deformation, developed under decreasing P-T conditions and evolving from ductile to brittle regime. The deformational events can be summarized as follows (Fig. 3, Capponi and Crispini, 2002):

- HP-LT structures (pre-D1): linked to subduction and coeval with the eclogite stage. They show eclogite-blueschist facies foliation, rootless hinges of isoclinal folds. These structures are widespread all over in the Voltri and Palmaro-Caffarella units, but they don't show lateral continuity and so are not easily to correlate at regional scale;
- D1/D2 structures: related to exhumation and uplift processes, developed under Na-amphibole greenschist facies to greenschist s.s. conditions. They are represented by tight to isoclinal similarfolds, from cylindrical to highly non-cylindrical (Capponi et al., 1994). The overprinting of D1 and D2

schistosity plus the previous foliation, including the lithological surface, make a Composite Fabric (CF), which is the most evident surface in the field and controls the lithological contact. The juxtaposition between the Voltri and the Palmaro-Caffarella Unit has been related to the early exhumation stages (Federico et al., 2004);

- Ductile structures recording Extension Parallel to the Foliation (EPF): related to the nappe emplacement, developed under greenschist facies conditions. They are represented by: shear bands, boudins, foliation boudinage, and extensional veins (Capponi and Crispini, 1997). These kind of structures are characteristics of areas with high deformation degree (Platt and Vissers, 1980; Ramsay and Huber, 1987);

- Reverse Shear Zones (RSZs): related to the nappe emplacement, developed from greenschist to subgreenschist facies. They are represented by ductile to brittle-ductile shear zones, with related protomylonites and mylonites (sensu Sibson, 1977);

- D3 structures: linked to post-uplift collapsing processes, developed under greenschist facies conditions. They are represented by chevron folds with sub-horizontal axial plane and by ductile to brittle-ductile shear zones (Capponi, 1991; Capponi et al., 1994);

- D4 structures: related to backfolding and backthrusting systems, accompanied by zeolite facies re-crystallization. Highly asymmetrical open folds represent them, with wavelengths up to 10 km. These folds can evolve to reverse faults, with linked fault rocks classifiable as: crush-breccias, crush-microbreccias, protocataclasites, cataclasites and rarely pseudotachylites (sensu Sibson 1977; Capponi et al., 1999; Capponi and Crispini, 1997).

Deformations older than D4 are unequally developed in different sectors of the massif, while D4 occurs with similar features over the whole Voltri Massif.

D3 structures are different in the eastern and western sector, since they accommodate vertical shortening/horizontal extension and the development of folds or shear zones is driven by the attitude of regional foliation.

Substantial differences also exist in the progressive greenschist facies deformation, called D1/D2 structures, an unequal strain distribution with the D2 stain intensity increasing from west to east.

Both the dip change in regional foliation and the increasing strain intensity are explained by strain partitioning along the Sestri-Voltaggio zone acting in a contractional/transpressional regime (Capponi and Crispini, 2002).

Deformation	Tectonic event	Fabric	Metamorphism	Vergence
Early (preD_1) deformations	subduction	rootless hinges of isoclinal folds and related schistosity	eclogite to blueschist facies	unconstrained
D_1/D_2	exhumation-uplift of the metamorphic units and nappe emplacement	tight to isoclinal similar folds and related schistosity	Na-amphibole greenschist to greenschist facies s.s.	unconstrained
EPF extension parallel to the foliation	nappe emplacement	shear bands, boudinage, foliation boudinage, extensional veins	greenschist facies	scattered directions, with a NE-SW maximum
RSZ reverse shear zones	nappe emplacement	reverse, ductile to brittle-ductile shear zones	greenschist to low greenschist facies	top to SW minor top to SE and NW
D_3	post-uplift collapsing	chevron folds with sub-horizontal axial plane ductile to brittle-ductile normal shear zones	low greenschist facies	vertical shorthening horizontal extension
D_4	backthrusting	open folds thrust faults	zeolite facies	top to E-NE

Figure 3: Summary table of deformational, tectonic events, and metamorphic conditions (Capponi and Crispini, 2002).

Recent works suggest that the eastern sector of the Voltri Massif could represent a "fossil" serpentinite subduction channel (Federico et al., 2007; Malatesta et al., 2012) instead the tectonic units to the east (i.e. the Palmaro-Caffarella, Cravasco-Voltaggio, Gazzo-Isoverde and Figogna units) could represent slices subducted at different depths and then accreted to the orogenic prism.

3.7 – Sestri-Voltaggio Zone

Görler (1962), Ibbeken (1962), Görler and Ibbeken (1964) defined the Sestri-Voltaggio Zone as a complex of rocks, occurring from Sestri Ponente to Voltaggio (Fig. 2) in a 5-6 km-wide N-S strip (Görler and Ibbeken, 1964).

The Sestri-Voltaggio Zone always captured the interest of the geologist due to its great complexity (Capponi et al., 2016). The western contact, of the Sestri-Voltaggio Zone, known as the Sestri-Voltaggio Line, has played a different role in the model proposed by the different authors. Since the work of Rovereto (1939) the Sestri-Voltaggio Line has been considered as the boundary between Alps and Apennines. Recently has been described as a contact between units from different crustal levels and with different metamorphic conditions (Cortesogno and Haccard, 1984; Capponi, 1991) or as an extensional fault that place low-pressure on high-pressure metamorphic units (Hoogerduijng Strating, 1991). In the last years Crispini and Capponi (2001) and Capponi et al., (2016) underlined a different behaviour of the Sestri-Voltaggio Line in geological time, changing from a boundary between different units to a dextral trascurrent system, in the different stages of the Alpine and late Alpine evolution (Capponi et al., 2016).

Three units were usually comprised in the Sestri-Voltaggio Zone: the Figogna, The Cravasco-Voltaggio and the Gazzo-Isoverde unit (Cortesogno and Haccard, 1984); but some authors (Hoogerduijng Strating, 1991; Capponi et al., 2016) proposed that only two units were comprised in the Sestri-Voltaggio Zone, i.e. the Cravasco Voltaggio and the Gazzo-Isoverde units (see below).

The Cravasco-Voltaggio Unit consists of metaophiolitic basement and related metasedimentary cover, which equilibrated in low temperature blueschist facies metamorphic peak conditions (300-350°C and 8 Kbar, Cabella et al., 1994).

Tha Figogna Unit is characterised by metaophiolite and related metasediment, but it is equilibrated in pumpellyite-actinolite facies metamorphic peak conditions. Hoogerduijng Strating (1991) considered this unit as the western portion of the Lavagna Nappe, because of its affinity with the Internal Ligurian Units; and hence as a portion of the Northern Apennines; he did not include this Unit in the Sestri-Voltaggio Zone.

The Gazzo-Isoverde Unit encompasses a metasedimentary succession, made up of dolostone with horizons of evaporite, limestone and schist, of Triassic-Liassic

age; for this reason this unit was referred to also as the Trias-Lias Unit in the previous literature (Capponi et al., 2016). The isolated outcrop of Case Ferrere (Capponi et al., 1998; Capponi and Crispini, 2008, see chapter 4) can also be ascribed to this Unit. The Gazzo-Isoverde unit shared the same low temperature blueschist metamorphic peak conditions as the Cravasco-Voltaggio Unit; this is also supported by deformations of calcite, that indicate a T>300°C (Crispini, 1996).

3.8 – Structural evolution of the Sestri Voltaggio Zone

The Gazzo-Isoverde and the Cravasco-Voltaggio units shared a common deformation history (Crispini and Capponi 2001).

$D1_{SVZ}$ and $D2_{SVZ}$ events are developed under blueschist facies conditions and are characterised by high shear strain. Highly non-cylindrical folds with axes sub parallel to stretching lineations that show two maxima for NW-SE and E-W trend with plunge either to the north and to the south (Crispini and Capponi 2001).

$D1_{SVZ}$ and $D2_{SVZ}$ folds occur from mm- to km-scale, and show a penetrative axial surface schistosity that represents the main foliation at regional scale (S2, Fig. 4, Crispini and Capponi, 2001).

The $D2_{SVZ}$ event is followed by thrusting ($Sth2_{SVZ}$) events, with main tectonic transport towards S-SW (Crispini, 1996), which is developed at the limit greenschist/pumpellyite-actinolite facies metamorphism. $Sth2_{SVZ}$ are deformed by $D3_{SVZ}$ open to close sub cylindrical folds, with NE-SW axes and SE dipping axial surfaces, during low-pressure retrogressive metamorphism (albite + chlorite + epidote assemblages; Crispini and Capponi, 2001).

Late fold system ($D4_{SVZ}$) shows no evidences of metamorphic recrystallization (rarely zeolites and calcite or quartz). These folds are linked to E-NE vergent thrust system that involves also Chattian formations of the Tertiary Piedmont Basin. These late events cause the tilting of the regional foliation up to step angle of dip in most the Sestri-Voltaggio Zone.

The same chronology and characteristics of structures can be described in the Monte Figogna Unit, but in it $D1_{SVZ}$ and $D2_{SVZ}$ events developed under lower metamorphic conditions (pumpellyite –actinolite facies, Crispini and Capponi 2001).

The juxtaposition of the three units of the Sestri-Voltaggio Zone occurred at different structural levels. The mylonitic contacts between the Cravasco-Voltaggio and the Gazzo-Isoverde units ($Sth1_{SVZ}$) are deformed by all the folding events (from $D1_{SVZ}$ to $D4_{SVZ}$), whereas the contact between these units and the Monte Figogna unit is post- $D2_{SVZ}$ event and can be linked to thrusting with top to SW main tectonic transport ($Sth2_{SVZ}$). $D3_{SVZ}$ and $D4_{SVZ}$ re-oriented all the stretching lineations in all the units (Crispini and Capponi, 2001).

The cartoon in Fig. 4 shows a three-dimensional reconstruction of the main structures that characterise the Sestri-Voltaggio Zone. The megastructures result from these deformational events and from the dissection caused by the later effect of two main systems of faults: N-S transcurrent steep faults and WSW-ENE normal faults (Crispini and Capponi, 2001).

For a review of the interpretations of the Sestri-Voltaggio Zone see Crispini et al. (2009) and Molli et al. (2010).

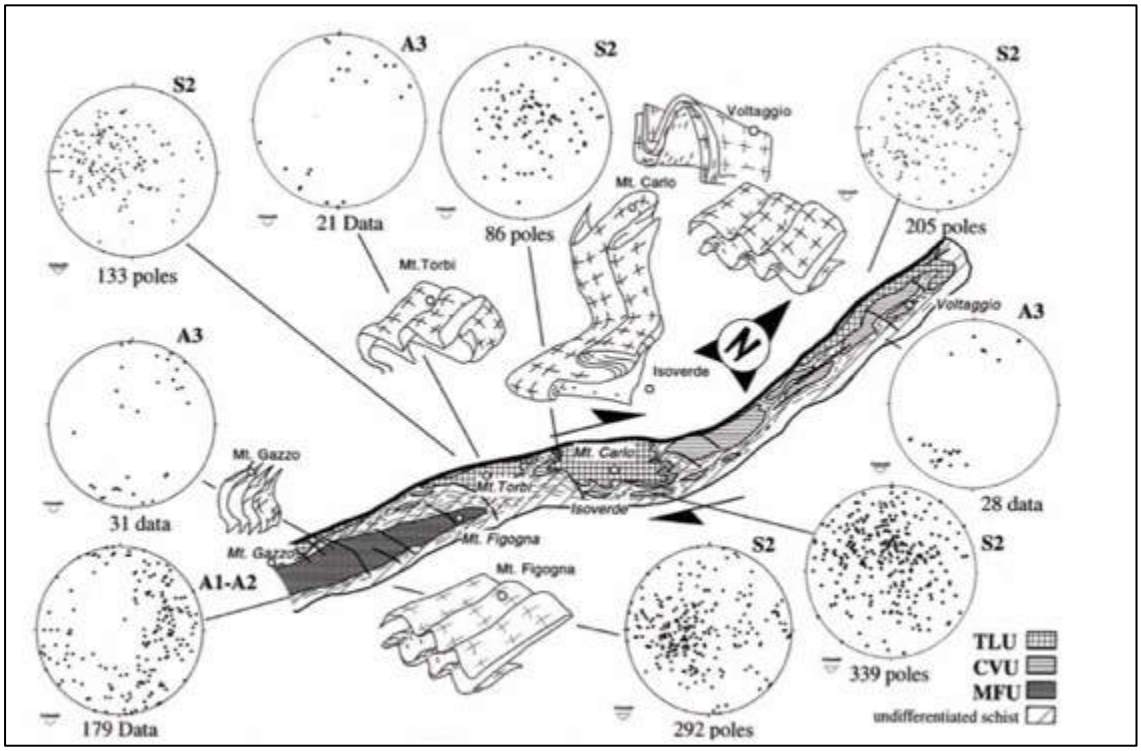

Figure 4: Simplified 3-D cartoon (not to scale) of the structures that characterise the main outcrops of the three units of the Sestri-Voltaggio zone (Crispini and Capponi 2001). The Stereoplots represent the main structural elements. TLU stands for Gazzo-Isoverde Unit, CVU for Cravasco-Voltaggio Unit, and MFU for the Monte Figogna Unit.

3.9 – The Tertiary Piedmont Basin.

The sedimentation of the Tertiary Piedmont Basin (TPB) occurred in the Oligo–Miocene during three main tectonic episodes, the exhumation of the Ligurian sector of the Western Alps, the opening of the Liguro-Provençal basin, and the formation of the Apennines thrust belt (Maino et al., 2013).

It unconformably overlies the Ligurian Alps and the Internal Liguride units (Northern Apennines) hiding their relatioships (Gelati and Gnaccolini, 1998).

The TPB sedimentary succession in the western sector (west of the Scrivia valley) begins with late Eocene-early Oligocene continental breccias (Costa Cravara breccias), followed by lower Oligocene transitional conglomerates (Molare Formation; Turco et al. 1994; Gelati and Gnaccolini, 1998 and references therein).

The Costa Cravara breccias contain coarse clasts of the same lithology as the underlying bedrock and are interpreted as slope breccias accumulated during a period of tectonic instability. They are indirectly dated at late-Eocene because they are deformed and eroded before deposition of the Molare Formation (Haccard and Lorentz 1979).

The Molare Formation consists of conglomerates and breccias with intercalations of sandstone, marls and siltstones with Oligocene fauna. The conglomerate clasts, at least in the lower layers, are strongly influenced by the bedrock lithologies, indicating together with sedimentological features, short-range transport; the same suggested by the sedimentological features.

Several authors studied the tectonic and sedimentary evolution of the TPB e.g. for instance, Gelati and Gnaccolini 1988; Bernini and Zecca 1990; Laubscher, 1992; Castellarin 1994; Vanossi et al. 1994; Dela Pierre et al. 1995; D'Atri et al., 1997; Piana et al., 1997; Capponi et al., 1999; Maino et al., 2013.

Subsidence and sedimentation of the TPB started at the beginning of the Oligocene, during a period of important tectonic activity, which include the opening of the Ligurian-Provençal basin to the south (Vanossi et al., 1994, Gueguen et al., 1998, Rollet et al., 2002). Its sedimentation continued during the formation, mainly in post- Tortonian age, of the Apennine thrust belt to the east (Dewey et al., 1989, Patacca and Scandone 1989, Castellarin, 2001). Despite these regional tectonic events and despite being located on the top of the Alpine/Apennine

junction on highly deformed basement (e.g. Miletto and Polino 1992), the TPB clastic infill is relatively undeformed (Carrapa et al., 2003, Carrapa and Garçia-Castellanos 2005).

The complex evolution of the TPB is well documented, although conclusions on its evolution are often contradictory as its origin and development is explained in terms of either compressional or extensional tectonics (Hoogerdujin Strating, 1991; Mutti et al., 1995; Schmid and Kissling 2000; Marroni et al., 2002; Carrapa et al., 2003; Carrapa and Garçia-Castellanos 2005; Maino et al., 2013). Because of the overprinting and reactivation of extensional and compressive structures, the stress/strain regime is poorly resolved, and the age of the deformations in the TPB is poorly constrained (Maino et al., 2013). Extension has been related to a first period of subsidence caused by the Oligocene opening of the Liguro-Provençal basin (Mutti et al., 1995; Gelati and Gnaccolini, 1998). The same authors suggest a Late Oligocene–Early Miocene inversion from an extensional to a compressional stress field, related to the Corsica-Sardinia drifting and to the thrust-activity of the Southern Alps.

Other works (e. g., Carrapa et al., 2003; Mosca et al., 2010) suggest that the TPB evolution was dominated by compression or transpression from the Oligocene until post-Pliocene time, with extension playing a minor role.

The role played by the extensional regime in the evolution of the TPB is, however, controversial; for more detail please refer to Maino et al. (2013).

3.10 – The Northern Apennines

The Northern Apennines are a typical “fold and thrust belt” consisting of several tectonic units belonging to different paleogeographic domains (Fig. 5; Decandia & Elter, 1972; Galli et al., 1972; Abbate et al., 1980; Abbate & Bortolotti, 1984; Principi & Treves, 1985; Cortesogno et al., 1987; Abbate et al., 1992a, b; Principi et al., 1992; Elter, 1994; Marroni and Pandolfi, 2007). The Ligurian units represent the uppermost units of the Northern Apennine nappe stack, and have been into two main groups, on the basis of stratigraphic and structural features: the Internal Ligurian Units (ILU) and the External Ligurian Units (ELU) (Abbate et al., 1970,

Decandia and Elter, 1972; Zanzucchi, 1978; Abbate et al., 1980; Marroni et al., 1992).

The ILU represent the top of the nappe pile and are characterised by an assemblage of Jurassic ophiolites and related sedimentary succession ranging in age from middle Jurassic to early Paleocene (Decandia and Elter, 1972; Abbate et al., 1980; Molli, 2008; Treves, 1984). This succession is interpreted as remnants of the Ligurian- Piemontese oceanic lithosphere (Decandia and Elter 1972, Rampone and Piccardo 2000 and references therein). In late Cretaceous-Paleocene time this lithosphere was underthrust, underplated and later exhumed in an accretionary wedge related to an east-dipping, low-rate subduction zone, and, particularly during pre-Oligocene orogenesis, these sequences were deformed, metamorphosed and tectonically disrupted into several units.

The ELU are distinguishable for the presence of Cretaceous-Paleocene calcareous dominant sequences (the Helmintoid Flysch) associated with complexes or pre-flysch formations called “basal complexes” (Molli et al., 2010).

Internal Ligurian Units and External Ligurian Units are characterised by a different structural history: the IL units display a west-verging evolution in the Alpine accretionary wedge. This evolution predates the eastward thrusting over the EL units, which are characterised by mainly east-vergent deformations.

These units are characterised by a very complex structural pattern due to overprinting of several folding phases associated with metamorphism (Elter, 1994; Di Biase et al., 1997 and references therein). Several authors (Ellero et al., 2001 and references therein) regard the Cravasco-Voltaggio and the Monte Figogna units as parts of the IL units. The metamorphic grade of the IL units in the metaophiolitic sequences (Cortesogno and Haccard 1984, Lucchetti et al., 1990, Hoogerdujing Strating, 1991), and in sedimentary sequences (Leoni et al., 1996) ranges, where present, from the advanced diagenesis of the shallowest unit to the HP-LT conditions (low temperature blueschist facies) of the deepest unit in the tectonic pile.

Above the deformed Ligurian units the Antola Unit, which consists of upper Cretaceous to Paleocene flysch, is thrust and the sedimentary succession of the Tertiary Piedmont Basin unconformably overlies the Ligurian and the Antola units (Elter and Pertusati, 1973). Beginning in late Oligocene, the Ligurian units were carried, with NE vergence, onto the more external domains of the Adria

continental margin (Marroni et al., 1992). Classically the Antola Unit has been related or with the External Ligurian units (Abbate and Sagri, 1984 and references; Cerrina et al., 2002; Levi et al., 2006), or with the Helminthoid Flysch of the Ligurian and Maritime Alps and therefore with a key role during the pre-Oligocene evolution of the Alps/Apennine orogenic system (Elter and Pertusati 1973; Elter 1997; Corsi et al., 2001).

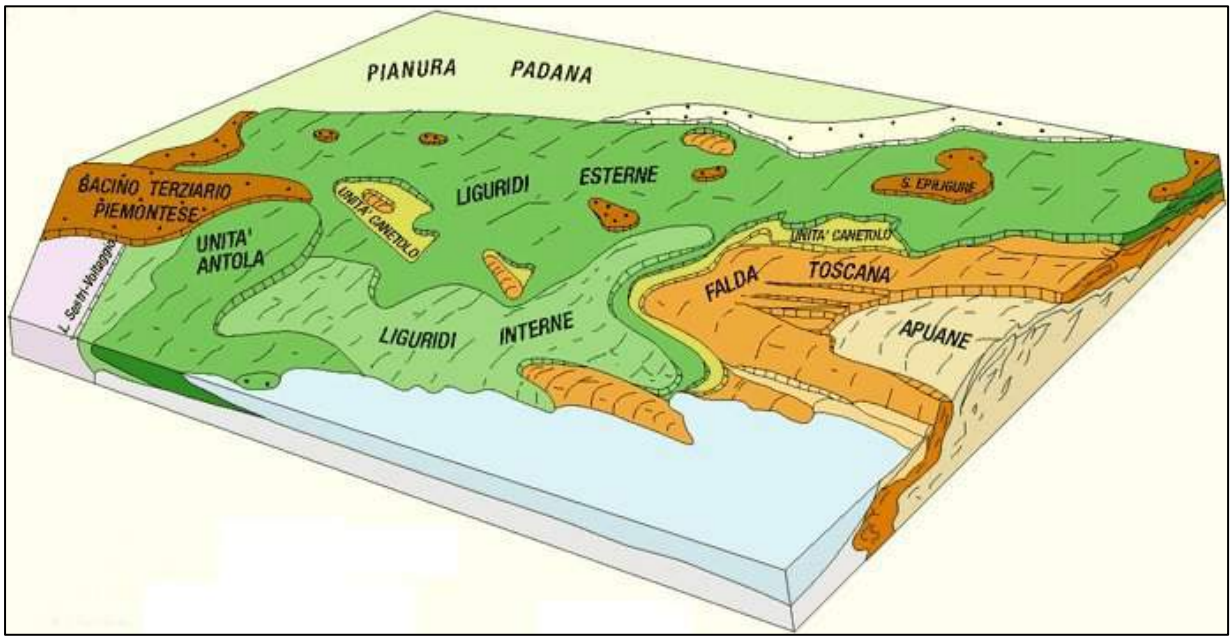

Figure 5: Block diagram of the major Northern-Apennines units and their relationships of superposition (Elter, 1994).

4 – The Lavagnina Lakes area

4.1 –Introduction

The study area (Fig. 6) is located in northwest Italy among the municipalities of Casaleggio Boiro, Lerma, Mornese, and Bosio (Alessandria, Italy; GPS coordinates WGS84, 44.600685° N, 8.784286° E). The area of the Lavagnina Lakes is known since the Roman age for its gold deposits along the Gorzente River (see paragraph 4.4).

This area has been selected for the present work since it is characterised by late- to post-orogenic tectonic events linked to the Alpine deformation (see below) and especially because these events are characterised by intense fluid-rock interaction that locally leaded, to gold mineralisation above cited. The fluid-rock interaction that took place along the ultramafic rocks, cropping out in the area (i.e. serpentinties and lherzolites), leads to the listvenitization of serpentinites (*sensu* Hansen et al., 2005) or to the total carbonation of the host rocks. This interaction is particularly intense along the core of the analysed structures (See chapter 5). The development of listvenites or carbonate levels is narrow in thickness (up to 2 m) and hence it is not represented in the geological map (Fig. 6).

4.1.1 – Geology of the Lavagnina Lakes area

The Lavagnina Lakes is located at the North-Eastern boundary of the Voltri Massif, close to the Sestri-Voltaggio Line, at the edge with the Tertiary Piedmont Basin (TPB).

The investigated area is mainly characterised by outcrops of peridotites, (lherzolites, dunites, pyroxenites), serpentinites, metabasites (metabasalts), metagabbros, lenses of metasediments, and listvenites (in decreasing order of volumetric extension). The serpentinites of the area are both massive and foliated due to a variable schistosity due to a variable strain partitioning; both the massive and the schistose serpentinites are characterised by variable degrees of fracturing.

Since the analysed stuctures and the host rock carbonation mainly took place within the peridotites, this lithotype will be described in more detail.

The peridotites of the area belong to the Unit that was called Erro-Tobbio Unit (Chiesa et al., 1975). For many years this Unit was considered different with respect to the Voltri Unit, since it was considered to display different metamorphic features, and with no metamorphic re-activation in the Alpine cycle (Capponi et al., 2016 and ref. therein). This lack led Chiesa et al (1975) to interpret such rocks as mantle slices that had escaped from the Alpine subduction and then been thrust onto the other rocks of the Voltri Massif, in a late Alpine phase.

However, later researchers (Piccardo et al., 1988; Capponi and Crispini, 1990; Drury et al., 1990; Hoogerduijn Strating et al., 1990; Scambelluri et al., 1991; Scambelluri et al., 1995, Scambelluri et al., 2001) also showed the occurrence of eclogite facies Alpine metamorphic re-equilibration in the Erro-Tobbio rocks, particularly well developed in metagabbro dykes, emplaced in peridotite. The bodies of peridotite (in places at the km-scale) that preserve mantle features from both the metamorphic and structural point of view are the result of huge strain partitioning, with Alpine metamorphic re-activation limited to kilometer-scale shear zones, where structural re-activation also occurs. This peridotite shows a deformational record from granular to tectonite to mylonite fabrics (Hoogerduijn Strating et al., 1990; Vissers et al., 1991; Hoogerduijn Strating et al., 1993; Rampone et al., 2005, Borghini et al., 2007). The granular peridotites are cut by shear zone structures (Drury et al., 1990; Vissers et al., 1991). The transition from the granular peridotites to the foliated peridotites is gradual; the progressive

development of tectonites from granular rocks is reflected by an increasing intensity of the foliation, marked by the elogantion of deformed pyroxenes grains (Dury et al., 1990; Visser et al., 1991). With progressive deformation, some tectonites in the large-scale shear zones evolved into Mylonites, characterised by thin bands and lenticular domains (Dury et al., 1990; Visser et al., 1991; Rampone et al., 2005; Borghini et al., 2007).

The peridotites are made up by partly serpentinized lhezolites (and lherzolite tectonites), dunites and pyroxenites, in decreasing order of volumetric extension.

The lherzolites are mainly massive, made up by ortho- and clino-pyroxenes, spinels, and plagioclase with frequently cm to dm thick piroxenite bands, and are characterised by a tectonite foliation. The lherzolites of the area also show a variable degree of serpentinization until their total transformation into serpentinites.

The dunites and pyroxenites are both present as bands or lenticular bands within the lherzolites.

The metabasites are lenticular bodies mainly derived from basalts; they show banded textures, partly obliterated by peciloblastic albite.

The metagabbros are lenticular bodies and can be distinguished into: Fe-Ti oxides metagabbros that are massive, characterised by olivine, plagioclase phenocrysts; and the metagabbros and metatroctolites that are massive, characterised by large- to medium-grained crystals with variously preserved magmatic textures.

The metasediments are mainly calcschist and micaschist with interbeds of quartz-carbonate layers; they are characterised by an intense schistosity and frequently by an intense weathering which makes them weakly coherent.

The listvenites are metasomatized mafic to ultramafic rocks in particular lherzolites and serpentinites, characterised by highly to total carbonation and silicification of the host rock. These rocks crop out mainly within or near fault and shear zones. They consist of strongly carbonated serpentinite, permeated by a hydrothermal carbonate matrix of Mg-Fe-Ca carbonates and quartz, with accessory serpentine, talc, Mg-chlorite, Cr-rich phengite (fuchsite) and ore-minerals, as hematite, magnetite, Fe-Ni or Fe-Cu sulphides and relict chrome-spinel (Pipino, 2001). Such rocks show a highly textural variability linked to the metasomatic processes.

At the northern border of the area, continental breccias and conglomerates belonging to the Tertiary Piedmont Basin (TPB) occur (Allasinaz et al., 1971; Spagnolo, 2004; Spagnolo et al., 2007; Capponi and Crispini, 2008; Capponi et al., 2009). In the area the TPB outcrops are limited by vertical faults (Capponi and Crispini 2002). The continental breccias, cropping out in this area, are related to "Brecce della Crosazza", and are made up by limestone and dolomitic limestone clasts with rare serpentinite pebbles and cobbles. The conglomerates are related to "Conglomerati di Molare", and are made up by pebbles, cobbles and boulders of serpentinites, metabasites, and locally metasediments and limestone.

The area also comprises, at Case Ferrere locality, a carbonatic klippe, bordered by thrust faults with a W-SW sense of shear (Capponi et al., 1998). The carbonatic klippe is made up by dolomite, dolomitic limestone, and grey crystalline selciferous limestone; related to "Dolomie del monte Gazzo" and to "Calcari di Gallaneto" of the Gazzo-Isoverde Unit (Capponi et al., 1998). The stratigraphic succession is deformed and overturned by open parallel folds, with upright axial planes and gently plunging to SE axes (Capponi et al., 1998).

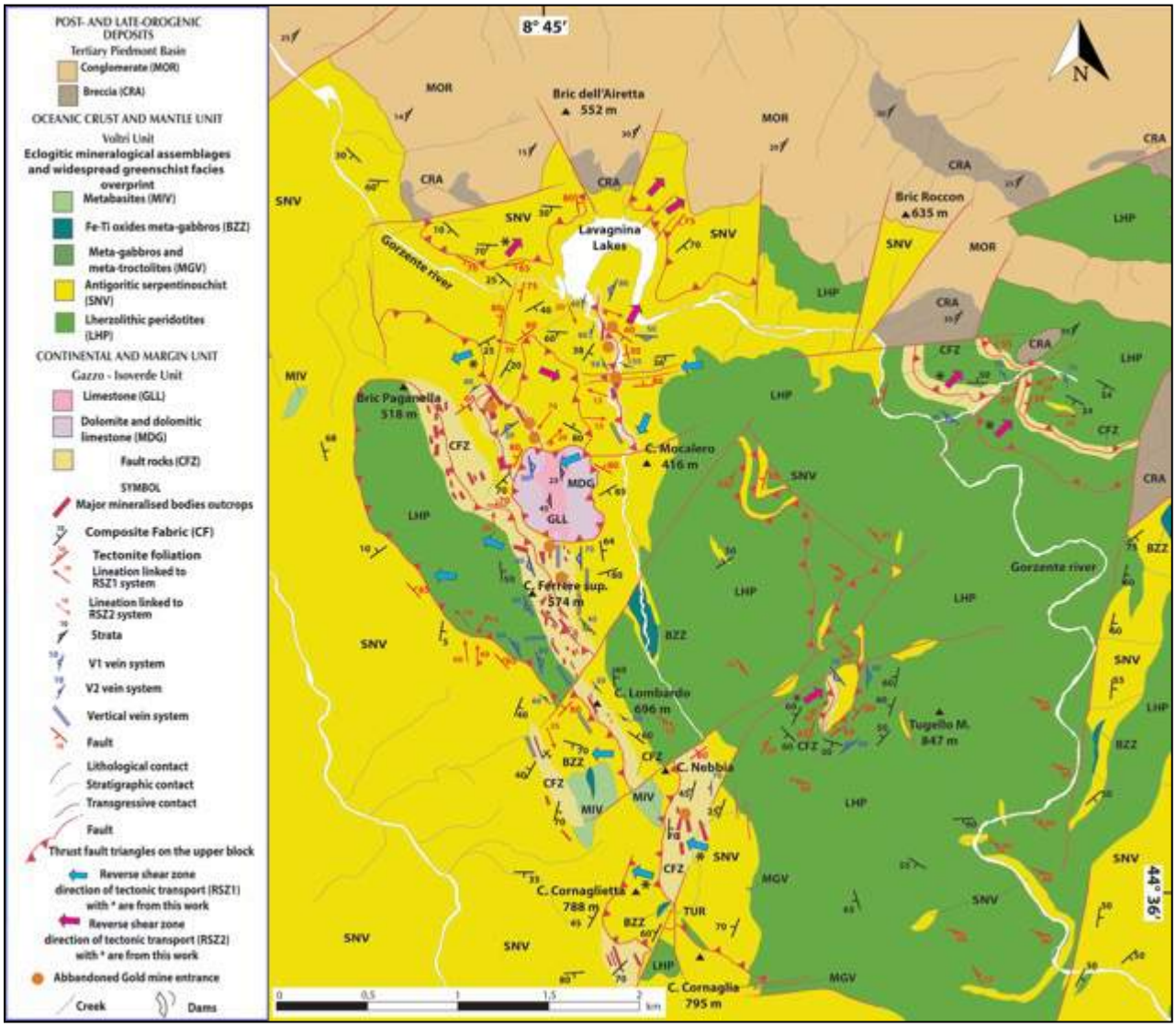

Figure 6: Structural sketch of the Lavagnina Lake area, redrawn with updates and georeferenced with QGIS open source software (after Spagnolo, 2004, see chapter 5 of this work).

From a structural point of view, the Lavagnina Lakes area shows the superposition of several deformations, which developed under structural conditions evolving from brittle-ductile to brittle regime (Capponi and Crispini 2002, 2008; Federico et al., 2009). These deformations are related to the Alpine deformations linked to subduction-collisional events.

The three Units described for this area (i.e. the Voltri Massif, the Sestri Voltaggio and the Tertiary Piedmont Basin deposits, see chapter 3) show evidences for a different tectono-metamorphic evolution between them. The Voltri Massif and the Sestri-Voltaggio zone show a common evolution from the D3/D4 events (Chapter 3) due to their coupling (Crispini and Capponi, 2001; Capponi and Crispini, 2002).

Moreover, the TPB deposits share the same evolution of both the Voltri Massif and Sestri-Voltaggio zone only for the late- to post-orogenic deformations; represented by vertical to sub-vertical faults.

The older Alpine structures recognizable in the Lavagnina Lakes area, characterised by D1 and D2 folds (see chapter 3). Since these folds are strongly transpositive, their schistosity superimposed to the previous foliation, give rise to a Composite Fabric (CF) that is the most evident surface on the field, and that controls the contact between lithologies, similarly to what is observed for the whole Voltri Massif (Capponi and Crispini, 2002). The composite fabric shows scattered orientations (Fig. 7); and this dispersion can be related to the subsequent deformational events.

The post-D1/D2 deformational events, in the Lavagnina Lake area, are characterised by a complex superposition of ductile, brittle-ductile to pure brittle structures; they are late- to post-metamorphic events. These structures have been developed in the upper structural level and for their features can be referred to the "*upper crustal deformation*" (UCD; Fig. 8) described by Capponi and Crispini (2002), Spagnolo et al. (2007), and Federico et al. (2009).

The brittle-ductile UCD events are widespread in all the investigated area, and are mainly represented by superposed systems of folds, systems of Reverse Shear Zones (RSZs, see below), and fault systems.

The UCD are characterised by two systems of folds, which show comparable features with the D3 and D4 folds described by Capponi and Crispini (2002).

D3 folds appear as gentle undulation of the sub-vertical CF. The D3 folds show axial surfaces NE-SW striking and gently to moderately dipping both to NNE and SSW, this dispersion can be related to the subsequent D4 phase.

D4 folds are mostly parallel open folds, with large wavelengths (metric to decametric); rarely accompanied by a spaced cleavage. D4 fold axes are N-S to NNW- SSE trending and are nearly horizontal; axial planes are N-S striking and moderately dipping to the West. D4 folds are overturned toward the NE and indicate a top-to E-NE sense of shear, comparable to what described by Spagnolo et al. (2007).

The systems of reverse shear zones, that characterise the UCD, accordingly to their structural features and kinematics, have been subdivided into two families (RSZ1-RSZ2, see the paragraph 4.2), and for their features are similar to those

described by Capponi and Crispini (2002), Spagnolo et al. (2007), Federico et al. (2009). These shear zones are characterised by several fault rocks types, which can be related to different structural levels and regimes, testifying a long period of activity and multiple reactivations of the shear zones.

Moreover RSZs damage zones are characterised by extensive fluid circulation, giving rise to vein networks, with different mineralisation, and associated wall rock metasomatic alteration. These veins networks are locally characterised by gold-bearing quartz and carbonates veins that were exploited until the Roman Age (Pipino, 1976; 1978; 1980; 1982; 2000; 2001; 2003).

In the range of the brittle-ductile UCD important N-S strike-slip/transpressive system and minor Riedel faults have been observed and described. The final stages of brittle tectonic evolution show normal and transtensive fault, which often reactivate the previous structures corresponding to what described by Spagnolo et al. (2007) and Federico et al. (2009). The structures described above are summarised in Fig. 8.

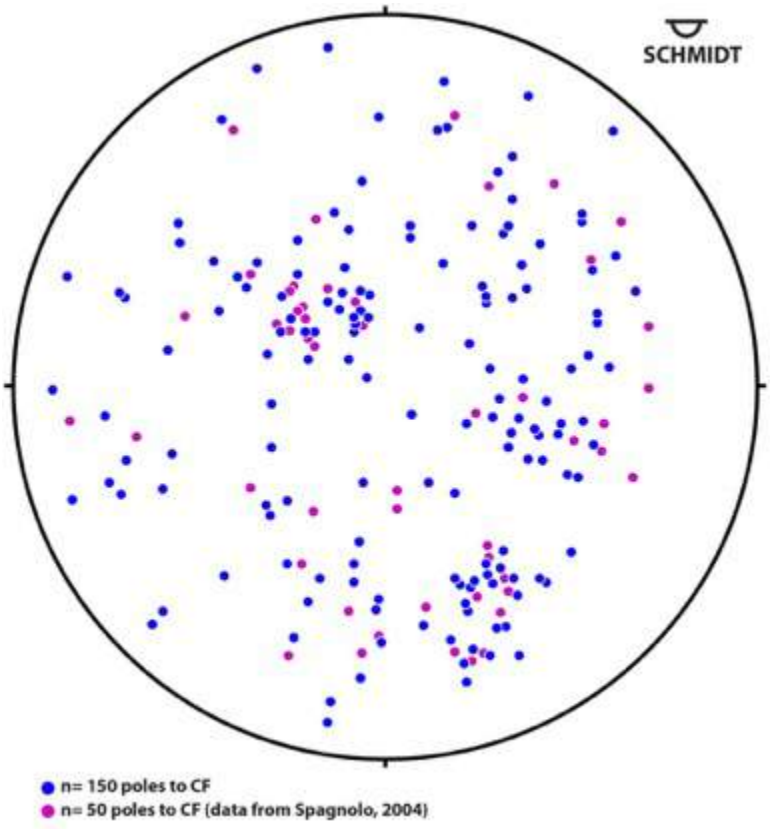

Figure 7: Stereographic projection of composite fabric of the Lavagnina Lakes area.

Structures-system	Description	Orientation	Association	Tectonic phase
D1/D2	D1 and D2 similar folds and composite fabric (CF)	D1/D2 hinge lines show scattered orientation on the axial plane, mostly plunging to N		Exhumation and nappe emplacement
RSZ1	Shear zones (RSZ1), gold-bearing veins	WNW-ESE striking Top to W-SW	V1: Fe-Mg carbonates, chalcedony-quartz gold-bearing veins	Collision
D3	Dragged folds with chevron style	Axes: NE trend moderate plunge	Shear zones (RSZ1)	Collision
RSZ2	Shear zones (RSZ2), hydraulic breccias, gold-bearing veins	Mainly sub-horizontal or gently dipping to W Top to E-NE	V2: Fe-Mg carbonates, chalcedony and quartz gold-bearing veins; V3: chalcedony and quartz with minor calcite	Transpression
D4	Open parallel folds (km scale)	Axes: NE-SW trend	Shear zones (RSZ2)	Transpression
S-s & NF	Strike-slip and normal faults	N-S strike-slip, minor Riedel NNE-SSW and NNW-SSE; E-W normal faults	Narrow carbonate alteration, Riedel secondary shear planes	Extension

Figure 8: Summary scheme of the main Upper Crustal Deformation.

4.2 – Brittle-ductile deformations

According to what described above, the Lavagnina Lakes area shows a complex superposition of several deformations, which developed under structural conditions evolving from brittle-ductile to brittle regime.

In this study the focus is concentrated on the brittle-ductile to pure brittle events that characterise the Upper Crustal Deformations (UCD), particularly on the systems of reverse shear zones, which occur in the area, for their peculiar feature (described above). Moreover, the gold-bearing veins, above described, are related to these systems of structures, and this underlines the relevance of studying these structures, their development, their relative chronology, and their interaction with fluids.

4.2.1 – Brittle-ductile shear zones (RSZ1 and RSZ2)

RSZ1 shear zones are developed at the lithological transition between serpentinites-lherzolites and serpentinites-carbonatic rocks, and are the oldest reverse shear zone structures recognised on the field. They developed under brittle-ductile deformation conditions, and are syntettonically with greenschist to sub-greenschist metamorphic conditions.

RSZ1 structures developed cm-thick mylonite, protomylonites and foliated cataclasites levels (*sensu* Sibson, 1977) with crystallization of carbonates, chlorite, quartz and talc. Occasionally non-permeating alteration is developed along the contacts, and it is made up by Fe-Mg carbonates and ferrous oxides similarly to what observed by Spagnolo et al. (2007).

The RSZ1 stystem is made up of shallow- to moderately dipping surfaces (Fig. 9a) characterised by the occurrence of slickenlines, slickensides, shear fibre lineations, and chatter marks (Fig. 9b) that indicate contraction, associated with minor strike-slip kinematics of the shear zones. The inferred sense of shear is top-to S–SW, with a minor top-to N–NW deviation. These shear zones are characterised by a brittle-ductile deformation and typically produce cm- to dm-thick layers of mylonites and protomylonites (sensu Sibson 1977). Well-developed drag folds, associated to these shear zones, testify their sense of shear.

The damage zones linked to the RSZ1 structures show veins (V1) and metasomatic alteration (ALT-1).

V1 veins are mm to cm wide, are Fe-Mg carbonates and chalcedony-quartz gold-bearing veins. They are mainly related to the filling of extensional or tension gashes fractures that open in in the footwall in response to thrust movement. V1 veins (Fig. 9c) are mainly striking NNE-SSW and are steeply dipping. These veins developed syntectonically with shear bands and locally are deformed by open folds; they show peculiar reddish colour which derives from secondary alteration minerals like lepidocrocite, ghoetite, and sulphur similarly to what described by Pipino (1976).

Limited to the shear surface zones, and to the veins wall, metasomatic alteration (ALT-1) causes carbonation and hydration of the bedrocks. Along the shear zones and veins occurring inside the ultramafic rock this alteration develops dm to m listvenite levels (*sensu* Hansen et al., 2005) or leads to the total carbonation of the bed rock. The occurrence of metasomatic alteration along RSZ1 shear surfaces and the presence of widespread veins testify the presence of syntectonic fluids during the evolution of RSZ1.

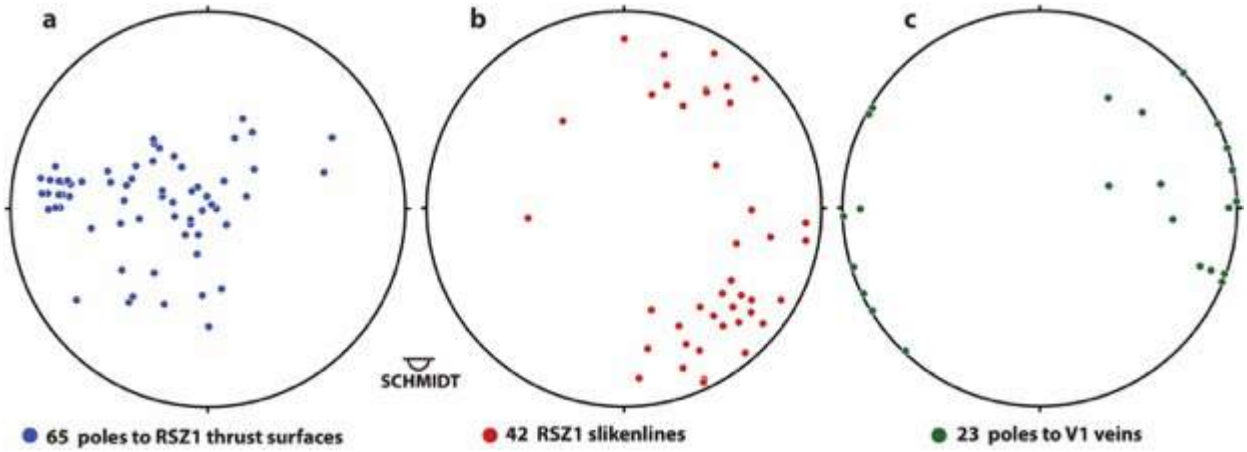

Figure 9: Stereographic projections. (a) Poles to RSZ1 thrust surfaces (65 points). (b) Slickenlines (42 points). (c) Poles to V1 veins (23 points).

RSZ2 developed under brittle-ductile to pure brittle deformation conditions, and from sub-greenschist to zeolite facies metamorphic conditions comparable to

the description made by Capponi and Crispini (2002) for this system in the Voltri Massif.

The RSZ2 show shear surfaces mainly sub-horizontal or gently dipping to W (Fig. 10a), and they often reactivate RSZ1 structures, since V1 vein fragments occur in the fault rocks of the RSZ2 structures.

Slickenlines on the surfaces are scattered and show a variable sense of shear, ranging from top-to NW, -SW and -NE (Fig. 10b) linked to contractional and minor strike-slip kinematics. Some of these structures show evidence for reactivation of previous discontinuities, with several types of fault rocks overprinting in the same shear zone and multiple sets of slickenlines on individual fault planes. The interference with pre-existing discontinuities can be, at least in part, responsible for the scatter in orientation of RSZ2 slickenlines.

RSZ2 damage zone are characterised by a larger volume both of fault rocks and of metasomatic alteration of the host-rocks. They also developed: two main sets of veins (V2-V3), hydraulic and cockade breccias, and two kind of metasomatic alteration (ALT-2, ALT-3).

V2 veins (Fig. 10c) are similar to V1 but more widespread, thick (up to 20 cm), and cut the previous V1 system. They are Fe-Mg carbonates, quartz, chalcedony, and locally gold-bearing. V2 are mainly related to the filling of extensional or Riedel shear fractures that open in the footwall in response to RSZ2 movement. V2 veins (Fig. 10c) are mainly striking NW-SE and usually they show high angle with respect to the shear plane, even if sometimes they are deflected into the shear plane showing a sub-horizontal attitude.

V3 veins are cm wide and not so widespread as V2; they are mainly chalcedony-quartz veins with minor calcite, moreover they are not gold-bearing. They are syn- to post-kinematic to RSZ2, and their occurrence was from contemporary to successive to D4 folds system, which limbs are sometimes sheared.

Hydraulic breccias represent a subclass of breccias, in which failure of the host rocks is due to fluid overpressure and the brecciated clasts of the host rocks are subsequently cemented by mineral precipitation from permeating fluids.

Cockade breccias, defined by Genna et al. (1996), in the area show similar genesis of the hydraulic breccias, but with a progressive encrustation of the host rocks clasts by envelops of hydrothermal minerals making up the cockade structures. The most common hydrothermal minerals, which make up the

envelopes in the observed cockade breccias, are quartz, with both colloform and crystalline textures, and carbonates.

In the Lavagnina Lakes area the hydraulic and cockade breccias occur, almost exclusively, in serpentinites, especially in massive serpentinites, and, these two textures are almost always associated.

Metasomatic alteration 2 (ALT-2) develops along the damage zone of the RSZ2 structures. It is more widespread than the ALT-1, as ALT-2 affects larger volumes of rocks, and it is also more intense. As ALT-1 also the ALT-2 is characterised by intense carbonation of the host rocks, but instead ALT-2 do not show listvenitization of the serpentinites. The metasomatic processes, linked to ALT-2, are heterogeneously distributed, and are strongly influenced by lithologies and by their structural features. In serpentinites, metasomatic alteration develops starting from the regional foliation, and then diffusely affects the damage zones of RSZ2 structures, producing listvenitization of the host rocks. In lherzolites, instead, the main alteration processes are fault-related, and deeply affect the core of the shear zones, also fostered by intense cataclasis and brecciation.

From this study has been observed that ALT-2 often generates, in the fault core, decimetric to metric pure carbonates levels with unique textures. These textures show complex internal features due to several interplays of fluid-rocks interactions (with cyclic events of fracturing, fluids circulation, and mineral precipitation) linked to RSZ2 movements. These peculiar textures have never been reported or described in bibliography, and hence will be referred as “fault-pearls” in analogy with the organic pearls. Structural, microstructural, and geochemical features of these textures will be described in chapters 5, 7, and 8 of this work.

Metasomatic alteration 3 (ALT-3) is the less developed and the less pervasive, and it is heterogeneously distributed. It is characterised by sepiolite (See chapter 5) and asbestos duplex structures (Ramsay and Huber, 1987) along shear planes.

In the Lavagnina Lake area, as described above, the gold mineralisations are related to the RSZs structures and their damage zone. The mineralisations are especially linked to both the V1 and V2 vein systems (see chapter 5), which show similar mineralogical composition: Ca-Mg-Fe-carbonates + quartz + chalcedony + native gold + sulphides. The major mineralised bodies mainly occur in the footwall of the RSZs as the filling of extensional fractures or as Riedel shear veins, especially

along the contact between lherzolites and the serpentinites or serpentinite schists, similarly to what is described by Spagnolo (2004).

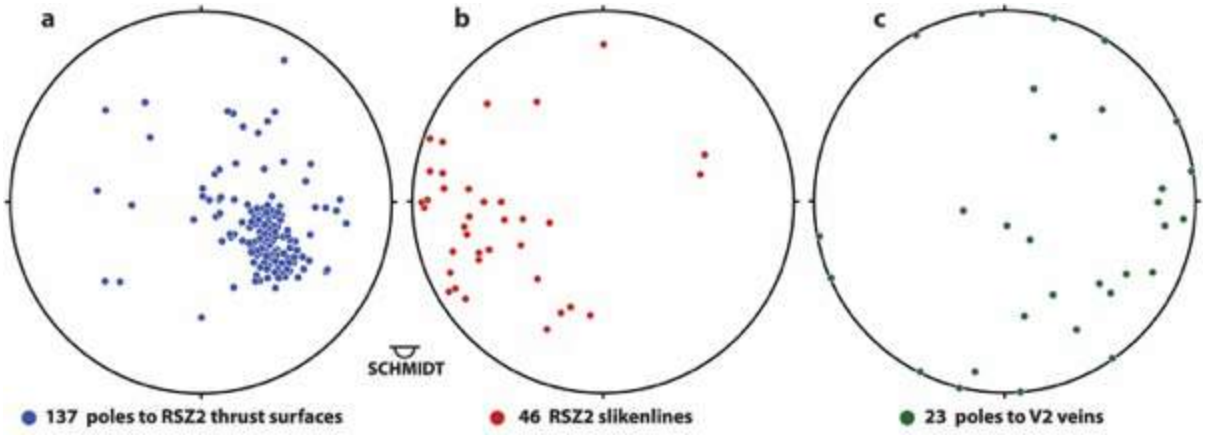

Figure 10: Stereographic projections. (a) Poles to RSZ2 thrust surfaces (137 points). (b) Slickenlines (46 points). (c) Poles to V2 veins (23 points). The data are from the field survey for this work.

4.2.2 – Strike-slip/oblique slip (transpressive) systems of fault

Strike-slip and oblique slip systems are common in the Lavagnina Lakes. These structures are characterised by kilometric scale, nearly vertical N-S striking faults, which are strictly related to positive flower structures. These structures are associated to minor Riedel faults NNE-SSW and NNW-SSE striking that can be defined as R and P shear faults, and are characterised by dm to m thick fault rocks levels.

Moreover, other faults that can be related to the strike-slip/oblique slip systems are hundreds of metres long, ESE-WNW striking, comparable to the strike-slip faults described by Federico et al. (2009). They show main sinistral strike-slip movement with minor contractional component and can be defined as R' Riedel shear faults.

Systems of E-W striking faults that cut all the previous structures and dip-slip reactivation of older fault planes occur during the final stage of the upper crustal deformation history, comparable to the description for the whole Voltri Massif by Capponi et al. (2001).

E-W systems have km-length and develop two kinds of slickenlines with both dextral and sinistral strike-slip (S-s, Fig. 8) motions.

Dip-slip (NF, Fig. 8) reactivation of pre-existing strike-slip / transpressive systems occur: it is characterised by slickenlines with both normal and inverse motion (Spagnolo et al., 2007).

4.3 – Metamorphism of the Lavagnina Lakes area

The rocks cropping out in the Lavagnina Lakes area belong to the Voltri Unit, as the other rocks belonging to this unit, were re-equilibrated in eclogite facies at about 50 Ma (Federico et al., 2005), then overprinted by greenschist facies conditions (Messiga and Scambelluri, 2001 and reference therein) at about 33 Ma (Federico et al., 2005). The greenschist overprint is more or less pervasive, depending on the reactivity of the rock chemistry and on the deformation (Capponi et al., 2016). The eclogite facies assemblages are more extensively and better preserved in the ultramafic rocks, which are less retrogressed in greenschist facies, whereas they are rare in metasediments, where the greenschist overprint is usually pervasive (Capponi and Crispini, 2002).

4.4 – Gold Mineralisations

Historically the exploitation of the gold deposits of the analysed area dates back to the Roman age and to the mythological city called “Rondinaria” (Pipino, 2001).

The Roman activity is testified by heaps of pebbles and cobbles along the Gorzente banks, that are similar to the heaps described along the Dora and Elvo River near Ivrea, linked to the exploitation of the gold deposits by Celtic populations and after by the Romans during the II and I century B.C. (Pipino, 2001). These heaps, along the Gorzente banks cover a surface of some square kilometres.

Probably also the gold mineralisations, from which the gold nuggets derives, were known in the area, but the first evidence of mining activity dates back to 1589 (Pipino, 2001). The mining activity continued until the early 1900s, and all the mine entrances and galleries present in the area date back to those years (Fig. 6).

In 1904 all the activities ceased, for more detail about the mining history please refer to Buisson and Leblanc (1985a, b) or to Pipino (1976, 1980, 1982, 2000, 2001, 2003).

The gold is unevenly distributed in the peridotites and serpentinites, with an average content from 0.1 to 2.0 gr/ton (Pipino, 2005). The most interesting gold mineralisations of the Lavagnina Lakes area could be divided into two types: *i*) quartz vein systems, or *ii*) lode mineralisations linked to fault-linked listvenites.

The mineralisations linked with the quartz vein systems mainly cut the peridotites and the serpentinites. The gold is present in plagues (mm in size), as native dendritic gold (up to 1 cm in size), or associated with sulphur (Pipino, 2005).

The lode mineralisations linked to the fault systems of the area are related to the carbonation and silicification, of peridotites and serpentinites, which took place along the fault until the total transformation of the host rock into listvenites. The mineralised bodies show a limited extension, they are from a dozen to a hundred meters long, and from decimetric to metric thick. The gold is present in plagues (mm in size) or associated with sulphur (Pipino, 2005).

An alloy of gold (80-85%), silver (10-15%), and copper (2-3%) makes up the gold of both the mineralisations (Pipino, 2005).

For more detail please refer to Pipino (1976, 1980, 1982, 2000, 2001, 2003).

5 – Geological and structural survey

5.1 – Field and structural analysis

For this study I applied different geological analysis and laboratory methods. In the study area detailed geological, structural surveys and mapping have been performed in order to identify the most striking structural features that characterise the area.

The geological analyses applied for the mesoscale structural analysis are:

I. Geological and structural surveys, scale 1:10000,
II. Kinematic analysis,
III. Point out of relative chronology between sets of structures,
IV. Targeted sampling of wall rocks, fault rocks, and veins.

I performed the geological survey from April 2015 to November 2016, and could be divided into two main phases:

- The first phase regards the geological survey of the Lavagnina Lakes area (about 32 km^2, Fig. 6 chapter 4) on the basis of a previous geological survey performed by Spagnolo (2004). The study area is located along the Gorzente River, with an average altitude of about 400 m a.s.l., and the most of the study area is part of the *"Parco Naturale delle Capanne di Marcarolo"*. The outcrops, in the study area, represent about the 15-20% of the entire area, due to the presence of bushy vegetation. Furthermore, some areas show a medium to high acclivity making the survey difficult. The higher percentages of outcrops are along the trail that is besides of the Lavagnina Lakes, along the rivers of the area (i.e. Gorzente and Tugello River), and along the major creeks (i.e. Paganella, Bisciarelle, and Moncalero Creek). I used the *Carte Tecniche Regionali (CTR)* as topographic base; in particular the elements number 195130, 195140 (scale 1:10000 of the "*Foglio Novi Ligure*"), 213010, and 213020 (scale 1:10000 of the "*Foglio Genova*"). On the basis of the geological survey data and the previous geological map (Spagnolo, 2004), I redrawn the geological map of the area and I realized a geo-referenced geological map (see below). I also realized a geological cross-section (A-A'-A"; geological map in the supplementary materials) oriented W-SW-NE, which is

approximately perpendicular to the strike of the main structures, in order to show their trend.

- The second phase regards the detailed structural analyses of four main outcrops (the Moncalero Creek fault, the Tugello Creek thrust, the Paganella Creek, and the Bisciarelle Creek thrust) considered the most interesting and the most representative for the aim of this work. For the detail see chapter 5.

The targeted sampling was used to prepare thin sections for petrographic and microstructural analysis, whole rock analyses, X-Ray Powder Diffractions, SEM-EDS and LA-ICP-TOFMs chemical analysis (see chapters 6, 7, 8).

The analysed area is characterised by outcrops of peridotites (lherzolites, dunites, pyroxenites), serpentinites, metabasites (metabasalts), metagabbros, lenses of metasediments, listvenites, dolomite and dolomitic limestone, grey crystalline selciferous limestone, and the deposits of the Tertiary Piedmont Basin.

The peridotites mainly crop out in the central and central-east sector, together with the serpentinites, they are volumetrically the most abundant lithotypes. They are made up by lhezolites (and lherzolite tectonites, chapter 4), dunites and pyroxenites, in decreasing order of volumetric extension.

The lherzolites (LHP, chapter 4) cropping out in the area, are massive, with parallel to sub-parallel pyroxenite bands, and are characterised by a variable fracturation degree that divide them into metric blocks. The lherzolite tectonites are sheared and highly deformed lherzolites as testified by folded pyroxenite bands; they include coarse tectonites as well as fine-grained mylonites, characterised by a tectonite foliation. They are dark-green in colour to fresh fracture, whereas they are greyish to reddish-brown when altered. The selective superficial erosion of the lherzolites, highlights the compositional banding (e.g. pyroxenite bands) and the tectonite foliation. They are made up by olvine, ortho- and clinopyroxenes, spinel and plagioclase.

The dunites and pyroxenites are both present as bands or lenticular bands within the lherzolites.

The dunite bands are cm to m thick, grey-green in colour to fresh fracture. The lighter colour emphasise them, but the superficial alteration makes them of difficult recognition on the field. However they are visible along the Gorzente in the riverbed, in particular near the damn of the Lavagnina Lakes. They are mainly

made up by olivine with minor spinels and plagioclase. The dunite bodies, for their dimension, are mainly not representable at the map scale.

The pyroxenites are cm to dm thick bands, green to dark-green in colour of difficult recognition on the field, but the selective superficial erosion highlights them. They are made up by ortho- and clinopyroxenes, with associated spinel and plagioclase. The pyroxenite bands, for their dimension, are mainly not representable at the map scale.

In the analysed area, the peridotites also show a variable degree of serpentinization, until they total substitution into serpentinites.

The serpentinites (SNV, chapter 4) crop out more or less homogeneously in the whole analysed area. They are both massive and schistose. They are dark-green in colour on fresh fracture, whereas they show an orange-brownish colour when altered. The massive serpentinites shows ortho- clinopyroxenes and sometimes olivine relicts. The serpentinite show a variable schistosity, due to a variable strain partitioning, until they become serpentinite-schists. Their schistosity is pervasive, and it is a composite fabric due to the superposition of deformation (see chapter 3, 4).

The metabasites (MIV, chapter 4) crop out mainly in the western sector of the analysed area. They are lenticular bodies more or less developed, within the lherzolites and the massive seprentinites. They show a granular appearance due to the ocellar texture, and they are green in colour on fresh fractures, but they often show an intense alteration that could make difficult the distinction of this lithotype with the metasediments. The metabasites are made up by pyroxenes, ocellar abite, epidote and chlorite.

The meta-gabbros (metagabbros and metatroctolites MGV and Fe-Ti oxides metagabbros BZZ, chapter 4) crop out scattered in the whole analysed area, within the lherzolites or the massive serpentinites.

The metagabbros and metatroctolites lens (MGV) are medium to coarse grained, and they are from dark-green to greyish-green in colour on fresh fracture, and brownish when altered. They are made up by plagioclase, pyroxenes, olivine, and minor epidote and garnet.

The Fe-Ti oxides metagabbros (BZZ) are less widespread with respect to the previous. They are dark-green in colour on fresh fracture, and brownish when altered. They show several superimposed deformation (chapter 3) that developed

augen to blastomylonitic textures. They are made up by plagioclase, amphiboles, garnet and epidote.

The metasediments, mainly calchschist and micaschists, are present as small outcrops in the analysed area. They show a grey colour with silver reflection due to the presence of mica, and brownish-rusty when altered. They show an intense schistosity, and they show widespread extensional carbonate veins, which cut the schistosity. On the field the metasediments are always intensely altered.

The listvenites, in the analysed area, are always associated to the faults and their damage zones (in chapter 4 are grouped in the CFZ). They are developed for the syn-tectonic carbonation over ultramafic rocks (in the analysed area over peridotites or sepentinites), up to 5 m thick. They show a peculiar yellowish-white colour due to the intense carbonation. They are fine to ultrafine grained; show a variable schistosity degree, and mylonitic textures. They often show widespread quartz and chalcedony veins. The listvenites, for their dimensions, are not always representable at the map scale.

The dolomite and dolomitic limestone (MDG, chapter 4), and the grey crystalline selciferous limestone (GLL, chapter 4), only crops out in the centre of the analysed area, near the Cascine Ferrere locality, and make up a carbonatic klippen (chapter 4).

The dolomite and dolomitic limestone (MDG) are grey in colour, microcrystalline, ca. 20 m thick, and they do not show a well-defined stratification.

The grey crystalline selciferous limestones (GLL) are dark-grey in colour, with argillites intercalations. The intercalations are black in colour, characterised by an intense schistosity, and cm thick.

The deposits of the Tertiary Piedmont Basin, in the analysed area, crop out almost only in the northern sector (chapter 4). These deposits could be distinguished in: continental breccias (CRA, chapter 4), related to the “Brecce della Crosazza”, and the conglomerates (MOR, chapter 4), related to the “Conglomerati di Molare”.

The continental breccias, in the analysed area, are made up almost exclusively by limestone and dolomitic clasts, angular in shape, and from mm to pluri dm in size. Within the breccias, serpentinite pebbles and cobbles are rare. These breccias crop out as metric lenses, divided in levels by sub-horizontal joints. They crop out

in direct contact with the peridotites or serpentinites, or as intercalation within the conglomerates.

The conglomerates in the area show sandstone intercalations. The conglomerates are made up by pebbles, cobbles and boulders with a composition that reflects the bedrock, in general the composition is made up by: serpentinites, metabasites, but locally metasediments and carbonates. The clasts are prevalently randomly oriented, from well rounded in the upper portion, to angular or sub-angular in the basal portion. The matrix has the same composition of the clasts, and becomes preponderant in the sandstone intercalation, highlighting the stratification otherwise not so evident.

5.2 – Laboratory methods

The laboratory methods applied are:

I. Geo-referenced geological map through the software: Map Publisher, QGIS (free downloadable at https://www.qgis.org/it/site/) Mac version and the app MotionX-GPS IOS version,

II. Image analysis through the software: iPhoto, Adobe Illustrator CS6 and Image-J (free downloadable at http://rsbweb.nih.gov/ij/) Mac Versions.

For this study all the field data were geo-referenced using the app MotionX-GPS; so all this information can be easily used inside a Geographic Information System (GIS).

I geo-referenced the CTR the elements number 195130, 195140 (scale 1:10000 of the "*Foglio Novi Ligure*"), 213010, and 213020 (scale 1:10000 of the "*Foglio Genova*"). Then I geo-referenced the pre-existent geological data of the analysed area using Map Publisher, in order to be able to work with QGIS.

Subsequently, using QGIS, I added the new data from this work (Fig. 6 chapter 4, and geological map in the supplementary material) in order to produce a geo-referenced map, with information linked to real geographical coordinates. The geo-referenced data included in the map are:

- The track for the outcrops,

- The lithotypes,
- The attitude of structural elements (fault surfaces, lineations, veins, composite fabrics, tectonite foliations, stratifications),
- The photograph of the outcrops and their related structures,
- The samples,
- The closed mine entrance.

For this work I decided to use QGIS, since it is free downloadable and in order to produce a geological map easily editable, shareable and quickly updatable.

The image analysis (see paragraph 5.4.1) has been realized on the samples of the fault pearls that characterise the Bisciarelle fault core (see paragraph 5.4.1) in order to obtain shape descriptors, statistically representative, of these textures.

I used iPhoto for the first step of the pre-processing of the photograph, especially to increase the chromatic contrast, since the analysed samples show a plain and monotonous colour. Then I used Adobe Illustrator CS6 for the second step of the pre-processing of the photos for the analysis, especially the command "image trace" in order to trace the edge of every single fault pearl, to obtain a "pearls-edges-map" (see paragraph 5.4.1).

For the last step of the image analysis I used Image-J, since it is free downloadable (Mac version, http://rsbweb.nih.gov/ij/) and it is largely used in literature (i.e. Keulen et al., 2007 and reference therein).

Then I processed the "pearls-edges maps" through this software to fit an ellipse onto each pearl and to obtain morphometric parameters. Once set the scale for spatial scaled images, to obtain values expressed in physical size, I performed the following measures:

- Circularity: with a maximum value of 1 represents a perfect circle; as the value approaches to 0.0, it indicates an increasingly elongated shape. Values may not be valid for very small measures,
- Roundness: it's the inverse of the Aspect Ratio, and use the area of the grains and the major axis of the best-fit ellipses,
- Orientation: The program fits the grains with equivalent best-fit ellipses and measures the angle between the major axis of the best-fit ellipses and the horizontal top edge of the image parallel to the shear movement,

- Particle size distribution: I used the maximum diameter of the carbonated coated grains obtained with ImageJ, and then I realized particle size distribution with Excel spread sheet.

These measures have been performed in order to obtain representative statistical data about the fault pearls shape descriptors.

5.3 – Outcrop scale structures

On the basis of the geological survey, I decided, for the field evidences of intense syn-tectonic fluid circulation and consequent fluid-rock interaction, to investigate with more detail four structures (Fig. 11). The fluid-rock interaction triggered the development, along these structures, of several types of metasomatic rocks and peculiar textures (see below). Based on my geological survey these four analysed structures belong to the brittle-ductile structures that affect the investigated area. The four structures analysed in detail are: the Moncalero, the Tugello, the Bisciarelle and the Paganella Creek Fault (Fig. 10). On the basis of the geological survey and the detailed study of these structures, their orientations, their tectonic directions of movement and for their deformational events, I related the Moncalero Creek Fault to the older system of regional reverse shear zones (RSZ1), the Tugello and the Bisciarelle Creek Fault to the younger system of regional shear zones (RSZ2), and the Paganella Creek Fault to the minor system of strike-slip/oblique slip systems and in particular a P-shear fault related to the older fault structures of the investigated area.

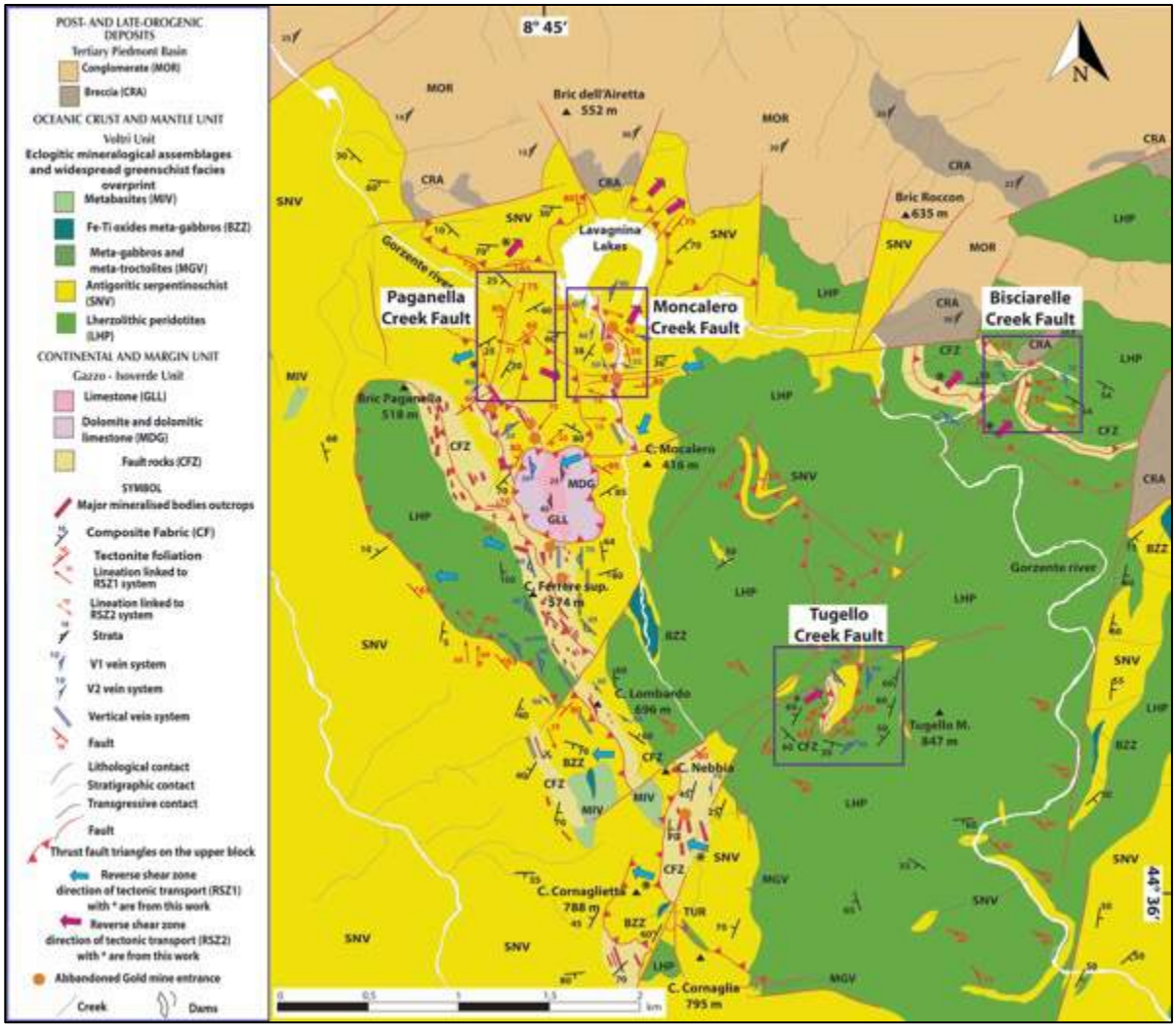

Figure 11: Structural sketch of the Lavagnina Lake area, redrawn with updates and georeferenced with QGIS open source software (after Spagnolo, 2004). In this sketch, the four structures analysed in detail are highlighted with the violet squares.

5.3.1 – Moncalero Creek Thrust Fault

5.3.1.1 – Outcrop scale structures

This area (GPS coordinates N 44° 36' 11", E 8° 45' 30", Fig. 11) is located along the Moncalero Creek, which is a left-side tributary of the Lavagnina Lakes.

The area is characterised by the occurrence of a trust fault exposed in a 100 m long outcrop (Fig. 12, 13). The bedrock is made up of massive serpentinites. Close to the analysed structure the serpentinites gradually become serpentinite schists characterised by a pervasive composite fabric. Moreover, the serpentinite schists,

approaching to the damage zone of the structure, show a widespread and dense network of brownish veins. These veins are made up by carbonates, are mm thick, and randomly oriented.

The fault damage zone is structurally complex, from the top to the bottom, three main structural domains have been identified, namely: damage zone of the hanging-wall, fault core, and damage zone of the footwall (Fig. 13). The analysed fault shows a symmetric damage zone developing a syn-tectonic metasomatic alteration linked to carbonatic-fluids. Moreover, the fluid-rock interaction is limited close to the damage zone of the structure.

The hanging-wall is made up of serpentinite and serpentinite schist up to 5 m thick. The rocks are characterised by a pervasive schistosity (Fig. 14a), gently dipping to E-SE, and near the fault core it is sub-parallel to the fault surface. The schistosity of the serpentinites and serpentinite-schist is a pervasive composite fabric (CF). In the hanging-wall P-shear fractures (Ramsay and Huber, 1987) occur, linked to the damage zone of the fault (Fig. 14b), they are NNE-SSW striking, and steeply dipping to E. Along the P-Shear fractures, syn-tectonic fluid-rock interaction took place, developing cm- to dm-thick levels of carbonated serpentinites referred to as listvenites (Chapter 4, Hansen et al., 2005), which consist of strongly carbonated serpentinite fragments, cemented by a hydrothermal carbonate matrix of Mg-Fe-Ca carbonates and quartz, with accessory serpentine, hematite, and magnetite.

The fault core is made up of listvenites, greenish to brownish due to the syn-tectonic carbonation of the bedrock and it is up to 60 cm thick. The syn-tectonic carbonation of the fault core is due to the crystallization of the strong to total carbonation of the serpentinites. The fault core is characterised by sigmoidal bodies, resembling duplex structures (Ramsay and Huber, 1987; Fig. 15, 16) showing a tectonic transport top to NW. The fault surface is weakly corrugated, WNW-ESE striking, sub-horizontal or gently dipping to E-SE. The fault surface shows two superposed sets of slickenlines and chatter marks. The slickenlines of both sets are up to 5 cm long, up to 0.5 mm thick, and up to 0.5 mm relief. The chatter marks of both sets are up to 4 cm long, up to 1 mm thick, cm width, and up to 0.5 mm relief. The two sets of slickensides show visible crosscutting relationships: the older mainly dips to E-SE and is linked to the top to W-WNW accordingly with the chatter marks sense of shear, marked by the duplex

structures and linked to a reverse movement. The slickenlines of the younger set have plunges around 40-60° and dip to NE accordingly with the chatter marks sense of shear. This set is linked to a main contractional phase with minor strike-slip / extensional movements top to SW (Fig. 14c).

The footwall is made up by serpentinite and serpentinite-schist up to ca. 4.5 m thick characterised by weak carbonation. Close to the fault surface it is characterised by R-shear fractures (Ramsay and Huber, 1987), linked to the damage zone of the fault (Fig. 4c), they are N-S striking, and steeply dipping to W.

The footwall damage zone is also characterised by carbonates veins (Fig. 17), which in most cases are extensional veins, and in some cases show hydraulic-breccias (Jébrack, 1997; Fig. 18). These veins are mm to cm wide, with a spacing of ca. 20-30 cm. They show a peculiar reddish colour due to the occurrence of secondary alteration minerals (Fig. 17) such as pyrite. These veins are mainly NNE-SSW (Fig. 14d) striking and are steeply dipping with high angle with respect to the thrust plane and they can be referred to as filled extensional fractures with shear component or as Riedel shear veins (Ramsay and Huber, 1987). The hydraulic-breccias are mm to cm thick, with a spacing of 10 to 50 cm. They show angular centimetric serpentinite clasts, which are unaltered by carbonates, and a reddish Fe-Mg carbonates matrix.

In this area has been done a sampling of the most interesting structures (Fig. 13) for the petrographic section (see below).

In the previous paragraph, has been shown that the analysed fault shows a symmetric damage zone. This characteristic depends on several factors, such as the host rock, the weakly corrugated fault surface, and the displacement; but the main factor for the symmetry of the Moncalero fault should be related to the same host rock both in the hanging wall both in the footwall and hence with the same mechanical properties. Structurally the fault shows the development of both brittle-ductile (duplex structures in the fault core) and brittle (P-shear fractures in the hanging wall, R-shear fractures, extensional veins and hydraulic breccias in the footwall) structures permeated by syn-tectonic carbonate fluids. The presence of both brittle-ductile to brittle regime deformation testifies a long-lived evolution of the structures, and the carbonation of both these kinds of structures testifies a long-lived circulation of carbonate fluids too.

The fault core is characterised by intense carbonation of the serpentinites with

the development of listvenites. In contrast to the fault core, the damage zones are characterised by a less developed and less widespread carbonation, and limited to the shear fractures (P-shear in the hanging wall and R-shear in the foot wall) and to the veins (extensional and hydraulic breccias in the footwall). Therefore, the carbonation of this area is strictly related to the structures that have acted as preferential pathway for the carbonate fluid circulation.

On the basis of the two sets of slicklenlines and chatter marks, and their crosscutting relationships, above described, at least two different stages of tectonic movement could be recognized. The older stage shows main top to W-WNW linked to a reverse movement; whereas the younger stage shows main top to SW, and it is linked to a main contractional phase with minor strike-slip / extensional movements.

The progressive development of the fault core from damage zones, and the development of different types of fault rocks, implies that different permeability properties occur in different regions of fault zones at different evolutionary stages (Fig. 19). The progression of fracturing in the damage zone increases permeability and connectivity and the whole fault zone behaves as a conduit for fluid flow.

The lateral propagation of the low-permeability fault core dissects the across and along strike continuity of the conduit, causing its progressive compartmentalisation into sectors with low hydraulic exchanges. The contrast between medium- to high-permeability damage zones and fault core boundary regions, imparts a directional anisotropy to permeability in fault zones, which act as conduits for fluid flow parallel to the fault strike and as barriers for fluid flow perpendicular to the fault strike.

In Figure 20 are summarized the main architectural characteristics, the physical properties, the sampling and X-ray analysis results of the Moncalero Creek fault.

The Moncalero Creek fault, for its orientation, the tectonic direction of movement and for the deformational events can be related to the first system of regional reverse shear zones (RSZ1) that affect the Lavagnina Lake area also compared to what described for the Voltri Massif by Capponi and Crispini, 2002; Federico et al., 2005 and Spagnolo et al., 2007.

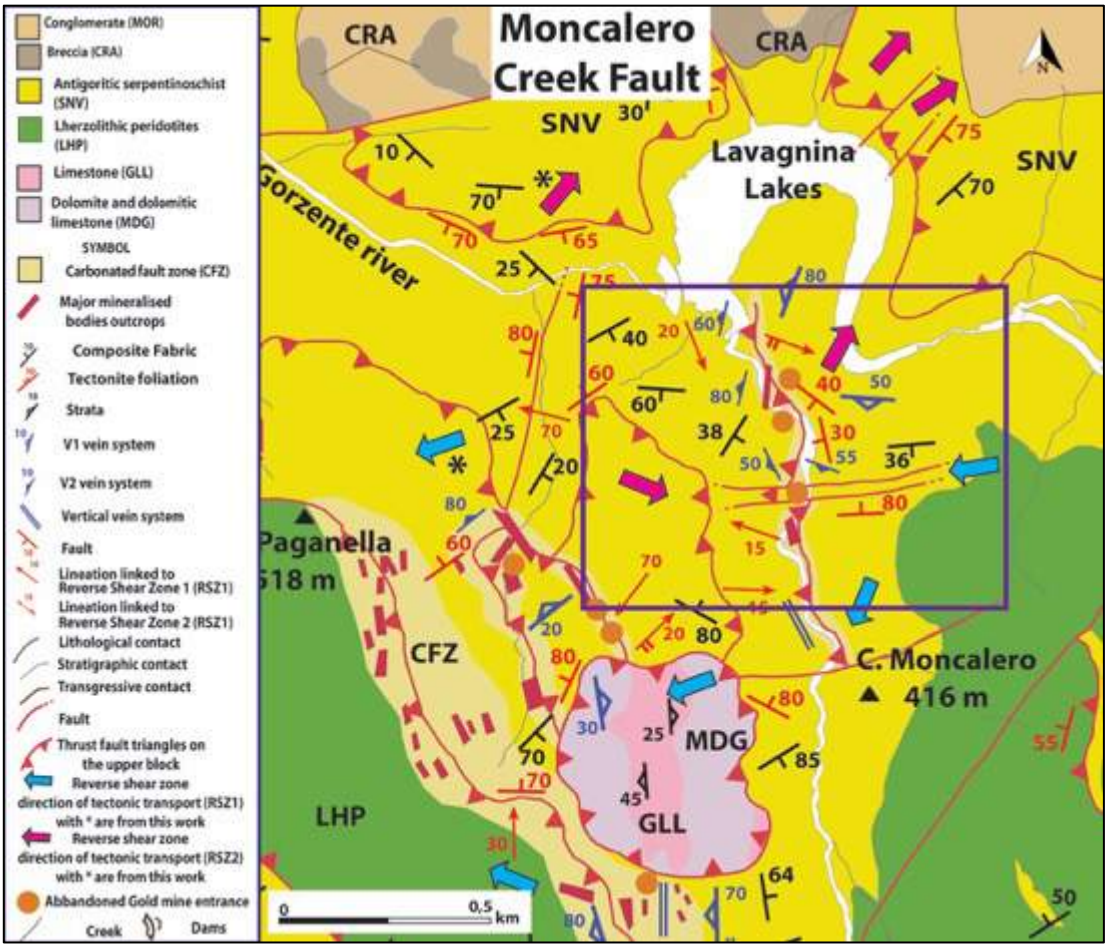

Figure 12: Structural sketch, magnification of the analysed area. The violet box highlights the Moncalero fault. For the positioning between the analysed areas please refer to Fig. 11 paragraph 5.3.

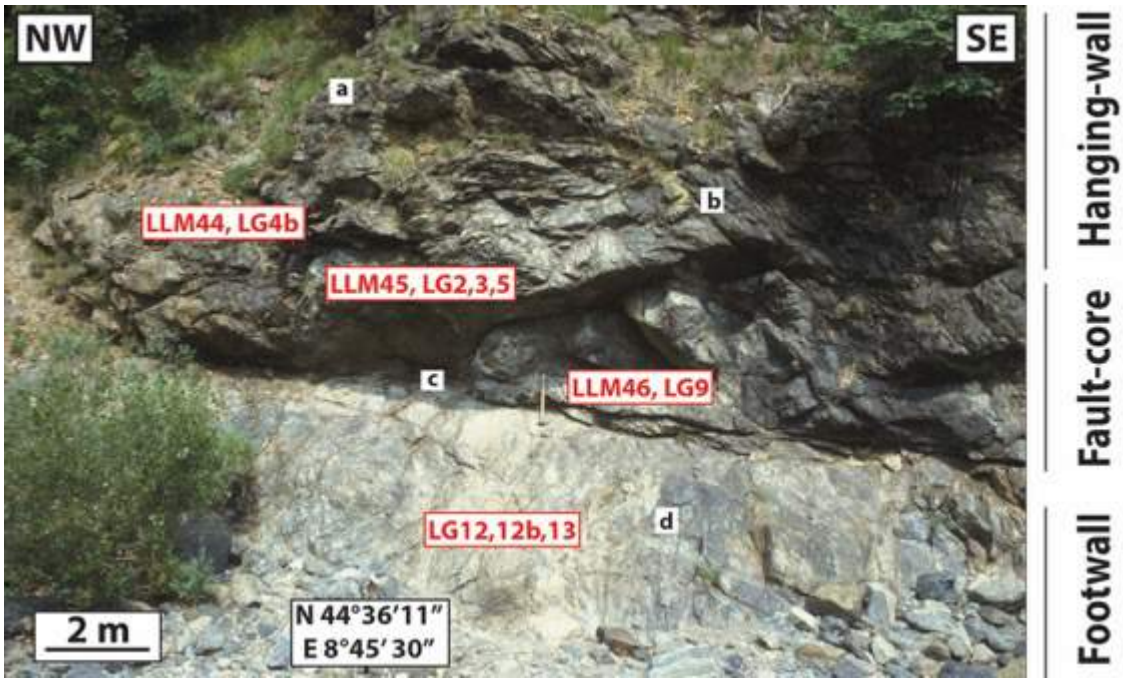

Figure 13: Moncalero thrust fault along the serpentinites. At the right side the three main structural domains are shown. In this figure are also shown the location of the samples (LLM and LG), and the location of the measured structural elements (a, b, c, d) shown in Fig. 4.

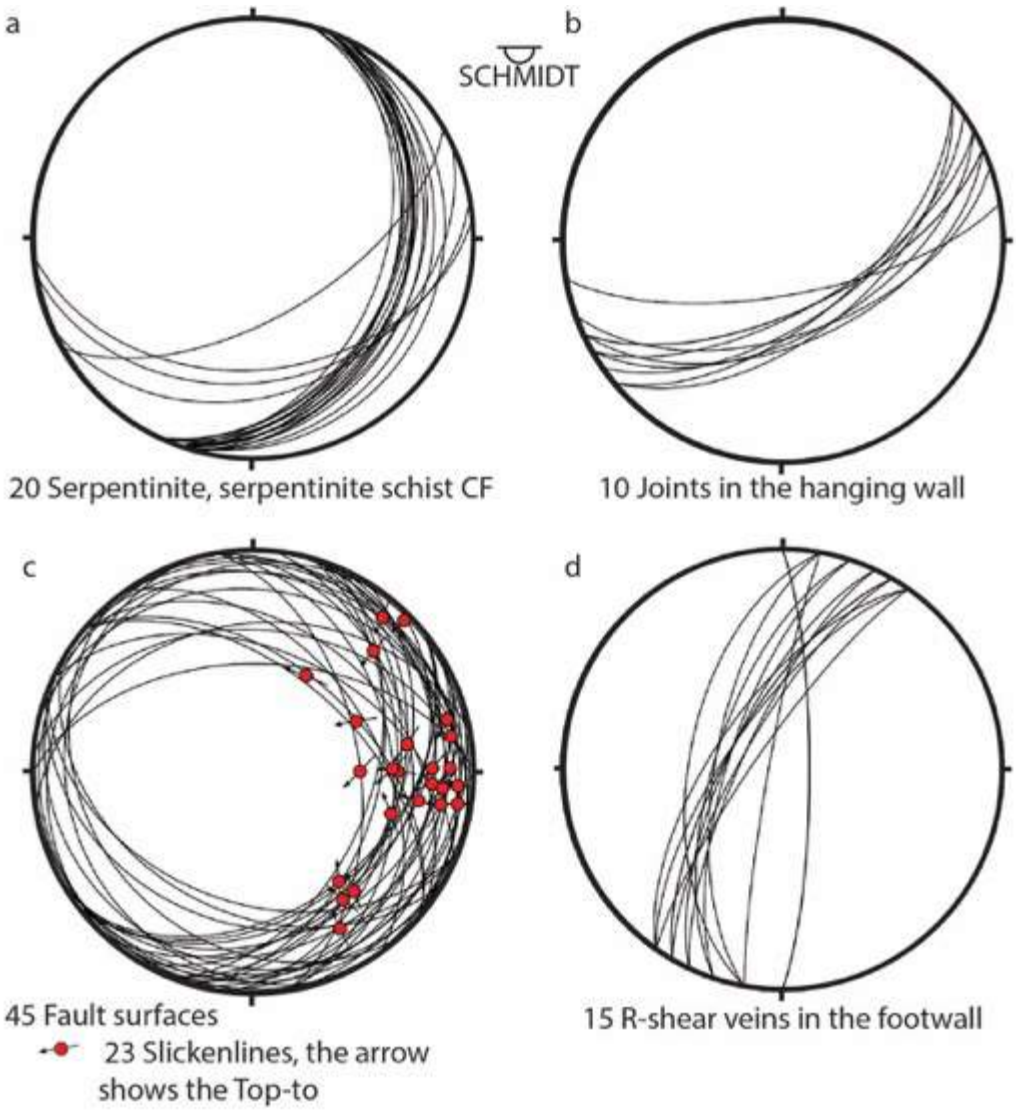

Figure 14: Structural elements of Moncalero outcrop.

Figure 15: Central portion of the fault core, marked by duplex structures, the sigmoidal bodies show a top-to NW.

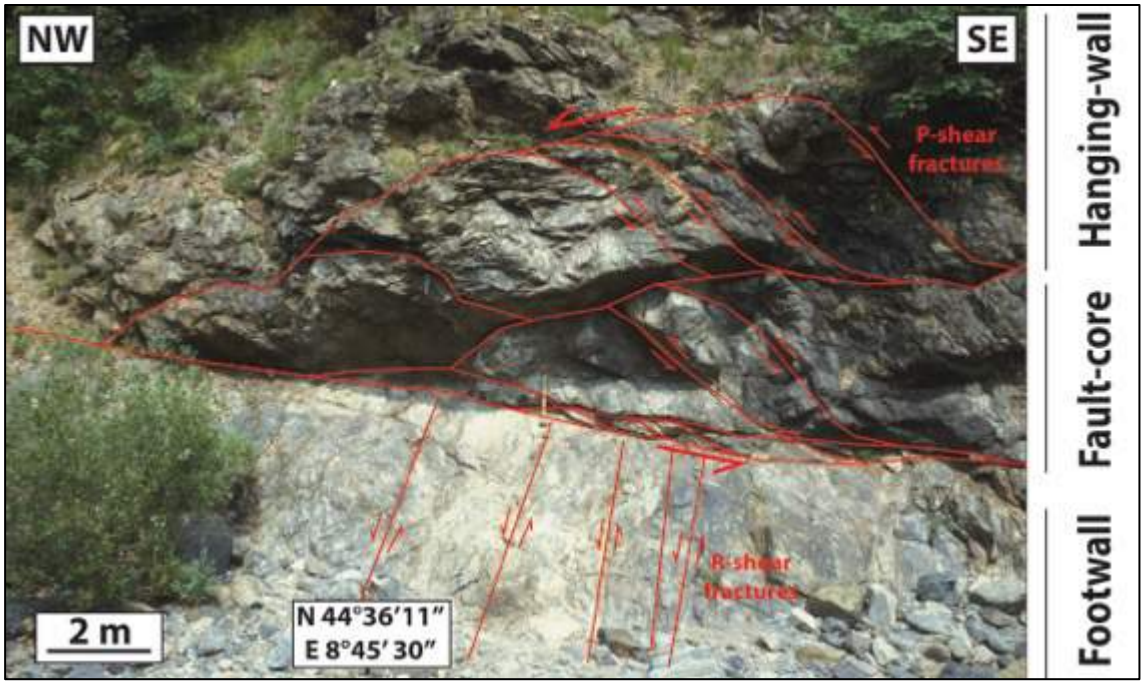

Figure 16: Structural sketch of the trust fault. In the hanging-wall has been highlighted the P-shear fractures, and in the footwall the R-shear fractures.

Figure 17: Extensional fractures, along the footwall, filled by carbonates. It is evident the carbonation close to the veins walls, related to carbonates fluid infilling. The peculiar reddish colour is due to the occurrence of secondary alteration minerals.

Figure 18: Detail of the footwall veins with hydraulic-breccia with serpentinite angular clasts surrounded by reddish carbonates matrix.

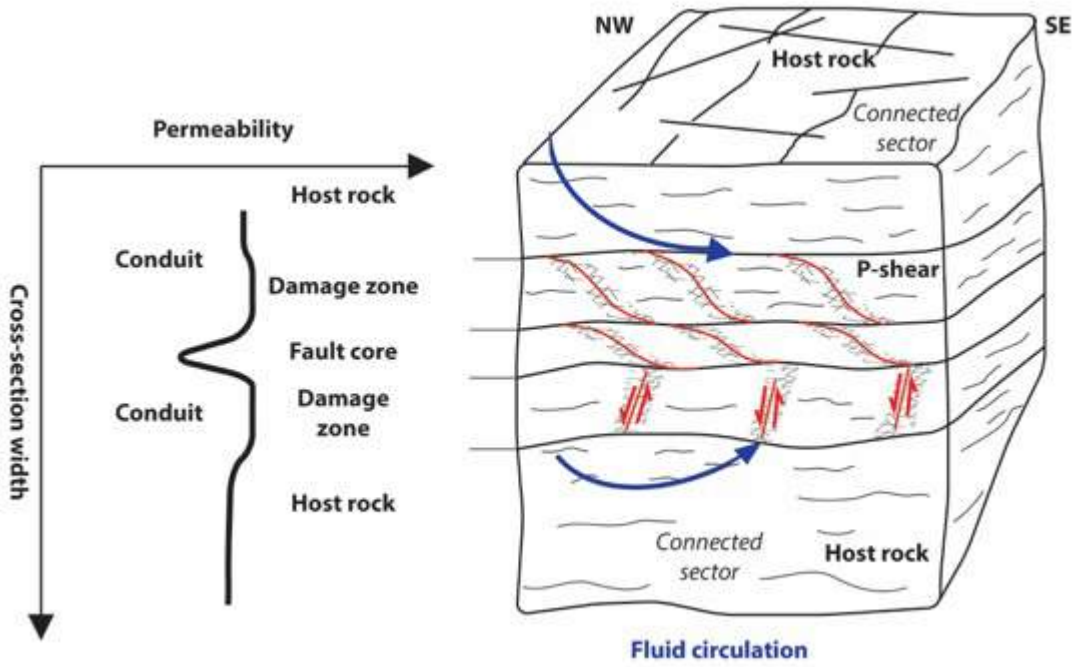

Figure 19: Cartoon showing the permeability structures of the Moncalero Creek Fault zone. The qualitative graph schematically shows the transition from a conduit to barrier behaviour of the fault zone.

Zone	Host rock	Hanging wall	Fault Core	Footwall	Host rock
Fault rock	None	Mylonitic Listvenite Levels along the P-shear	Listvenites	Highly foliated serpentinites with carbonation	None
Width	> 10 m	1.5 m	ca. 60 cm	5 m	>10 m
Rock Fault rock description & Structures	Serpentinites and serpentinite schists	Mylonitic listvenites (ML) P-shear fractures with carbonated serpentinite clasts (up to 40% vol.) abundant carbonate matrix (up to 60% vol.)	Totally carbonated listvenites Duplex structures	Highly foliated serpentinites with carbonation R-shear fractures Extensional veins Hydraulic breccias (HB)	Foliated, serpentinite Extensional carbonates and quartz veins
Grain size		mm to cm	mm to cm	HB: mm to cm	
Porosity	5-10 %	0-5 %	0-5 %	10-15 %	10-15 %
Bulk Strain	Small dilatation	Noncoaxial strain	Shear strain	Large dilatation	Small dilatation
Fluid Pathway	Composite Fabric permeability	Potential Seal P-shear fractures permeability	Potential Seal Duplex structures permeability	Composite Fabric permeability	Composite Fabric permeability
Permeability m/s	10^{-6} - 10^{-7}	ML: 10^{-7} - 10^{-8} 10^{-4} - 10^{-5}	10^{-8} - 10^{-9}	10^{-4} - 10^{-5}	10^{-6} - 10^{-7}
Sample	LLM44 LL4b	LLM45 LG2,3,5	LLM46 LG9	LG12,12b,13	LLM58D LL4C2,6
RX					Vein Qtz+Fe-Mgs+Dol
Fluid inclusions	The sample of quartz veins with mm to cm quartz crystal ad hoc prepared for the study of fluid inclusions, have highlighted that the quartz of this study area contains no useful fluid inclusions.				

Figure 20: Moncalero Creek fault zone architecture, with the main features summarised. The porosity and permeability values are qualitatively, and they were obtained using the measure done for the hydrogeological map of the Terzo Valico dei Giovi by Rete Ferroviaria Italiana (Free downloadable on: www.va.minambiente.it/File/Documento/162745); in this scheme consider them as qualitative. The mineral abbreviations are after Kretz, 1983.

5.3.1.2 – Microstructures

As observable on the field, the serpentinite and serpentinite schist belonging to the hanging wall of the Moncalero Creek Fault (Sample LLM45, LG2, LG3, LG5 Fig. 13, 20), show variable textures and variable degree of carbonation. The thin section from the hanging wall of the serpentinite (sample LLM45) shows serpentinite schist, which still display primary textures. The massive serpentinites is made up of serpentine (80 vol. %), carbonates (10 vol. %), structural relicts of pyroxenes (ca. 2 vol. %), and oxides (ca. 2 vol. %).

Toward the fault core (LG2, 3, 5 sample) the rock is made up of serpentine (80 vol. %), carbonates (15 vol. %) and quartz (ca. 5 vol. %). The serpentinite schist shows S-C' fabric; serpentinte sigmoidal bodies define these bands. The S-C' fabric is characterised by microcrystalline red carbonates (100-150 μm in size; Fig. 21a, b) that partially to totally replace the serpentine. The sense of shear, accordingly with the shear bands, is a left-lateral movement that shows a top to NW accordingly to the fault movement.

Carbonate veins cut all the previous textures. These veins are pluri-mm to cm long, 500 μm thick and are randomly oriented.

The listvenites, developed along the P-Shear fractures (described above), are made up of strongly to totally carbonated serpentinite clasts and are matrix supported (Fig. 21c, d). They are made up of quartz and carbonates (up to 60 vol. %), and serpentinite clasts (40 vol. %). The serpentinite clasts of the breccia are angular to sub angular in shape, and they still preserve an older foliation. Some clasts along the foliation show carbonate patches. The clasts are up to 5 mm in size, and they are randomly oriented.

Carbonates and quartz made up the matrix of the breccia. The carbonates are coarse grained up to 500 μm in size, and they are randomly oriented. The quartz is fine grained up to 100 μm in size, and shows granoblastic textures.

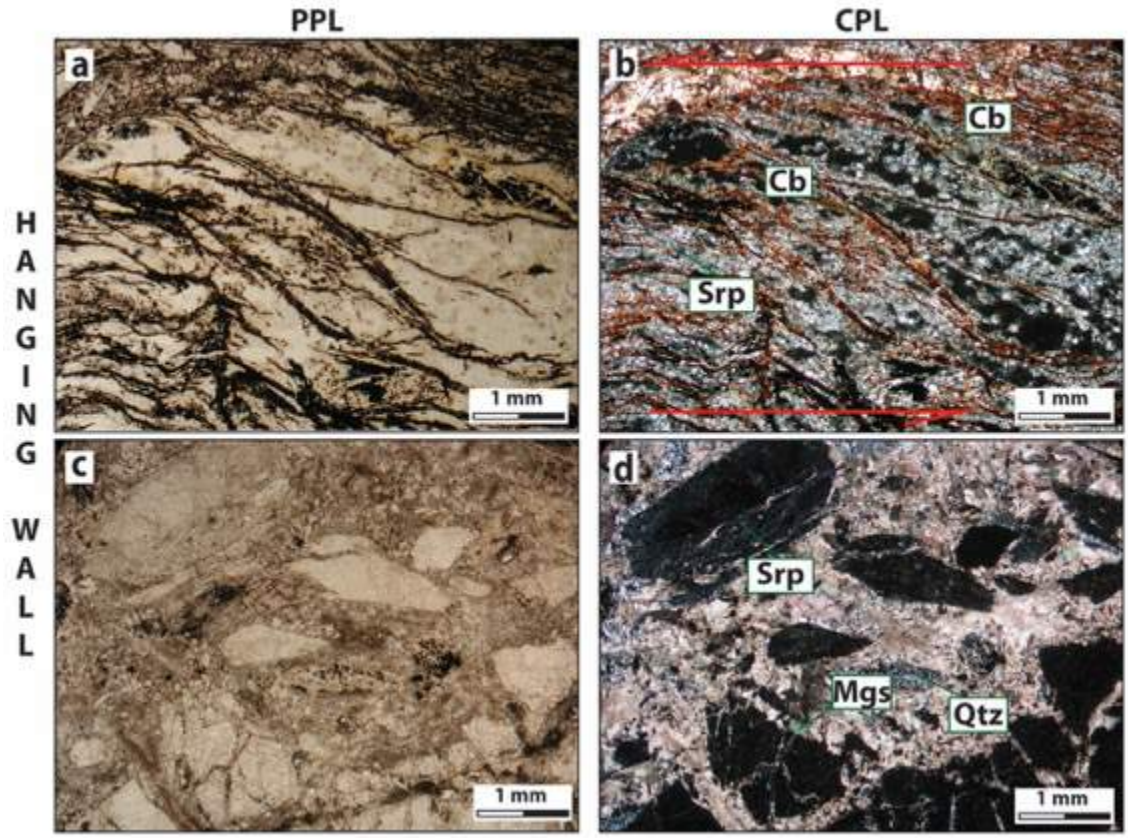

Figure 21: Photomicrograph of the hangingwall of the Moncalero Creek fault; the photomicrograph in the left side are in plane polarised light (PPL), whereas the photomicrograph in the right side are in crossed polarised light (CPL). (a, b) Serpentinite schist with S-C' fabric marked by red carbonates. (c, d) Fine crush breccia made up by serpentinite clasts and carbonates and quartz matrix.

The fault core (Sample LLM46, LG9, Fig. 13, 20) is made up by carbonates (80 vol. %) and quartz (30 vol. %). The carbonates are from medium to coarse grained (from 100 to 300 μm, Fig. 22a, b), and randomly oriented. The quartz is from fine to medium grained (from 50 to 100 μm, Fig. 22a, b). In thin section a mixture of carbonates and quartz makes up the fault core.

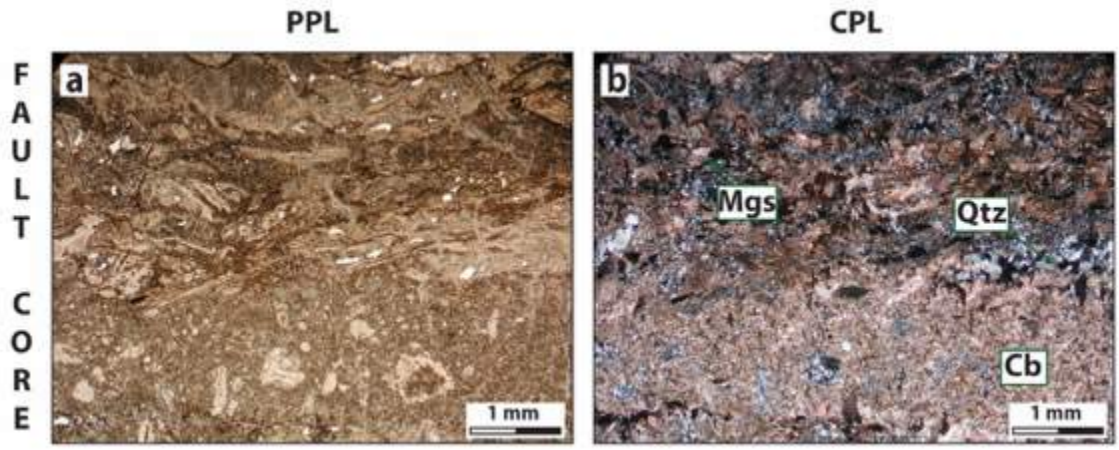

Figure 22: Photomicrograph of the fault core of the Moncalero Creek fault; the photomicrograph in the left side are in plane polarised light (PPL), whereas the photomicrograph in the right side are in crossed polarised light (CPL). (a, b) Listvenites made up of carbonates and quartz.

The footwall (Sample LG12, LG12b, and LG13, Fig. 13, 20) is made up of carbonated serpentinites (Fig. 23a, b), which show a strong foliation marked by serpentine and carbonates. The carbonates show elongated crystals up to 200-300 μm long, and represent the 60 vol. %. The crystals are oriented parallel to the foliation. Moreover, have been observed two types of carbonates veins, but no clear crosscutting relationships have been observed. The first system (Fig. 23a, b) is characterised by micro-veins that cut the foliation at ca. 50-60°, and they are made up of carbonates. These veins are up to 400 μm thick, and cm spaced. These veins do not show a clear evidence for their growth mode, since the crystals are randomly oriented. The second system of veins (Fig. 23c, d) is characterised by polyphasic growth, are mm to pluri-mm thick, they cut the foliation at high angle at ca. 70-80°, and they are made up of carbonates. These veins show at least two growth steps, since the 50% of the volume of these veins is made up of fine crystals up to 200 μm long, whereas the other 50% of the volume is made up of coarser crystals up to 1 mm long. Both the finer and the coarser crystals are randomly oriented. The contacts between the two portions of the veins, as well as the contact between the vein walls and the host rock, are irregular or wavy.

In Figure 24 are represented the mineral phases present in the three main different structural domains.

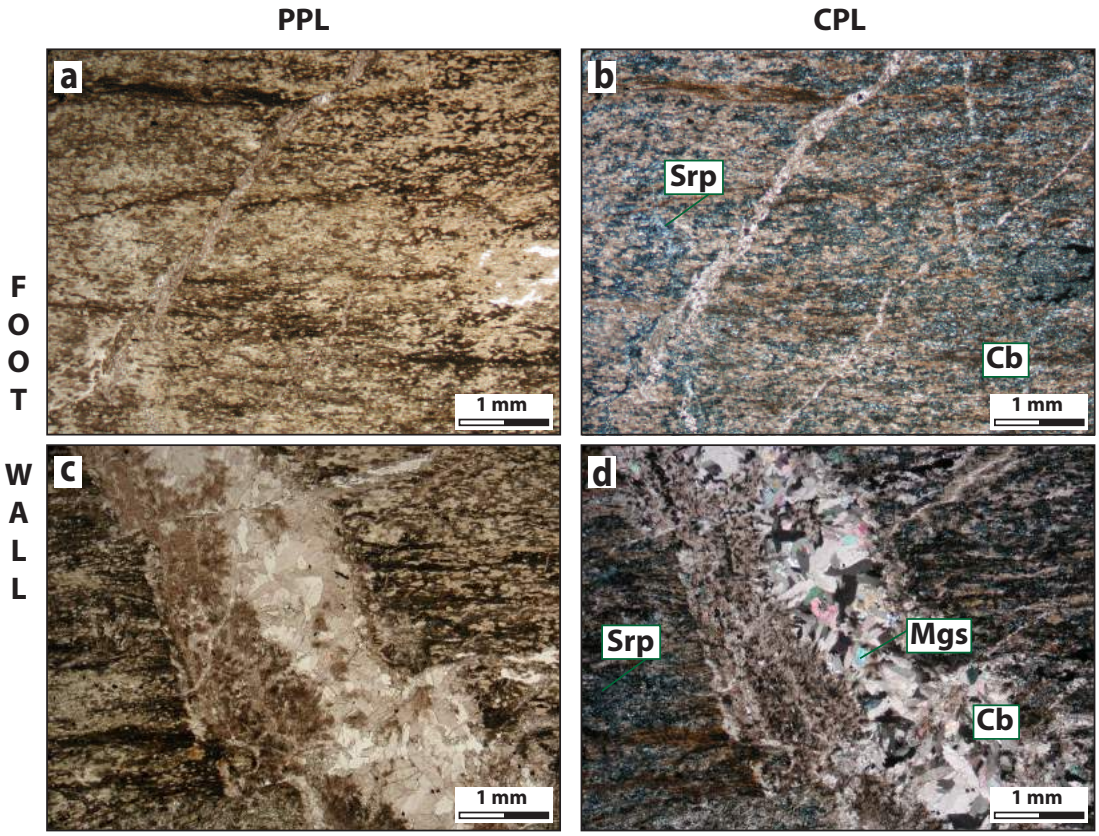

Figure 23: Photomicrograph of the foot wall of the Moncalero Creek fault; the photomicrograph in the left side are in plane polarised light (PPL), whereas the photomicrograph in the right side are in crossed polarised light (CPL). (a, b) Foliated carbonated serpentinites, cut by the first type of carbonate veins. (c, d) Vein characterised by composite poliphasic growth.

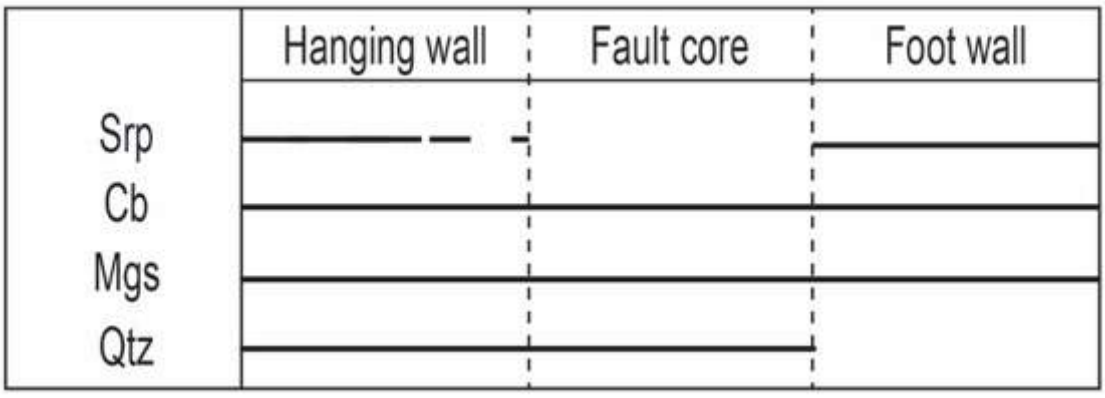

Figure 24: Summary of the mineral phases present in the three main different structural domains. The mineral abbreviations are after Kretz, 1983.

5.3.2 –Tugello Creek Thrust Fault

5.3.2.1 Outcrop scale structures

The analysed area (GPS coordinates N 44° 35’ 8”, E 8° 46’ 21”, Fig. 11 paragraph 5.3) is located along the Tugello Creek, near the Tugello Mount. The area is characterised by the occurrence of a thrust fault exposed in a 300 m long outcrop (Fig. 25, 26). The analysed structure is developed approximately at the lithological transition between serpentinized lherzolites and serpentinites. The lherzolites are mainly massive, made up by ortho- and clino-pyroxenes, spinels, and plagioclase with frequently cm to dm thick piroxenite bands, and are characterised by a tectonite foliation. Near the damage zone of the structure the serpentinized lherzolites show an increasing degree of fracturing, delimiting m to pluri-m boulders. The serpentinites in this area are both massive and foliated. Especially near the damage zone of the structure, and close to the fault core, the serpentinites are characterised by an intense composite fabric. Moreover, in this area the serpentinite schists show a widespread veins networks. The veins are made up by carbonates, are cm thick. Generally, these veins have a scattered orientation, anyway at least two main sets of veins can be distinguished (see below).

The fault damage zone is structurally complex (Fig. 25, 26, 27, 28), from the top to the bottom of this structure, three main structural domains have been identified, namely: damage zone of the hanging-wall, fault core, and the damage zone of the footwall (Fig. 26). The analysed structure shows an asymmetric damage zone, more developed in the footwall, with intense cataclasis, producing incoherent fault rock; it is characterised by widespread (up to 10 m) and intense syn-tectonic carbonation until the total replacement of the host rock producing a 5-10 cm thick level entirely made up of dolomite. This syn-tectonic metasomatic alteration produces carbonated serpentinites with saponite, dolomite and sepiolite.

The hanging-wall (Fig. 26, 27) is made up of mainly unaltered serpentinized lherzolites dark green in colour, and up to 20 m thick. The damage zone in the hanging-wall is up to 5 m thick, it is characterised by synthetical P-shear (P, accordingly to the shear fracture system described by Ramsay and Huber, 1987) conjugate shear fractures (Fig. 29a), which displace sigmoidal serpentinized

lherzolite bodies. These P-shear fractures are NNW-SSE striking, dipping to ENE at relatively high angles (45-60°) and show a sense of shear with a top to WSW.

Near the fault core, the damage zone is characterised by fault gouges (after Sibson, 1977) up to 70 cm thick. These fault gouges are made up of mm- to cm-sized serpentinite clasts (10 to 20% in volume), and serpentinite matrix (90 to 80% in volume). Complex extensional vein network, filled by carbonates cut the gouge, the veins are 3-4 cm thick. One set of this network is sub-parallel to the fault slip surface, and it is the most common.

The damage zone of the fault core is structurally complex with peculiar structures with different mineralogical composition (i.e. chalcedony shear veins and sepiolite duplex structures, Fig. 27, 28).

Near the contact with the serpentinized lherzolites, the damage zone (Fig. 28) is made up of incoherent serpentinite fault gouge (after Sibson, 1977), up to ca. 2 m thick and brownish in colour due to the syn-tectonic circulation of carbonatic fluids. Here the serpentinite fault gouge shows mm-sized serpentinite clasts (10 % in volume) and carbonate matrix (90 % in volume). Under the serpentinite gouge there is a level, up to 0.5 m thick, marked by sigmoidal bodies (duplex structures Ramsay and Huber, 1987) indicating a reverse sense of shear with top-to NE.

Approaching to the fault core the serpentinite gouge become yellowish in colour, and the carbonated serpentinite matrix also shows the development of clay minerals (Supplementary material S1: PP34 XRD analysis).

The fault core (Fig. 27) at its top is made up of sepiolite and quartz (Supplementary material S2: PP35 XRD analysis), brownish in colour, up to ca. 15 cm in thickness and ca. 100 m long. This level is parallel to the fault surface, and it is characterised by sigmoidal bodies resembling duplex structures (Ramsay and Huber, 1987) showing a reverse sense of shear with top-to NE.

Under the sepiolite level there is a striated chalcedony shear vein, milky in colour with flow banding-like textures (Faber et al., 2014), up to ca. 10 cm in thickness and exposed for the length of the fault. Inside the chalcedony shear veins carbonated serpentinitic clasts and carbonate clasts are present (up to 1 cm in diameter).

In contact with the chalcedony, there is a massive level whitish in colour and up to ca. 5-10 cm thick. This level is made up of dolomite (Supplementary materials S3: PP37 XRD analysis), and shows peculiar carbonated-coated grains (Smith et al.,

2011; Rempe et al., 2014; Rowe and Griffith 2015). This level is due to the precipitation and crystallization of carbonates due to the circulation of syn-tectonic fluids. The carbonated-coated grains structures are from mm to cm in size, well rounded, showing central clasts made up of serpentinites.

The fault surface is weakly corrugated, NNE-SSW striking, with a main dip to W-NW, with a tectonic transport direction with top-to-NE (Fig. 29b) accordingly with the chatter marks. Two sets of slikenlines (Fig. 29b) occur on the fault surface with visible crosscutting relationship: the older plunge to the W, the chatter marks mostly show a top-to E with major reverse component and minor strike-slip component. The younger set, which cut the first, plunge both to NE and SW, the chatter marks mostly show a top-to NE with major reverse component. The different plunge of the two sets of slickenlines is due to the corrugated fault surface.

The damage zone that characterises the footwall, below the fault surfaces, is characterised by carbonated fault gouge (after Sibson, 1977) of ca. 3 m thick, yellowish in colour. This level is strongly incoherent and carbonated (Supplementary materials S4: PP41 XRD analysis) with serpentinite rounded blocks up to 1 m in diameter (20% in volume) and carbonated serpentinite matrix (80% in volume).

Below the fault gouge, the footwall is made up of highly foliated (Fig. 28b) fractured and veined serpentinites (Fig. 27, 28a) that also show massive domains. The foliation of the serpentinites (Fig. 29c) is a pervasive composite fabric due to the superposition of deformation (see chapter 4).

The vein network inside the serpentinites is linked to the syn-tectonic circulation of fluids inside the damage zone of the fault. The vein network can be distinguished into two sets, on the base of their orientations and their compositions. The older set is made up of widespread extensional carbonate veins up to 3 cm thick, with a spacing of 10 cm. This set show two main orientations (Fig. 29d): parallel to sub parallel to the fault surface close to it, and with high angles with respect to the fault surface.

The extensional carbonate veins are cut by a younger set of tension gashes veins (Ramsay and Huber, 1987), filled by chalcedony near the vein walls and by quartz in the central part of the veins (Fig. 28, 29d, 30), up to 2 cm thick with a spacing of 30-50 cm, striking N-S, dipping whit high angle (60-80°).

In this area has been done a sampling of the most interesting structures (Fig. 26) for the XRD analysis and petrographic section (see chapter 6).

In the previous paragraph, has been shown that the analysed fault shows an asymmetric damage zone, more developed in the footwall with respect to the hanging wall. The asymmetric development of the damage zone depends on several factors as the different rocks that make up the hanging wall and the footwall. In this case the fault surface represents a bimaterial interface separating different elastic bodies.

Structurally the fault shows the development of both brittle-ductile (duplex structures) and brittle (P-shear fractures, tension gashes) structures permeated by syn-tectonic carbonate fluids. The presence of both brittle-ductile to brittle regime deformation testifies a long-lived evolution of the structures, and the carbonation of both these kinds of structures testifies also a long-lived circulation of carbonate fluids too.

Approaching to the fault core, both from the hanging wall and both from the footwall damage zone, this fault shows an increase in the carbonation degree, until the total replacement of the host rock with a carbonate level.

On the basis of the two sets of slikenlines and chatter marks, and their crosscutting relationship, above described, at least two different stages of tectonic movement could be recognized. The older stage shows a top-to E with major reverse component and minor strike-slip component, whereas the younger show a top-to NE with major reverse component.

The progressive development of the fault core from damage zones, and the development of different types of fault rocks, implies that different permeability properties occur in different regions of fault zones at different evolutionary stages (Fig. 31). The progression of fracturing in the damage zone increases permeability, especially in the footwall, which is more developed in thickness, and connectivity. The whole fault zone behaves as a conduit for fluid flow.

The lateral propagation of the low-permeability fault core dissects the across and along strike continuity of the conduit, causing its progressive compartmentalisation into sectors with low hydraulic exchanges. The contrast between medium- to high-permeability damage zones and fault core boundary regions, imparts a directional anisotropy to permeability in fault zones, which act

as conduits for fluid flow parallel to the fault strike and as barriers for fluid flow perpendicular to the fault strike.

In Figure 32 are summarized the main architectural characteristics, the physical properties, the sampling and X-ray analysis results of the Tugello Creek fault.

The Tugello Creek thrust, for its orientation, the tectonic direction of movement, and for its deformational events can be related to the second system of regional reverse shear zones (RSZ2) that affect the Lavagnina Lake area (Capponi and Crispini, 2002; Federico et al., 2005; Spagnolo et al., 2007).

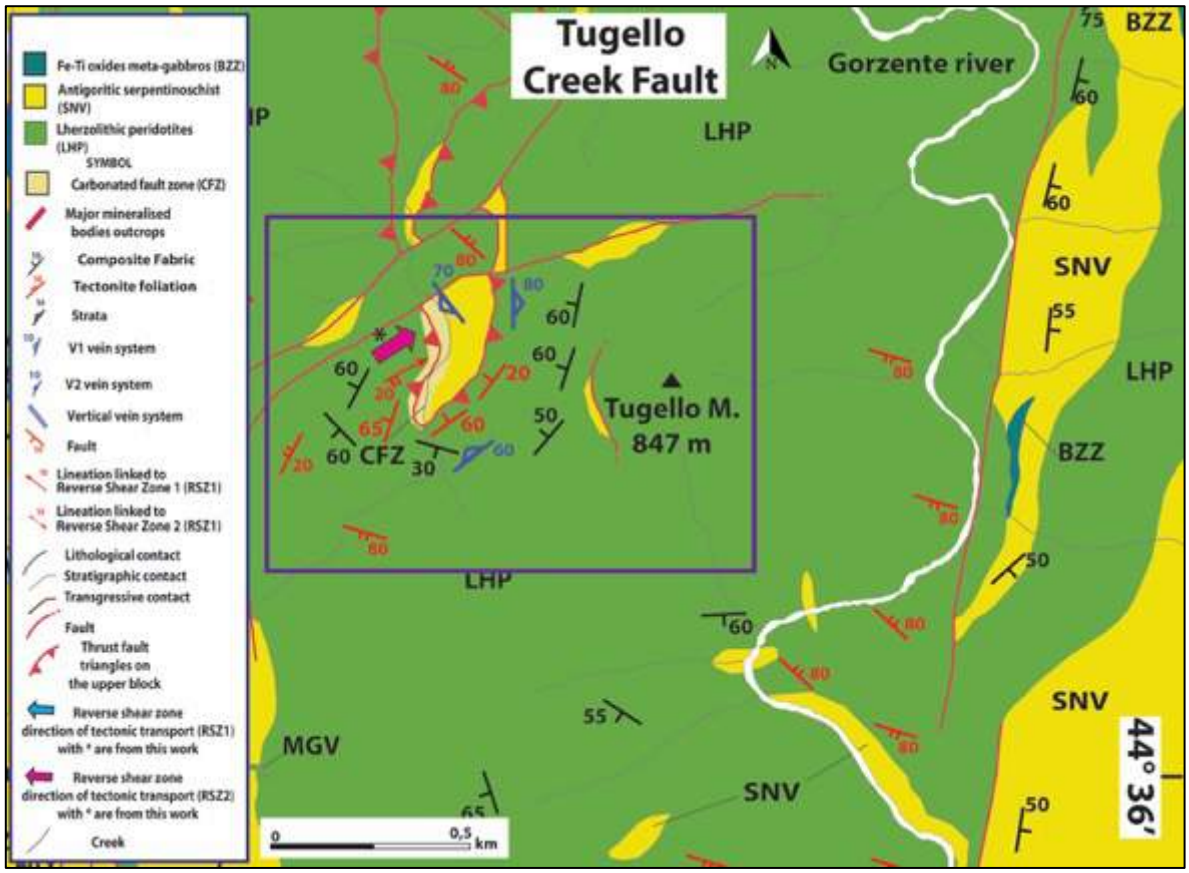

Figure 25: Structural sketch, magnification of the analysed area. The violet box highlights the Tugello Fault near the Tugello Mountain. For the positioning between the analysed areas please refer to Fig. 11 chapter 5.3.

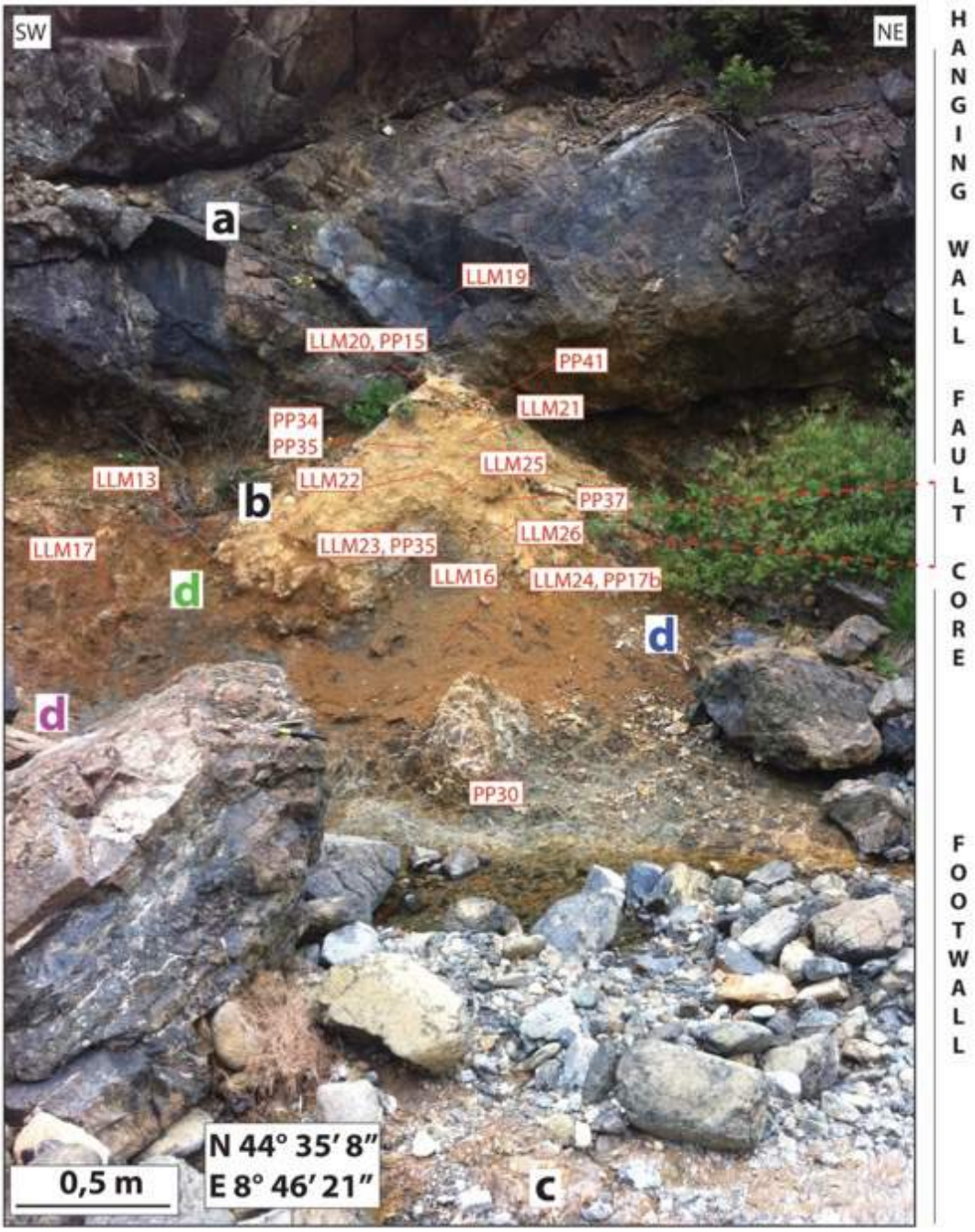

Figure 26: The Tugello Creek thrust. On the right side the three main structural domains are shown. In the figure are also shown the location of the samples (LLM, PP), and the positions of the measured structural elements (a, b, c, d) of Fig. 5. The colours, of the letters for the different structural elements, are the same shown in Fig. 29.

Figure 27: Portion of the duplex structure made up of sepiolite.

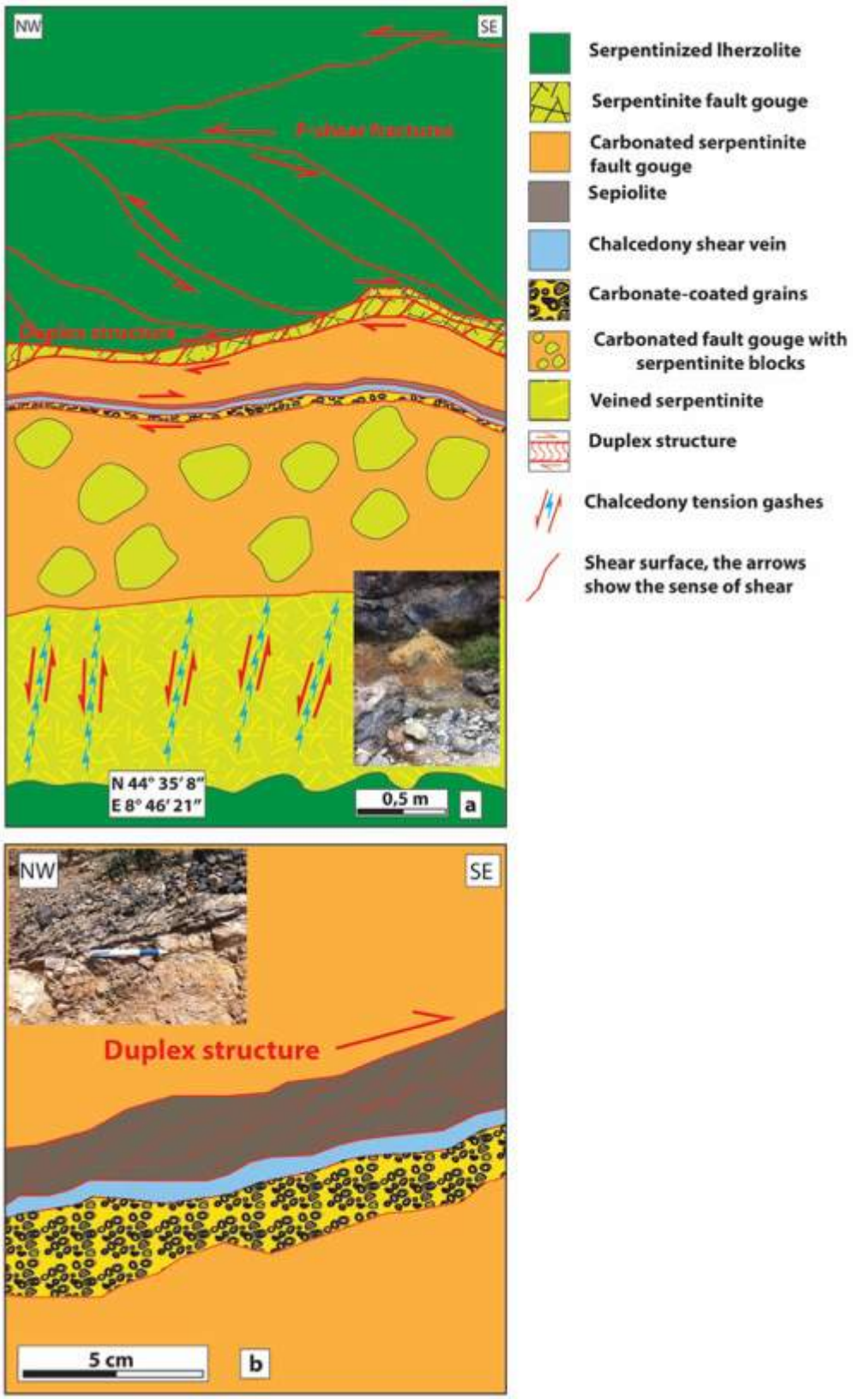

Figure 28: (a) Structural sketch of the Tugello Creek Thrust, the small photograph represents the outcrop. (b) Structural sketch of the central portion of the fault core, characterised by duplex structure, made up of sepiolite (grey level), with a sense of shear top to NE, chalcedony shear vein (blue level), and carbonate-coated grains level (yellow level); the small photograph represents the fault core. (c) Schematic relationship between rock types.

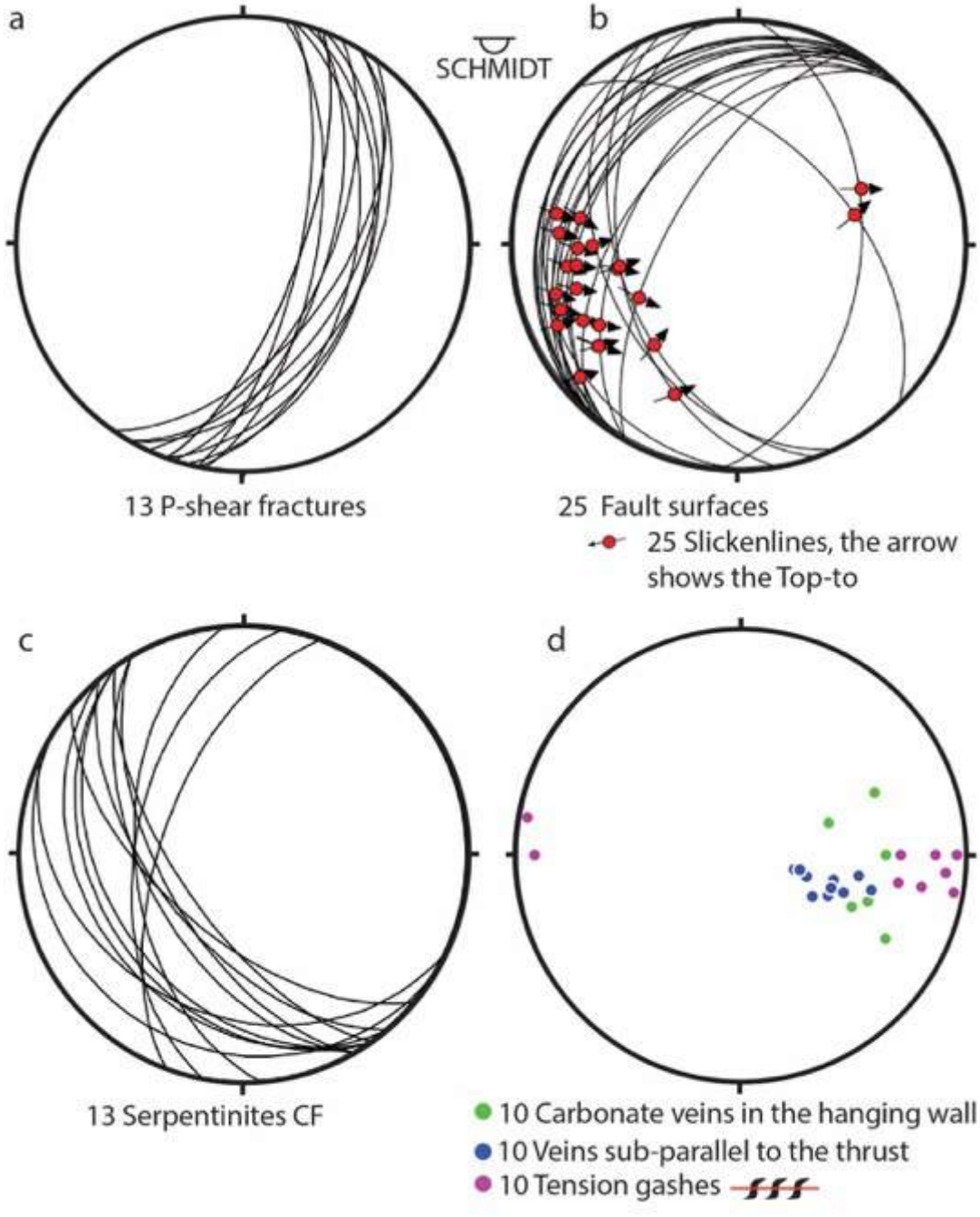

Figure 29: Structural elements of Tugello outcrops. For the tension gashes has been measured the plane represented with the red near the number of measures.

Figure 30: Tension gashes filled by quartz and chalcedony.

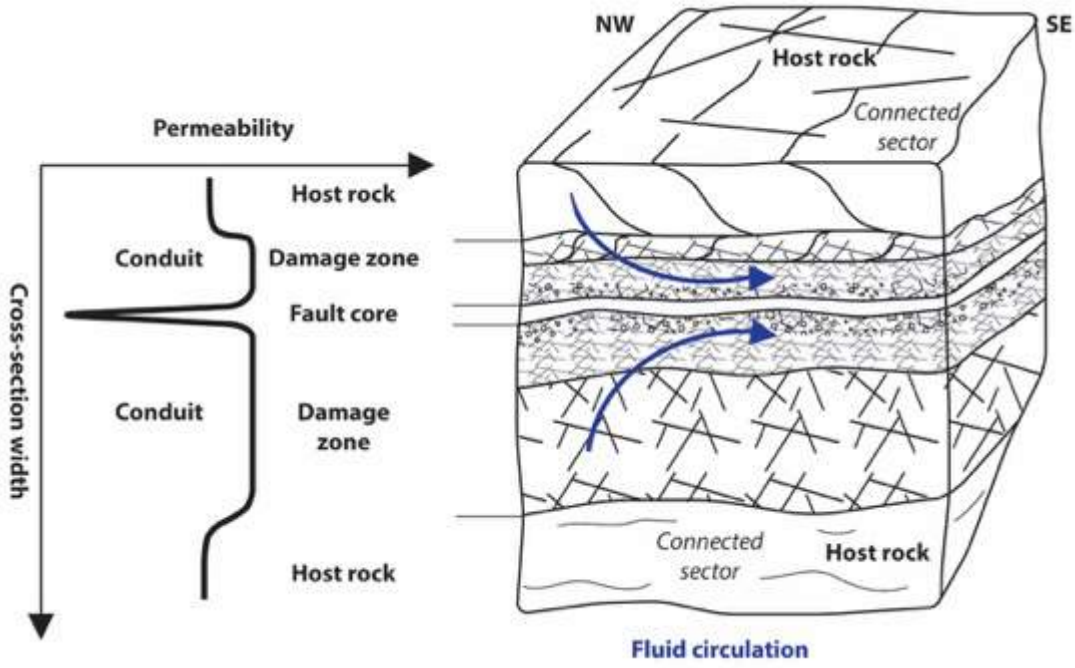

Figure 31: Cartoon showing the permeability structures of the Tugello Creek Fault zone. The qualitative graph schematically shows the transition from a conduit to barrier behaviour of the fault zone.

Zone	Host rock	Hanging wall	Fault Core	Footwall	Host rock
Fault rock	None	Serpentinite Serpentinite Fault gouge	Sepiolite Chalcedony shear vein Carbonate-coated grains	Carbonated Serpentinite Fault gouge	None
Width	> 20 m	70 cm	ca. 40 cm	3 m	15 m
Rock Fault rock description & Structures	Serpentinized lherzolites P-shear fractures	Fault gouge strongly incohesive; serpentinite clasts (10% vol.) abundant carbonate matrix (90% vol.) duplex stuctures	Sepiolite with duplex structures Top-to NE Chalcedony shear vein (CSV) Carbonate-coated grains (CCG)	Gouge strongly incohesive; abundant serpentinite clasts serpentinite boulders (20% vol.) abundant carbonated serpentinite matrix (80% vol.)	Foliated, fractured and veined serpentinite Extensional carbonates veins Quartz & chalcedony tension gashes
Grain size		mm to cm	CCG: mm to cm	mm to cm	
Porosity	0-5 %	10-15 %	< 5 %	20-30 %	5-10 %
Bulk Strain	Small dilatation	Noncoaxial strain	Shear strain	Noncoaxial strain	Large dilatation
Fluid Pathway	Pervasive P-shear fractures	Dynamic Conduit	Potential Seal	Dynamic Conduit	Fractures & CF permeability
Permeability m/s	10^{-6} - 10^{-8}	10^{-4} - 10^{-7}	CSV: 10^{-8} - 10^{-9} CCG: 10^{-6} - 10^{-7}	10^{-4} - 10^{-7}	10^{-6} - 10^{-7}
Sample	PP30 LLM19	PP34,41	PP15a,16b,18,35, 37 CAL1 LLM20,21	LLM13,14,16,17, 22,23,25,26 PP13b	LLM15,24,27,28, 58b PP8,8a,17,19,11a
RX			Sepiolite: Qtz+Sep CCG Qtz+Dol+Mgs+ Clc+Cen		
Fluid inclusions	The sample of quartz veins with mm to cm quartz crystal ad hoc prepared for the study of fluid inclusions, have highlighted that the quartz of this study area contains no useful fluid inclusions.				

Figure 32: Tugello Creek fault zone architecture, with the main features summarised. The porosity and permeability values are qualitatively, and they were obtained using the measure done for the hydrogeological map of the Terzo Valico dei Giovi by Rete Ferroviaria Italiana (Free downloadable on: www.va.minambiente.it/File/Documento/162745); in this scheme consider them as qualitative. The mineral abbreviations are after Kretz, 1983.

5.3.2.2 – Microstructures

The host rock is made up of serpentinized lherzolite (Sample PP30, LLM19, Fig. 26, 32) that shows typical textural features of the lherzolite (Fig. 9). It is made up of olivine (45 vol. %), ortho- and clinopyroxenes (30 vol. %), serpentine (up to 20%), and opaque minerals (5 vol%). The rock is characterised by hypidiomorphic texture and medium to coarse grain size. The olivine is euhedral and undeformed. The olivine is overgrown by serpentine and shows mesh textures (Fig. 33a, b). In thin section, can be distinguished ortho- and clinopyroxenes; they are partially replaced by serpentine along the edges (Fig. 33a, b) and also along the cleavage planes. Serpentine veins cut all the previous structures (Fig. 33a, b). They are mm to cm long, and up to 500 μm thick.

The rare opaque minerals, spinels, are overgrown by chlorite and shows holy-leaf textures (Fig. 33a, b).

Massive serpentinite and serpentinite schist make up the hanging wall (Fig. 33c, d). They do not show textural features of the lherzolite. They are made up of serpentine (up to 90 vol. %) opaque minerals (up to 5 vol. %) and chlorite (up to 5 vol. %). They show a weak foliation marked by serpentine crystals elongated parallel to the foliation (100-150 μm long). The opaque minerals are mainly represented by spinels, which are overgrown by chlorite and show holy-leaf textures.

Toward the fault core (Sample PP34, PP41, Fig. 26, 32), the hanging wall is made up of incoherent serpentinite fault gouge and shows mm-sized serpentinite clasts (10 % in volume) and carbonate matrix (90 % in volume). The serpentinite clast are randomly oriented and nearly totally replaced by carbonates.

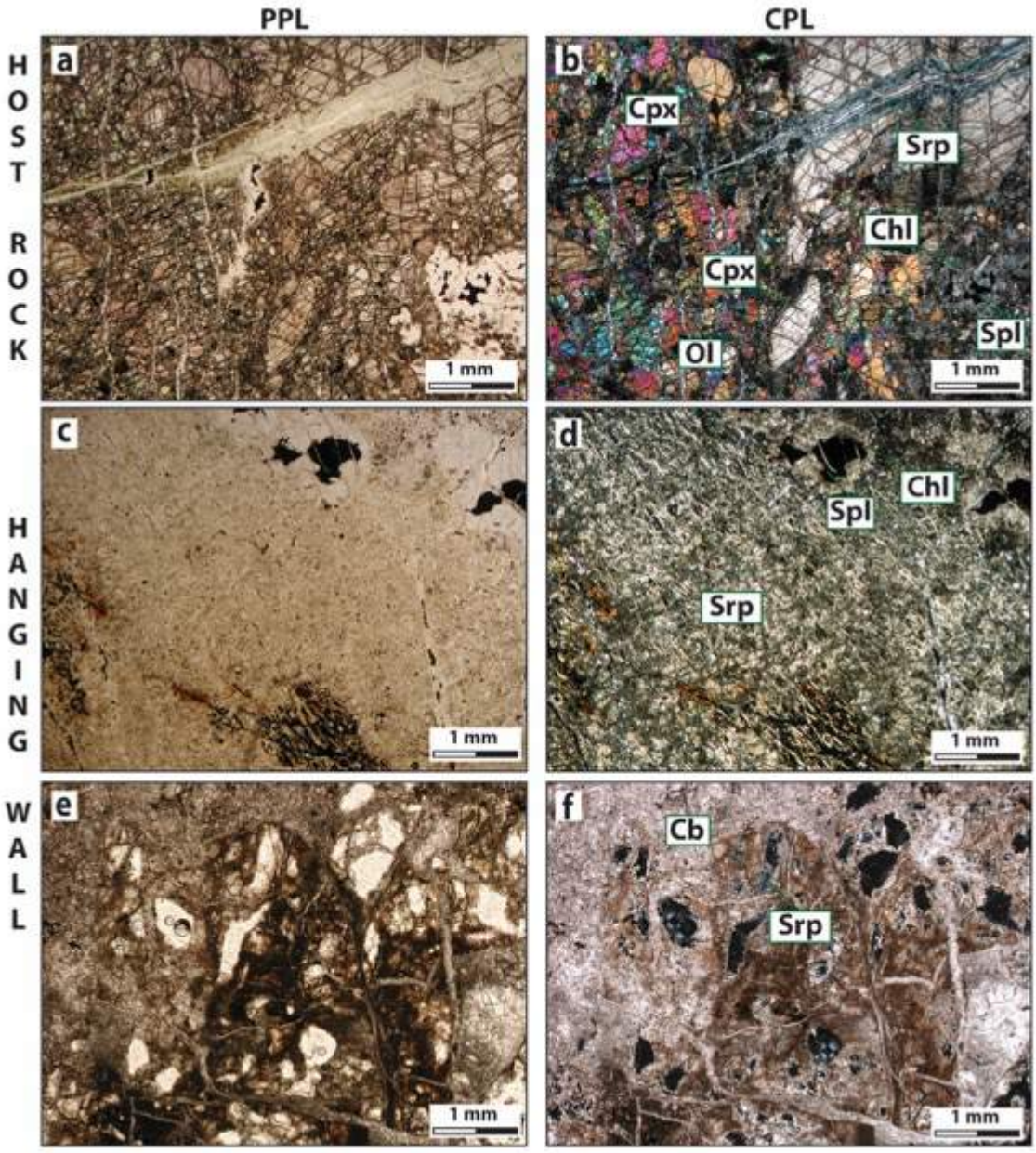

Figure 33: Photomicrograph of the hangingwall of the Tugello Creek Thrust Fault; the photomicrograph in the left side are in plane polarised light (PPL), whereas the photomicrograph in the right side are in crossed polarised light (CPL). (a, b) Host rock made up of serpentinized lherzolites. (c,d) Serpentinites of the hanging wall. (e,f) Carbonated serpentinite fault gouge.

Thin sections of the fault core (Sample LL20, LL21, Cal1, PP15a, PP16b Fig. 26, 32, 34) show that the central part of the fault core of the Tugello Creek Fault is made up of chalcedony shear veins and a carbonate level characterised by carbonate-coated grains (Fig. 34a, b). The thin sections (sample LLM22) as observed on the field show two portions with distinct mineralogical composition: the chalcedony shear vein and the carbonate band. The chalcedony shear vein is made up of both fibrous chalcedony, up to 5mm long, and microcrystalline quartz (Fig. 34a, b; 34c, d), and it is characterised by patches made up of clay minerals.

Within the chalcedony shear veins are present angular clasts made up of carbonates with hematite and opaque minerals. The carbonate clasts are up to 1 mm in size, are randomly oriented, and up to 30 vol. %. Near the contact with the carbonate bands, the shear veins is mainly made up of fibrous chalcedony (Fig. 34c, d), which closer to the contact shows a layer with mylonitic textures. This layer is up to 1.2 mm thick. The chalcedony shear vein sharply passes to the carbonates band (Fig. 34c, d).

In contact with the chalcedony, the carbonates band is characterised by carbonate-coated grains. These grains are from mm to sub-mm in dimensions, are from sub angular to well round in shape, are randomly oriented, and up to 70 vol. %. These grains, on the basis of the dimensions, are heterogeneously distributed. Finally, the coated-grains are matrix supported. Generally, these coated-grains show only one level of coating (Fig. 34a, b, c, d), but in few cases the coating levels are up to three (Fig. 34a, b, c, d). The central part of the carbonate-coated grains, in order of abundance, is made up of namely: *i*) carbonate clast (up to 99%), and *ii*) carbonated serpentinite clasts (up to 1%). The central clasts are from mm to sub-mm in size. Generally, the shape of the central clasts influences the final shape of the texture. The coating levels are made up of carbonate elongate crystals, they are up to 100-120 μm long, and they are radially oriented. The matrix is made up of carbonates, with crystals up to 100 μm long.

Multiple slip zones cut the carbonate-coated (Fig. 34e, f). This slip zones are characterised by ultrafine carbonates crystals, they are darker than the surrounding carbonates, and they are up to 7 mm thick. Thin black lines, similar to stylolite, define these surfaces (Fig. 34e, f). Domains characterised by carbonates micro-breccias, can be observed between the different surfaces. These domains are characterised by carbonates clasts up to 0.2-0.3 mm in size. These clasts are from angular to well round in shape (Fig. 34e, f), and they are up to 60 vol. %.

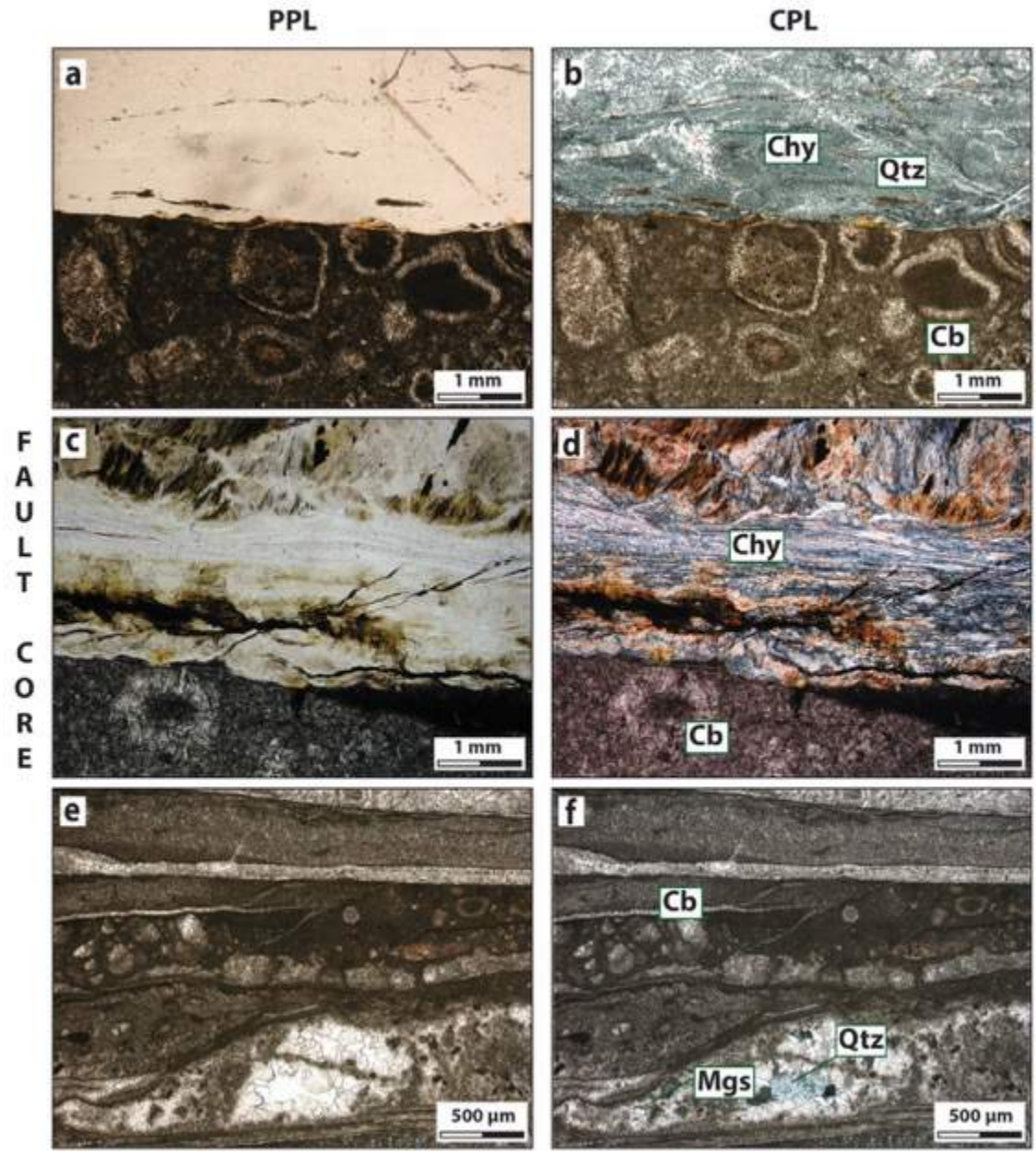

Figure 34: Photomicrograph of the fault core of the Tugello Creek Thrust Fault; the photomicrograph in the left side are in plane polarised light (PPL), whereas the photomicrograph in the right side are in crossed polarised light (CPL). (a, b) The chalcedony shear vein made up of fibrous chalcedony (Chy) and microcrystalline quartz. (c, d) Chalcedony with mylonitic textures near the contact with the carbonates band. (e, f) Multiple slip zones in carbonates, are visible plagues of microcrystalline quartz.

Below the fault core, the footwall is made up of incoherent serpentinite fault gouge (Fig. 35a, b) similarly to what observed in the hanging wall and shows mm-sized serpentinite clasts (10 % in volume) and carbonate matrix (90 % in volume). The serpentinite clast are randomly oriented and nearly totally replaced by carbonates.

Away from the fault core, the serpentinites are schistose with more massive domains. In thin sections the serpentinites are made up of serpentine (99 vol. %)

and opaque minerals (1 vol. %). The serpentinites are characterised by S-C' textures (Fig. 35c, d) showing a sense of shear that reflects the fault movement.

The massive domains, inside the serpentinites, are made up of serpentine (up to 90 vol. %), olivine relicts (up to 5 vol. %) and pyroxenes relicts (both ortho- and clinopyroxens, up to 5 vol. %). The olivine is up to 500 μm in size and it is overgrown by serpentine. The pyroxenes, both ortho- and clinopyroxens, are mm in size. The pyroxenes are partially replaced by serpentine along the edges (Fig. 35e, f) and also along the cleavage planes.

In Figure 36 are represented the mineral phases present in the three main different structural domains.

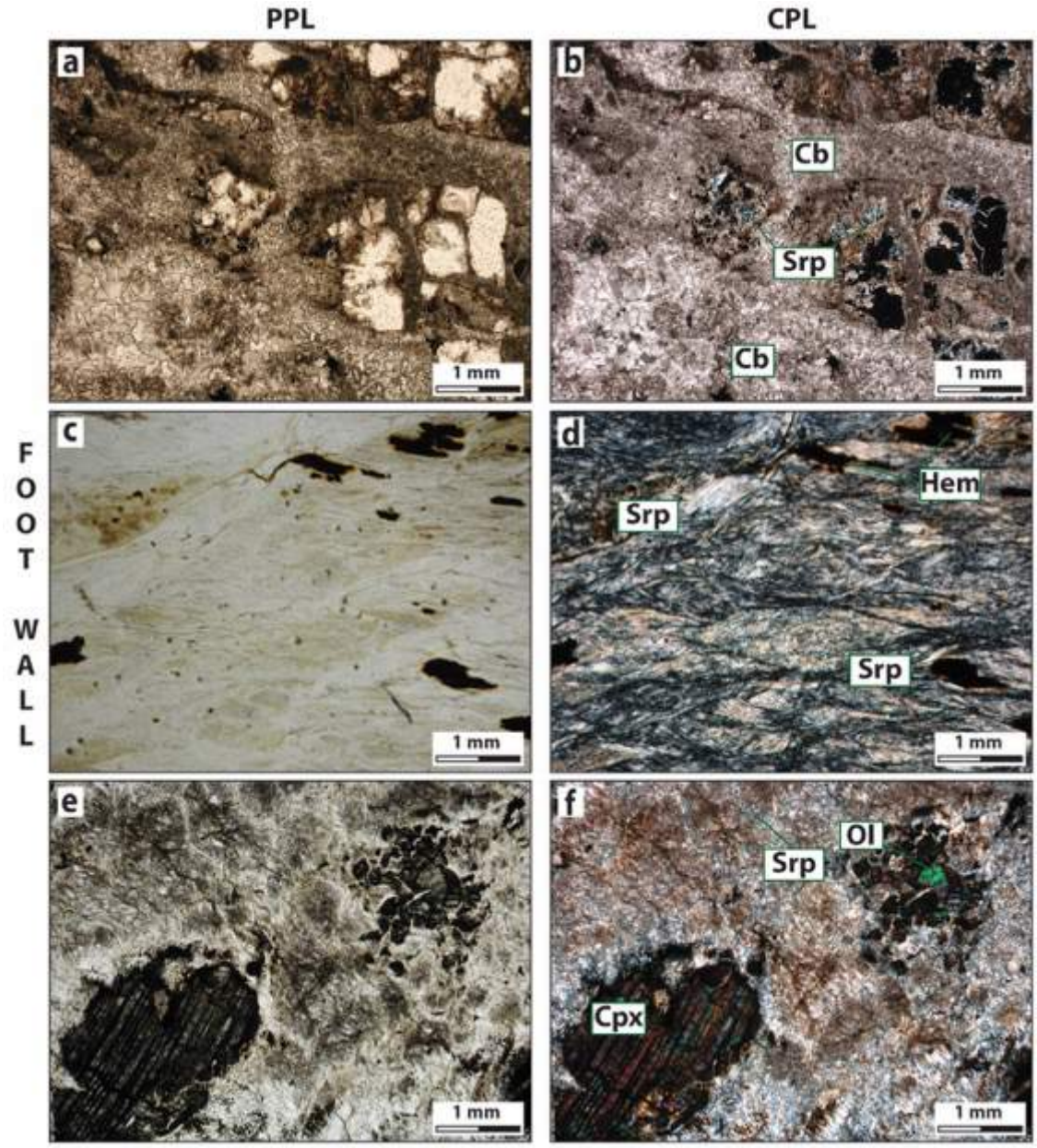

Figure 35: Photomicrograph of the foot wall of the Tugello Creek Thrust Fault; the photomicrograph in the left side are in plane polarised light (PPL), whereas the photomicrograph in the right side are in crossed polarised light (CPL). (a, b) Carbonated serpentinite fault gouge. (c, d) Serpentinite schist. (e, f) Massive serpentinite with pyroxens and olivine relicts.

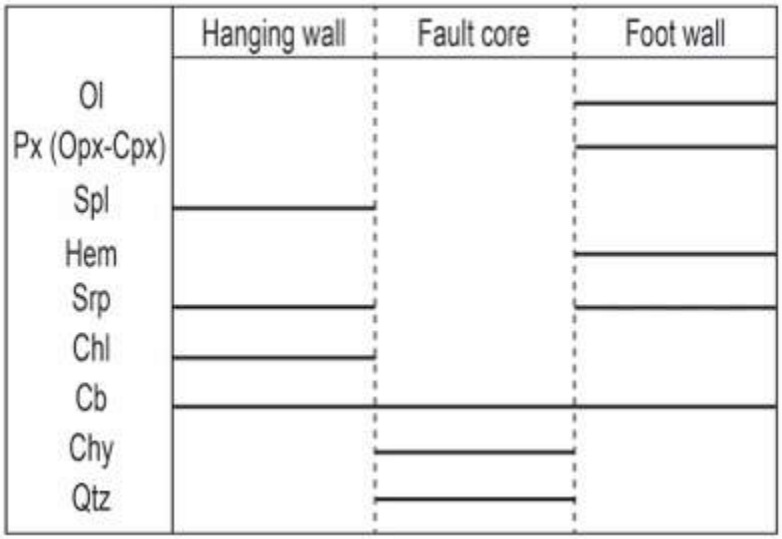

Figure 36: Summary of the mineral phases present in the three main different structural domains. The mineral abbreviations are after Kretz, 1983, except for chalcedony (Chy).

5.3.3 – Paganella Creek Fault

5.3.3.1 – Outcrop scale structures

This area (GPS coordinates N 44° 36' 5", E 8° 45' 2", Fig. 11 paragraph 5.3) is located along the Paganella Creek, which is a left-side tributary of the Gorzente River.

This area (Fig. 37, 38, 39) is characterised by the occurrence of a fault exposed in a 50 m long outcrop. The analysed structure crops out in serpentinites (Fig. 38), which in this area show a pervasive composite fabric and a variable degree of carbonation linked to the circulation of syn-tectonic fluids. Approaching the structure, especially close to the fault core the serpentinites gradually pass to mylonitic listvenites (see below).

The fault damage zone from the top to the bottom shows three main structural domains, namely: damage zone of the hanging-wall, fault core, and the damage zone of the footwall (Fig. 39). The analysed structure shows a symmetric damage zone, producing different kinds of fault rocks, and it is characterised by intense syn-tectonic carbonation, especially along the fault core.

The hanging-wall is mainly made up by carbonated serpetinites greenish-yellowish in colour, approaching the fault core the serpentinites gradually pass to mylonitic listvenites over ca. 1.5 m (Hansen et al., 2005). The listvenites consist of strongly carbonated serpentinite, cemented by a hydrothermal carbonate matrix of Mg-Fe-Ca carbonates and quartz, with accessory serpentine, hematite, and magnetite. The foliation that characterises the listvenites is NE-SW striking, and gently dipping to SE (Fig. 41a) and it is a pervasive composite fabric.

The fault surface shows slickenlises, slickensides, and chatter marks. The last ones show two kind of movement: i) older normal dip-slip movement and ii) younger left-lateral strike-slip movement (Fig. 38, 39).

The fault surface is weakly corrugated, NNE-SSW striking, steeply dipping to W-WNW (Fig. 41b). The surface along the listvenites shows mm long slickenlines and cm black chatter marks made up of dolomite, magnesite, quartz, clinochlore, and clinoenstatite (Supplementary material S5a: LLM35 XRD analysis). The chatter marks are up to 5 cm long, cm wide, and with mm relief. The fault shows a normal dip-slip movement of the fault with a top-to W-WNW accordingly to the

slickensides (Fig. 40). Two superposed set of slikenlines occur on the fault surface with visible crosscutting relationships. The older slickenlines, linked to the normal movement of the fault, is perpendicular to fault striking, down-dip whereas the younger set, which cuts the first, is NNE-SSW striking, gently plunging to SW to sub-horizontal linked to a left- lateral movement of the fault accordingly to the slickensides.

The fault core (Fig. 39) is made up of three different kinds of structures. Brownish carbonate-coated grains (Smith et al., 2011; Rempe et al., 2014; Rowe and Griffith 2015) occur along the contact with the fault surface. The carbonated-coated grains are mm to cm in diameter, up to 80 vol.%, and are matrix supported. These coated grains often show a serpentinitic central clast from mm to cm in size, angular to sub-angular in shape. The central serpentinite clasts show several layers of coating (up to three) with radial brownish carbonates crystals. The shape and the dimensions of the central clast influence their final shape, from elongated to sub-spherical. These structures are randomly oriented well sorted, but without a graded bedding. The matrix is made up by brownish carbonates matrix, up to 20 vol.%. The level made up by the carbonated-coated grains is ca. 30 cm thick (Fig. 42).

The central part of the fault core is made up of cockade-breccia similar to those described by Jébrak (1997), whitish-yellowish in colour, up to ca. 25 cm thick (Fig. 43a). The breccia clasts are made up of carbonated serpentinite clasts (Fig. 43a). The clasts are angular to well round in shape, up to 5 cm in diameter, and up to 60 vol.%. The clasts do not show a preferential orientation. Generally, the smaller clasts are nearest to the vein walls, whereas the bigger ones are along the central part showing a reverse graded bedding. The serpentinite clasts show coatings up to two levels; the first is made up of brownish carbonates whereas the other is made up of whitish carbonates; the crystals of the coatings are radially oriented, and are up to 5 mm long. The matrix of the hydraulic-breccia is made up of whitish carbonates; it is up to 40 vol. %, and it is linked to the precipitation from the circulating syn-tectonic fluids.

The lowest level of the fault core (Fig. 32) is made up of incohesive black level of foliated gouge (Fig. 43b) made up of magnesite, quartz, dolomite, clinochlore, and clinoenstatite (Supplementary material S6: LLM7 XRD analysis), up to 5 cm thick. This level is highly foliated and shows sigmoidal bodies resembling duplex

structures (Ramsay and Huber, 1987) suggesting a left-lateral sense of shear accordingly to the sense of shear of the fault.

The footwall is made up of highly foliated serpentinite. Near the fault core the foliation of the serpentinites is dragged accordingly to the left- lateral movement of the fault. The foliation of the serpentinites strikes NE-SW, and dips to SE (Fig. 41c).

Moreover, the serpentinites show, at about 5 m away from the fault core, two sets of veins (Fig. 45) namely: *i*) extensional carbonate veins (Fig. 41 d, 45a) and *ii*) brownish-black veins (Fig. 41e, 45b).

The extensional calcite veins are whitish in colour, up to 3 cm thick with a spacing of ca. 70 cm. This set of veins cuts the foliation, and is NNW-SSE striking, and steeply dipping to W.

The brownish-black veins (Fig. 45b) show the central part made up of black carbonates (up to 3 cm thick) and near the vein walls are made up of brownish-orange carbonates (up to 2 cm thick) with a spacing of ca. 1 m. Also this set of veins cuts the foliation, and is striking NNW-SSE, and steeply dipping to E. Their peculiar brownish-orange colour derives from secondary minerals crystallization such as pyrite, linked to the syn-tectonic circulation of fluids.

In this area has been done a sampling of the most interesting structures (Fig. 39) for the XRD analysis and petrographic section (see chapter 6).

Structurally the fault shows the development of both brittle-ductile structures (duplex structures) and brittle (hydraulic-breccias) structures permeated by syn-tectonic carbonatic fluids. The Paganella fault, with respect to the other analysed structures (Tugello and Bisciarelle fault), volumetrically shows a minor development of fault rocks, and also the carbonation is less widespread, and limited close to the structure.

The progressive development of the fault core from damage zones, and the development of different types of fault rocks, implies that different permeability properties occur in different regions of fault zones at different evolutionary stages (Fig. 46). The progression of foliation in the damage zone increases permeability, and connectivity; the whole fault zone behaves as a conduit for fluid flow.

The lateral propagation of the low-permeability fault core dissects the across and along strike continuity of the conduit, causing its progressive compartmentalisation into sectors with low hydraulic exchanges. The contrast between medium-permeability damage zones and fault core boundary regions,

imparts a directional anisotropy to permeability in fault zones, which act as conduits for fluid flow parallel to the fault strike and as barriers for fluid flow perpendicular to the fault strike.

In Figure 47 are summarized the main architectural characteristics, the physical properties, the sampling and X-ray analysis results of the Paganella Creek fault.

The Paganella Creek fault, for its orientation, the left-lateral strike slip movement, and for its deformational characteristic can be related to minor system of P-shear faults, accordingly to what described by Spagnolo et al. (2007).

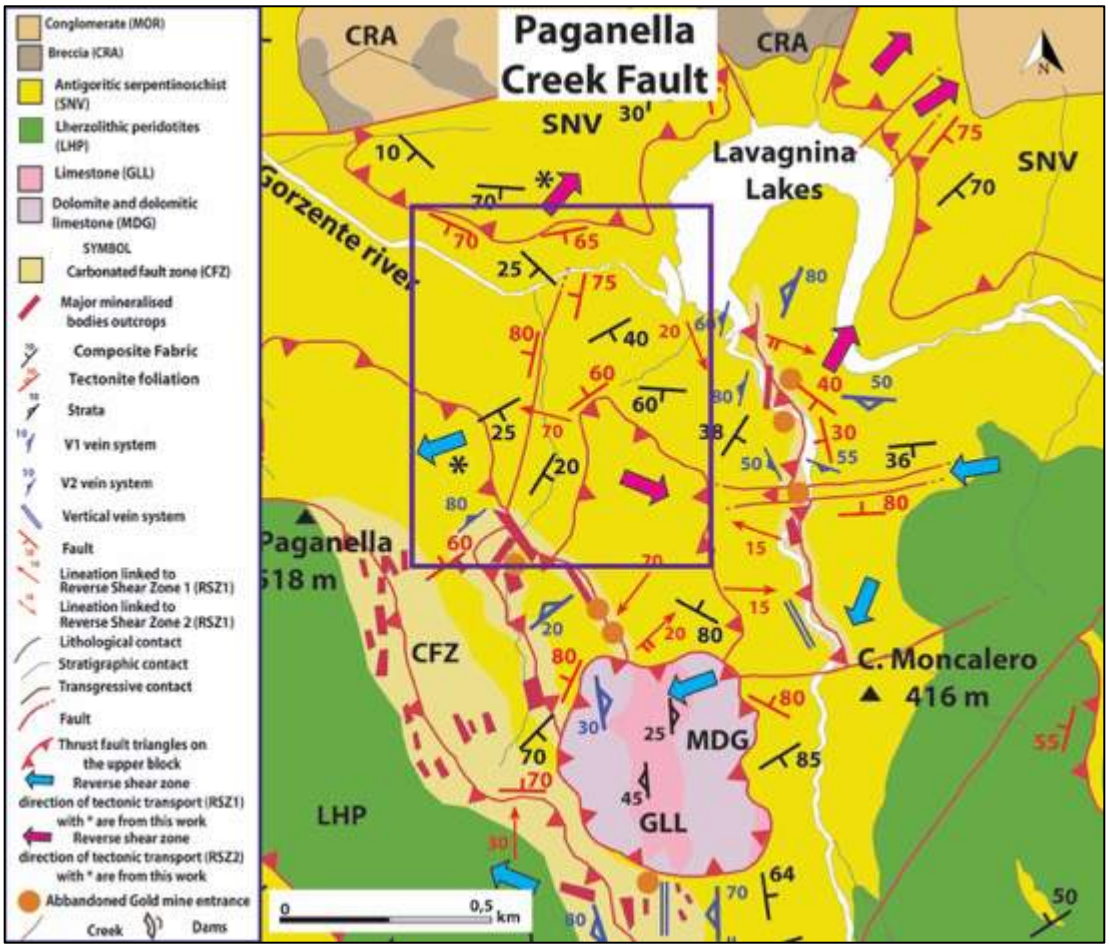

Figure 37: Structural sketch, magnification of the analysed area. The violet box highlights the Paganella fault. For the positioning between the analysed areas please refer to Fig. 13 chapter 5.3.

Figure 38: Paganella Creek fault.

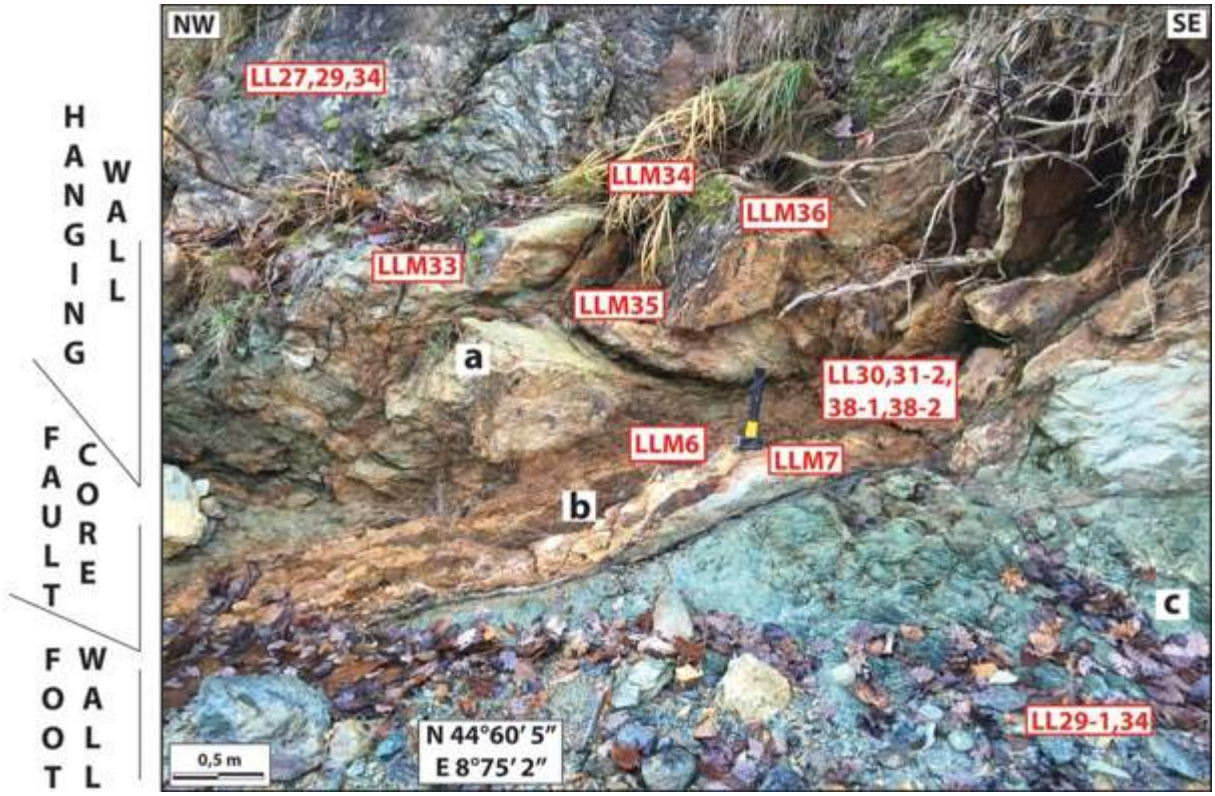

Figure 39: Paganella fault zone. On the left side the three main structural domains are shown. In the figure are also shown the location of the samples (LLM, LL), and the position of the measured structural elements (a, b, c) of Fig.5.

Figure 40: Fault surface marked by lineations and black dolomitic grooves showing a normal movement.

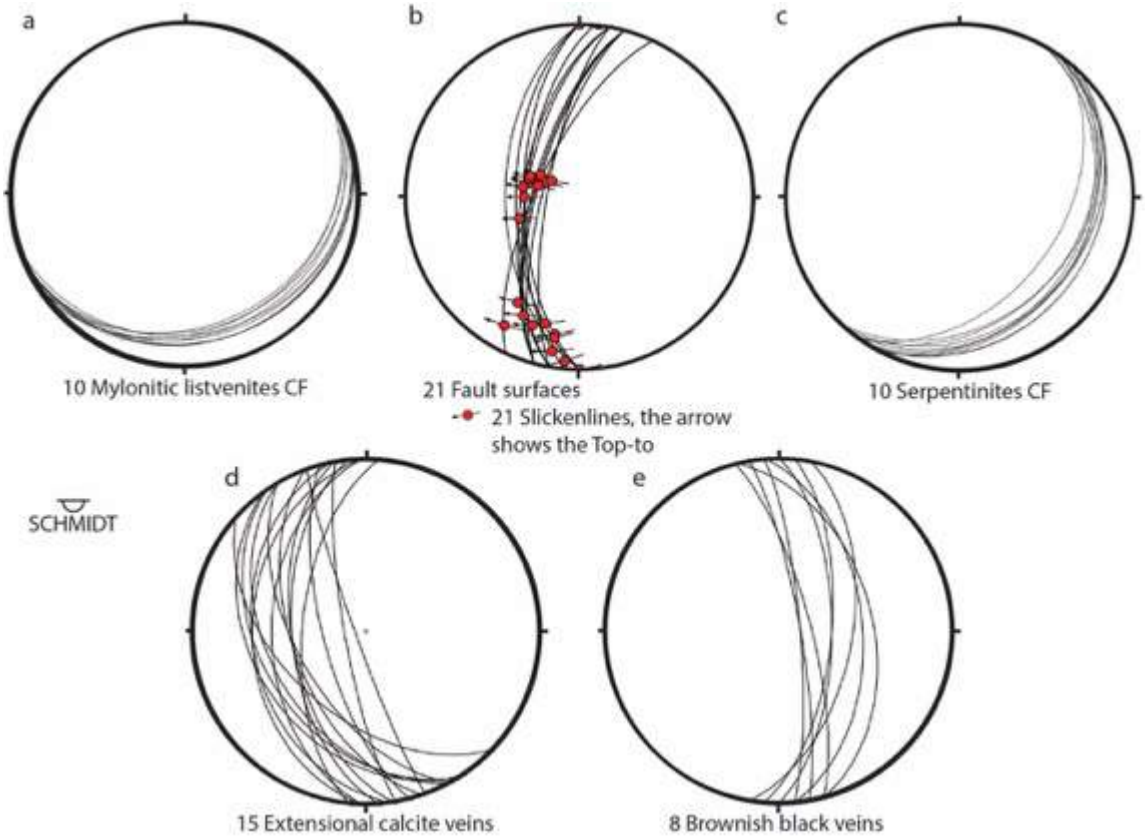

Figure 41: Structural elements of Paganella outcrop.

Figure 42: Polished slab of carbonated-coated grains with central angular to sub angular serpentinite clast.

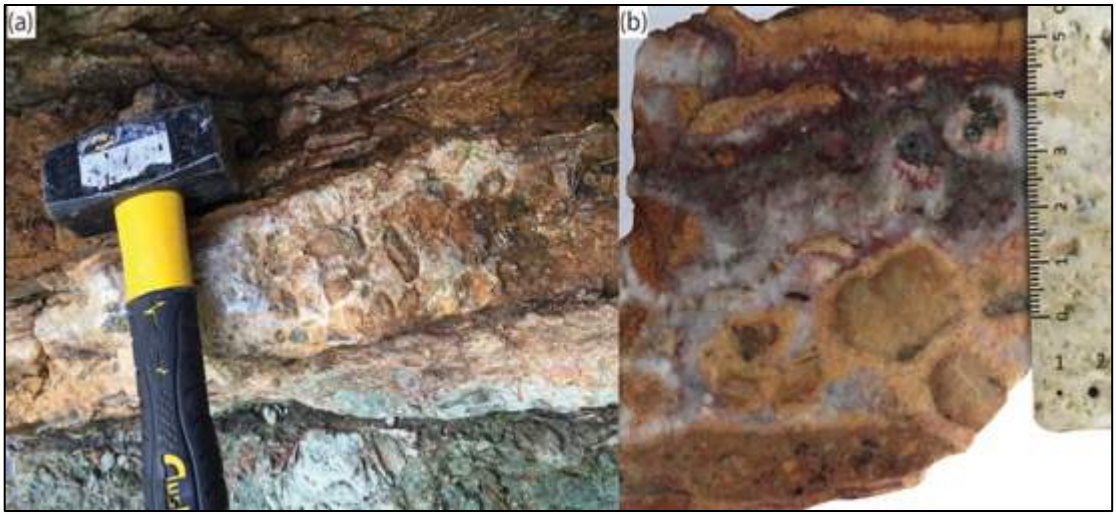

Figure 43: (a) Detail of cockade-breccias near the fault surfaces. (b) Polished slab of cockade-breccias sample (LLM7) the serpentinite clasts show no preferential orientation and reverse graded bedding, and few clasts are replaced by carbonates.

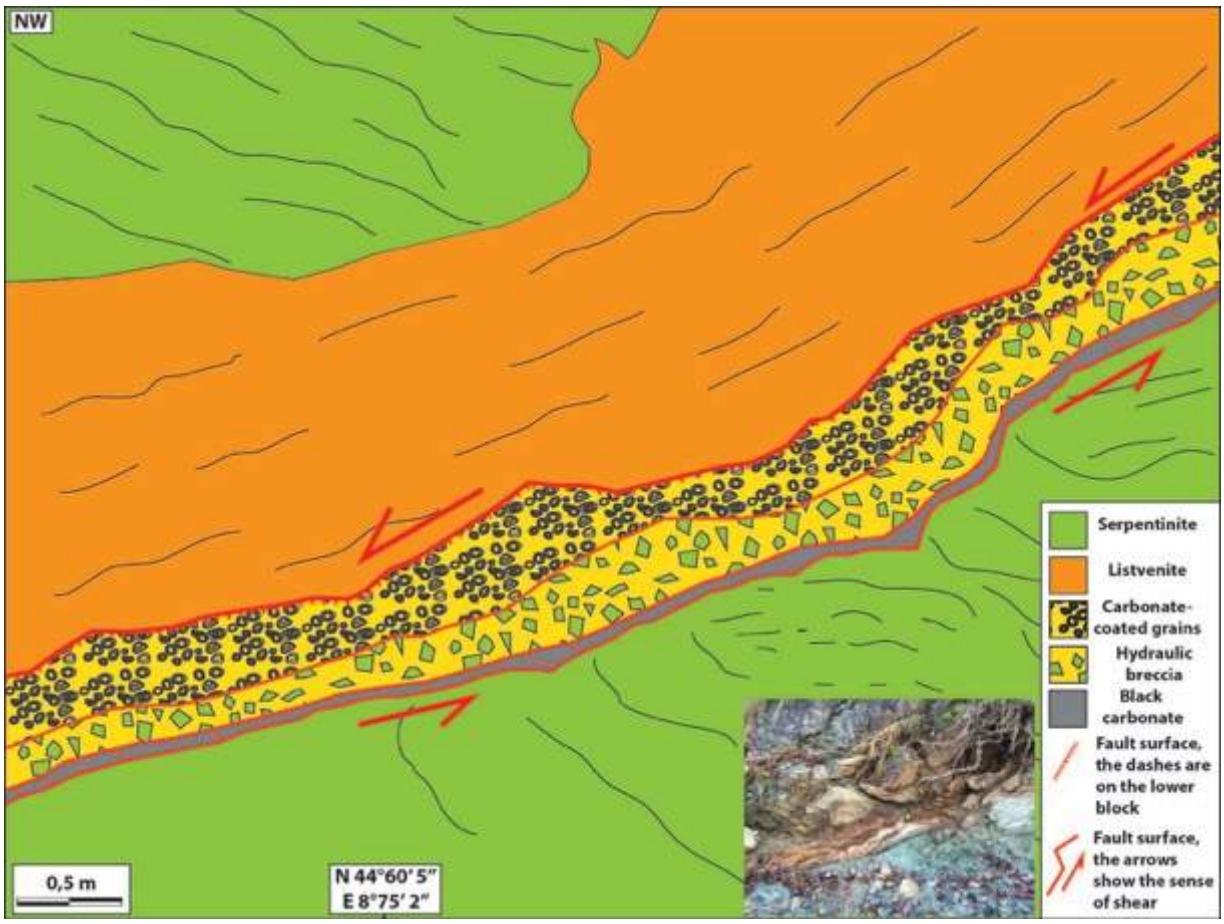

Figure 44: Structural sketch of the Paganella Creek fault, the small photograph represents the outcrop.

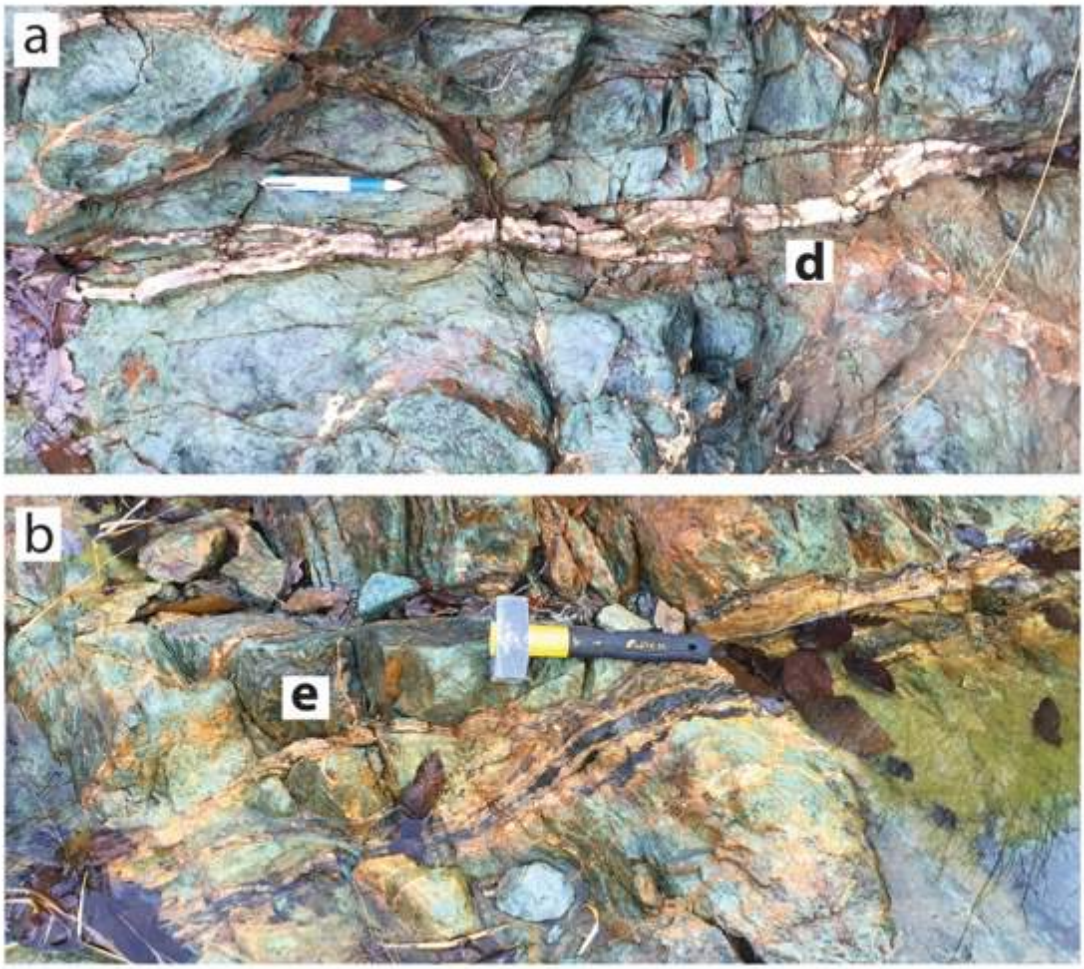

Figure 45: Type of veins characterising the serpentinites of the Paganella Creek, both characterised by a small alteration halo. (a) Extensional calcite veins; the growth vectors are still recognizable. (b) Veins characterised by different filling: the central part is made up of black carbonates, whereas the vein walls are made up of brownish carbonates. In this figure is also shown the position of the measures of the veins (d, e) of Fig. 5.

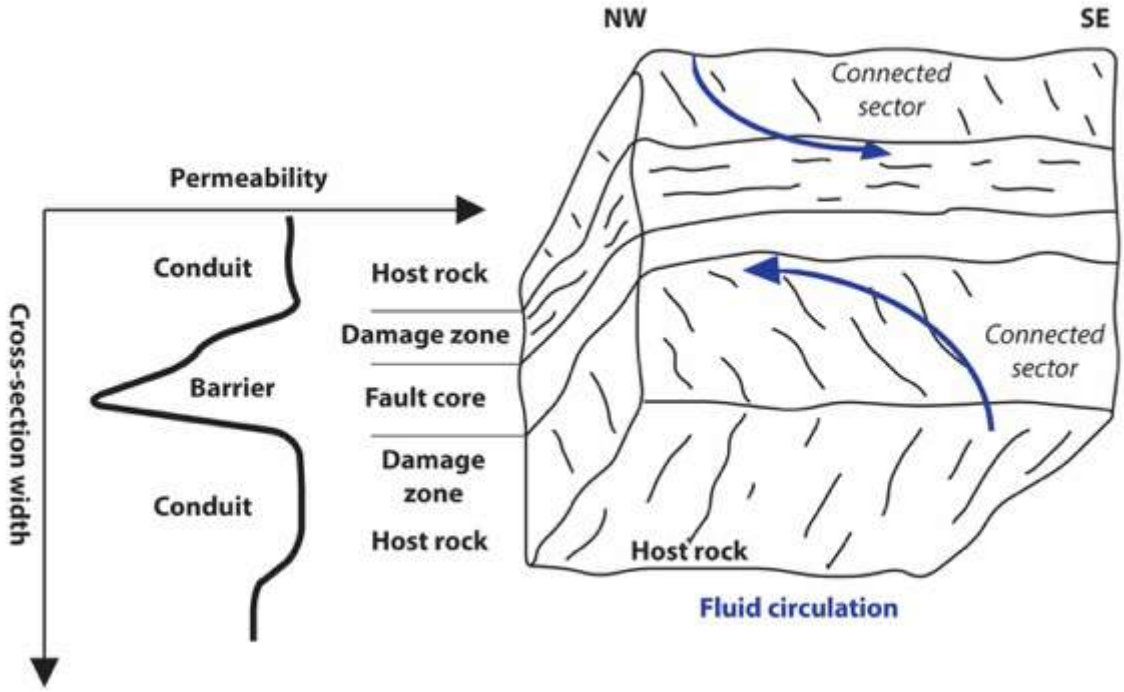

Figure 46: Cartoon showing the permeability structures of the Paganella Creek Fault zone. The qualitative graph schematically shows the transition from a conduit to barrier behaviour of the fault zone.

Zone	Host rock	Hanging wall	Fault Core	Footwall	Host rock
Fault rock	None	Mylonitic Listvenites	Carbonate-coated grains Cockade breccias Foliated fault gouge	Highly foliated serpentinites	None
Width	> 10 m	1.5 m	ca. 60 cm	5 m	>10 m
Rock **Fault rock description** **&** **Structures**	Serpentinites and serpentinite schists	Carbonated serpentinite clasts (up to 20% vol.) abundant carbonate matrix (up to 60% vol.)	Carbonate-coated grains (CCG) Cockade breccias (CB) Foliated fault gouge (FFG) Duplex structures	Highly foliated serpentinites Drag folds Extensional carbonate veins Brownish-black-orange carbonate veins	Foliated, serpentinite Extensional carbonates veins
Grain size		mm to cm	CCG: mm to cm CB: up to 5 cm	mm to pluri-cm	
Porosity	5-10 %	10-15 %	CCG: < 5% CB-FFG: < 5%	10-15 %	5-10 %
Bulk Strain	Small dilatation	Noncoaxial strain	Large dilatation	Noncoaxial strain	Large dilatation
Fluid Pathway	Pervasive fractures and joints	Potential seal	CB-FFG Potential Seal CCG: vuggs permeability	Composite Fabric permeability	Composite Fabric permeability
Permeability m/s	10^{-6} - 10^{-7}	10^{-8} - 10^{-9}	CB-FFG: 10^{-8} - 10^{-9} CCG: 10^{-6} - 10^{-7}	10^{-4} - 10^{-6}	10^{-6} - 10^{-7}
Sample	LL27,29,34	LLM33,35,36	LLM6,7 LL30,31-2, 38-1,38-2	LLM 29-1,34	LLM10,58c LL29,32-2 37-1,37-2
RX		Sap+Dol	FFG: Qtz+Dol+Mgs+ Clc+Cen CCG: Qtz+Fe-Mgs+Dol		
Fluid inclusions	The sample of quartz veins with mm to cm quartz crystal ad hoc prepared for the study of fluid inclusions, have highlighted that the quartz of this study area contains no useful fluid inclusions.				

Figure 47: Paganella Creek fault zone architecture, with the main features summarised. The porosity and permeability values are qualitatively, and they were obtained using the measure done for the hydrogeological map of the Terzo Valico dei Giovi by Rete Ferroviaria Italiana (Free downloadable on: www.va.minambiente.it/File/Documento/162745); in this scheme consider them as qualitative. The mineral abbreviations are after Kretz, 1983.

5.3.3.2 – Microstructures

The thin sections of the serpentinites of the hanging wall of the Paganella Creek fault (Sample LLM33, Fig. 39, 47), show micro-textural features that reply the structural features seen on the field. The serpentinite-schists are made up by serpentine (90-95 vol. %), carbonates (ca. 4 vol. %), quartz (1 vol. %) and oxides (1 vol. %). In thin section are recognizable isoclinal micro-folds, which develop a pervasive axial surface schistosity, superposed to an older foliation defining the composite fabric. The composite fabric is characterised by microcrystalline serpentine (100-150 μm long) elongated parallel to the fabric (Fig. 48a, b). The serpentinites, also show mylonitic textures characterised by S-C' fabric (Fig. 48a, b), serpentinte sigmoidal bodies define these bands, and the sense of shear, accordingly with the shear bands, is a left-lateral movement. The composite fabric and the S-C' fabric are characterised by microcrystalline carbonates (100-150 μm in size; Fig. 48a, b) that partially to totally replace the serpentine.

Veins cut all these previous structures (Fig. 48a, b). These veins are pluri-mm to cm long and up to 0.5 mm thick. They are made up by carbonates (50 vol. %) and quartz (50 vol. %). With respect to the general grain size of the section, the carbonates and quartz crystals inside these veins are coarse grained up to 300-400 μm in size. Generally it is difficult to recognize a crystallization order between the carbonates and quartz inside the veins, since them are visible both along the vein walls, and both in the central part of the veins.

Approaching toward the fault core (Sample LLM35, Fig. 39, 47, 48c, d), it is difficult to recognize the structures above described. The rock is made up by carbonates (ca. 62 vol. %), serpentine (20 vol. %), oxides (5 vol. %), and pyroxenes relicts (ca. 3 vol. %). The composite fabric is not always recognizable. The pyroxenes relicts are both clino- and orthopyroxenes, are randomly distributed, and are up to 2 mm in size. These crystals are partially serpentinized along the cleavage, and carbonates gradually replace the serpentine.

A carbonate veins network, randomly oriented, cuts the composite fabric. The veins are mostly extensional, accordingly to their crystals growth; they are up to 300-400 μm thick.

Slip zones characterised by S-C structures cut all the previous structures. These slip zones are up to 2 mm thick. The sigmoidal bodies are marked by carbonates

along the edges, whereas the central part is made up by fine-grained quartz (100-150 μm in size, Fig. 48c, d).

Close to the fault core (Sample LLM36, Fig. 3, 11, 12e, f) the rock is made up by carbonates (ca. 70 vol. %), serpentine (15 vol. %), oxides (3 vol. %), and pyroxenes relicts (ca. 2 vol. %). The fine crush breccias level is made up of sub-angular to well round clasts made up of carbonates and black aggregate, and they are up to 40-50 vol. %. The clasts are mm in size, and seem to be oriented accordingly to the sense of shear defined by the shear bands. The matrix is made up of fine serpentine and carbonates crystals up to 0,2-0,3 mm in size, and it is up to 60-50 vol. %. The pyroxenes relicts (Fig. 48e, f) are both clino- and orthopyroxenes, are randomly distributed, and are up to 1 mm in size. These crystals are partially serpentinized along the cleavage, and carbonates gradually replace the serpentine.

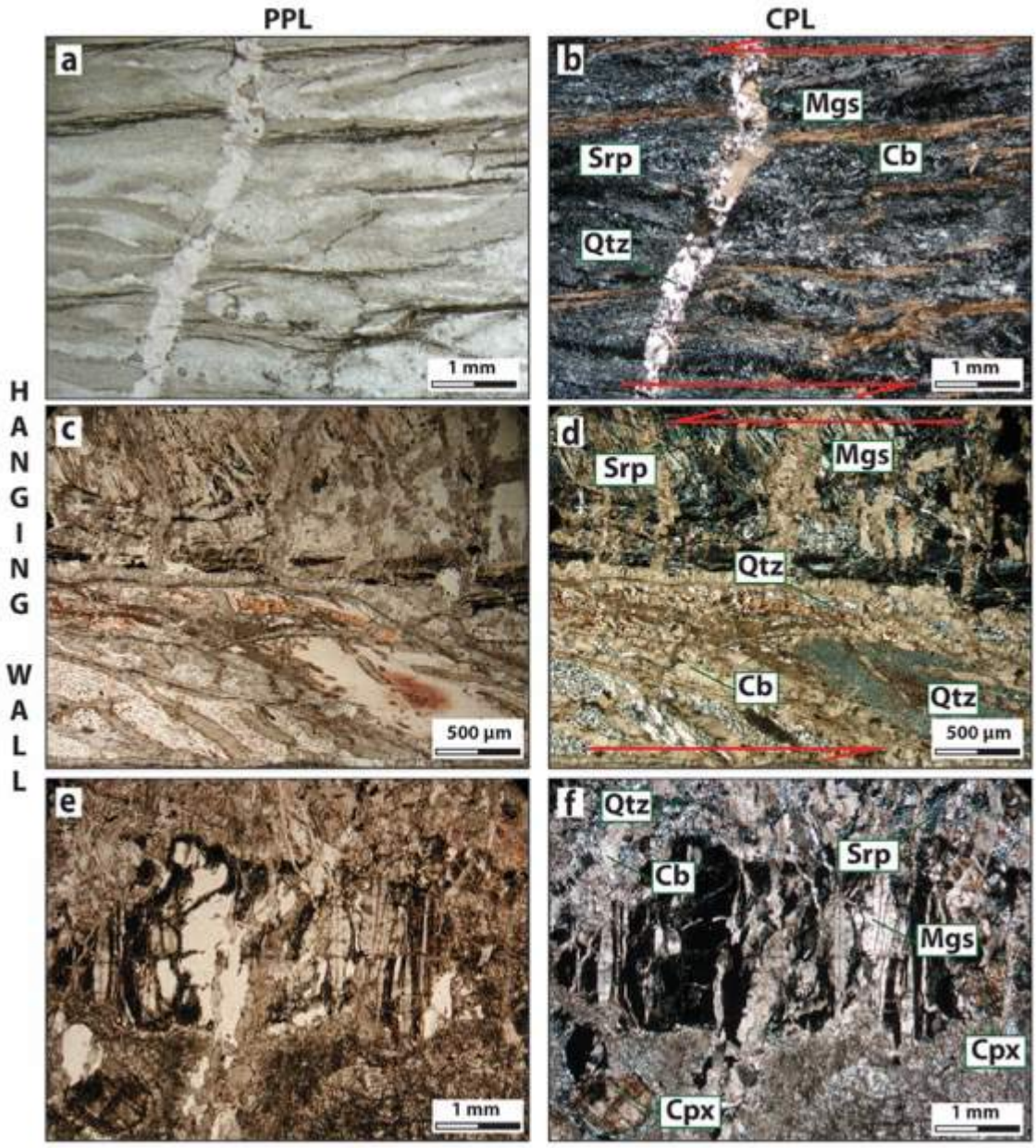

Figure 48: Photomicrograph of the hangingwall of the Paganella Creek Fault; the photomicrograph in the left side are in plane polarised light (PPL), whereas the photomicrograph in the right side are in crossed polarised light (CPL). (a,b) Carbonated serpentinites, is evident the carbonation mainly localized along the foliation. (c, d) Slip zones characterised by S-C structures, the sigmoidal bodies are marked by carbonates along the edges, whereas the central part is made up by fine-grained quartz. (e, f) fine crush breccias level made up of sub-angular to well round clasts made up of carbonates and black aggregate.

Thin sections of the fault core (Sample LLM6, LLM7, LL30, LL31-2, LL38-1, LL38-2, Fig. 39, 47, 49) shows that the shape and the dimensions of the central clast of the carbonated-coated grains (Fig. 49 a, b) influence their final shape, from elongated to sub-spherical. These grains are randomly oriented well sorted but without a graded bedding. The central clasts are made up of sub-mm to mm

angular to rounded fragments of serpentinite, and are up to 30 vol. % (Fig. 49a, b). The serpentinite fragments show a variable degree of carbonation, and are from partially to totally replaced by microcrystalline (ca. 20-30 μm long) carbonates. The serpentinite clasts only partially replaced show the foliation that characterises the host rock (Fig. 49c, d). The microcrystalline carbonates that replace the previous serpentinte clasts are randomly oriented. Inside the central clasts, along the foliation of the clasts, quartz is present (Fig. 49c, d). The quartz crystals are equigranular of about 150-200 μm in size, and show granoblastic textures. Over the central serpentinite clasts are present at least two levels of carbonates coatings. Generally the first coatings, the one closer to the central clast, is characterised by shorter crystals with respect to the second ones. The crystals of the first coatings are ca. 50 μm long, and are radially oriented. The crystals of the second coatings are ca. 100-120 μm long, and radially oriented too. In some portions of the sections the carbonated-coated grains are clast supported, and in some portion are matrix supported. In the portions where the carbonated-coated grains are clast supported, the matrix is made up of carbonates from 20 to 100 μm in size. The carbonate crystals are randomly oriented, and the carbonate-coated grains represent the 70 vol. %. Where the carbonated-coated grains are matrix supported, the matrix represents the 80 vol. %. The matrix is made up of fine carbonate crystals, from 20 to 30 μm in size, and generally in this portions the carbonated-coated grains are elongated instead sub- to well-rounded.

Slip zones cut all the previous structures and textures (Fig. 49e, f). These slip zones (Fig. 49e, f) are 0.5 to 1 mm thick, are characterised by levels of micro-breaccias, and shear bands which show a left sense of shear accordingly to the fault movement, and are defined by the black aggregate made up of dolomite, magnesite, quartz, clinochlore, and enstatite as the chatter marks described in paragraph 5.1.3.2 (Supplementary material S5a: LLM35 XRD analysis).

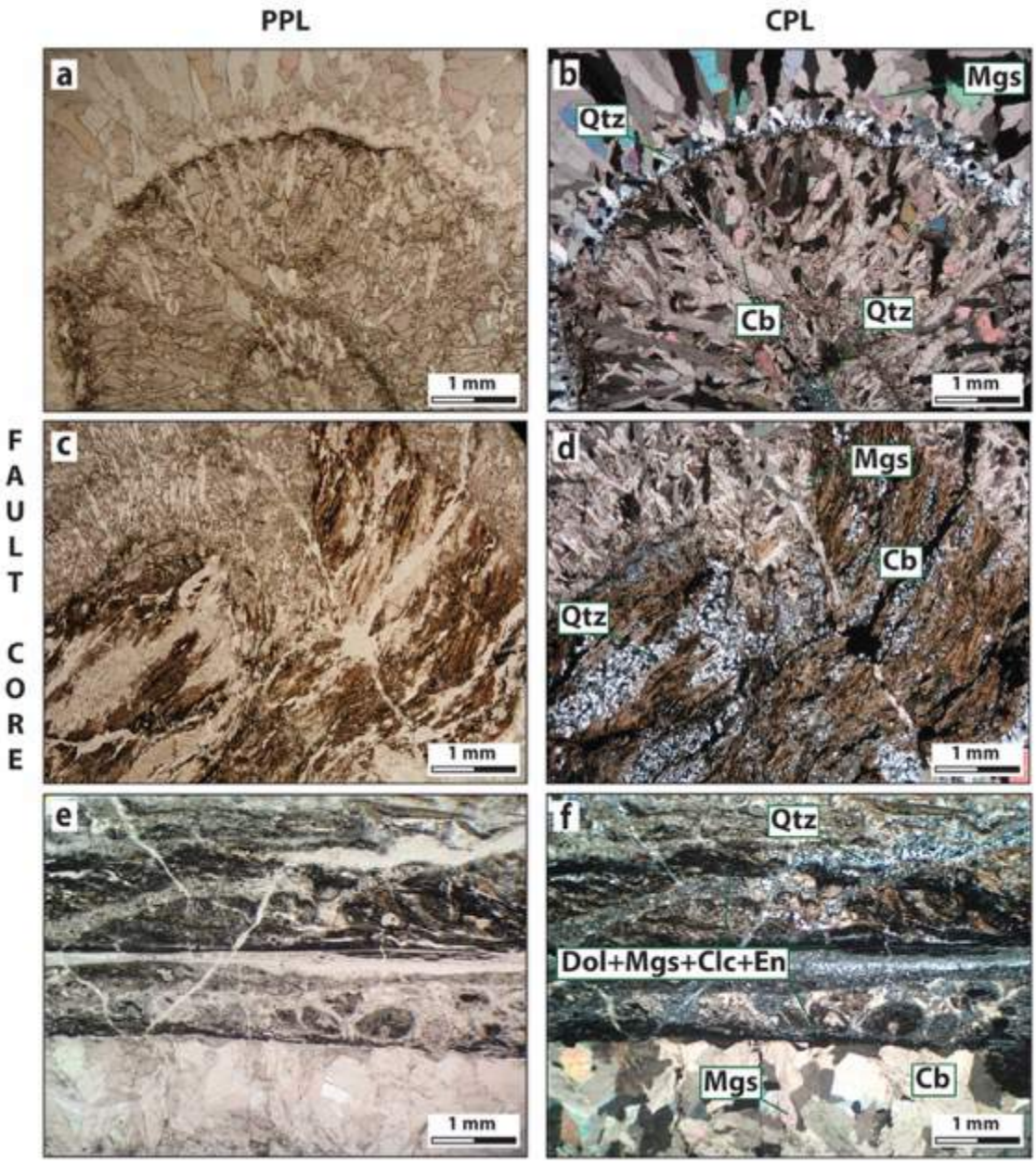

Figure 49: Photomicrograph of the fault core of the Paganella Creek Fault; the photomicrograph in the left side are in plane polarised light (PPL), whereas the photomicrograph in the right side are in crossed polarised light (CPL). (a,b) Coatings of the carbonated-coated grains. (c,d) Carbonated coated grains with central serpentinite clasts. (e,f) Slip zone inside the listvenites.

The thin sections of the serpentinites of the footwall of the Paganella Creek fault (Sample LLM29-1, LLM34, Fig. 39, 47, 50a, b), show micro-textural features that reply the structural features seen for the hanging wall. The serpentinite-schists are made up by serpentine (90-95 vol. %), carbonates (ca. 4 vol. %), quartz (1 vol. %) and oxides (1 vol. %). In thin section are recognizable isoclinal micro-folds, which develop a pervasive axial surface schistosity, superposed to an older foliation defining the composite fabric. The composite fabric is characterised by

microcrystalline serpentine (100-150 μm long) elongated parallel to the fabric (Fig. 50a, b). The serpentinites, also show mylonitic textures characterised by S-C' fabric (Fig. 50a, b), serpentinte sigmoidal bodies define these bands, and the sense of shear, accordingly with the shear bands, is a left-lateral movement. The composite fabric and the S-C' fabric are characterised by microcrystalline carbonates (100-150 μm in size; Fig. 14a, b) that partially to totally replace the serpentine.

In Figure 51 are represented the mineral phases present in the three main different structural domains.

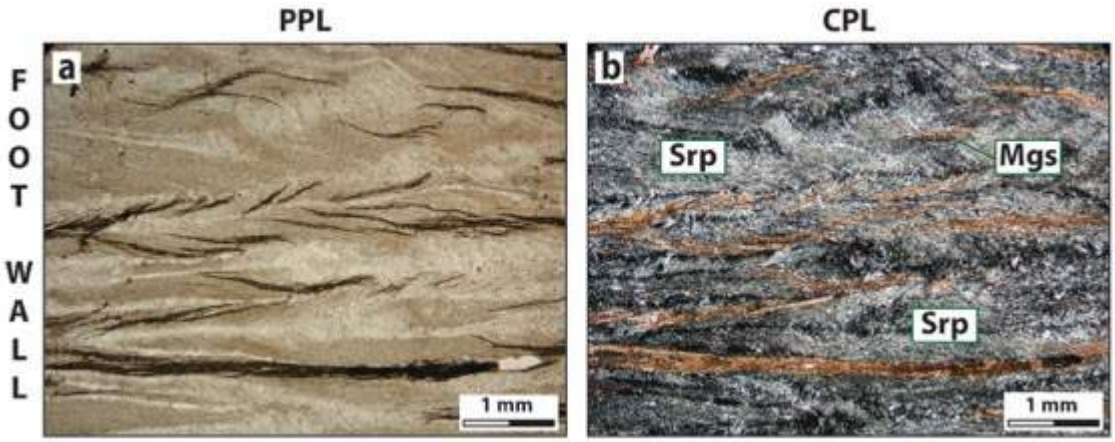

Figure 50: Photomicrograph of the foot wall of the Paganella Creek Fault; the photomicrograph in the left side are in plane polarised light (PPL), whereas the photomicrograph in the right side are in crossed polarised light (CPL). (a,b) Carbonated serpentinites, is evident the carbonation mainly localized along the foliation.

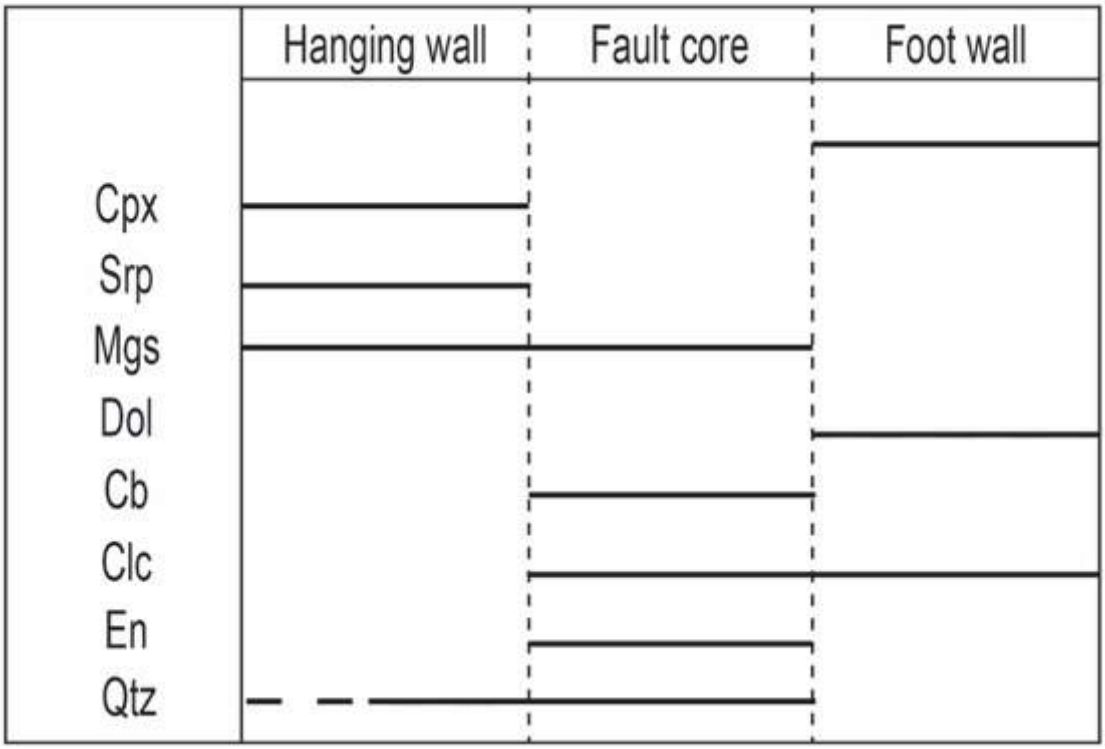

Figure 51: Summary of the mineral phases present in the three main different structural domains. The mineral abbreviations are after Kretz, 1983.

5.3.4 – Bisciarelle Creek thrust fault.

5.3.4.1 – Outcrop scale structures

This area (GPS coordinates N 44° 36' 4", E 8° 47' 2", Fig. 11 paragraph 5.3) is located along the Bisciarelle Creek, which is a right-side tributary of the Gorzente River.

The studied area is characterised by the occurrence of a thrust fault exposed in a 100 m long outcrop (Figs. 52, 53, 54, 55). This structure is developed approximately at the lithological transition between serpentinized lherzolites and serpentinites. The analysed structure shows an asymmetric damage zone, more developed in the footwall, with several meters of different fault rock types (i.e. fault gouge, cataclasites and ultracataclasites) with intense cataclasis, and carbonation.

The serpentinized lherzolites at the top of the structure are up to 10 meters thick; they are intensely fractured, with two principal sets of joints. The older set is vertical to sub-vertical, which is cut by the younger set that dips to NW with angle of about 45-50° (Fig. 54).

From the top to the bottom, three main structural domains have been identified, namely: damage zone of the hanging-wall, fault core, and the damage zone of the footwall (Fig. 54, 56).

The damage zone in the hanging-wall is made up of serpentinites and serpentinite schist foliated fault gouge (up to 10 m thick) greenish to brownish in colour. The brown colouring is due to the carbonation linked to the syn-tectonic fluid-rock interaction. They show a composite fabric with progressive carbonation toward the fault core. Inside the serpentinite schist there are some poorly coherent domains (at 1 m, 2.8m, and 3.8 m from the fault core) characterised by intense foliation. Moreover, the serpentinite fault gouges are characterised by one system of extensional veins, with carbonate infilling. These veins (Fig. 57a, 58) are oriented parallel to sub-parallel to the fault and are up to 2-3 cm thick, following the schistosity too (Fig. 56a). They are NE-SW striking, and gently dipping to NW; in some in some cases they cut at low angle (ca. 15 to 20°) the foliation of the serpentinites. Over the fault core there is a ca. 50 cm thick level mainly made up by

carbonates and emerald green saponite fault gouge (after Sibson, 1977; Supplementary material S7: RB1 XRD analysis; Fig. 55), poorly coherent; the emerald green saponite develops a layering between the carbonates, parallel to sub-parallel to the fault.

The fault core (Figs. 53, 55, 59a, b, c) is sub-horizontal or gently dipping and structurally complex with several peculiar structures with different mineralogical composition (i.e. chalcedony shear veins, peculiar Ca-Mg±Fe carbonates fault pearls, quartz injection-veins; for more details, see below).

The fault core shows several multiphase parallel shear surfaces that are weakly corrugated, sub-horizontal or gently dipping to W (Fig. 57b). These surfaces shows slickenlines, slickensides and chatter marks. The slickenlines are up to 5 cm long, mm wide, and with mm to sub-mm relief. The chatter marks are up to 6 cm long, 2-3 cm wide, and mm relief. The shear surfaces show slickenlines that dip to W-NW, and chatter marks showing a tectonic transport with a top-to E-NE, with a major component of reverse movement and a minor of left-lateral strike slip movement.

From top to the bottom is ca. 70 cm thick with at least five levels with different characteristics, but all linked to the intense syn-tectonic fluid circulation and consequent fluid-rock interaction.

The top of the fault core is made up by Ca-Mg±Fe carbonates (SEM-EDS, LA-ICP-TOFMS; see analysis, chapter 8), with peculiar fault pearls whitish in colour and up to ca. 10-15 cm thick (Figs. 58a, c). The fault pearls structures are from mm to pluri-cm in size, mainly spherical, and are directly graded.

Chalcedony shear veins cut the previous carbonatic levels; they are milky in colour with flow banding-like textures (Faber et al., 2014) and up to ca. 10-15 cm thick (Figs. 57a, b), with widespread gold particles up to 20 microns in diameter, with concentrations up to 2 ppm (see LA-ICP-TOFMS chapter 8). The shear veins could be divided into two types of chalcedony-rich shear veins namely VB and VA: VB are entirely made up of chalcedony and occur above to the VA (Fig. 58b). The VA veins are made up of chalcedony with fault pearls clasts and occur at the upper contacts of the carbonate-coated grains levels (Figs. 59a, b). The carbonate-coated grains, inside VA, represent the 10-20 vol.%. Linked to VA, mm injection-veins (e.g. Monzawa and Otsuki, 2003; Otsuki et al., 2003; Boullier et al., 2009; Brodsky et al., 2009; Fondriest et al., 2012; Rowe et al., 2012a, b; Rowe and Griffith, 2015) are

also present; they are made up of angular to sub-angular micro-carbonate clasts (up to 1.5 mm, and 10 vol. %) and carbonated-coated grains (up to 0.5 mm, and up to 10-15 vol. %) with chalcedony or fine-grained quartz matrix (500 microns, see chapter 8). Both the two types of veins, show surfaces characterised by slikenlines and chatter marks. The slickenlines are up to 10 cm long, up to 0.5 mm wide, and up to 0.5 mm relief. The chatter marks are up to 10 cm long, up to 3 cm wide, and with relief up to 2 mm.

The central part of the fault core is made up of Ca-Mg±Fe carbonates (SEM-EDS, LA-ICP-TOFMS; see chapter 8, 9), with fault pearls (Figs. 59a, 60a, b, c, d), whitish in colour and up to ca. 20 cm thick. These structures are from mm to dm in size, mainly spherical, and well sorted (see paragraph 5.4.1 for detailed description of shape and dimensions). The fault pearls are up to 80 vol. %.

Several slip zones cut this level (Fig. 59c), they are similar to mirror-like surfaces (Evans et al., 2014; Rowe and Griffith, 2015; Viti et al., 2016). These slip zones show slickenlines and chatter marks. The slickenlines are up to 10 cm long, mm wide, and with mm to sub-mm relief. The chatter marks are up to 10 cm long, mm wide, and with mm to sub-mm relief. The chatter marks over these surfaces show a top-to NE. These slip zones are marked by an intense comminution from mm to sub-mm, by the absence of fault pearls, which moreover, appear poorly fractured or deformed, and show evidence for rotation along the slip surfaces.

The fault pearls (Figs. 60a, b, c, d) sharply passes through a level made up by cockade breccias, similar to those described by Genna et al., (1996), up to ca. 20 cm thick. The breccia clasts are cm, angular and made up of serpentinite and carbonated serpentinites, and they are up to 50 vol. %. The matrix is made up by crystalline carbonates. From the top to the bottom the level is characterised by an increase in clast dimensions, with decrease of the carbonatic matrix. These carbonate-coated grains will be widely described in their microtextures and compositional characteristics in the chapter 8.

The lowest portion of the fault core, at the bottom, is made up by crystalline limestone, from greyish to whitish in colour and up to ca. 30 cm thick. This level is very competent, unaltered and not folded.

The damage zone that characterises the footwall (Figs. 52, 53, 54, 55, 56) is more complex; it is up to ca. 11 m and shows more kind of fault rocks and structures. From the top, nearest to the fault core, to the bottom have been

recognized the following fault rocks and structures namely:

- Carbonated fault gouge (after Sibson, 1977): greenish in colour, made up by serpentinite clasts up to ca. 4 mm (25% in volume). The serpentinite clasts are randomly oriented inside a carbonated-serpentinite matrix (up to 85% in volume), this level is up to 1,5 m;
- Carbonated cataclasites (after Sibson, 1977): greenish in colour, made up by serpentinite clasts up to ca. 4 cm (40-50% in volume). The serpentinite clasts are randomly oriented inside a carbonated-serpentinite matrix (up to 50-60% in volume), this level is up to ca. 1,5 m;
- Duplex structures (Ramsay and Huber, 1987): whitish in colour, made up by saponite (Supplementary material S8: LLM2B1 XRD analysis) up to 20 cm thick (Fig. 61), characterised by sigmoidal bodies which show a sense of shear with top to NE, consistent with the sense of shear of the structure;
- Cataclasite (after Sibson, 1977): dark-green to brownish in colour, up to 2 m in thickness, made up by serpentinite clast, few millimetres in size. The serpentinite clasts are well rounded and well sorted (40-50% in volume), and are surrounded by reddish carbonate microcrystalline matrix (50-60% in volume);
- Ultracataclasite (after Sibson, 1977): whitish in colour, up to 1m in thickness, made up by serpentinite angular clasts up to ca. 1 cm. The serpentinite clasts are randomly oriented (5-10% in volume). The serpentinite clasts are surrounded by a reddish carbonate microcrystalline matrix (up to 90-95% in volume);
- Hydraulic breccias (Jébrack, 1997): greenish-whitish (Fig. 62) in colour, the level is up to 30 cm in thickness, made up of serpentinite angular to sub-angular clasts from cm to dm in size. The serpentinite clasts are surrounded by whitish carbonate matrix. From the bottom to the top of the hydraulic breccias there is a decrease in serpentinite clasts size and simultaneous matrix increase;
- Veined serpentinite: serpentinite and serpentinite schist, several portions show brownish alteration linked to carbonation especially along the pervasive schistosity. Moreover, veined serpentinite and serpentinite schist are characterised by extensional veins randomly oriented (Fig. 57d), cm in

thickness (Fig. 63) cutting the schistosity (Fig. 57d). The veins are filled by carbonates, with elongate blocky to fibrous crystal, and by chalcedony. The vein systems are cut by shear zone characterised by serpentinite sigmoidal bodies (duplex structures Ramsay and Huber, 1987), which indicate a sense of shear with top-to NE.

The structures, above described, are cut by (Fig. 56) R-Shear fractures (Ramsay and Huber, 1987; Fig. 57e) that are NNW-SSE striking, dipping at relatively high angles (40-60°) and show a tectonic transport with a top to NE. They disrupted the Ca-Mg±Fe carbonates central part of the fault core, at least, in 4 slices (Fig. 52, 53, 54, 55, 56).

The syn-tectonic carbonation of the damage zone of the thrust fault is characterised by heterogeneously distributed cabronation. This carbonation is widespread and is particularly intense in the fault core with the total substitution of the previous rock with a level of Ca-Mg±Fe carbonates, and in the footwall is characterised by saponite duplex structures.

In the previous paragraph, has been shown that the analysed fault shows an asymmetric damage zone, more developed in the footwall with respect to the hanging wall. The asymmetric development of the damage zone depends on several factors as the different rocks that make up the hanging wall and the footwall. In this case the fault surface represents a bimaterial interface separating different elastic bodies.

Structurally the fault shows the development of both brittle-ductile (duplex structures) and brittle structures (e.g. cataclasites, fault gouges, and breccias) permeated by syn-tectonic carbonate fluids. The presence of both brittle-ductile to brittle regime deformation testifies a long-lived evolution of the structures, and the carbonation of both these kinds of structures testifies a long-lived circulation of carbonate fluids too.

The progressive development of the fault core from damage zones, and the development of different types of fault rocks, implies that different permeability properties occur in different regions of fault zones at different evolutionary stages (Fig. 64). The progression of fracturing in the damage zone increases permeability, especially in the footwall that is more developed in thickness, and connectivity. The whole fault zone behaves as a conduit for fluid flow.

The lateral propagation of the low-permeability fault core dissects the across and along strike continuity of the conduit, causing its progressive compartmentalisation into sectors with low hydraulic exchanges. The contrast between medium- to high-permeability damage zones and fault core boundary regions, imparts a directional anisotropy to permeability in fault zones, which act as conduits for fluid flow parallel to the fault strike and as barriers for fluid flow perpendicular to the fault strike. This anisotropy was maintained until the development of the R-Shear fractures

In Figure 65 are summarized the main architectural characteristics, the physical properties, the sampling and X-ray analysis results of the Tugello Creek fault.

On the basis of the two slicklenlines and chatter marks the analysed structure shows a tectonic transport top-to E-NE, with a major component of reverse movement and a minor of left-lateral strike slip movement.

The Bisciarelle Creek thrust, for its orientation, the tectonic direction of movement and for the deformational events can be related to the second system of regional reverse shear zones (RSZ2) that affect the Lavagnina Lake area, also compared to what described for the Voltri Massif by Capponi and Crispini, 2002; Federico et al., 2005 and Spagnolo et al., 2007.

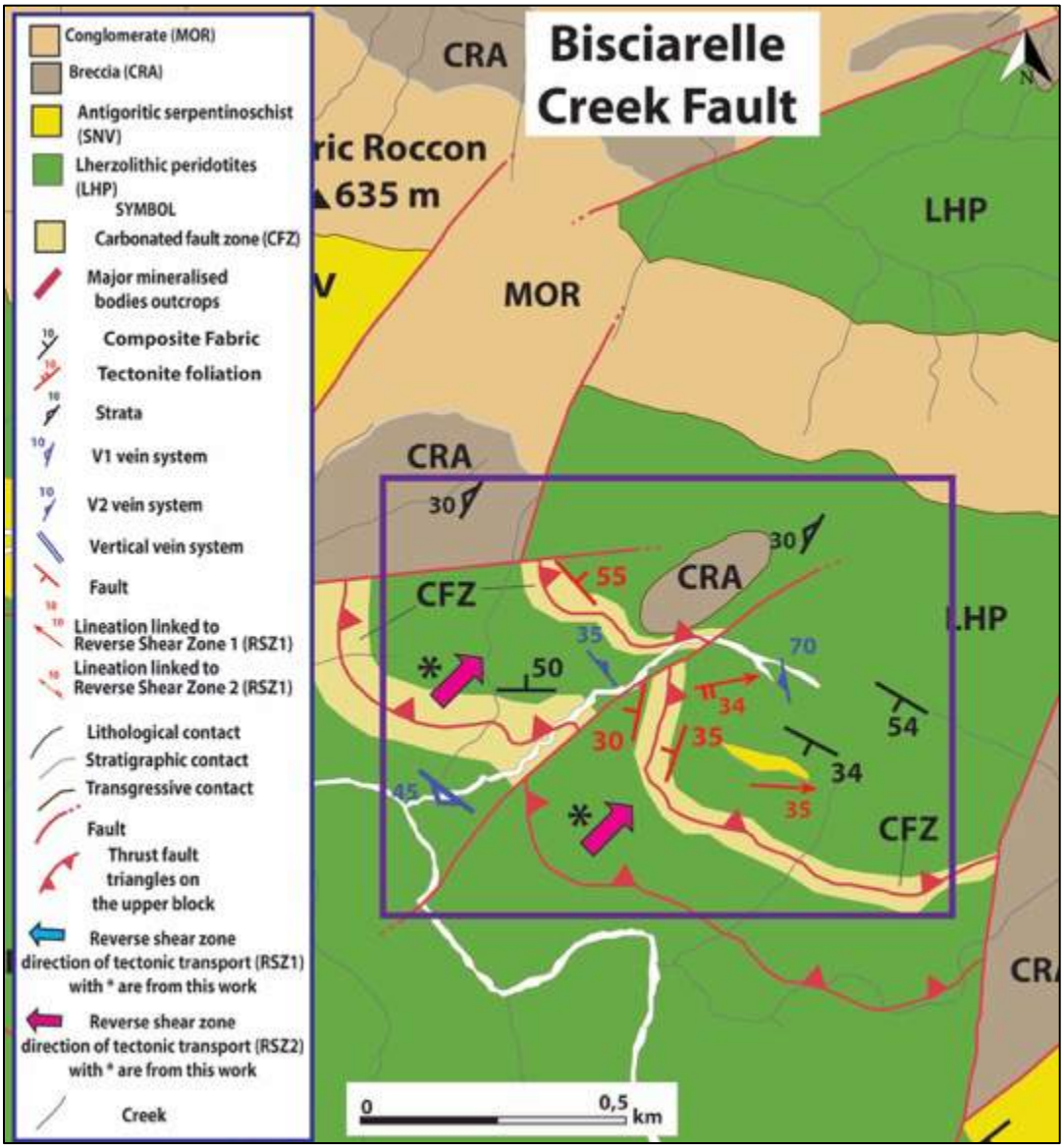

Figure 52: Structural sketch, magnification of the analysed area. The violet box highlights the Bisciarelle fault. For the positioning between the analysed areas please refer to Fig. 11 paragraph 5.3.

Figure 53: Bisciarelle Creek thrust fault.

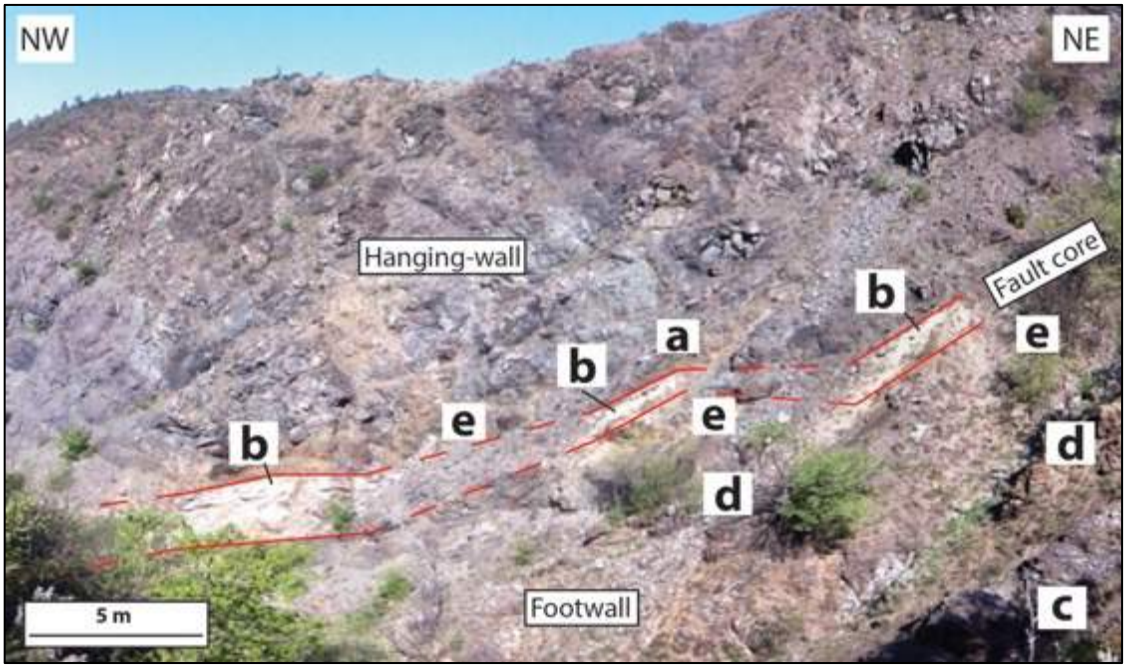

Figure 54: The three main structural domains of the fault are shown. IN this figure is also shown the position of the measured structural elements (a, b, c, d, e) of Fig. 6.

Figure 55: Location of the samples in the area.

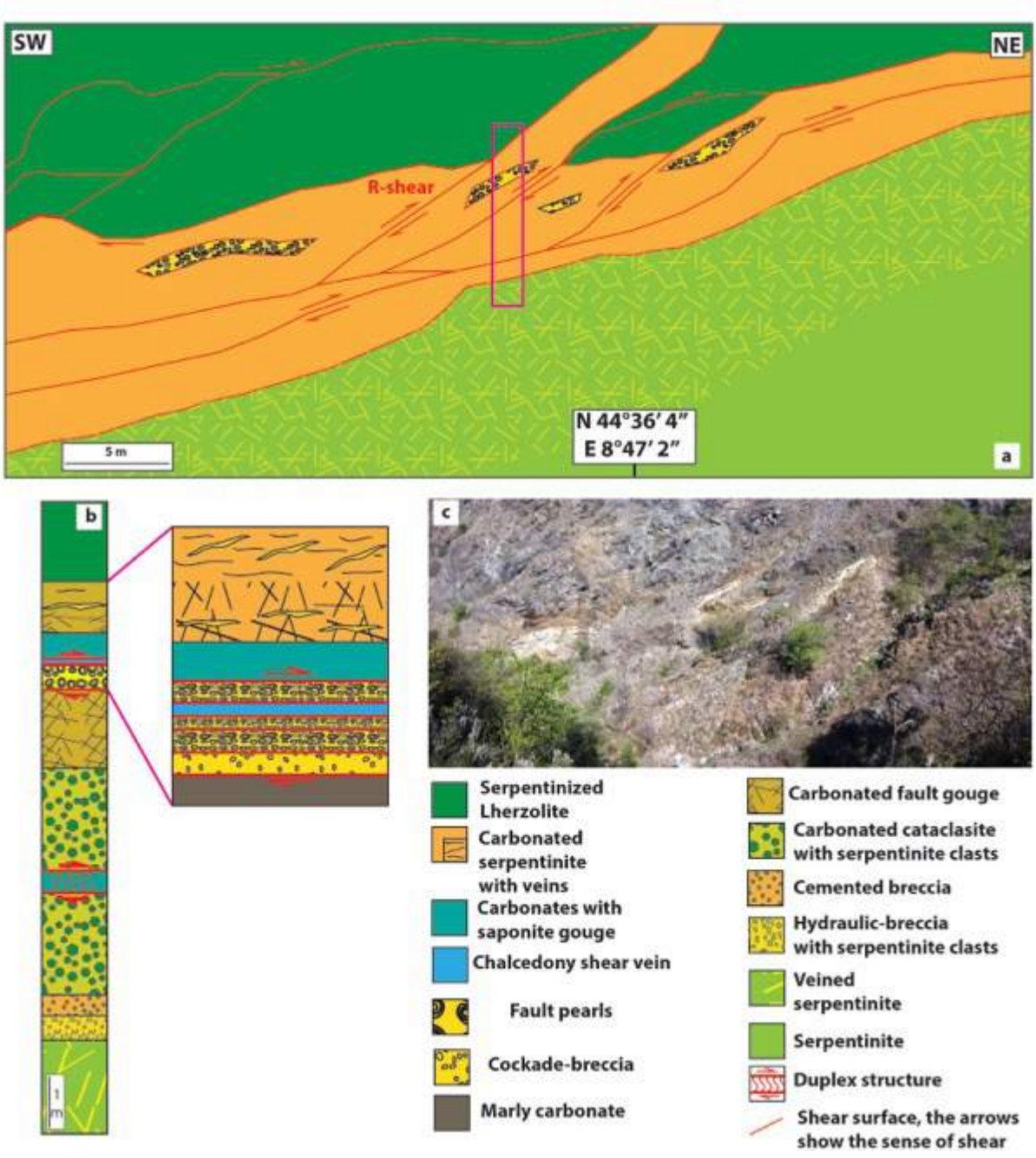

Figure 56: (a) Structural sketch of the Bisciarelle Creek Fault, from a panoramic view. The purple inset with the purple star, in Fig. a, highlights the magnification, shown in fig. (b), of the detail of the fault rock relationship, with a detail of the fault core. (c) Photograph of the outcrop.

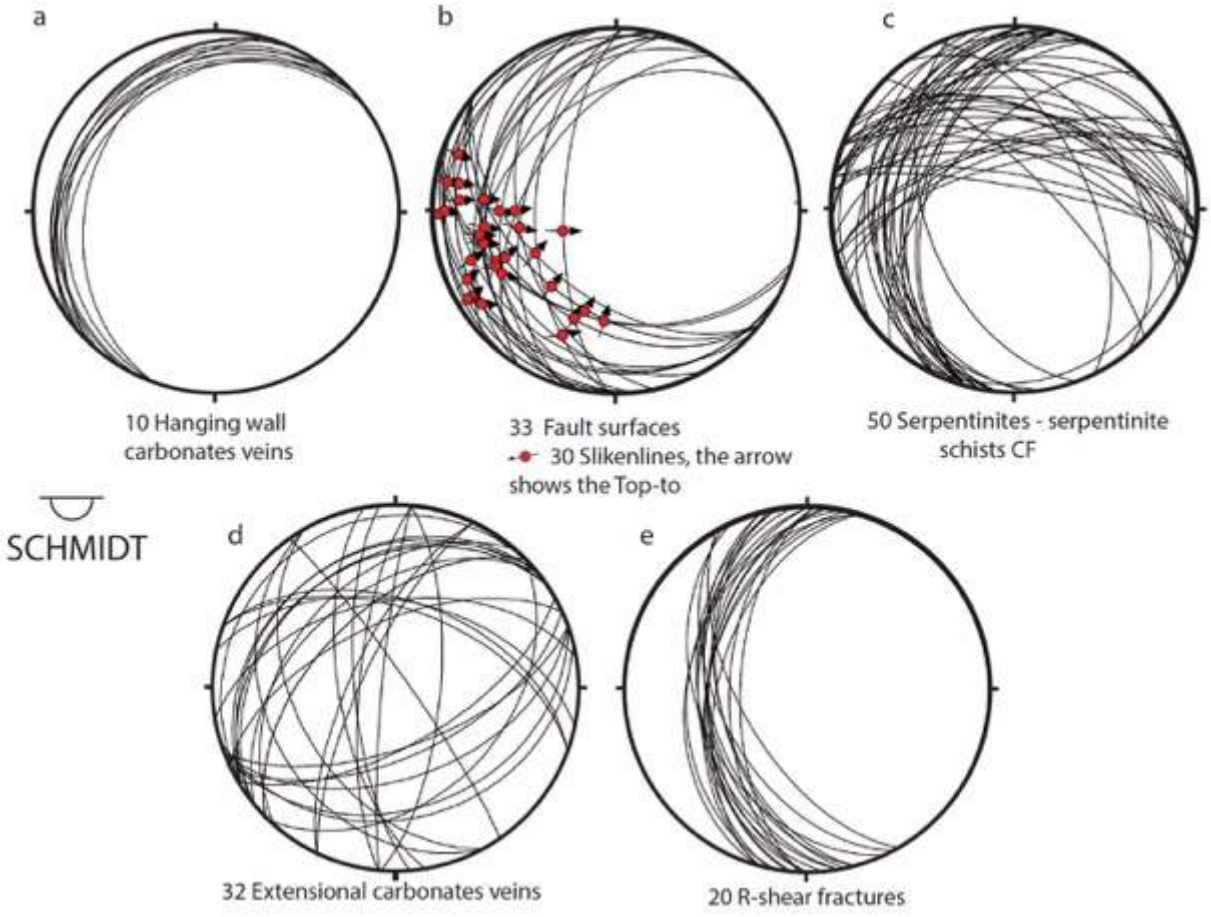

Figure 57: Structural elements of Bisciarelle outcrop.

Figure 58: Extensional carbonate veins in the hanging-wall damage zone.

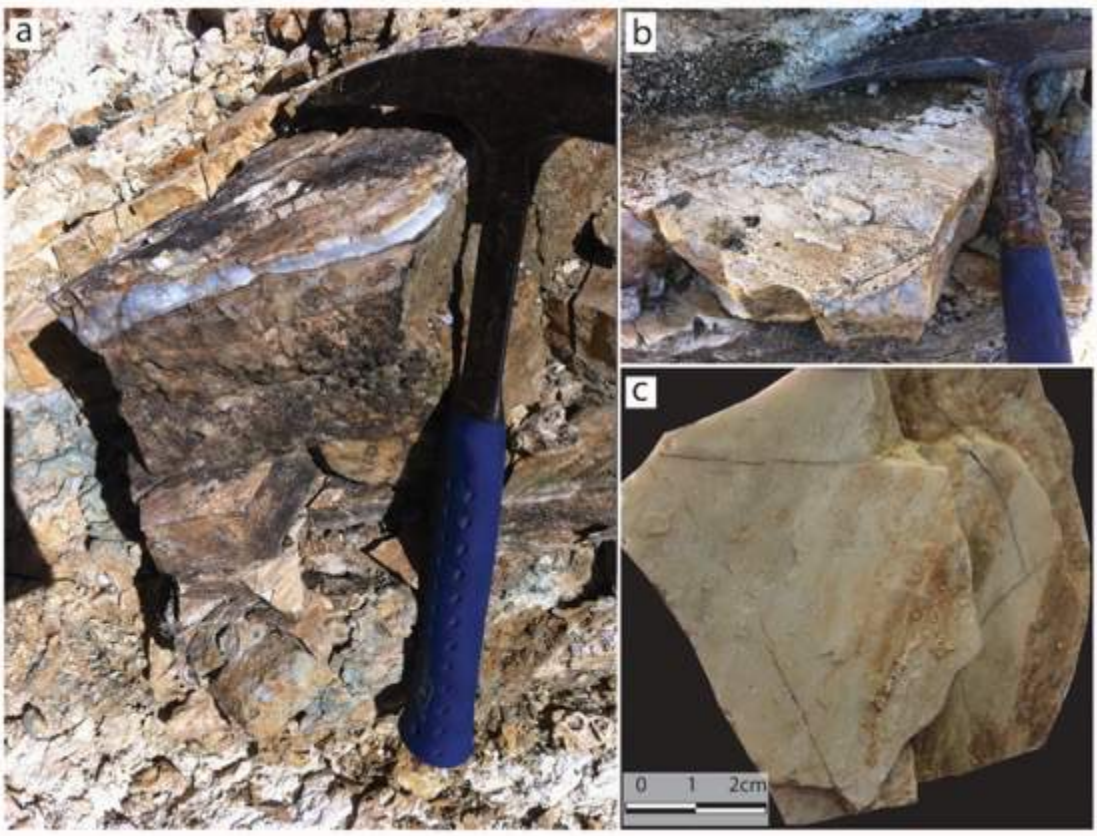

Figure 59: The fault core of the Bisciarelle Creek thrust. (a) View of the whole fault core with the chalcedony shear vein at the top and the carbonate-coated grains level. (b) Magnification of the surface of the chalcedony shear vein, with slickenlines and grooves. (c) Mirror-like slip surface magnification.

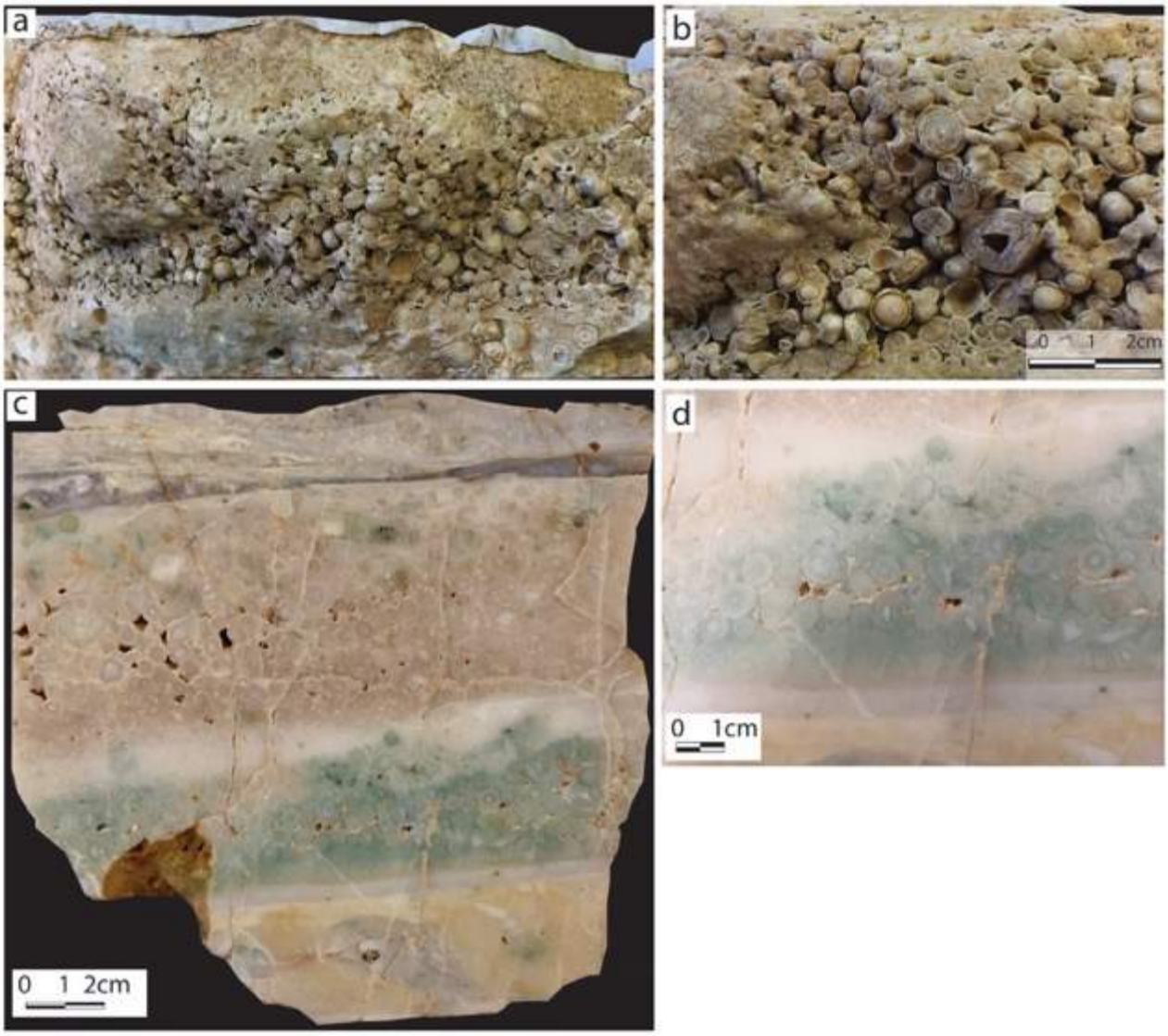

Figure 60: Central part of the Bisciarelle fault core, sample LLM32. (a) Detail of the carbonate-coated grains level from sample LLM32. (b) Magnification of the carbonate-coated grains. (c) Polished slab of sample LLM31. (d) Detail of the carbonate-coated grains from the polished slab.

Figure 61: Duplex structure made up of saponite.

Figure 62: Detail of the hydraulic-breccia, with serpentinite angular to sub-angular clasts and carbonate matrix.

Figure 63: Carbonate veins in the serpentinite of the footwall.

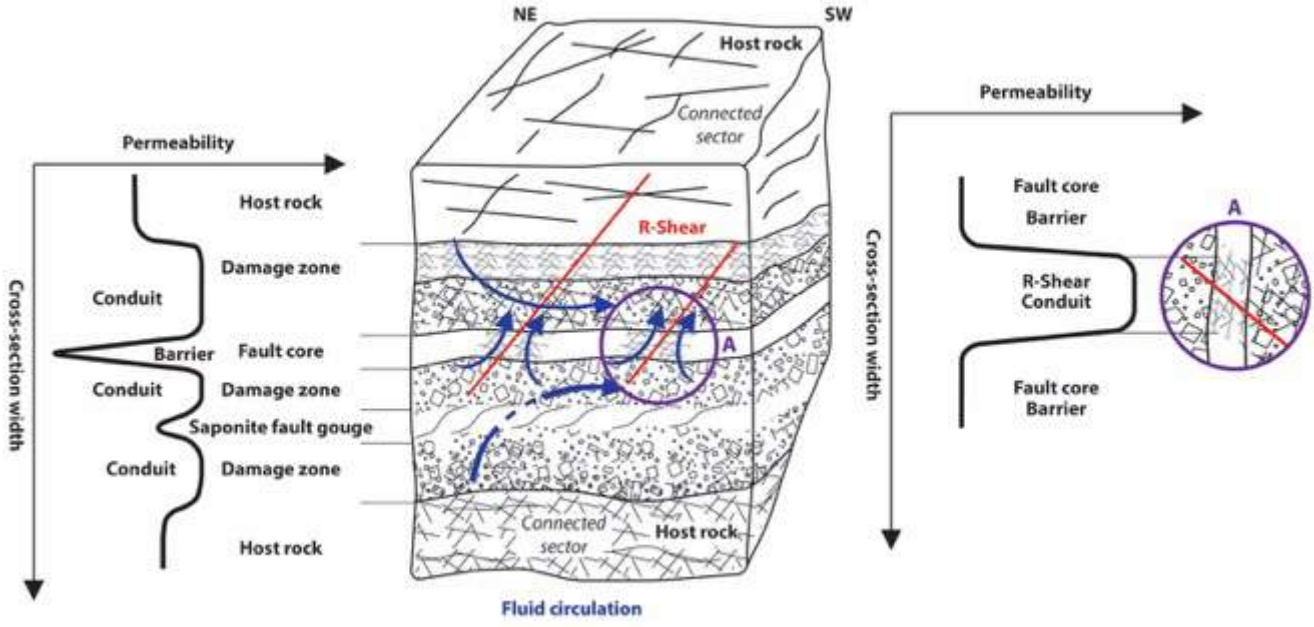

Figure 64: Cartoon showing the permeability structures of the Bisciarelle Creek Fault zone. The qualitative graph, on the left side of the picture, schematically shows the transition from a conduit to barrier behaviour of the fault zone. The qualitative graph, on the right side of the picture, schematically shows the transition from barrier behaviour of the intact fault core to conduit behaviour after the development of the R-Shear fractures.

Zone	Host rock	Hanging wall	Fault Core	Footwall	Host rock
Fault rock	None	Carbonated Serpentinite fault gouge Carbonates and emerald green saponite fault gouge	Chalcedony shear veins Fault pearls Cockade breccias Crystalline limestone (CL)	Carbonated Fault gouge (CFG) Carbonated cataclasites (CC) Cataclasites (C) Ultracataclasites (UC) Hydraulic breccias (HB)	None
Width	> 10 m	10 m	ca. 70 cm	11 m	15 m
Rock Fault rock description & Structures	Serpentinized lherzolites Intensely fractured Two sets of joints	Gouge strongly incohesive; serpentinite clasts (30% vol.) abundant serpentinite matrix (70% vol.) Saponite with duplex structures Extensional carbonate veins	Chalcedony shear veins (CSV) Fault pearls (FP) Shear surfaces	CFG strongly incohesive; serpentinite clasts (20% vol.) carbonated serpentinite matrix (80% vol.) CC clasts (40-50%) matrix (50-60%) C clasts (40-50%) matrix 50-60%) UC clasts (5-10%) matrix (90-95%) Saponite duplex structure	Foliated, serpentinite Extensional carbonates veins
Grain size		mm to cm	FP: mm to cm	mm to pluri-cm	
Porosity	0-5 %	20 %	CSV: 0% FP: 5-10 %	20 %	5-10 %
Bulk Strain	Small dilatation	Noncoaxial strain	CSV Shear strain	Noncoaxial strain	Large dilatation
Fluid Pathway	Pervasive fractures and joints	Dynamic Conduit	CSV Potential Seal FP: vuggs permeability	CFG-CC-HB potential seal C-UC Dynamic Conduit	Composite Fabric permeability
Permeability m/s	10^{-6} - 10^{-8}	10^{-4} - 10^{-5}	CSV: 10^{-8} - 10^{-9} FP: 10^{-6} - 10^{-7}	10^{-4} - 10^{-5}	10^{-6} - 10^{-8}
Sample	RB10,11	RB1,2,3,4,5, 6,7,8,9	LLM1,2,4,5,31, 32,STAR,58a LL10,10bis,10-2, 10-3, 12,13a,13b, 13c,14a2,15	RB12,13,14,15 16,17,18	LLM24,30
RX		Saponite: Sap+Dol	CSV: Qtz FP: Dol+Cal+Mgs+Sap CL: Cal+Dol+Ctl		
Fluid inclusions	The sample of quartz veins with mm to cm quartz crystal ad hoc prepared for the study of fluid inclusions, have highlighted that the quartz of this study area contains no useful fluid inclusions.				

Figure 65: Bisciarelle Creek fault zone architecture, with the main features summarised. The porosity and permeability values are qualitatively, and they were obtained using the measure done for the hydrogeological map of the Terzo Valico dei Giovi by Rete Ferroviaria Italiana (Free downloadable on: www.va.minambiente.it/File/Documento/162745); in this scheme consider them as qualitative. The mineral abbreviations are after Kretz, 1983.

5.4 – The detail over the Bisciarelle Creek thrust fault

On the basis of the previous observation made in this area, for the presence of structures and microstructures with unique textures and peculiar mineralogical compositions, which have never been described before, I decided to concentrate the study on these peculiar fault pearls. In order to do this, targeted samples have been taken with different objectives, namely:

1 – An ad hoc sampling of the fault pearls has been performed in order: to perform image-analysis of the carbonated-coated grains (see below),

2 – An ad hoc sampling along a sampling profile, perpendicular to the fault strike (for more details see paragraph 5.3.4.1 and chapter 8), to perform a petrological study from the bedrock to the fault core, and to achieve mass transfer calculations and mass transfer profile (see chapter 7).

3 – An ad hoc sampling of the fault pearls for the petrographic thin and thick sections, for the chemical analysis with the SEM-EDS (see chapter 8), and to perform high-resolution elemental image with an innovative technique the Laser-Ablation Inductively-Coupled-Plasma Time-of-Flight-Mass-Spectrometry (for the detail of this technique see chapter 6, and for the results see chapter 8).

An ad hoc sampling of the quartz-chalcedony veins has been performed in order to realize fluid inclusions analysis. Unfortunately, the samples, suitably prepared, have highlighted the lack of fluid inclusion inside the quartz.

5.4.1 – Morphological analysis of the fault pearls

5.4.2 – Introduction

The morphological image analysis has been widely used in geology, not only to quantitatively characterise different lithotypes, but also to constrain their origin or the deformational processes that involved them (Pittarello and Koeberl, 2013). Hence I performed image analysis, for quantitative and statistical measure of the fault pearls.

5.4.3 – Fault pearls sample

The sample used for the image analysis is the sample LLM31 (Paragraph 5.3.4.1, Fig. 55), taken from the fault core of the Bisciarelle Creek thrust fault. The sample has been cut both parallel and orthogonal with respect to the slickenlines of a visible shear surface at the top of the sample, in order to obtain slabs that capture potential differences of fault pearls morphology at different orientations with respect to the shear direction.

Figure 66 represents the sample scan, from the cut parallel to the slickenlines, used for the image analysis. All the scans have been previously processed through graphic programs, especially using the Image Trace function of Adobe Illustrator, in order to outline the single fault pearl perimeter and area. Only the outer layer, of every single fault pearls, has been highlighted for the processing. In this way has been obtained a "*Fault pearls maps*" on the cut parallel with respect to the slickenlines (Fig. 67) and one map obtained on the cut orthogonal with respect to the slickenlines (Fig. 68).

These maps, then, have been processed through the free software Image-J (Mac version, http://rsbweb.nih.gov/ij/)to fit an ellipse onto each fault pearl and obtain morphometric parameters. Once set the scale for spatial scaled images, to obtain values expressed in physical size, the following measures have been performed:

- Circularity: with a maximum value of 1 represents a perfect circle; as the value approaches to 0.0, it indicates an increasingly elongated shape. Values may not be valid for very small measures,

- Roundness: it's the inverse of the Aspect Ratio, and use the area of the pearls and the major axis of the best-fit ellipses,

- Orientation: The program fits the pearls with equivalent best-fit ellipses and measures the angle between the major axis of the best-fit ellipses and the horizontal top edge of the image parallel to the shear movement,

- Particle size distribution: I used the maximum diameter of the fault pearls obtained with ImageJ, and then I performed particle size distribution with Excel spread sheet.

These measures have been performed in order to obtain representative statistical data about the fault pearls shape descriptor.

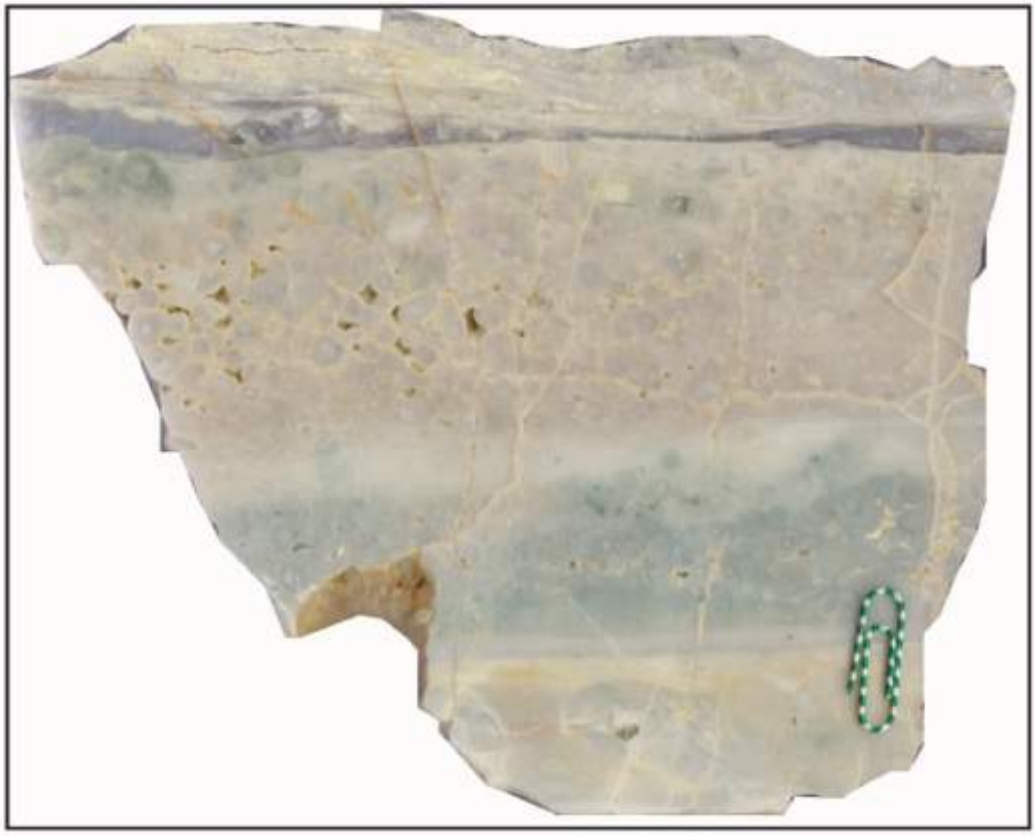

Figure 66: Fault pearls sample used for morphological analysis. The slabs used for this analysis were cut parallel and orthogonal to the slickenlines of this sample.

5.4.4 – Image analysis results from the polished slab cut parallel to the slickenlines.

The fault pearls, from the polished slab cut parallel to the slickenlines (Fig. 68) have a round shape. This is quantitatively shown by the distribution of the measured circularity values, which have a negative skew towards the highest value of 1 (Fig. 69a). This result is consistent with the measured fault pearls roundness, which has a mean of 0.74 and a maximum value of 1 (Fig. 69b). Along the slickenline direction, fault pearls do not show a predominant orientation because the distribution of their orientation angles is polymodal and range between 20° and 160° (Fig. 69c), with a weak spike at 101 degrees. Particle size distribution measurements show a good sorting of the fault pearls dimensions (Fig. 69 d), as their size distribution is unimodal with a mean value of about 0.5 cm and a slightly positive skew (maximum size: 1.8 cm).

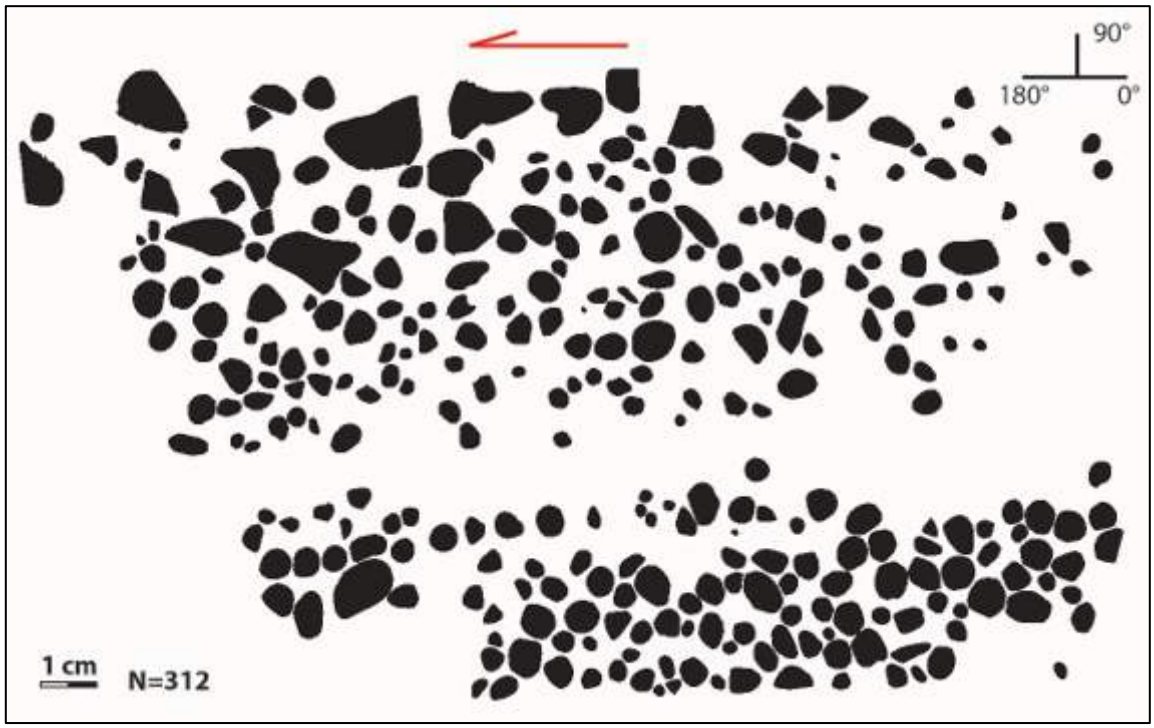

Figure 67: "Fault pearls map" obtained after the processing of the scan parallel with respect to the slikenlines (312 fault pearls). On the top right the orientation used by ImageJ, the red arrow shows the slip direction accordingly to the fault movement.

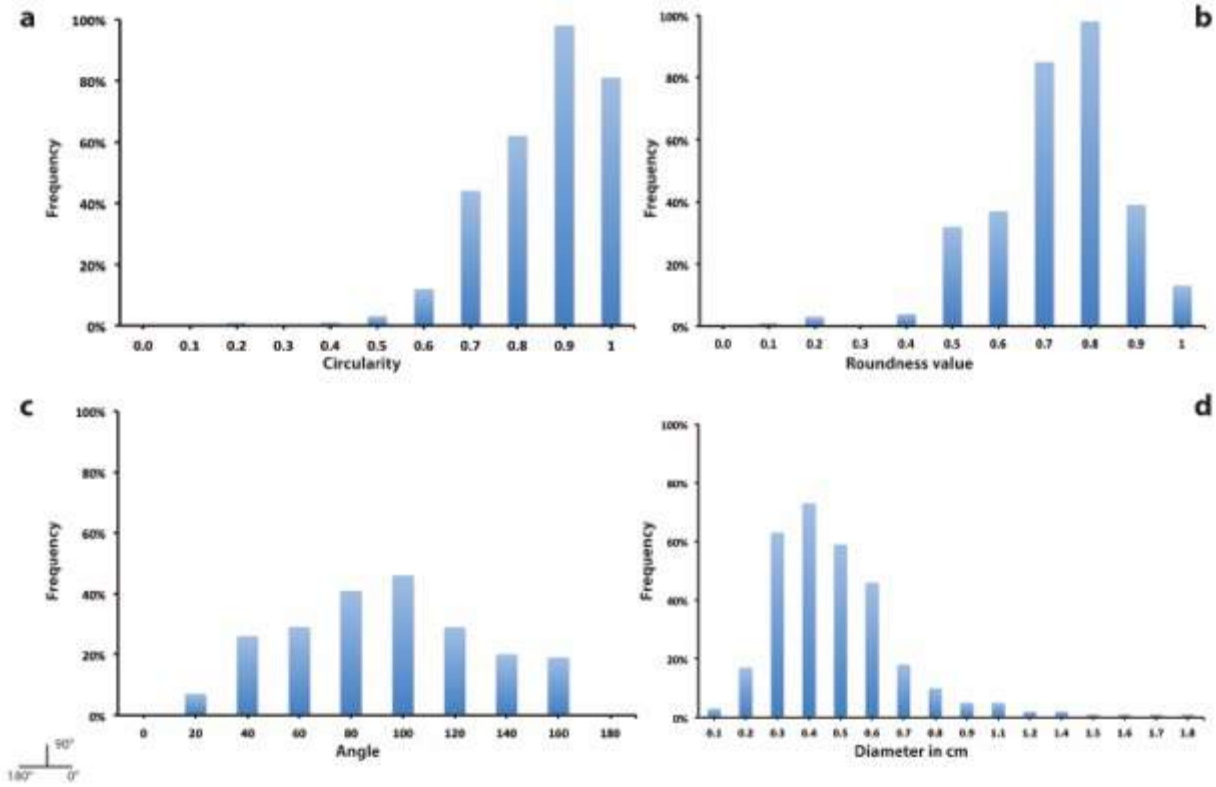

Figure 68: Results of morphometric analysis of the fault pearls from the slabs oriented parallel to the slickenlines of the shear surfaces. (a) Circularity plot. (b) Roundness plot. (c) Orientation plot. (d) Particle size distribution.

5.4.5 – Image analysis results from the polished slab cut orthognal to the slikenlines

The fault pearls, from the polished slab cut orthogonal to the slickenlines (Fig. 69, mosaic of the fault pearls from several slab) show a round shape too. Image analysis has been performed over four slabs in order to have a representative number of fault pearls shape descriptors.

They show a high circularity (Fig. 70a) with the mean value of 0.75 and a maximum value of 1 (perfect circle). This is in line with the measured roundness (Fig. 70b), whose mean value is equal to 0.70 and the maximum to 0.98. The carbonated-coated grains are also variable inclined with respect to the shear direction (Fig. 70c), as their orientation angles range between 20° and ca. 180°. Finally, fault pearls size distribution shows a mean dimension of 0.5 cm, but in this case most of the measured dimensions are comprised between 0.1 cm and 0.5 cm and no unimodal distribution is evident (Fig. 70d).

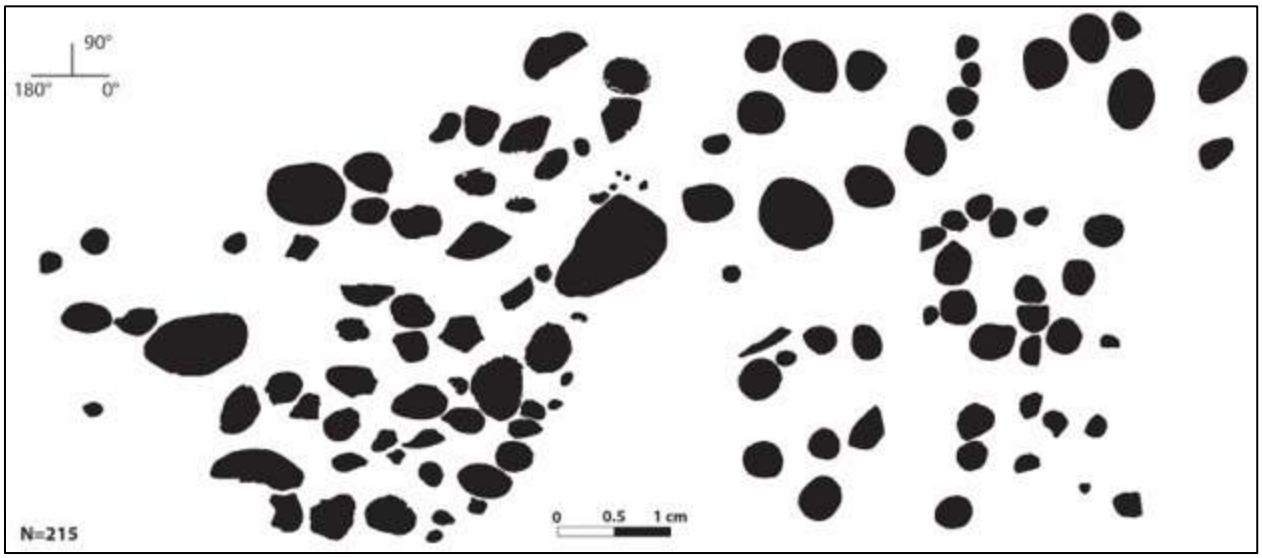

Figure 69: "Fault pearls map" obtained after the processing of the scan orthogonal with respect to the slikenlines (75 fault pearls). On the top left the orientation used by ImageJ.

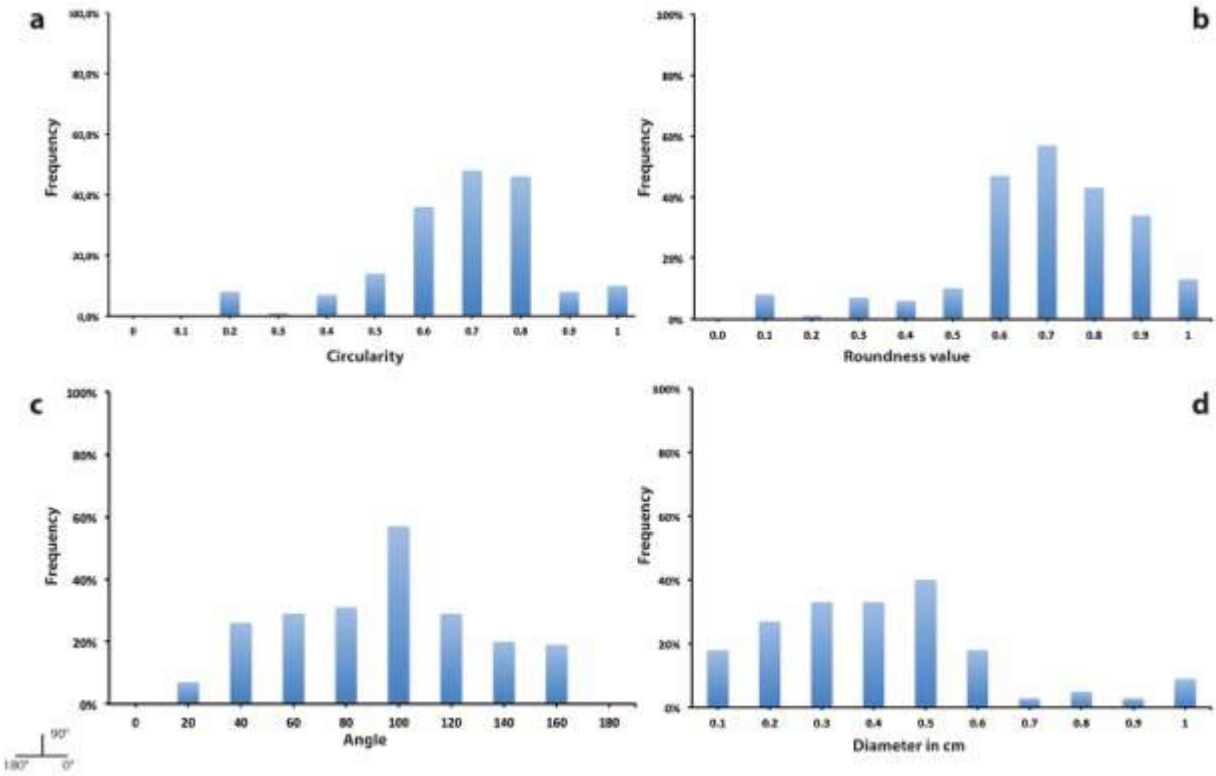

Figure 70: Results of morphometric analysis of the fault pearls grains from the slabs oriented orthogonal to the slickenlines of the shear surfaces. (a) Circularity plot. (b) Roundness plot. (c) Orientation plot. (d) Particle size distribution.

Thus, morphometric image analysis results show that the fault pearls have circular shape irrespective to the direction of observation (parallel and orthogonal to the slickenlines) also with values that indicate perfect circular shape. These values are in line with the roundness values, hence the fault pearls in three-dimensions can be considered as nearly perfect spheres or as very spherical textures.

The fault pearls show almost the same dimension, even if the grain size distribution is not perfectly the same, and have an average dimension of about 0.5 cm.

The fault pearls show a slight deviation from a circular shape lack a preferred orientation with respect to the shear direction. This hypothesis is also witnessed by the orientation data, that show a weak peak at 101° on the face parallel to the slickenlines, which show that the orientation of some of the fault pearls is linked to the fault movement and by the substantial lack of comminution and cataclasis of the fault pearls. Moreover, there is no close packing, no indentation or pressure solution evidences between different grains of the smallest fault pearls in the sample because carbonates and in part chalcedony occupy the volume between distinct grains. This demonstrates that, in general, fault pearls did not grow in contact with each other within the fault rock, and that no or only poor friction was active between them.

6 – Analytical Methods

6.1 – X-ray Powder Diffraction

I carried out preliminary qualitative identification of the mineral assemblages in the studied samples by X-Ray Powder Diffraction (XRPD).

Analyses were performed at the DISTAV (Department of Earth Sciences, Environment, and Life) of the University of Genoa using a Philips PW 3710 diffractometer equipped with a Co anode (Ni- filtered *CuKa* radiation, current 20 mA, voltage 40 kV). The analytical conditions have been the following:

- Scan Axis: Gonio
- Start Position: 3,0100° 2θ
- End Position: 79,9900° 2θ
- Step Size: 0,0200° 2θ
- Scan Step Time: 1,0000 s
- Scan Type: Continuous
- Anode Material: Co
- K-Alpha1: 1,78901 Å
- K-Alpha2: 1,79290 Å

6.2 – Petrographic analysis

Eighty-two polished thin sections were prepared from fault and whole rock samples. These sections were used to determine rock mineralogy by petrographic observations and microfrabric analysis.

6.3 – Scanning Electron Microscopy - Energy Dispersive X-ray Spectroscopy (SEM-EDS)

I performed the SEM-EDS analyses of rock minerals at the DISTAV of University of Genoa using a SEM Vega3 – TESCAN type LMU system equipped with an EDS

EDAX APOLLO XSDD with DPP3 analyser. Single spot EDS analyses were performed at 20 kV accelerating voltage and 1.2 nA beam current at the specimen level for 60 live second counting time with a spot size of 370 nm and working distance of 15 mm. Concentrations of major chemical components were calculated on an *anhydrous basis* with ZAF corrections and using natural silicates and oxides for calibration. These analyses were functional to the chemical identification of carbonates (i.e. ferroan-dolomite, ferroan-magnesite, dolomite, and magnesite) and chalcedony in the thin sections. Quantitative analyses provided the average concentration of the major components CaO, MgO, FeO, MnO, SiO_2 and Al_2O_3. Subsequent analyses carried out with Laser Ablation Inductively Coupled Plasma Time-of-Flight Mass Spectrometry (LA-ICP-TOFM) used some of these these values (for more see below) as internal standards for the quantification of minor and trace components in the carbonate-coated grains and chalcedony shear veins.

6.4 – Whole rock chemical analyses

The concentrations of major and trace elements in the whole rock samples have been determined at the Activation Laboratories Ltd (Ontario, Canada) combining a set of analytical techniques namely: Lithium mataborate/tetraborate fusion Inductively Coupled Plasma-Mass Spectrometry (ICP-MS), Instrumental Neutron Activation Analysis (INAA). Loss on Ignition (LOI) has been determined for each sample by weight difference after ignition at 1000°C. Table 1 shows the limits of detection for the ICP-MS analyses of the major components and LOI analysis, Table 2 lists the limits of detection for the trace elements, and Table 3 lists the typical ICP/MS standards.

6.4.1 – Lithium mataborate/tetraborate fusion ICP-MS

With this technique, samples are prepared and analysed in a batch system. Each batch contains a method reagent blank, certified reference material and 17% replicates. Samples are mixed with a flux of lithium metaborate and lithium tetraborate and fused in an induction furnace. The melt obtained with this procedure is immediately poured into a solution of 5% nitric acid containing an

internal standard, and mixed continuously until completely dissolved. The samples are run for major oxides and selected trace elements on a combination of simultaneous/sequential Thermo Jarrell-Ash ENVIRO II ICP and Varian Vista 735 ICP. Calibration is performed using 7 prepared USGS and CANMET certified reference materials. One of the 7 standards is used during the analysis for every group of ten samples.

The fused samples are diluted and analysed by Perkin Elmer Sciex ELAN 6000, 6100 or 9000 ICP/MS. Three blanks and five reference materials have been analysed per group of samples. Sample duplicates have been fused and analysed every 15 samples. Recalibration was carried out every 40 samples.

Oxide	Detection Limit (%)
Al_2O_3	0.01
CaO	0.01
Fe_2O_3	0.01
K_2O_3	0.01
MgO	0.01
MnO	0.001
Na_2O	0.01
P_2O_5	0.01
SiO_2	0.01
TiO_2	0.001
Loss on Ignition	0.01

Table 1: Major elements detection limits chart.

Element	Detection Limit	Upper Limit	Element	Detection Limit	Upper Limit	Element	Detection Limit	Upper Limit
Ag	0.5	100	Hf	0.1	1	Sn	1	1
As	5	2	Ho	0.01	1	Sr	2	10
Ba	3	300	In	0.1	200	Ta	0.01	500
Bi	0.1	2	La	0.05	2	Tb	0.01	1
Ce	0.05	3	Lu	0.002	1	Th	0.05	2
Co	1	1	Mo	2	100	Tl	0.05	1
Cr	20	10	Nb	0.2	1	Tm	0.005	1
Cs	0.1	1	Nd	0.05	2	U	0.01	1
Cu	10	10	Ni	20	10	V	5	5
Dy	0.01	1	Pb	5	10	W	0.5	5
Er	0.01	1	Pr	0.01	1	Y	0.5	1
Eu	0.005	1	Rb	1	1	Yb	0.01	1
Ga	1	500	Sb	0.2	200	Zn	30	10
Gd	0.01	1	Sm	0.01	1	Zr	1	10
Ge	0.5	500						

Table 2: Trace elements detection limits chart (ppm).

Element	W2	Cert.	Element	W2	Cert.	Element	W2	Cert.	Element	W2	Cert.
V	256	262	Y	21	24	Ce	24	24	Yb	2.06	20.5
Cr	90	93	Zr	99	94	Pr	2.5	5.9	Lu	0.33	0.33
Co	44	44	Nb	7.5	7.9	Nd	14	14	Hf	2.64	2.56
Ni	67	70	Mo	0.7	0.6	Sm	3.38	3.25	Ta	0.5	0.5
Cu	105	103	Ag	<0.5	0.05	Eu	1.1	1.1	W	<0.2	0.3
Zn	72	77	In	<0.2	-	Gd	3.5	3.6	Tl	0.1	0.2
Ga	18	20	Sn	<0.5	-	Tb	0.62	0.63	Pb	8	9.3
Ge	2	1	Sb	0.78	0.79	Dy	3.8	3.8	Bi	<0.05	0.03
As	<5	1.24	Cs	0.95	0.99	Ho	0.76	0.76	Th	2.3	2.5
Rb	20	20	Ba	164	182	Er	2.3	2.5	U	0.49	0.53
Sr	193	194	La	11.3	11.4	Tm	0.32	0.38			

Table 3: Typical ICP/MS standards (119 measurements).

6.4.2 – Instrumental Neutron Activation Analysis (INAA)

Au, As, Cr, Sc, Sb, and Ir have been analysed by Instrumental Neutron Activation Analysis (INAA). INAA is a technique based upon the measurement of radioactivity that has been induced by irradiation of the samples by neutrons. The primary source of neutrons for irradiation is usually a nuclear reactor. Each activated element emits a "fingerprint" of gamma radiation, which can be measured and quantified.

With this technique, a 30g aliquot of each sample is encapsulated in a polyethylene vial and irradiated with flux wires and an internal standard (1 for 11 samples) at a thermal neutron flux of 7×10^{12} n cm^{-2} s^{-1}. After a 7-day period, to allow Na-24 to decay, the samples are counted on a high purity Ge detector with resolution of better than 1.7 KeV for the 1332 KeV Co-60 photopeak. Using the flux wires, the decay-corrected activities are compared to a calibration developed from multiple certified international reference materials. The standard present is only a check on accuracy and is not used for calibration purposes.

One standard is run for every 11 samples. One blank is analysed per work order. Table 4 lists the limits of detection for Au, As, Cr, Sc, Sb, and Ir.

Element	Detection Limit	Upper Limit
As	0.5	10
Au	2 ppb	30,000 ppb
Cr	5	100
Sc	1	10
Sb	0.2	200
Ir	5 ppb	10

Table 4: INAA limits of detection (ppm, ppb for Au and Ir).

The accuracy for Au, As, Cr, Sc, Sb, and Ir was determined by analysis of reference material DMMAS 120 to be better than 7% in all cases.

6.5 – Laser Ablation-Inductively Coupled Plasma-Time of Flight Mass Spectrometry

Since the Laser Ablation-Inductively Coupled Plasma-Time of Flight Mass Spectrometry (LA-ICP-TOFMS; Fig. 71) is a non-conventional analytical technique, hence I introduce a detailed explanation regarding its functioning and the methodology with which compositional maps are generated.

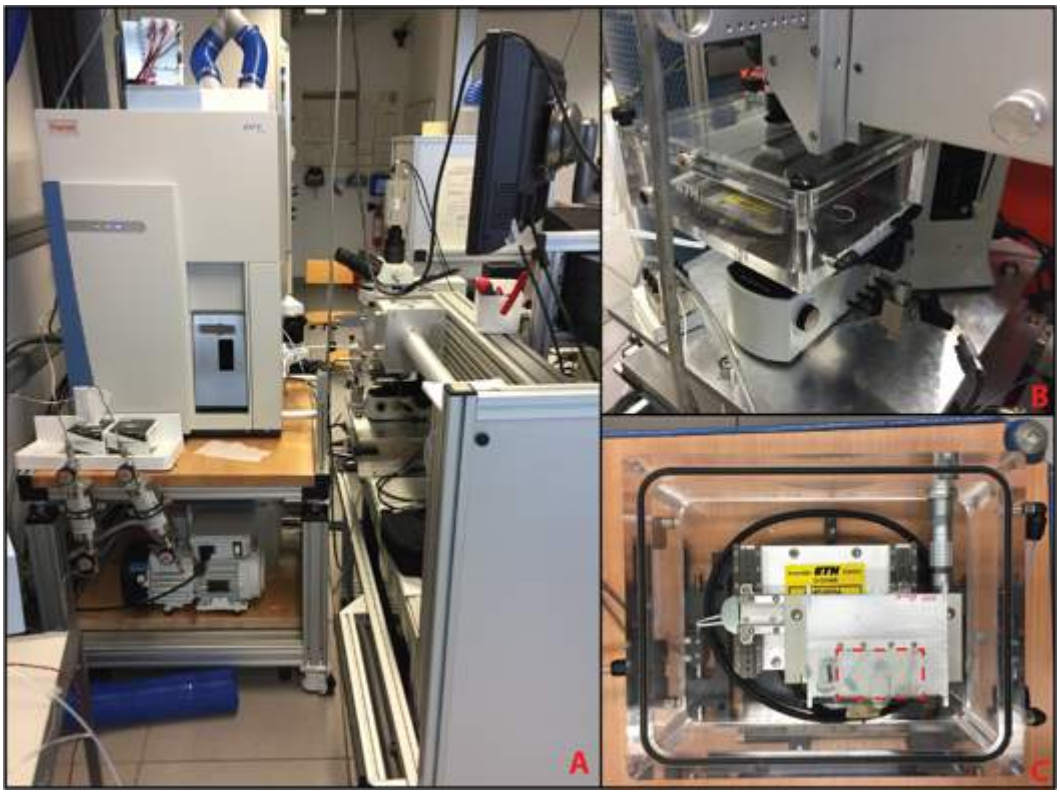

Figure 71: Prototype LA-ICP-TOFMS instrument used for the chemical imaging of sample LLM* at ETH Zurich (A): General view the optical bench (right), ablation cell, and TOF Mass Spectrometer (left) making the instrument. The argon fluoride excimer LA system is outside the field of view of the image. (B) In-house built ablation cell used to analyse the sample. (C) Detail of the ablation cell containing sample LLM*. The red dashed line highlights the position of LLM*.

6.5.1 – LA-ICP-TOFMS Imaging Methods

Elemental imaging by laser ablation inductively coupled plasma time-of-flight mass spectrometry (LA-ICP-TOFMS) was carried out at ETH Zurich (Zurich, Switzerland). Elemental imaging was completed with an established protocol (Burger et al., 2015; Gundlach-Graham et al., 2015; Gundlach-Graham and Günther, 2016) using an icpTOF ICP-TOFMS instrument (TOFWERK AG, Switzerland) combined with an Argon-Fluoride (ArF) laser ablation system (193 nm, ~10-ns pulse duration, GeoLas C, Lambda Physik, Goettingen, Germany; Gunther et al., 1997). For this study is used a low-dispersion LA "tube cell" (Wang et al., 2013), developed in-house that is designed for high-resolution LA-ICPMS imaging applications. The gas-flow profile and small working volume of this LA cell allow for transfer of ablated aerosol packets with temporal durations of single to tens of milliseconds, depending on ablation characteristics. Low-dispersion LA aerosol

transport allows the laser to be fired at repetition rates from 20–100 Hz without image blurring caused by pulse-to-pulse mixing (Woodhead et al, 2007; Triglav et al., 2010). It also improves the detection limit for small LA shots, because less noise is sampled across the duration of the temporally narrow aerosol clouds compared to conventional high-dispersion LA cells (Leach and Hieftje, 2002, 2005). Importantly, research of several groups has demonstrated that low-dispersion LA combined with high-speed ICPMS detection is the most promising route to quantitative high-resolution elemental and isotopic imaging by LA-ICPMS (Van Elteren et al., 2013, 2016; Van Malderen et al., 2015, 2016). Here, is combined the ICP-TOFMS instrumentation with low-dispersion LA because TOFMS provides full-mass spectrum acquisition at compatible speeds, and this full-spectrum detection enables the complete characterization of the elemental composition of the material being imaged, which is essential for the quantification of elements in samples with heterogeneous and/or unknown element distributions.

6.5.2 – Data Acquisition Conditions

Laser ablation was conducted in a helium atmosphere (99.999%, PanGas AG, Dagmersellen, Switzerland) and ablated aerosols were carried to the ICPMS in a stream of argon gas (99.996%, PanGas AG, Dagmersellen, Switzerland). Operating conditions of the LA and ICP-TOFMS instruments are provided in Table 6. To generate an elemental image by LA-ICPMS, the sample was scanned underneath the pulsed laser beam so that adjacent LA spots line up edge-to-edge and consecutive lines scans are arranged to create a rectangular grid of the LA spots. For image collection of the fault pearls sample, has been used a LA frequency of 25 Hz, and LA-spot diameter of 10 μm, a line scan speed of 250 μm/sec, and 1000 LA shots per line. The TOFMS spectral acquisition rate was 333 Hz (3 ms per spectrum), so that more than 10 complete mass spectra were recorded across each LA peak. Data from groups of ten consecutive line scans were recorded in single TOFMS data files, so that the TOFMS data was divided between 100 files, each composed of data from an array of 1000 x 10 LA shots. Laser focus was adjusted between each of these batches of 10 line scans; however, the focus distance of the laser to sample was not adjusted across line scans. For imaging a large area, such as the square centimetre imaged here, surface flatness is critical. The LA and ICP-

TOFMS instruments were operated continuously and automatically for the image collection period, with the TOFMS system triggering each new batch of 1000 x 10 LA shots. Total image acquisition time was 14.5 hours. Before and after collection of the LA-ICP-TOFMS data of the fault pearls sample, signal from NIST SRM 610 was collected and used to establish relative sensitivity factors element quantification. In Figure 72, are reported the single-laser-shot limits of detection (LODs) obtained from sensitivities determined from ablation of the NIST 610 SRM; these LODs serve as a reference for detectable concentrations in the elemental images of the fault pearls sample.

We found that the temporal profile of the ablated aerosol depended strongly on ablation characteristics of the rock matrix and the laser focus across the image. The surface of the thin-rock section was not flat (parallel to glass slide it was mounted on) across the line scan direction. To minimize the effect of surface slope across the line-scan distance, the height of the sample has been adjusted to bring the laser into focus at the middle position of each batch of 1000 x 10 LA spots. Because the temporal profile of the LA aerosol strongly depends on ablation characteristics, misfocus of the laser can lead to poorly resolved (i.e. longer duration) LA-generated ICP-TOFMS signals. In particular, the effect of poorly resolved LA aerosols can be seen in the top left quadrant of the developed elemental images (cf. Fig. 73). This section of the images shows elemental distributions that are smeared from right to left (line-scan direction) because there is carry-over of signals from previous LA shots into the time bins corresponding to signals from adjacent LA shots. This causes high-abundance signals to tail into adjacent pixels to the left. Apart from the top-left ~3x3 mm section of the LA-ICP-TOFMS images, LA peaks were well resolved across all line scans, which is apparent from the sharpness of the complete elemental images compared to the section of the images with poorly resolved LA transients. Generally, LA-ICP-TOFMS transients from each LA shot had intensities below 1% of the peak height within 30 ms; this translates to a resolvable element concentration range of at least 100 from pixel-to-pixel (i.e. within 10 μm).

Laser Ablation	
Cell	Tube Cell
Laser Wavelength	193 nm
Laser-Spot Shape	circle
Laser-Spot Diameter	10 µm
Repetition Rate	25 Hz
Line Scan Speed	200 µm s^{-1}
Fluence	15 J cm^{-2}
Carrier Gas (He)	2.2 L min^{-1}
ICP-TOFMS	
Injector Diameter	1.5 mm
Nebulizer Gas (Ar)	0.60 L min^{-1}
Intermediate Gas (Ar)	0.76 L min^{-1}
Outer Gas (Ar)	17 L min^{-1}
Sampling Depth	5.0 mm
Plasma Power	1600 W
Oxide Ratio $^{232}Th^{16}O/^{232}Th$ (NIST 610)	0.53%
$^{238}U/^{232}Th$ (NIST 610)*	1.04
TOFMS Spectral Acquisition Rate	333 Hz, (100 TOF pushes averaged per spectrum)
Notched (Attenuated) Masses	16, 18, 32, 40

Table 5: Operating parameters for LA-ICP-TOFMS imaging.

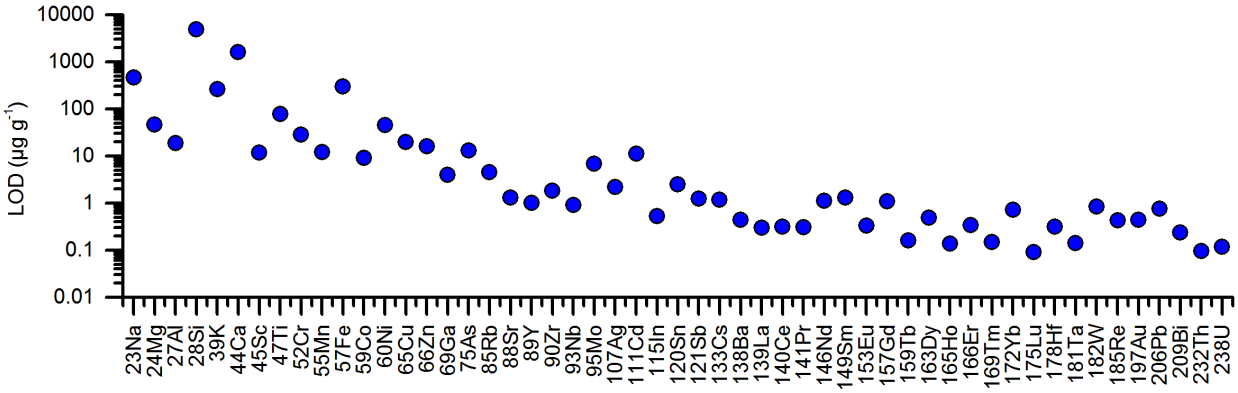

Figure 72: Single-shot limits of detection obtained from pulse-resolved NIST610 Analysis

6.5.3 – Data Processing, Quantification, and Image Construction

To correct for elevated baselines caused by abundant species in the ICP-TOFMS mass spectra, a baseline-fitting algorithm has been used (Tofware ver. 2.5.10, TOFWERK AG; run in IgorPro ver. 7.02, Wavemetrics Inc.) to model and subtract the baseline before integration of mass spectral peaks. Detailed evaluation on the impact of baseline subtraction on abundance sensitivity performance and accuracy

of quantification for LA-ICP-TOFMS can be found elsewhere (Hendriks et al., 2017). Following baseline subtraction and mass-spectral peak integration, TOFMS data has been divided into the peak intensities associated with each single LA pulse (i.e. pixel) with a custom-written Matlab (version R2015a, Mathworks, MA) program. Briefly, this Matlab program sections the ICP-TOFMS data so that the signal for each LA event is integrated across 40 ms and the LA peak integration regions are aligned based of time of the first LA event and the laser frequency. In addition, gas blank signals for each mass channel are subtracted from the integrated single-pulse signals. To generate an image, integrated single-LA-pulse intensity data from each analyte isotope are arranged in a 2D array of line scan position vs. line scan number; each single-element image is square and contains data from 10^6 LA events: 1 cm x 1 cm, 1 megapixel.

To quantify the elements in each pixel of the LA-ICP-TOFMS images, a 100% mass normalization approach has been used, in which the concentrations of elements in each pixel are normalized to 100% mass of the major and minor species present in the rock sample (Gratuze; 1999). To account for the mass of elements that could not be measured, such as oxygen and carbon, has been assumed that major elements were present in either their most stable oxide or carbonate forms: contribution of carbon and oxygen to total mass ablated in each LA event was based on these stoichiometries. Table 5 reports the species and the oxide or carbonate correction factor used for the 100% mass normalization quantification of elements in each pixel.

Details of the 100%-mass normalization strategy are reported elsewhere (Burger et al., 2015; Gundlach-Graham et al., 2015; Gundlach-Graham and Günther, 2016), but a brief summary of the procedure is provided specific to the quantification of the dolomite sample imaged here. Pixel-by-pixel quantification was performed in a custom-written LabVIEW program (ver. 13.0.1f5, National Instruments Corp., USA). In this 100%-normalization quantification strategy, first has been used the average single-pixel intensity values from LA of NIST SRM 610 to establish elemental sensitivities in units of ion counts $pixel^{-1}$ $concentration^{-1}$. For isotope intensities from each LA spot (i.e. each pixel), has been determined the elemental concentrations according to the standard external-calibration approach for LA first developed by Longerich, Jackson, and Günther (Longerich et al., 1996). This quantification is described by equation 1, where R is the response of each

isotope *i* in counts per LA shot, *C* is the concentration of the element represented by isotope *i*, *Cal* refers to the external standard, *Samp* refers to the sample, and *IS* denotes the internal standard.

$$C_{i,Samp} = S_{i,Samp}\left[\frac{C_{i,Cal}}{R_{i,Cal}}\left(\frac{R_{IS,Cal}}{R_{IS,Samp}} \times \frac{C_{IS,Samp}}{C_{IS,Cal}}\right)\right] \quad \textbf{(1)}$$

A single isotope signal was not chosen for as the internal standard because no element is ubiquitous throughout the imaged region. Instead, the responses of all analyte isotopes have been summed (cf. Table 2) so that the internal standard signal at all LA positions accounts for ablation yield; equation 2 reflects this internal standardization strategy.

$$C_{i,Samp} = S_{i,Samp}\left[\frac{C_{i,Cal}}{R_{i,Cal}}\left(\frac{\sum_i^n R_{i,Cal}}{\sum_i^n R_{i,Samp}} \times \frac{C_{IS,Samp}}{\sum_i^n C_{i,Cal}}\right)\right] \quad \textbf{(2)}$$

For 100% mass normalization quantification, the determined concentrations have been normalized for each pixel ($C_{i,Samp}$) such that the sum of all concentrations of all *elemental species* in each pixel equals 100%. To correct for the presence of oxide and carbonate groups, a correction factor, K_i, was applied at each pixel. The 100%-normalized concentration of each element *i* is, then, the original determined concentration of that element multiplied by the 100%-normalization correction factor.

$$C_{i,Samp,100\%Norm} = C_{i,Samp} \times \left(\sum_i^n C_{i,Samp} \times K_{i,Species}\right)^{-1} \quad \textbf{(3)}$$

Whereas all elements were quantified based on their predominant species as reported in Table 5, the concentrations of all major components were converted to the equivalent mass concentrations of their most stable oxide forms. Thus, the concentration-distribution images of elements present in the rock sample as carbonates (i.e. Mg, Ca, Mn, Fe, Sr, and Ba) reflect the true mass concentration of each element, but not the true concentration of their molecular species. False-colour element concentration distribution images were generated in Matlab and were all plotted on a linear scale of either the weight percent oxide or mass

fraction of the element in each pixel. The false-colour scale of all elemental images span concentration ranges from 0 wt % or 0 ppm to 99.5% of the maximum concentration value: this scaling provides best image contrast and encompasses most of the concentration range. Figures 73b-e provides example quantified elemental images of major, minor, and trace elements across the thin-rock sample.

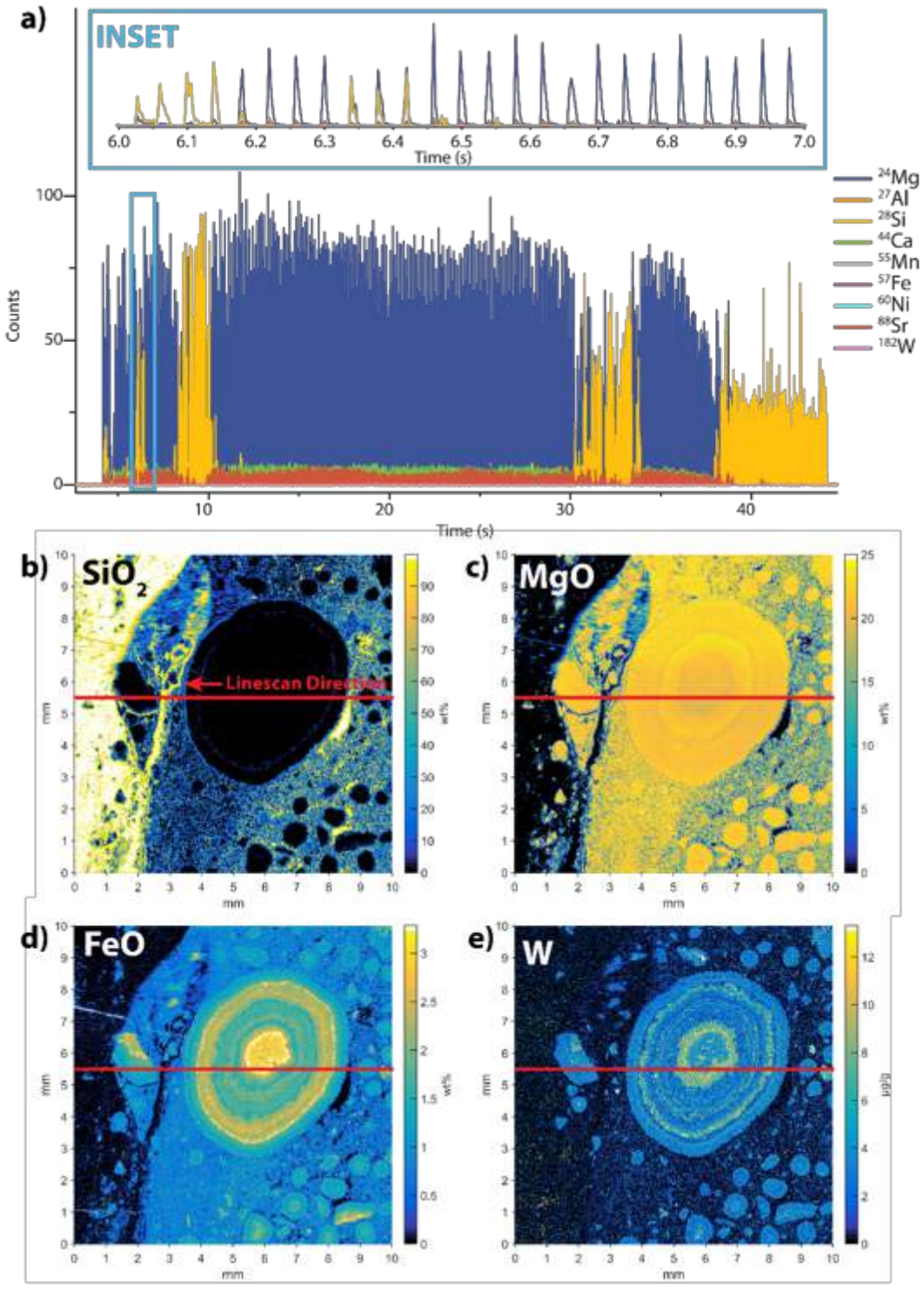

Figure 73: a) Transient ICP-TOFMS data from 1000 LA events of a single line of the final elemental image. In the inset, one second of ICP-TOFMS data is provided. Here, the LA frequency of 25 Hz is apparent as well as the separation between signals from each LA event. The signals from each of the transient peaks are integrated across 40 ms around the signal peak to generate the isotopic signals associated with each pixel of the LA-ICP-TOFMS images. b-e) Quantified elemental images of major, minor, and trace components of the dolomite sample. In each image the position of line 460 is indicated with a horizontal red line. The line scan direction for LA-ICPM image collection was from left to right, as indicated in b.

Elements Quantified	Isotope Used	Quantified Species	Correction Factor For 100% Normalization of Carbonate/Oxide Species	Single-Shot Sensitivity (counts/µg g-1)	Elemental LOD (µg g-1)
Na	23Na	Na2O	1.35	0.04	4600
Mg	24Mg	MgCO3	3.47	0.11	46
Al	27Al	Al2O3	1.89	0.13	19
Si	28Si	SiO2	2.14	0.07	4900
K	39K	K2O	1.20	0.04	160
Ca	44Ca	CaCO3	2.50	0.00	1600
Sc	45Sc	Sc	1.00	0.41	12
Ti	47Ti	TiO2	1.67	0.03	77
Cr	52Cr	Cr	1.00	0.30	28
Mn	55Mn	MnCO3	2.09	0.53	122
Fe	57Fe	FeCO3	2.07	0.01	300
Co	59Co	Co	1.00	0.43	9
Ni	60Ni	Ni	1.00	0.09	45
Cu	65Cu	Cu	1.00	0.12	20
Zn	66Zn	Zn	1.00	0.09	16
Ga	69Ga	Ga	1.00	0.51	3.9
As	75As	As	1.00	0.16	13
Rb	85Rb	Rb	1.00	1.08	4.5
Sr	88Sr	SrCO3	1.68	1.65	1.3
Y	89Y	Y	1.00	2.04	1
Zr	90Zr	Zr	1.00	0.98	1.8
Nb	93Nb	Nb	1.00	1.50	6.8
Mo	95Mo	Mo	1.00	0.23	6.8
Ag	107Ag	Ag	1.00	0.58	2.2
Cd	111Cd	Cd	1.00	0.14	11
In	115In	In	1.00	2.29	0.52
Sn	120Sn	Sn	1.00	0.97	2.5
Sb	121Sb	Sb	1.00	0.82	1.2
Cs	133Cs	Cs	1.00	2.96	1.2
Ba	138Ba	BaCO3	1.44	2.76	0.44
La	139La	La	1.00	3.59	0.3
Ce	140Ce	Ce	1.00	3.41	0.31
Pr	141Pr	Pr	1.00	4.66	0.31
Nd	146Nd	Nd	1.00	0.87	1.1
Sm	149Sm	Sm	1.00	0.74	1.3
Eu	153Eu	Eu	1.00	3.10	0.33
Gd	157Gd	Gd	1.00	0.93	1.1
Tb	159Tb	Tb	1.00	6.81	0.16
Dy	163Dy	Dy	1.00	1.69	0.49
Ho	165Ho	Ho	1.00	7.15	0.14
Er	166Er	Er	1.00	2.38	0.34
Tm	169Tm	Tm	1.00	7.83	0.15
Yb	172Yb	Yb	1.00	1.68	0.71
Lu	175Lu	Lu	1.00	8.33	0.09
Hf	178Hf	Hf	1.00	2.50	0.32
Ta	181Ta	Ta	1.00	8.28	0.14
W	182W	W	1.00	1.45	0.83
Re	185Re	Re	1.00	2.35	0.43
Au	197Au	Au	1.00	2.64	0.44
Pb	206Pb	Pb	1.00	1.67	0.75
Bi	209Bi	Bi	1.00	5.76	0.23
Th	232Th	Th	1.00	11.12	0.1
U	238U	U	1.00	10.54	0.12

Table 6: Elements Quantified and Limits of Detection

7 – Mass Transfer Calculations

7.1 – Introduction

By definition, mass transfer calculations consist of a set of procedures whereby fluid-rock interaction processes generated by chemical diffusion between fluid and rock are quantitatively determined using whole rock chemical analysis (e.g., Grant, 1986). Since their early geochemical applications (Gresens, 1967) mass transfer calculations gained much popularity in the scientific community, as testified by their use in a large number of studies focussing on several geological environments (e.g., Grant, 1986; MacLean and Kranidiotis, 1987; Bohlke, 1989; Dilles and Einaudi, 1992; Ague, 1994; Baumgartner and Olsen, 1995; Salvi and Williams-Jones, 1996; Ague, 1997; Garofalo, 2004b; Garofalo, 2004a; Grant, 2005; Garofalo, 2012). In these studies, sets of quantification methods were devised to determine fluid-rock mass transfers. A critical evaluation of these methods, and in particular of their limits of applicability, is beyond the scope of this work. Here, we highlight the fact that such studies are invariably based on one fundamental step – i.e., the identification of one or more indexes of comparison between an altered rock subjected to fluid-driven metasomatism and its unaltered protolith. Such indexes are called *mass factors* (e.g., Grant, 1986) and provide a measure of the proportions of mass that are lost or gained by a rock during its interaction with a geofluid. Mass factors and protolith identification are the heart of mass transfer calculations, as their erroneous or ambiguous determination generates flawed interpretations of a metasomatic process (e.g., discussion in: Garofalo, 2004b; Garofalo, 2004a).

In a mass of rock subjected to a metasomatic process, mass factors are evaluated identifying the so-called *immobile elements*. These are couples of components whose concentration ratios, measured in various aliquots of the metasomatised rock mass, are constant. An example of how immobile elements can be determined is reported in the scatter plot of Figure 74 (modified from: MacLean and Kranidiotis, 1987), which shows how the concentrations of two immobile components may be identified in a compositional plot. If fluid-rock interaction would cause mass gain of two immobile components of the rock, the concentration ratios of these components in distinct aliquots of this rock would lie

along a line but closer to the origin of the axis. Thus, mass gain would determine the absolute concentrations of the immobile components to be lower than those of the protolith, but would maintain their ratio constant. In contrast, if alteration would cause an overall mass loss the opposite trend would be observed. Deviations from a linear trend would prove mobility of one component respect to the other (Fig. 74).

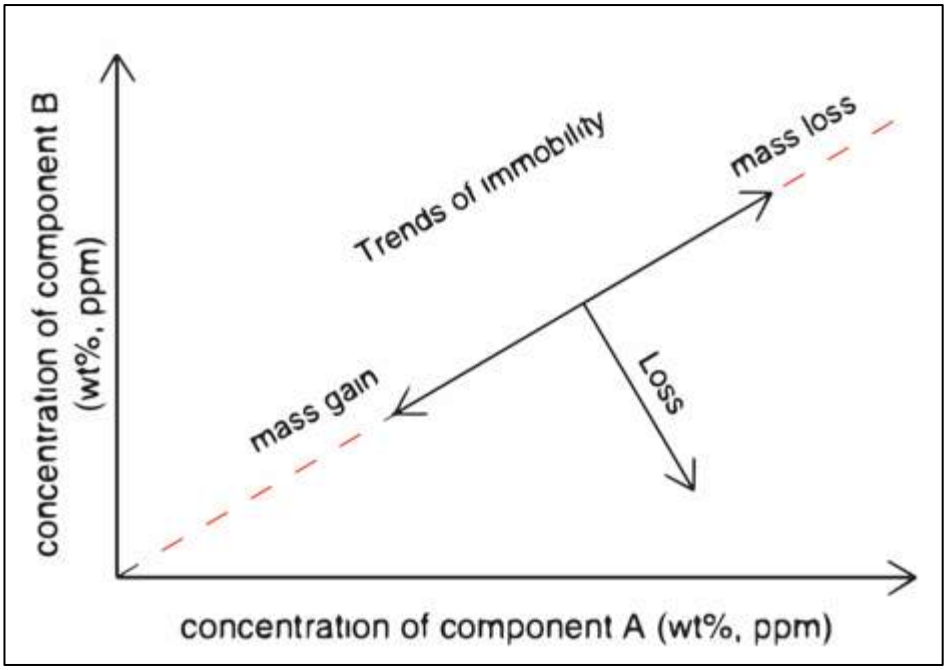

Figure 74: Immobility trends, in regimes of gains and losses, identified in a mass of rock subjected to fluid-rock interaction. The two axes show the variations in concentration of two rock components (either major, minor, or trace elements) in distinct aliquots of a rock.

With this method have been identified a representative number of couples of immobile components in the RB1-RB10 profile. I subsequently calculated a *multiplication factor* of all samples using:

$$MF_x = \frac{c_i^0}{c_i^x} \qquad (1)$$

where MF_x is the multiplication factor of sample x, c_i^x is the concentration of immobile component *i* in sample x, c_i^0 is the concentration of immobile component *i* in the protolith. Note that if c_i^x corresponds to component B of Fig. 79 and c_i^0 corresponds to component A, the multiplication factor is the reciprocal of the slope of the trend line of Fig. 79. Such slope is the inverse of *mass factor* as defined by Grant (1986, p. 1977 – eq. (5)), and should not be confused with that definition.

The protolith composition used for the mass transfer calculations was considered sample RB10, which is the least altered serpentinized lherzolite of the studied profile (Fig. 76, see also below). Mass transfers have been determined for all samples using (Mountain and Williams-Jones, 1996; Garofalo, 2004b; Garofalo, 2004a):

$$\Delta Ci = (C_i^A \, MF_x) - C_i^O \quad (2)$$

where ΔCi is the mass of component i exchanged per unit mass of protolith (reported as g/100 g or g/ton).

7.1.1 – Sampling strategy for mass transfer calculations

Sample LLM* (Fig. 75) used for compositional imaging with Laser Ablation-Inductively Coupled Plasma Time of Flight Mass Spectrometry has been collected at the Bisciarelle fault core and was used to determine elemental distribution in the zones of the fault filled with fault pearls and chalcedony.

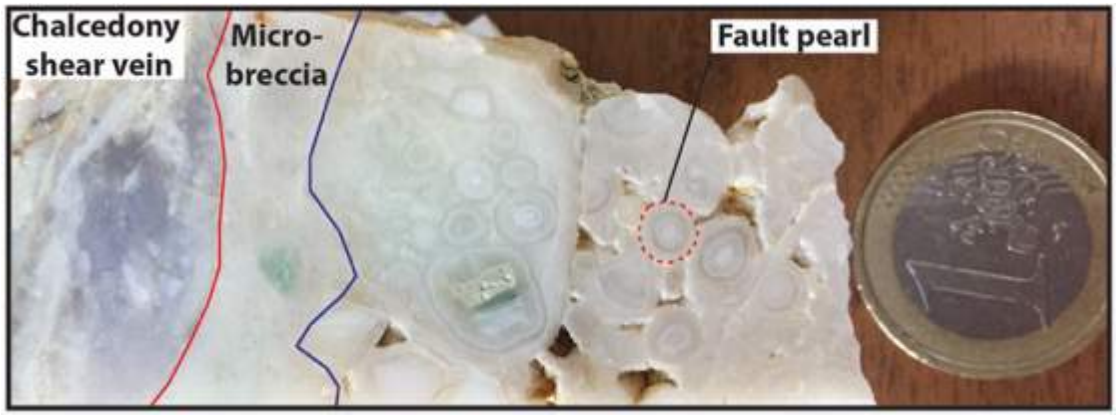

Figure 75: Sample LLM* showing the contact between the chalcedony shear vein and the carbonate micro-breccia (highlighted by the red line) and the contact between the carbonate micro-breccia and fault pearls (highlighted by the blue line). The red dashed line points out one fault pearls.

Being collected in an area of the fault adjacent to the RB1-RB10 wall rock profile, sample LLM* allows documenting the frictional and fluid-assisted processes occurring within the fault at the time of wall rock alteration. Such documentation provides in turn potential feedbacks between the fluid flow occurring within the fault and the mass transfer processes occurring at the contact between fault and host rock.

The samples used for mass transfer calculations (RB1 - RB10, Fig. 76; Fig. 55 paragraph 5.4.3.1) were collected starting from the most carbonated portion of the fault damage zone, which is located at ca. 50 cm from the fault core, and followed a direction that was orthogonal with respect to the fault strike. Ten samples have been collected along this direction for a distance of about 15.5 m towards the least altered lherzolite host. The first of these samples (Fig. 76) was collected at the fault core, and the remaining ten along the profile at progressively increasing distance from the fault contact. The aim of this sampling has been collecting aliquots of serpentinized lherzolite showing the mineralogical and chemical changes generated by hydrothermal alteration at the time of fluid-rock interaction. As no other fault is crosscutting or splaying off the one studied here, all the mineralogical and chemical changes documented here refer to one single event of fluid-rock interaction. The close spacing of the samples along the profile allows defining progressive mineralogical and chemical changes of the lherzolite with high accuracy, in particular it allows the definition of which components were transferred from the fluid to the rock – and vice versa – during that process. These constraints provide in turn insights into the physical, chemical, and mechanical properties of the fault itself.

Sampling was conducted in an area where large sets of secondary carbonate veins and surface weathering were scarse or absent. The ten samples (Fig. 76) were used to prepare 10 polished thin sections for petrographic documentation and also to determine the concentrations of major, minor, and trace elements in the whole rock using a set of analytical techniques (see below).

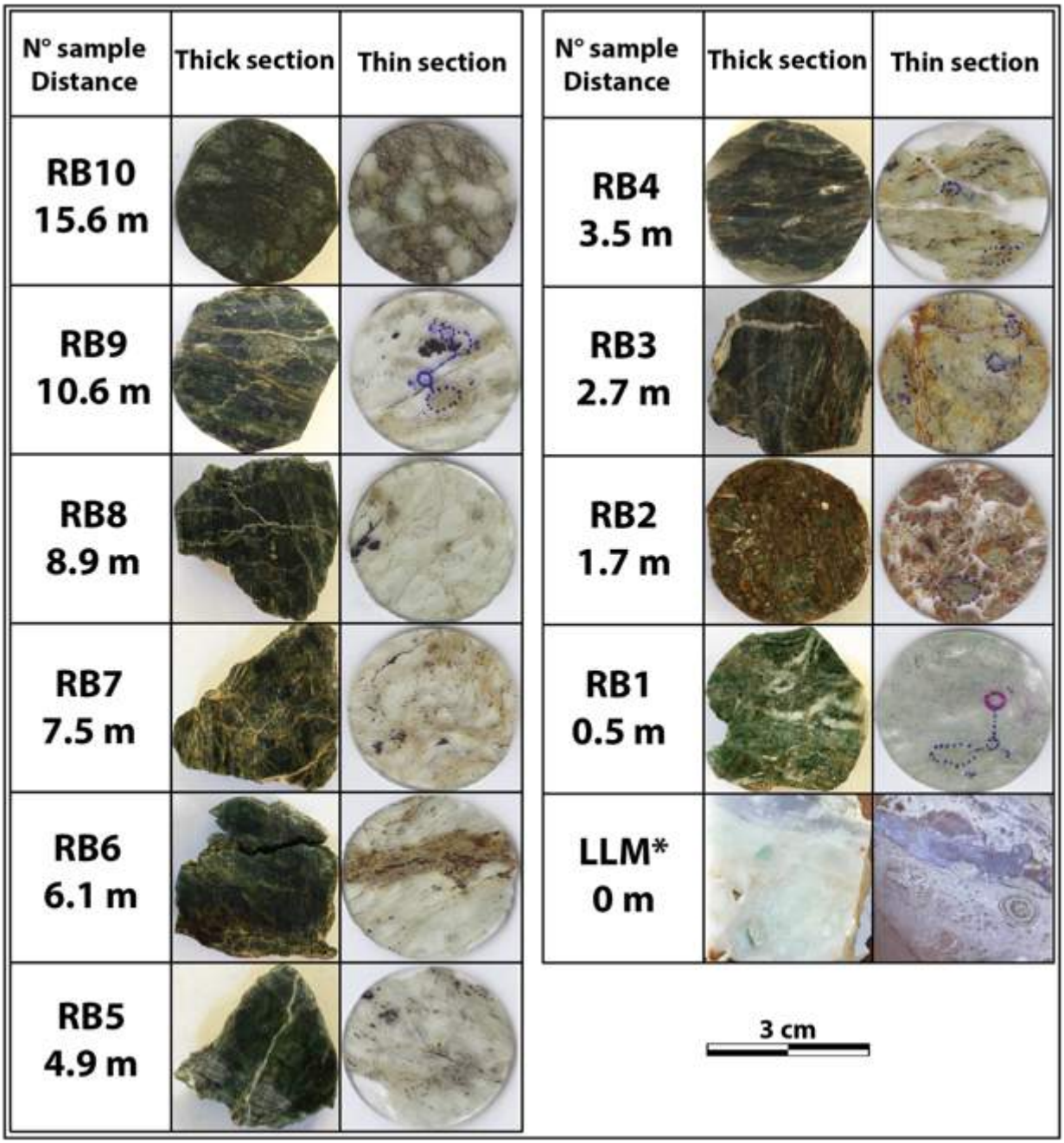

Figure 76: Samples of the RB1-RB10 profile listed at the measured progressive distance from the Bisciarelle fault core. Small-scale images of polished slabs and thin sections are reported to highlight systematic variations of rock textures.

7.2 – Meso- and microscopic characteristics of hydrothermally altered lherzolite

From the Bisciarelle fault core to the unaltered lherzolite, the collected samples show a systematic variation of mineralogical composition, which is essentially controlled by the degree of dolomitisation and rutile-ilmenite precipitation.

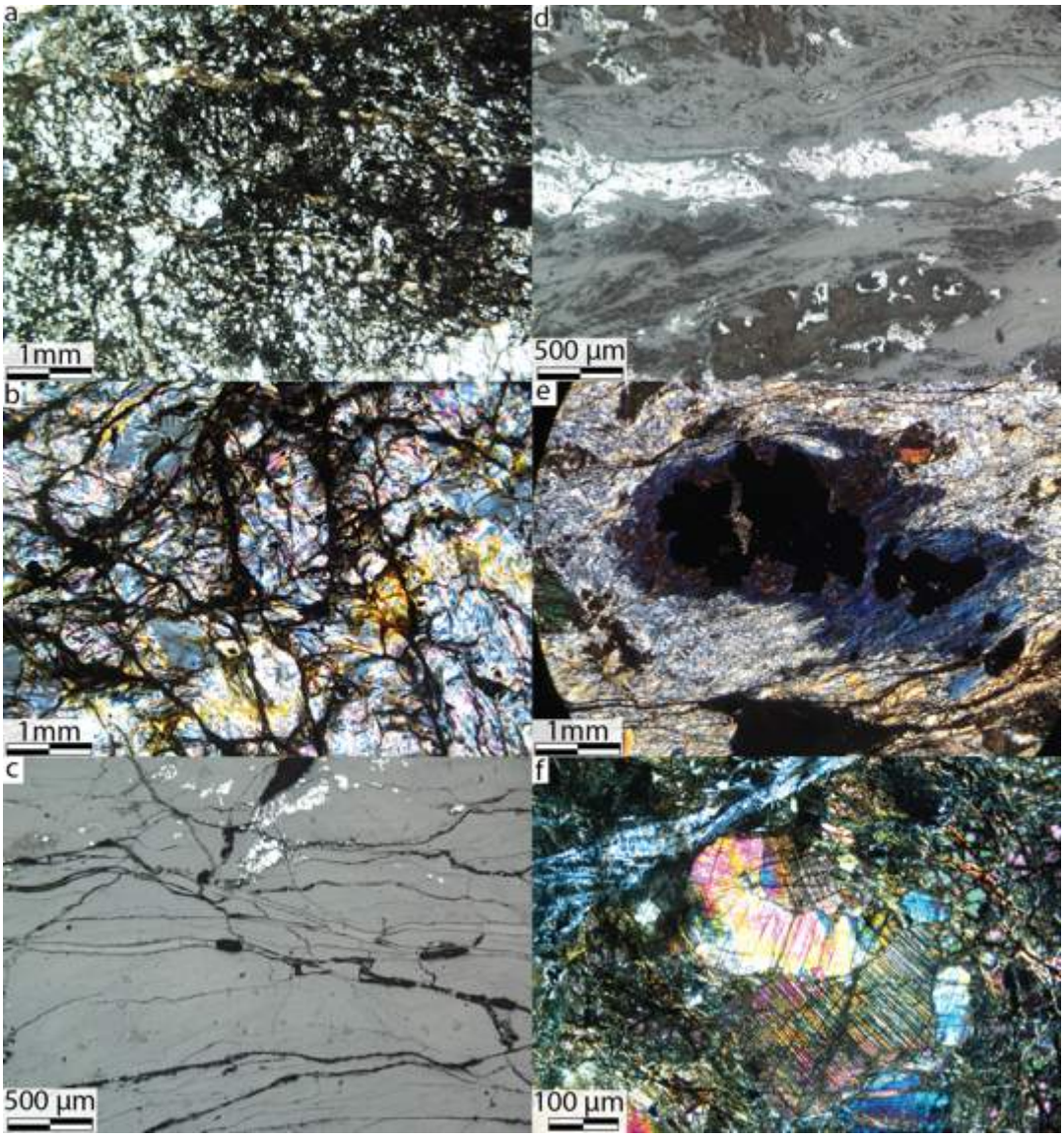

Figure 77: Photomicrograph of the striking features of RB1-RB10 samples. (a) Cataclastic dolomite with saponite. (b) Serpentinite schist without any textural feature of the lherzolite. (c) Oxide phases almost displaced along carbonatic veins. (d) Ilmenite and rutile mainly occurring along the seprpentinized lherzolite foliation. (e) Progressive modal increase of clino- and orthopyroxenes; oxides do not occur along the foliation. (f) Least altered serpentinized lherzolite, with clino-orthopyroxene, olivine, serpentine and rare opaque minerals.

Mesoscopically, all samples with the exception of the most distal RB10 show a pervasive foliation and those collected at 1 m (RB2), 2.8 m (RB4), and 3.8 m (RB5) are non-cohesive or poorly cohesive.

The fault core is mainly made up of fault pearls inside the carbonates portion and by chalcedony along the shear veins. The fault core does not show oxides or opaque minerals.

The sample RB1 located at 0.5 m from the fault is a cataclastic dolomite that contains blocks of fractured carbonate veins. These veins are extensional since their growth vectors are still recognizable, but they are fractured and comminuted into the cataclastic texture.

The sample RB2 located at 1 m from the fault core is a non-cohesive serpentinite, made up of millimetric to centimetric clasts having angular to sub-angular shape. The clasts preserve an internal mylonitic foliation, along which are carbonates associated with rutile, ilmenite, and minor pyrite (<1 vol %). Between 2 m to 8.9 m from the fault core, the rock shows several foliation levels (3.5-4.9 m) and mylonitic textures (6.1-8.9 m). Dolomite mainly occurs within the foliation.

At the microscopic scale, the host rock adjacent to the fault core (i.e., sample RB1 Fig. 77a) is made almost entirely by cataclastic dolomite and emerald green saponite (Supplementary material S7: RB1 XRD analysis), which occurs as a fine-grained dissemination between carbonate crystals. Serpentine, ilmenite, and rutile constitute the wallrock at 1-2.8 m from the fault core (Fig. 77b). The samples from this part of the host rock profile do not preserve any textural feature of the lherzolite, and are turned into a dolomite, rutile, and ilmenite assemblage. Dolomite replaces in part the Ti-Fe phases (Fig. 77c), showing that this is essentially the most stable phase close to the fault contact. In general, a thin network of carbonate veins crosscuts the rock from this part of the profile.

Samples collected between 3.8 and 5 m from the fault core (RB5-RB7) are still constituted by serpentine, but show a progressive modal increase of ilmenite and rutile, which are mainly occurring along the foliation (Fig. 77d). Coupled to this increase there is a general decrease in carbonate abundance. However, at 5 m from the fault core the rock is still crosscut by a dense network of calcite veins, showing that the halo of carbonatic alteration developed for at least that distance from the fault core. However these samples show fluctuating concentrations of carbonate

and Fe-Ti oxides along the foliation, and pyroxenes remnants with respect to the near samples. The concentration of carbonates, Fe-Ti oxides and pyroxene remnants, in example, is higher in RB5 and RB7, whereas in RB4, RB6, and RB8 there are no carbonates, and minor concentration of Fe-Ti oxides and pyroxene remnants.

Samples collected at 6.4 - 7.8 m from the fault core (RB8 - RB9) show a progressive modal increase of the clino- and orthopyroxenes that are typical of the protolith lherzolite (Fig. 77e). Such increase is coupled with a progressive decrease of modal serpentine, rutile and ilmenite. At 9.6 m from the fault core, the host rock is not foliated and shows only few carbonatic veins. This is the least altered serpentinized lherzolite (RB10), located at 14.5 m from the fault core and made of ortho- and clinopyroxenes, olivine, serpentine, and rare opaque minerals (<1 vol% - Fig. 77 f). The rare opaque minerals occur along the serpentine.

7.3 – Mass transfer calculations results

A comparison between the composition of sample RB10 and that of typical serpentinized lherzolites documented in the Erro-Tobbio massif (Fig. 78) shows that there is no significant compositional difference between sample RB10 and that of other lherzolites outcropping in the area. Small deviations from an ideal y=x linear fit are shown only by some components as L.O.I., Dy, Ho, and Yb. This demonstrates unequivocally that the most distal sample of the RB10-RB1 host rock profile is indeed a good representative of the hydrothermally unaltered rock of the area, and as a consequence that our considerations on mass transfer across the Bisciarelle fault are well founded because they are referred to a protolith composition that is homogeneous.

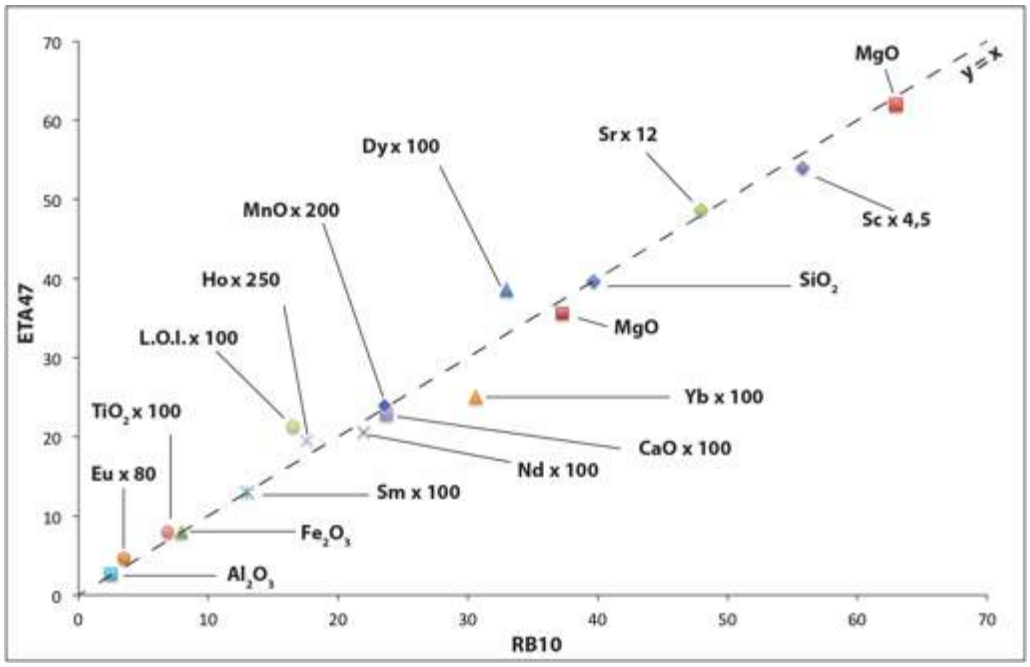

Figure 78: Comparison between the concentrations of the major components of lherzolite RB10 *vs.* concentration of the corresponding components of a typical serpentinized lherzolite outcropping in the Erro-Tobbio area (data from: Scambelluri et al., 2001). Some concentrations are scaled in order to avoid the clustering of data point close to the origin of the axes. Note that the linear fit y=x is independent from the plotted dataset

Immobile elements have been determined comparing the concentrations of Al_2O_3 with those of other components in the RB10-RB1 dataset (Fig. 79; S8 supplementary materials). Figure 79 is a selection of these comparisons and shows that the compositional trends of the pairs Al_2O_3-TiO_2, Al_2O_3-CaO, Al_2O_3-Y, and Al_2O_3-Ce approach quite closely linear trends converging towards the origin of the axes. Thus, the geochemically unrelated components Al_2O_3, TiO_2, CaO, Y, and Ce can be considered immobile (or quasi-immobile) with respect to the studied process (cf. Figs. 79 a, b, c, d). Perfect immobility cannot be demonstrated rigorously for these components because their concentration ratios are not exactly constant (i.e., they do not form exactly linear trends in Fig. 79). These deviations, which are mainly shown by the samples that are closer to the fault contact, are explained by the evidence for an increased abundance of dolomite veinlets splaying off the Bisciarelle fault and crosscutting the host lherzolite for a distance of several meters from the fault contact (Figs. 77 a, b, c). The effect of these veinlets in the bulk rock analyses is that of *mass addiction*, that is introduction of an external contribution from mineral precipitation due to fracturing and mass advection

within the rock (cf., Reed 1997; Barnes H. L., 1997). In principle, mass addition may generate significant modifications to the protolith composition, which in turn results in a modification of the linear trends expected in case of diffusion of immobile components through the rock. From a practical standpoint, the evidence for some deviations from a perfectly immobile behaviour of Al2O3, TiO2, Y, and Ce in the RB10-RB1 lherzolite generates uncertainties in the evaluation of mass factors, and as a consequence, uncertainties in the calculated mass transfers. However, these uncertainties affect only the samples closest to the fault contact, and do not jeopardize considerations of element mobility for the remaining samples of the data set. For instance, the linear trends shown by the pairs Al_2O_3–TiO_2, Al_2O_3–Ce, and Al_2O_3–Y (Figs. 79 a, c; and by all REEs – not shown here) can only be generated by an immobile behaviour of these components in a regime of mass loss. Such behaviour is evident in the samples located away from the fault contact, whereas those marking a distance of about 2 m or less from the contact show significant departures from linearity. This implies that precipitation of dolomite, saponite, ilmenite, and rutile within the altered lherzolite (Fig. 80f) generated a systematic decrease of the concentrations of these components in the rock without a modification of their constant ratios up to about 2 m from the contact. Interestingly, a similar linear trend is shown by Al_2O_3–CaO (Fig. 79b), which implies that dolomite precipitation in most of the lherzolite took place in a regime of poor Ca mobility, i.e., the Ca necessary for dolomite deposition was provided mostly locally and not introduced externally by the fluid that permeated the fault zone. Loss of linearity for Al_2O_3–CaO and other plots related to the samples closest to the fault implies that Ca and all other components were introduced by *both* diffusional transport and mass advection (microfracture precipitation) in that portion of the host rock. In conclusion, mass transfer calculations referred to the most distal part of the profile allow definition of exact constraints on element mobility due to a dominant diffusional transport in the host rock. Calculations referred to the samples immediately adjacent to the fault – for which no immobility trends can be clearly identified – provide only semi-quantitative constraints due to the mixed contributions of diffusional and advectional types of mass transport (see below).

Compositional plots provide constraints on the geochemical behaviour of mobile rock components as well. The pairs Al_2O_3–SiO_2, Al_2O_3–MgO, and Al_2O_3–

Fe_2O_3 (Figs. 79f, g, h) show flat trends that are similar to each other because they correspond quite systematically to significant changes in Al_2O_3 concentrations without corresponding changes in SiO_2, MgO, and Fe_2O_3 (i.e., compositional plots are mostly parallel to the x axis of the plots). Notably, Al_2O_3 variations occur at both sides of the immobility lines, i.e., they correspond to both gains and losses within the lherzolite profile, and the only sample not following such trend is RB1 collected at the fault wall. In contrast, the Al_2O_3–LOI pair (Fig. 79e) shows a trend that plots systematically at one side of the immobility line, notably on the mass gain side. These trends imply that precipitation of dolomite, saponite, ilmenite, and rutile in the alteration halo took place during removal and addition of SiO_2, MgO, and Fe_2O_3 from neighbouring portions of the host lherzolite, i.e., without substantial contribution from an external fluid. At the same time, this alteration took place during substantial addition of volatiles, specifically CO_2 and H_2O, from an external fluid. These results are important; as they show that chemical components that were consistently added to the host lherzolite by the fault fluid were the volatiles (see also below), but not silica and other key components constituting the alteration assemblage. Indeed, the key components constituting these phases were either immobile/quasi-immobile (Al, Ti, Ca) or mobile only at the local scale within the lherzolite (Si, Mg, Fe). The evidence for the pairs Al_2O_3–SiO_2, Al_2O_3–MgO, and Al_2O_3–Fe_2O_3 of sample RB1 plotting at, or very close to, the immobility line (Fig. 79f, g, h) is consistent with this result.

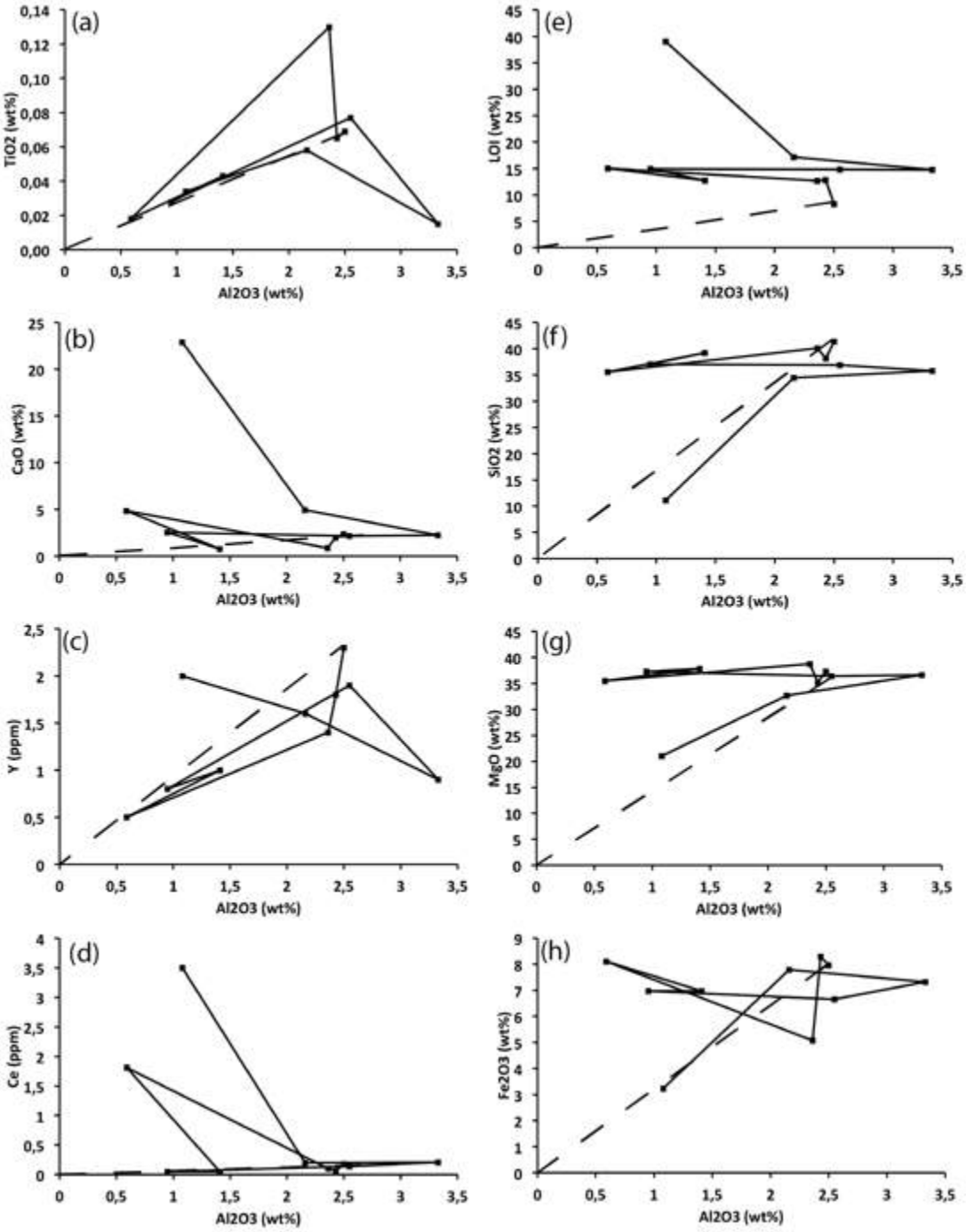

Figure 79: Comparison between concentrations of Al_2O_3 and concentrations of a set of rock components from the R10-R1 profile. Solid lines join adjacent samples. The dashed lines are not best fits, but simply connect the origin with the RB10 concentrations.

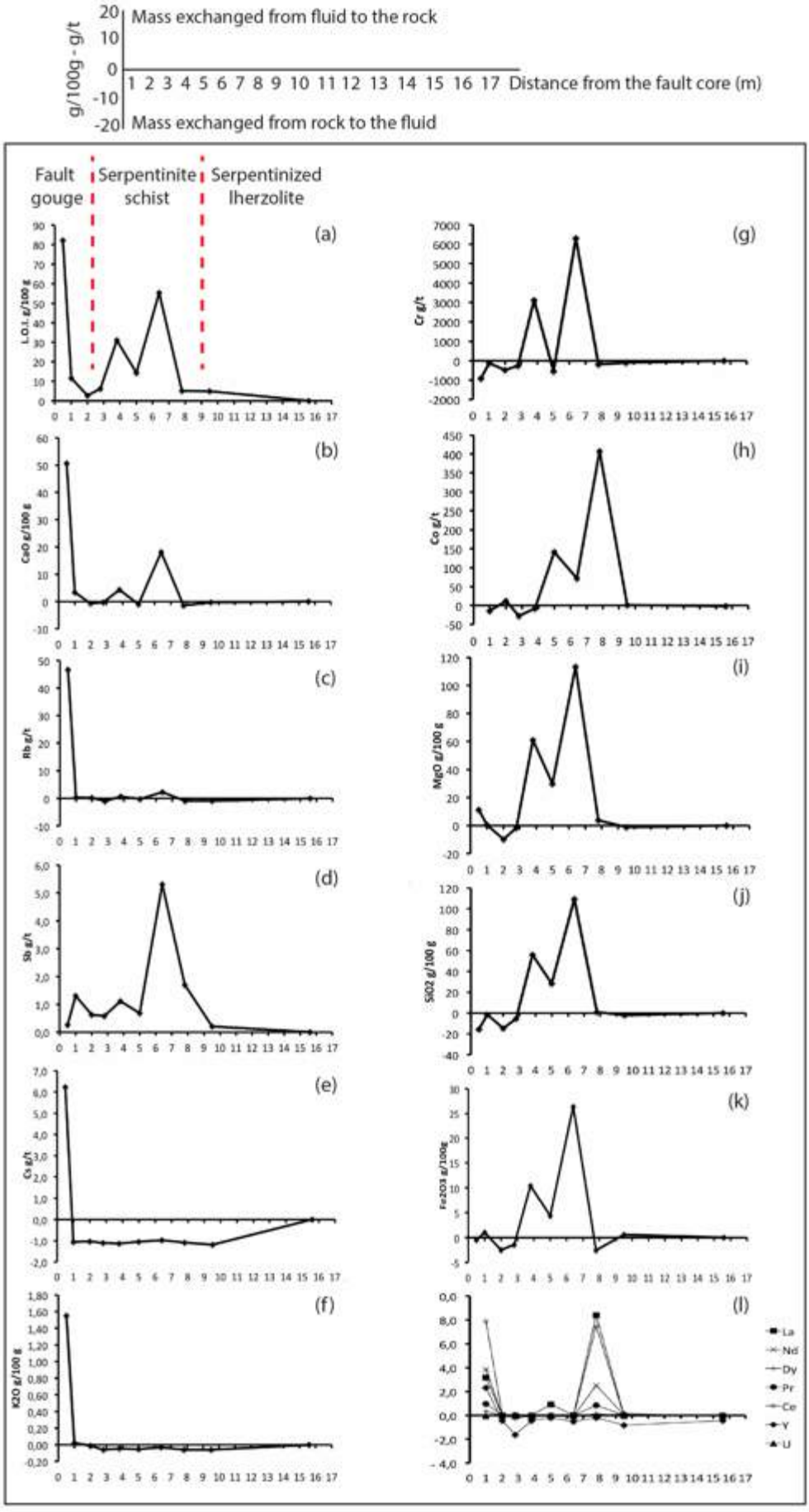
g/100g - g/t
20
10
0
-10
-20
Mass exchanged from fluid to the rock
1 2 3 4 5 6 7 8 9 10 11 12 13 14 15 16 17 Distance from the fault core (m)
Mass exchanged from rock to the fluid
Fault gouge
Serpentinite schist
Serpentinized lherzolite
(a)
L.O.I. g/100 g
(b)
CaO g/100 g
(c)
Rb g/t
(d)
Sb g/t
(e)
Cs g/t
(f)
K2O g/100 g
(g)
Cr g/t
(h)
Co g/t
(i)
MgO g/100 g
(j)
SiO2 g/100 g
(k)
Fe2O3 g/100g
(l)
La
Nd
Dy
Pr
Ce
Y
U

Figure 80: Mass changes of selected major, minor, and trace components of the lherzolite host rock reported as a function of distance from the fault core. Such plots define the "mass transfer profiles". At the top of the figure there is a simplified sketch.

The mass of components exchanged between lherzolite and fault fluid at Bisciarelle have been calculated using relation (2) and Al_2O_3 as immobile component (Method section). A representative selection of these transfers are plotted in Fig. 80, which shows how these transfers vary as a function of distance from the fault core. These plots form *mass transfer profiles* (Garofalo, 2004 a, b and reference therein), i.e., amounts of components per unit mass of protolith that were transferred from the fault fluid into the rock, or vice versa, during the dolomite, saponite, ilmenite, and rutile alteration. In principle, profiles in which mass transfers systematically increase their values at progressively closer distances from the fault identify components that were transferred from the fluid to the rock, whereas profiles showing systematically decreasing values identify components that were transferred from the rock to the fluid. Profiles in which mass transfers are both positive and negative, and do not show any systematic trend at progressively closer distances from the fault, refer to components that were only partly mobile during alteration.

In the RB10-RB1 dataset, the components showing profiles that are consistent with transfer from the fluid to the rock are the volatiles and Sb (Fig. 80a, d). Thus, at a distance of 8 m from the fault contact, about 5 grams of CO_2 and H_2O were added by the fluid to each 100g of lherzolite at the time of alteration, and at a distance of 1 m such transfer became about 12 grams (Fig. 80a). These values correspond to an increase of volatile mass of 63-140% with respect to the protolith, which is however less than the remarkable volatile addition calculated for the fault contact (>600%). As discussed above, a combination of diffusional transport and microfracture precipitation took place close to the fault, and this does not allow an evaluation of the true mass transfer adjacent to the fault. Therefore, the mass transfer values calculated close to the fault contact should be taken as semi-quantitative.

With regard to the other components that were systematically transferred from the fluid to the rock, Sb shows additions that vary between 0.2 and 5 g per ton of protolith (Fig. 80d), which correspond to very large additions (>100%). The vast

majority of all other components show profiles with mixed mass transfers corresponding to both additions and subtractions with respect to the protolith (i.e., positive and negative excursions of the profiles across the zero-mass-change line of Fig. 80). These mixed transfers are observed in major (SiO_2, MgO, Fe_2O_3; Fig. 80 j, i, k) and trace rock components (Co, Y, Cs, U; Fig. 7 h, e, l). Especially, this behaviour is highlighted by the two peaks that are consistently coupled within the interval 4.9-7.5 m from the fault core. These peaks correspond to the variable abundance of specific minerals within the rock, namely pyroxene remnants, carbonates, oxides, and discontinuous quartz veins, all of which occur along the foliation or in thin veins (<1mm in thickness) with a modal abundance that does not vary systematically Figure 4. Within the considered distance from the fault core, the coupled peaks mark the transfer from the fluid to the rock of SiO_2 (Fig. 80j), MgO (Fig. 80i), Fe_2O_3 (Fig. 80k), Ba, Nb, Ta, Sn, and U (not shown in Fig. 7), which are associated with the precipitation of carbonates and chalcedony veins within the damage zone of the fault (see chapter 8). In particular, the SiO_2, MgO, and Fe_2O_3 peaks may be mainly associated with the persistence of altered pyroxenes within the rock, while those of Cr (Fig. 80g), Sb and maybe also Co (Fig. 80h) could be related to a short-range mobilisation of oxides and sulphides along the foliation. Both small veins and short-range mobilisation with consequent re-precipitation are not homogeneously distributed and hence are not strictly related to the distance from the fault core.

8 – Mineralogical and chemical composition of the Bisciarelle creek fault rock

All the coherent samples of rock, taken in the field, are oriented samples in order to obtain oriented petrographic sections to be able to correlate the orientation of the kinematic indicators in section to the fault movement.

The thin sections, showed in figure below, are polished thin sections 60 μm thick, hence the interference colour could be different from those classical for the mineral described.

8.1 – Petrographic observations of the bedrock

The bedrock is made up of serpentinized lherzolite (RB10 sample) that shows typical textural features of the lherzolite (Fig. 81). It is made up of ortho- and clinopyroxenes, olivine, serpentine, and rare opaque minerals (<1 vol%). In thin section, different domains can be distinguished namely: *i*) domains made up of serpentine with ortho- and clinopyroxenes cores, partially replaced by serpentine along the edges (Fig. 81a). Both kinds of pyroxens also show serpentine replacement along the cleavage planes; *ii*) domains made up of serpentine with mesh textures with olivine core (Fig. 81b); and *iii*) domains made up of serpentine with bastite textures after pyroxenes replacement (Fig. 81c).

The serpentine occurs also in secondary veins that cut all the previous textures (Fig. 81a). The rare opaque minerals, rutile and ilmenite, occur along the serpentine mesh textures (Fig. 81d).

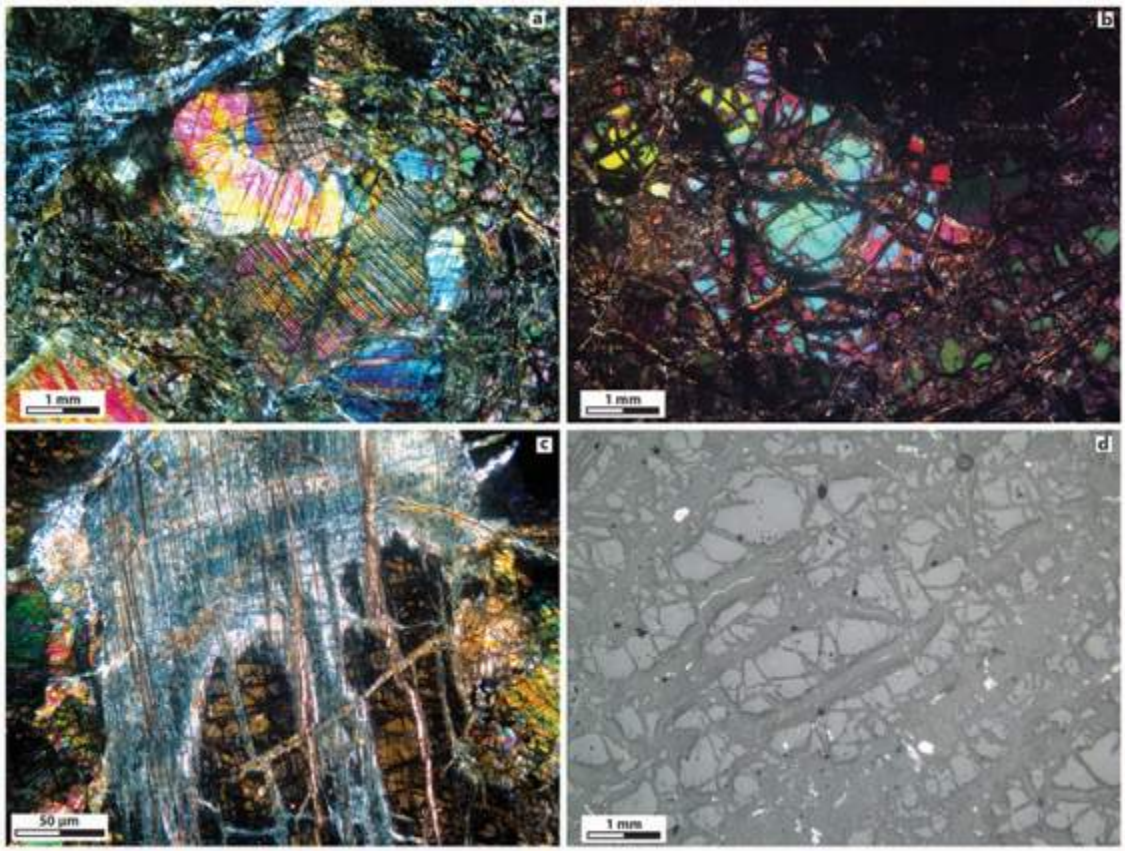

Figure 81: Petrographic images of the serpentinized lherzolite. (a) Ortho- and clynopyroxenes replaced by serpentine along the edges, in the section are also visible olivine remnants and secondary serpentine veins that cut all the previous textures (cross-polarised light). (b) Serpentine mesh texture with olivine core (cross-polarised light). (c) Serpentine with bastite textures after replacement of pyroxenes along the cleavage plane, the core is yet well preserved (cross-polarised light). (d) The rare opaque minerals along the serpentine mesh textures (reflected-light).

8.2 – Petrographic observations of the hanging-wall fault rock

The damage zone in the hanging-wall is made up of serpentinites and serpentinite schist (for field details refer to chapter 5.3.4.1). The thin section of serpentinite samples closer to the serpentinized lherzolite (RB9, 8), are unaltered and show a foliation boudinage along which remnants of ortho- and clynopyroxenes are present and are re-oriented along the foliation (Fig. 82a). Opaque minerals, mainly ilmenite and rutile, are aligned along the foliation (Fig. 82b). Parallel to the foliation, sometimes, extensional syntaxial carbonates veins are presents, up to 0.2 mm in thick (Fig. 82c).

In thin sections (sample RB7, 6, 5, 4; Fig. 55, paragraph 5.4.3.1) the serpentinites show mylonitic textures characterised by microlithons (Passhier and

Trouw, 1998) showing a sense of shear that reflects the fault movement with a top-to E-NE (Fig. 82d). In the section remnants of ortho- and clynopyroxenes almost completely replaced by serpentine are present.

The thin section of the sample RB2 (Fig. 55, paragraph 5.3.4.1) shows angular to sub angular clasts mm in size (Fig. 82e). Despite the sample RB2 is relatively close to the fault core (1 m), no carbonates are presents.

At the microscopic scale, the host rock adjacent to the fault core (RB1 sample, Fig. 55, chapter 5.3.4.1) is a poorly coherent carbonates level. In thin section the sample is made up of cataclastic sub-angular to well round dolomite grains (Supplementary material S7: RB1 XRD analysis), these grains are fine-grained and randomly oriented (Fig. 82f). Dolomite grains are surrounded by emerald green saponite (Supplementary material S7: RB1 XRD analysis), which makes a dark felt around the carbonates.

The foliation, visible on the field and on the sample, in thin section is poorly recognizable and only few dolomite veins mark it. These veins do not preserve growth evidence, are up to 0.3 mm thick, and along the vein-walls are yellowish whereas in the central part are whitish. In most cases these veins are fractured and randomly re-oriented.

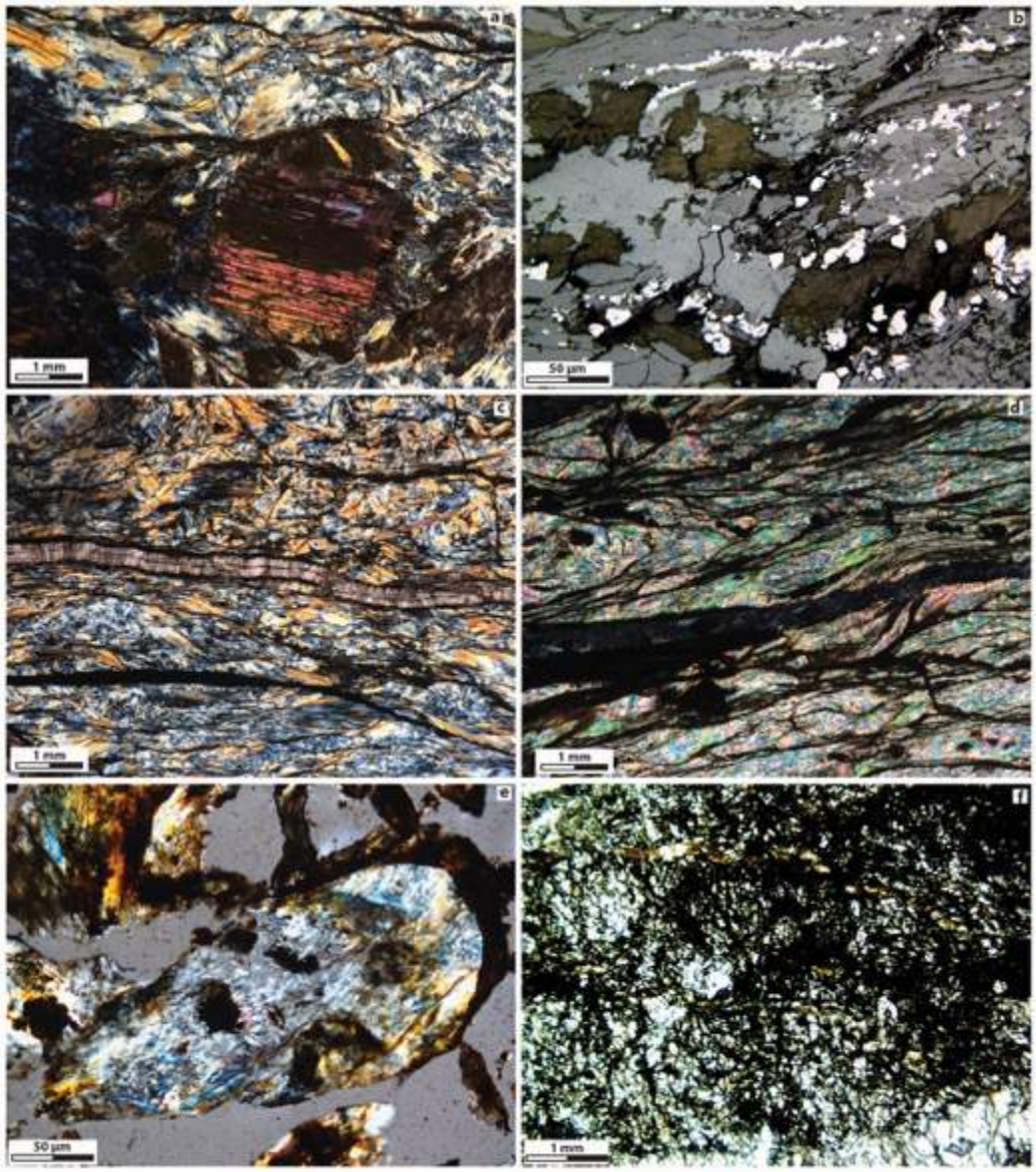

Figure 82: Thin sections of hanging-wall fault rocks. (a) Remnants of pyroxenes re-oriented along the foliation (cross-polarised light). (b) Opaque minerals aligned along the foliation (reflected-light). (c) Extensional syntaxial carbonates veins parallel to the foliation (cross-polarised light). (d) Mylonitic textures characterised by microlithons (cross-polarised light). (e) Serpentinites gouge, showing angular to sub angular clasts (cross-polarised light). (f) Cataclastic sub-angular to well round dolomite grains (plane-polarised light).

8.3 – Petrographic observations and chemical composition of the fault core from SEM-EDS analysis

Petrographic observations confirm that the fault core is essentially made up of two zones having distinct textural and compositional properties (Fig. 83, 84). One is the zone hosting the carbonate and the other is the chalcedony, present as filling in the vuggs between fault pearls and in shear veins that crosscuts the carbonate zone (Fig. 83).

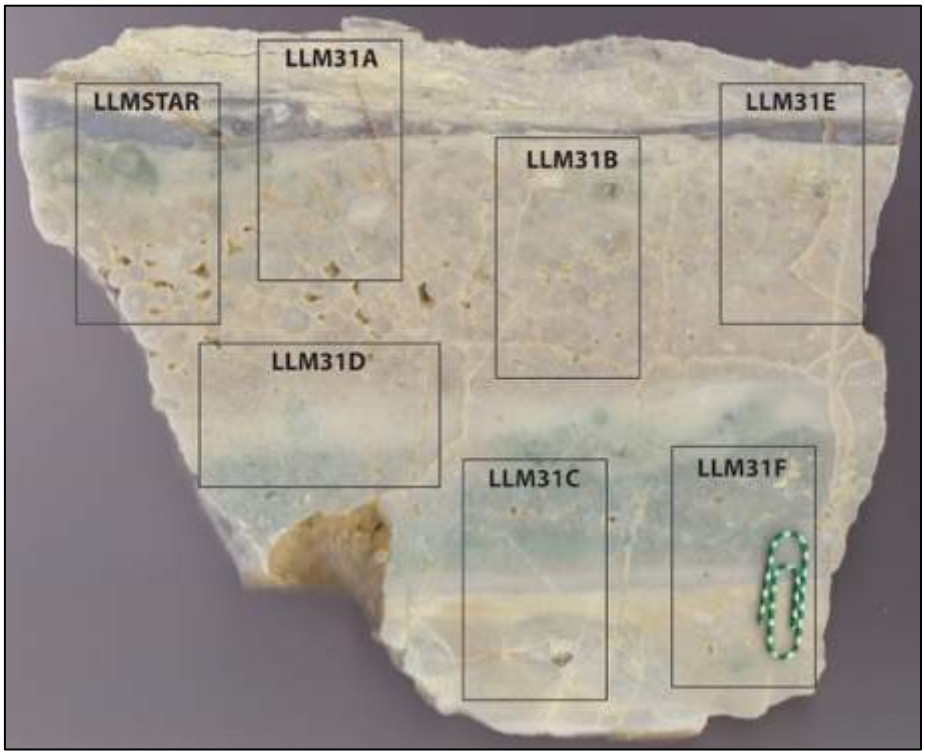

Figure 83: Location of sections of LLM31 sample.

The first zone is mostly made by fault pearls, made up of ferroan dolomite, even if a more complex mineralogical composition is suggested by the juxtaposition of a large number of heterogranular and concentrically zoned carbonate-coated grains set within a dark matrix (see below, Fig. 84). In contrast, the chalcedony zone is texturally massive and compositionally more homogeneous.

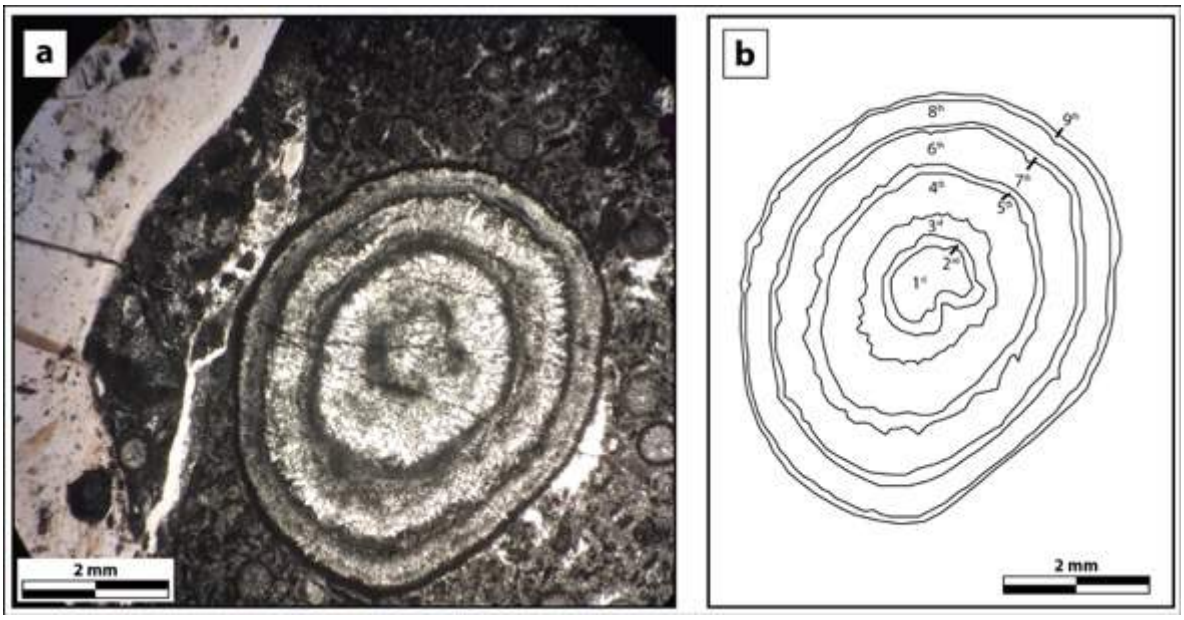

Figure 84: Textural characteristics of the sample LLM* analysed via LA-ICPTOFMS and a set of other analytical techniques (a): Large fault pearl developed at the contact with a chalcedony layer of the fault. Note that the contrast between fibrous texture of the thickest concentric layers and the more massive and darker thin layers (plane-polarised light). (b): Schematic representation of the largest fault pearl, which is made of nine concentric layers.

The fault pearls show distinct textural developments and are variable in size (see paragraph 5.4.1). Their core is made of, in decreasing order of abundance: *i*) coarse radial carbonates crystals (Fig. 85a, 60%), *ii*) fine grained carbonate (30%), *iii*) clast of fractured carbonated-coated grains (Fig. 85b, up to 4 mm; 6%), and *iiii*) relic of carbonated serpentinite clast (Fig. 85c, up to 4 mm, 4%).

The largest fault pearls show a complex internal texture whereas the smallest ones show a simpler and more massive internal texture. Large fault pearls are made of relatively thick (up to 8 mm) and fibrous dolomite bands that alternate regularly with thinner (up to 2 mm), massive, and partly laminated dark carbonate bands. Several alternations (up to 9 in Fig. 84, but up to 18 in Fig. 85a) of these levels can be identified in the larger fault pearls. Grain size reduction is visible between the fibrous and laminated bands. Smaller fault pearls show in general a thin and massive external carbonate rim that borders a fibrous dolomite core. Only rarely small grains show multiple alternations of massive and fibrous bands.

Both large and small fault pearls have a surprisingly regular round shape, showing that only mineral precipitation controlled their shapes. Also, there is no

close packing, no indentation or pressure solution evidences between different grains of the smallest fault pearls in the sample because carbonates and in part chalcedony occupy the volume between distinct grains. This demonstrates that, in general, fault pearls did not grow in contact with each other within the fault rock, and that no or only poor friction was active between them.

Inside several fault pearls structures (Figs. 86a, b, c; 87a) and in several carbonate single crystals (Fig. 87b), BSE- and SE-SEM images highlight porosity between different fault pearls bands (Fig. 86b), especially inside the dark laminated ones, or skeletal porosity inside the crystals core or along crystal boundaries, that should be related to decarbonation processes during fault slips. The SEM images highlight the epitaxial concentric growth bands of the fault pearls (Fig. 86b, c, d; 87a), and it is especially evident from the textural relations between the large and thick dolomite bands that depart radially from the cores of the fault pearls and the successive outer bands. The thick bands are made of aggregates of zoned dolomite prisms, which grow with a plumose texture from the core towards the outside (Fig. 86b). These thick bands terminate at thin and massive bands, but the successive plumose bands grow along the same radial directions, showing a clear epitaxial (or hetero-epitaxial) growth of fault pearls. Specific characteristics of the pearl layers are the textural relationships between fault pearls and outside matrix, which grow also epitaxially.

fault pearls with clast of fractured carbonated-coated grains core are slightly rounded, and show: i) a carbonatic microbreccia in the central part (Fig. 85b), or ii) clast of fractured fault pearls (Fig. 86c). The clasts of the microbreccia are angular and non-oriented. The central part is then reworked as the other fault pearls, and shows several alternations of thick and fibrous dolomite bands that alternated to regularly with thinner, massive, and partly laminated dark carbonate bands. Generally, these kinds of fault pearls are near the contact with chalcedony shear vein or along secondary slip zones.

fault pearls with carbonated central serpentinite clast (Fig. 85c) are the rarest of all, and are like the clast-cortex aggregates described by Rempe et al. (2014). The serpentinite clast is used as core grains overgrown by several alternations of thick and fibrous dolomite bands that alternated regularly with thinner, massive, and partly laminated dark carbonate bands.

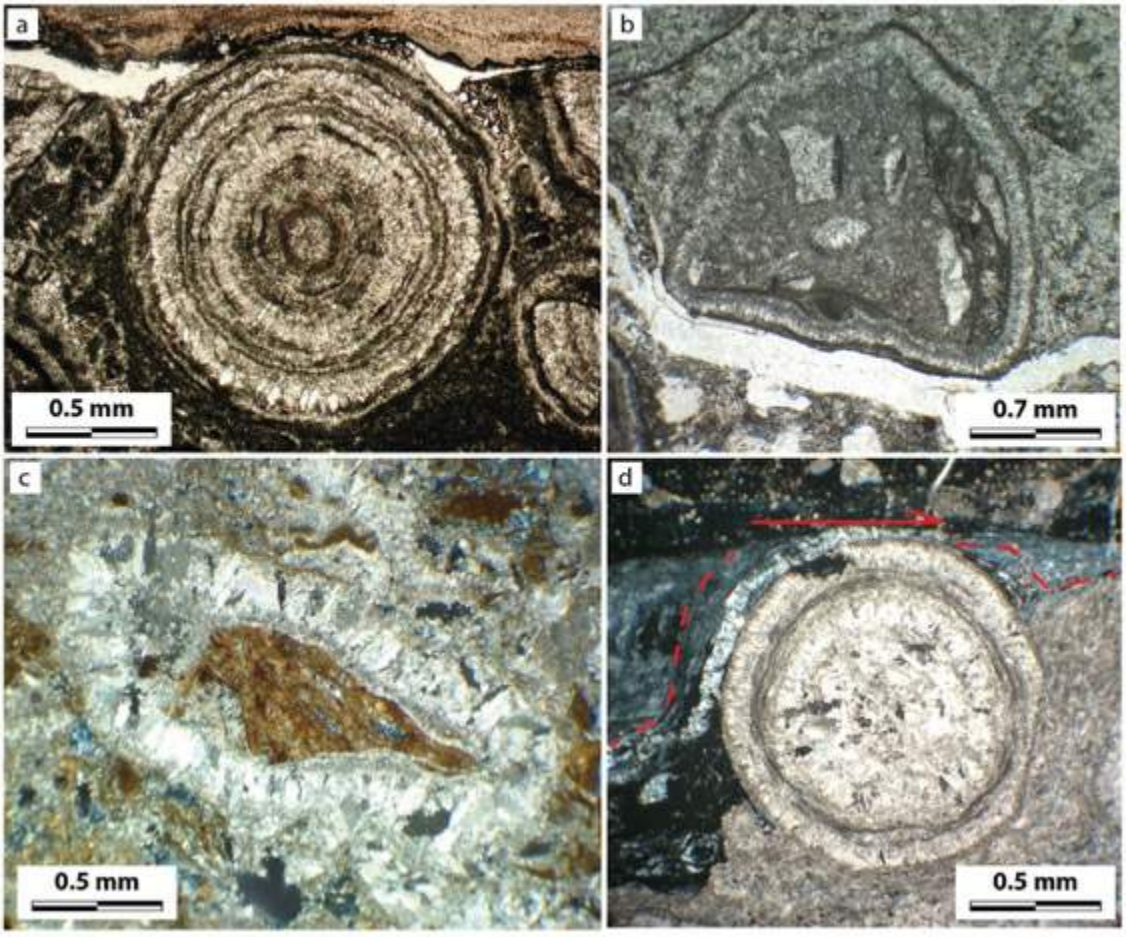

Figure 85: fault pearls types. (a) Fault pearl with central carbonatic core and several concentric layers (up to 18). (b) Fault pearl with microbreccia core. (b) Fault pearl with carbonated serpentinite clast. (d) Fault pearl near the contact with chalcedony shear vein. The red dashed line highlights the dark lamination, which indicate a dextral sense of shear.

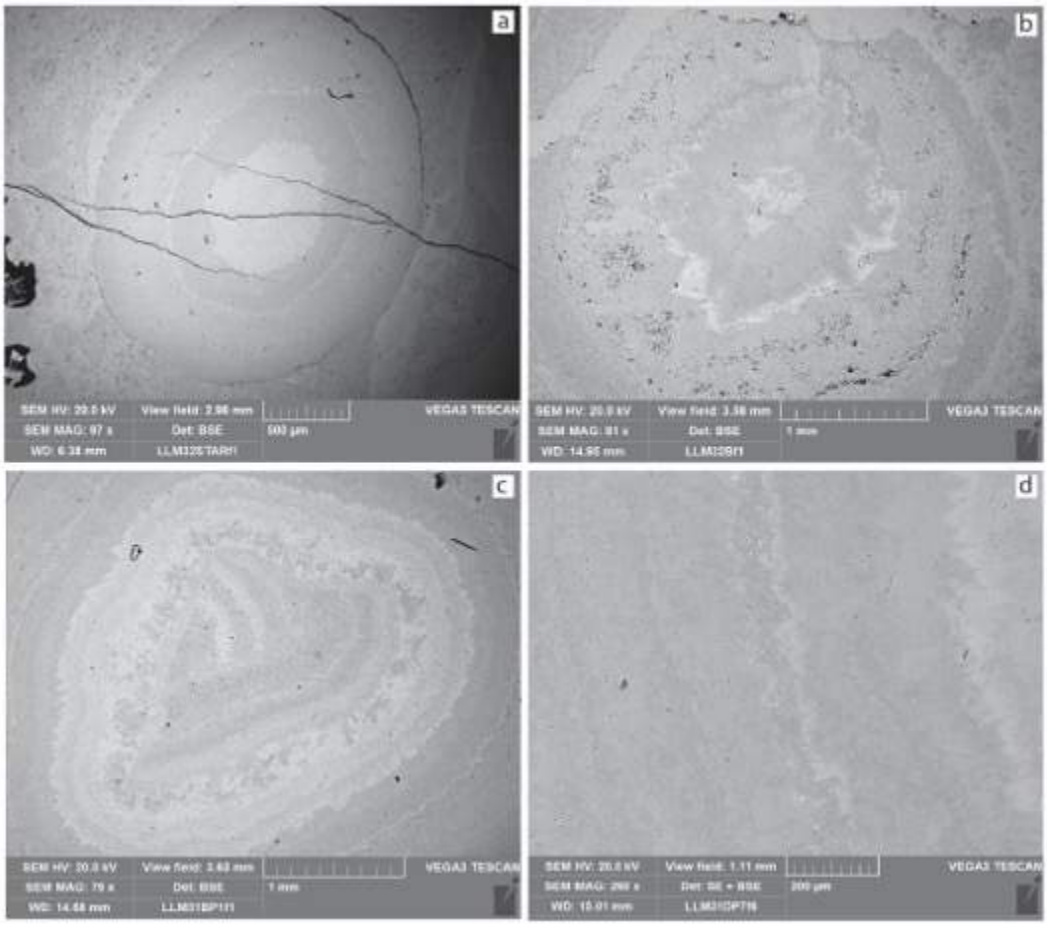

Figure 86: SEM images of fault pearls. (a) BSE image of fault pearl with coarse radial carbonates crystals core. (b) BSE image, magnification of the core; this image, also, highlight porosity between different bands of the fault pearl. (c) BSE image of fault pearl with a clast of fractured fault pearls. (d) SE+BSE image, magnification of the levels of the fault pearls.

Several fault pearls show, near the contact with chalcedony shear veins, evidence for rotation, marked by dark lamination (Fig. 85d) with a dextral sense of shear, in accordance with the general thrust movement.

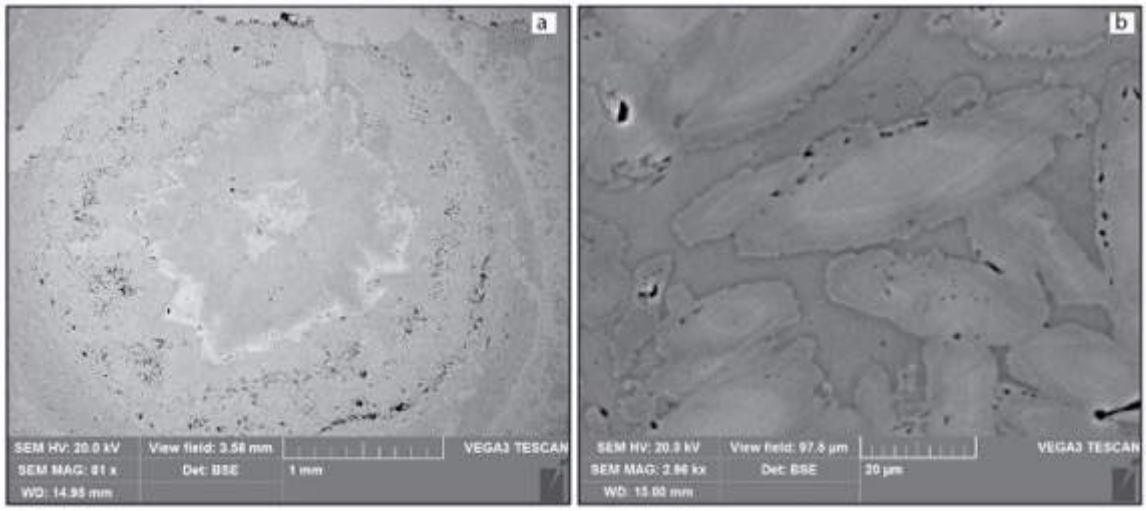

Figure 87: SEM images showing high porosity. (a) High porosity along carbonates bands inside fault pearls, especially inside the thinner, more massive and dark laminated bands (BSE-SEM image). (b) Zoned single dolomite crystals, with evident skeletal porosity along crystal boundaries. The zonations are due to high contrasted conditions (BSE-SEM image).

The Bisciarelle fault rock is made of fault pearls of different dimensions set in a micro- or cryptocrystalline matrix made up of dolomite and chalcedony. The contacts between carbonate-coated grains and matrix show clear epitaxial textures, sometimes between dolomite and chalcedony.

The main mineralogical constituents of the fault pearls are dolomite, with subordinate calcite (Fig. 88). These phases are euhedral and optically continuous within the fault pearls, and their dimensions are different from those of the matrix dolomite. Dolomite is volumetrically the most abundant mineral of the carbonate-coated grains, and precipitates several times with slightly different compositions within individual grains. Due to these moderate compositional variations, the SEM images of the fault pearls (Figs. 86, 87) have been set with the highest possible contrast, and as a consequence the images may show some artefacts.

Within individual fault pearls, dolomite shows little variations of FeO contents, sometimes below the limit of detection of SEM-EDS analyses (see below). Indeed, the measured range of CaO concentrations in all analysed fault pearls is 28-31 wt%, MgO: 19-22 wt%, and FeO: 0.65-3 wt%. Thus, the distinct zonation from core to rim that is clearly evident in all petrographic and BSE images (Figs. 83a, d; 84a) do not correspond to significant variations of major element concentrations of single dolomite crystals, but rather to variations of minor and trace components.

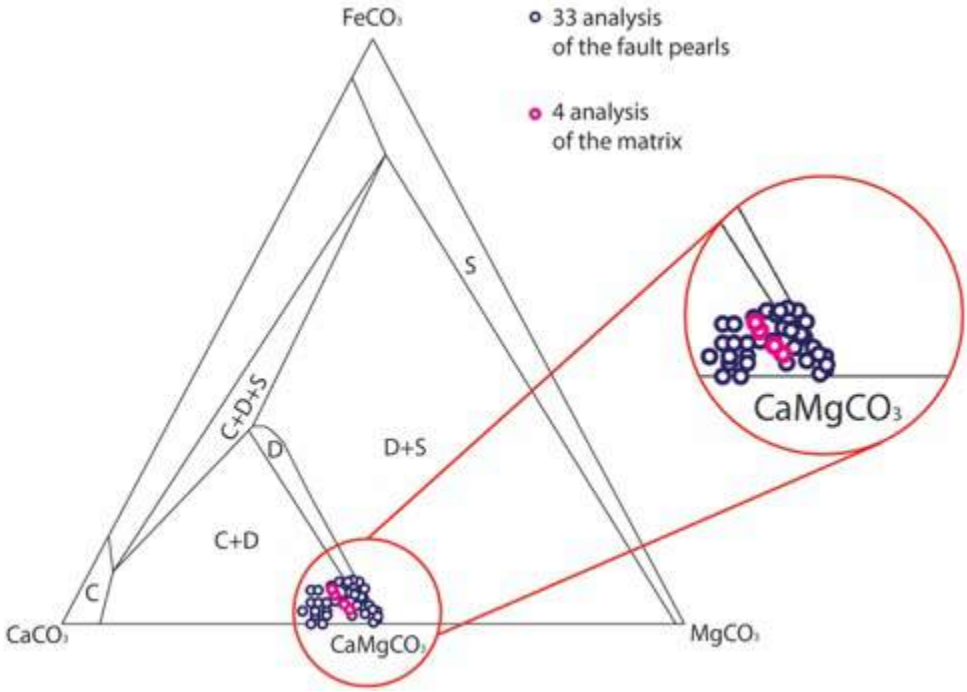

Figure 88: experimental stability fields at 450°C of carbonates belonging to the system FeCO3-CaCO3-MgCO3 (modified after: Rosenberg, 1967). Blue circles are the analyses of fault pearls, whereas the purple circle represents the analyses of the matrix. S= magnesite-siderite solid solution; D= dolomite; C=calcite.

The matrix of the fault rock is made by an assemblage of fine-grained, euhedral dolomite and anhedral chalcedony and quartz (Figs. 89; 90a, b; 91a, b, c, d). The dimensions of individual crystals of dolomite here are from mm to sub-mm, and they tend to have a prismatic habitus, whereas the dimensions of the quartz grains and chalcedony are from sub mm to μm (Fig. 90e, f).

Within the matrix between the fault pearls, (Supplementary material S9: SEM-EDS analysis) dolomite shows little variations of FeO contents, sometimes below the limit of detection of SEM-EDS analyses (see below). Indeed, the measured range of CaO concentrations in the analysis is 29-29.77 wt%, MgO: 21-21.87 wt%, and FeO: 0.88-0.93 wt% (Fig. 88). In general, these carbonates are Mn-poor, but in four spot analyses I determined a MnO range of 0.18-0.41 wt%.

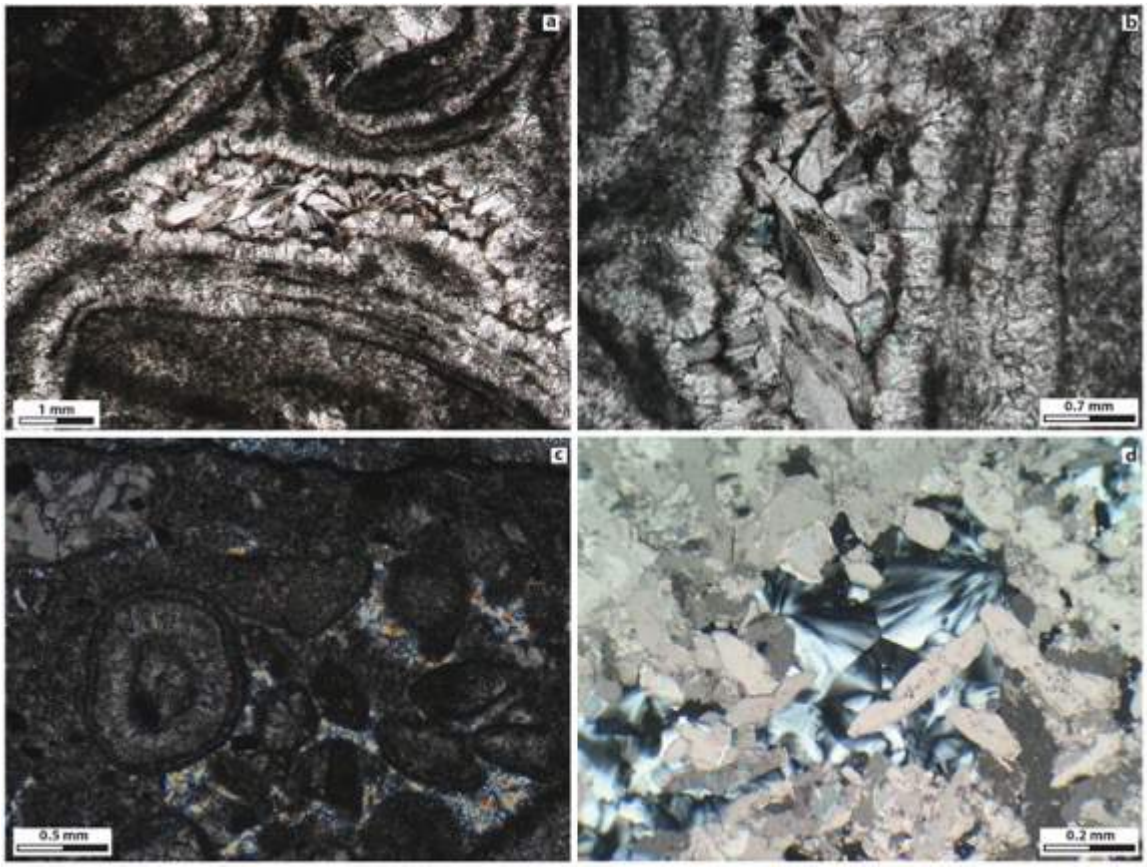

Figure 89: Matrix and vuggs between the fault pearls, the photographs are in cross-polarised light. (a) Dolomite filled vugg. (b) Magnification of dolomite crystals of Fig. a; they show central phantoms with high porosity. (c) Chalcedony filled vugg. (d) Magnification of the chalcedony with fibrous textures inside a vugg.

Chalcedony that occupies anhedral vuggs between the fault pearls can be distinguished into several textures namely: *i*) moss-textures (Fig. 90a), *ii*), fibrous radial (Fig. 90b), *iii*) wall lining with central jigsaw texture (Fig. 90c), and *iiii*) flamboyant textures (Figs. 90d, e), but the characteristic that is shared by all the structures is the high porosity (Fig. 10d, e). This porosity can be related to an initial deposition of hydrated silica gel, and linked to the crystallization and subsequent fluids release. Particularly, moss-textures, occurs as isolated spheres and, accordingly to Moncada et al. (2012), are developed by surface tension effects when silica gel nucleates on impurities suspended in solutions. These are spherical micro-textures with radially fibrous chalcedony (Fig. 90a). Flamboyant textures are fibrous aggregates forming a radial pattern (Figs. 90d, e). This indicates different growth stages in its development. It began with the inner circle and then moved to outer part. These textures are thought to develop from aggregates of

fibrous chalcedony with rounded external surfaces, which originate as silica gel and then recrystallized. Wall lining and massive chalcedony can be found both in the small voids between fault pearls and in shear veins. In the central part of the chalcedony (Fig. 90c) jigsaw textures are present. These textures are characterised by microcrystalline to crystalline aggregates with interpenetrating boundaries. All these type of silica contains no useful fluid inclusions. Particularly in fig. 90e is also shown a detail of the contact between the termination of a carbonate-coated grain and the outside chalcedony matrix. With its round shape, the delicate thin layer of chalcedony, at the immediate contact with the carbonate-coated grains, mimics the prismatic habitus of the dolomite, showing a clear epitaxial growth.

The fault pearls are cut by two types of chalcedony-rich shear veins, which we named VA and VB.

VA veins are made up of chalcedony with carbonate angular clasts (up to 30 vol. %) and occur at the upper contacts of the grain-rich levels (Fig. 91a). In thin sections VA veins are made up almost entirely of fine to ultra-fine grains (200 microns, 91c) with dispersed textures that resemble moss, jigsaw, flamboyant (*sensu* Moncada et al., 2012), which indicate flashing of the fluids, and fibrous textures. Linked to VA, mm injection-veins are also present (Fig. 91e); they are made up of angular to sub-angular micro-carbonate clasts (up to 1.5 mm) and carbonated-coated grains (up to 0.5 mm) with chalcedony and fine-grained quartz matrix (500 microns). VB veins are entirely made up of chalcedony and occur at the top of VA (Figs. 91b, d).

These textures, under scanning electron microscope investigations show non-oriented high porosity probably related to the recrystallization over a hydrous precursor accordingly to Moncada et al., (2012).

A 2-3 mm thick layer of dolomite-rich matrix marks the contact between this band and the carbonate-coated grains. This banding provides a strong control on the chemical composition of the fault rock.

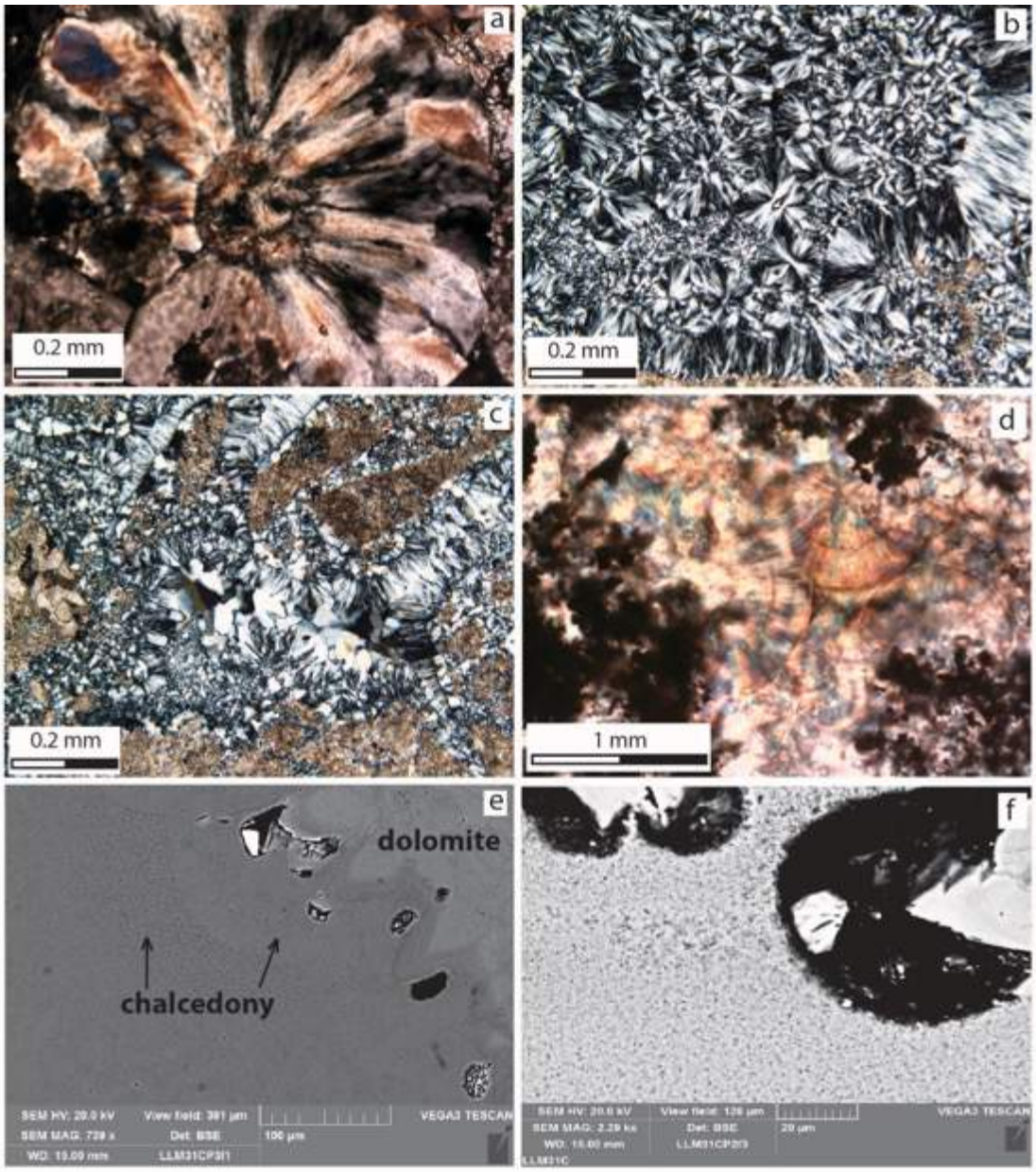

Figure 90: Chalcedony microstructures. (a) Photomicrograph of moss-textures, the diameter of the sphere is 1 mm. (b) Photomicrograph of fibrous radial chalcedony. (c) Photomicrograph of wall lining chalcedony. In the central part of the photomicrograph can be recognized jigsaw textures. (d) High porosity inside chalcedony matrix along shear vein (BSE-SEM image). (e) Micro-porosity in chalcedony in volume between distinct fault pearls (SE-SEM image), and evidence of epitaxial growth at the immediate contact between the dolomite crystals and the massive chalcedony.

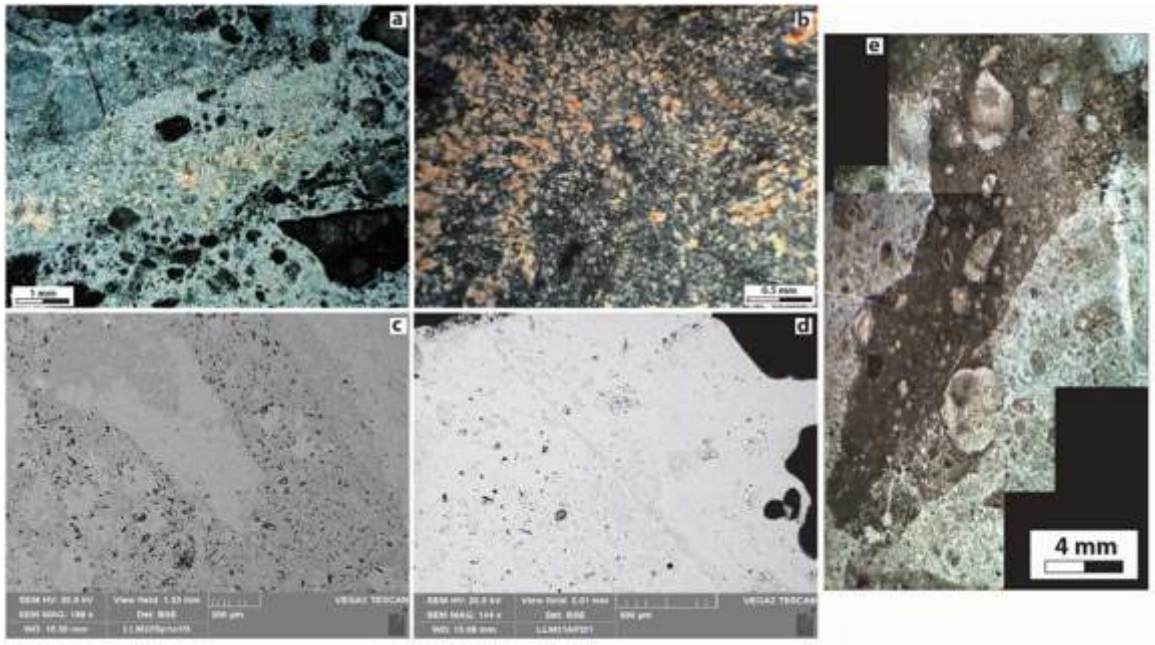

Figure 91: (a) VA vein in thin section, cross-polarised light. (b) VB vein in thin section, cross-polarised light. (c) SEM-BSE image of chalcedony shear vein VA. Dolomite angular to sub-angular clasts are visible surrounded by the chalcedony matrix. The chalcedony here is massive and shows high non-oriented porosity. (d) SEM-BSE image of chalcedony shear vein VB. (d) Injection vein with angular to sub angular clasts, surrounded by micro crystalline quartz.

Petrographic observations show that the chalcedony documented within the shear vein and in the enclaves constrained by neighbouring carbonate-coated grains is devoid of fluid inclusions.

Similar to the carbonates of the fault pearls, this chalcedony has also a constant composition. Its SiO_2 concentration ranges between 99.87 and 100 wt%; but in some spot analysis carried out in the moss texture (Fig. 87a) SiO_2 ranges between 90 and 92 wt% and Al_2O_3 between 0.10 and 0.3 wt% (Supplementary material S9: SEM-EDS analysis) the rest consists of volatiles (H_20, since close to the spot area carbonates are not present).

Clear evidence for friction occurs along secondary slip surfaces in carbonate (Fig. 93a, b), chalcedony shear surfaces (Fig. 93c, d), and between the carbonate and chalcedony zones shown by contact a 2-2.5 mm-thick level of micro-breccia at their contact (Fig. 81, 87a).

Secondary carbonate slip zones show intense comminution, and in thin section they appear as dark, highly porous, and micro- to cryptocrystalline layers. The high porosity of the secondary carbonate slip zones could testify recrystallization after carbonate thermal decomposition. These slip surfaces are extremely smoothed like mirror-like slip surface, and marked by micron sized slickenlines (250 micron in

thickness) and chatter marks (Fig. 93a), and show sub-micron (from 200 nanometer to 1 micron in diameter) carbonate grains coating over all the surfaces (Fig. 93b). Only few grains are interested by cataclasis developing a fine crush breccia with angular to sub angular clasts (up to 5 mm). The fine crush breccia clasts are recycled by different subsequent episodes of carbonate coatings, being the core of new carbonated-coated grains.

The tops of chalcedony shear veins are blistered and marked by slickenlines and grooves from sub-millimetre to micron in size (200 microns, Fig. 93c). The striking feature of these slip surfaces is the presence of sub-micron (150 nanometer) idiomorphic quartz surrounded by filamentous silica matrix. The filamentous silica (Fig. 93 d) is similar to what described by Verberne et al., (2014) and Hayward et al., (2016) as linked to mechanical amorphization due to seismic slip.

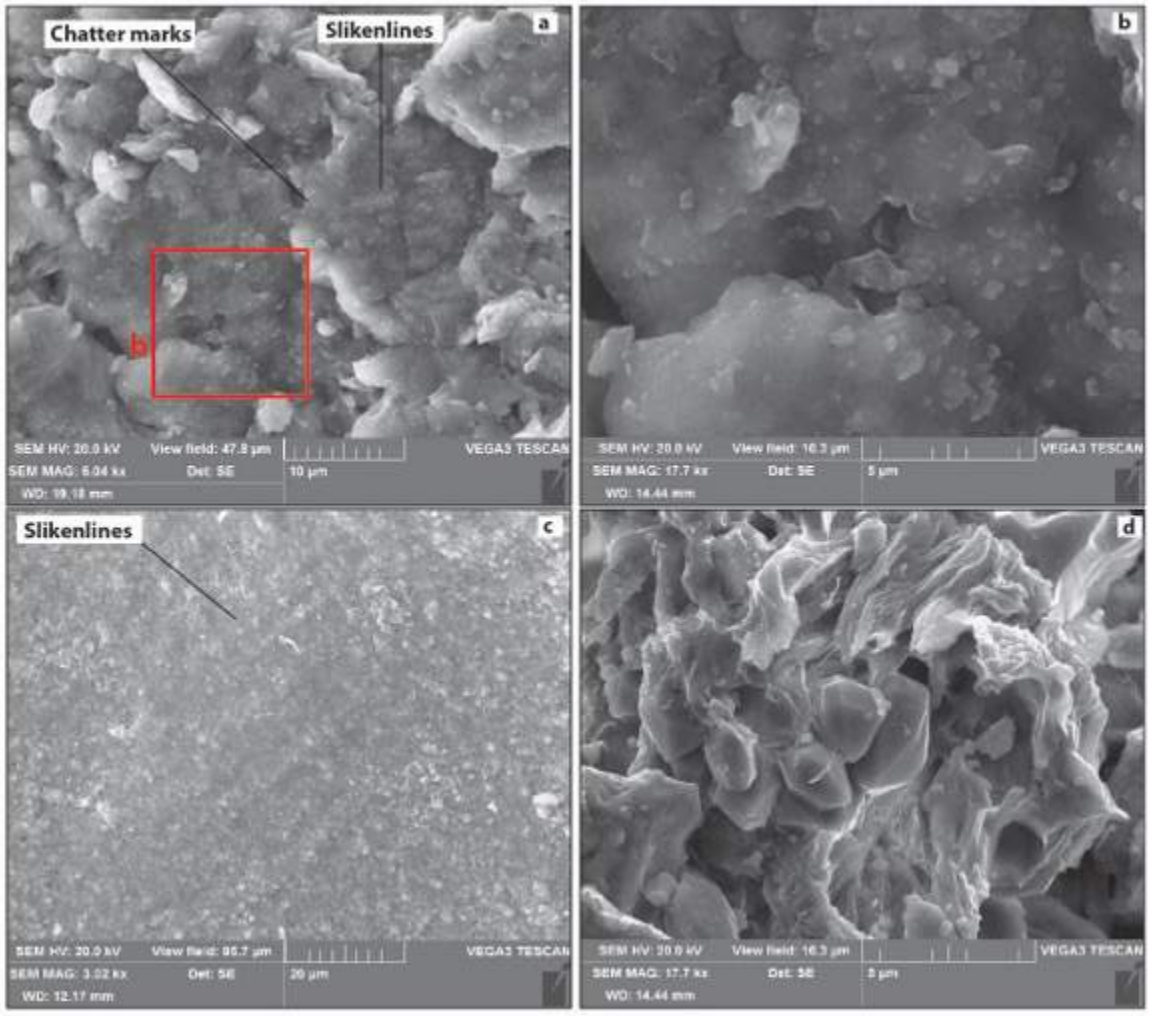

Figure 92: Micro textural characteristics of slip surfaces (SE-SEM images). (a) Carbonate slip surface marked by micrometric chatter marks and slickenlines. The red square indicates figure b area. (b)

Magnification of figure a, it shows micrometric to sub-micrometric-grained carbonate coating. (c) Chalcedony slip surface marked by micrometric slickenlines. (d) Chalcedony shear surface marked by idiomorphic quartz surrounded by filamentous silica matrix.

8.4 – Chemical composition of fault rock from LA-ICPTOF-MS elemental imaging

A detailed reconstruction of mineral and chemical compositions of the Bisciarelle fault core rock must take into account the possible variability of chalcedony and carbonates. An analytical challenge is the fact that chalcedony is very fine-grained and hence difficult to be analysed by single-spot analyses (20 μm diameter). Another question is the evidence for poor compositional variability of the carbonates, which cannot be defined by variations of major components.

The innovative technique that we use here to capture variations of trace element concentrations in rocks and minerals is elemental imaging via LA-ICP-TOF-MS (Gundlach-Graham et al., 2015). With this technique, we analysed a 10000x10000 μm subset of sample LLM*. The results of these analyses are high-resolution (10 μm), large-format (1 cm^2) compositional images of the major-, minor-, and trace elements in the sample (Figs. 94, 95, 96, see chapter 6 for details on analytical acquisition and limits of detection of this technique).

The LA-ICP-TOF-MS elemental imaging confirms the evidence for a substantially constant composition of fault pearls, chalcedony, and matrix of the fault rock; however, it adds also new surprising details on the spatial distribution of minor and trace elements, which together make the concentric banded texture of fault pearls. Thus, elemental imaging confirms the SEM evidence for the fault pearls dolomite having invariably high concentrations of CaO (25-30 wt%, Fig. 94b) and MgO (20-25 wt%, Fig. 94c), but the proportions of the minor and trace elements vary significantly within the round and concentric fabric, and in part also between fault pearls of different size. Similarly, SiO_2 concentration in chalcedony is 98-99% wt% (Fig. 94a) but it is spatially variable and coupled with variations of a significant number of minor and trace components.

In order of abundance, important minor and trace constituents of the large fault pearl of Figs. 94, 95, 96 are SiO_2 (<10 wt%, Fig. 94a), FeO (1-3 wt%, Fig. 94d), Al_2O_3 (0.2-0.3 wt.%, Fig. 94f), K_2O (<0.3 wt%, Fig. 94g), MnO (300-1000 μg/g, Fig. 94h),

SrO (300-700 μg/g, Fig. 94i), Ni (100-450 μg/g, Fig. 95a), Cr (150-200 μg/g, Fig. 95b), Cu (<80 μg/g, Fig. 95c), Co (5-35 μg/g, Fig. 95d), W (2-12 μg/g, Fig. 15f), Cs (4-10 μg/g, not shown), Y (3-4 μg/g, Fig. 95i), and Pb (2-4 μg/g, not shown). The spatial distribution of these chemical components varies in a systematic way, as the thin and massive dolomite bands of the fault pearl are consistently enriched in SiO_2, Al_2O_3, K_2O, Mn, Co, Pb, Cs, Cr, Y, and Cu with respect to the large, fibrous bands. In contrast, the fibrous dolomite has relatively higher concentrations of FeO, Sr, and W. The large number of metals systematically enriched within the thin bands explains their relatively dark interference colours and reflective features documented at all scales with different analytical techniques (Fig. 85, 86, 87). Also, the occurrence of a larger proportion of silicate constituents (Si, Al, K) – rather than carbonate constituents – within the thin bands demonstrates that the latter have probably a complex mineralogical composition.

The correlation between the fault pearls fabric and the corresponding trace element composition is not the only characteristic feature of this fault rock. The smaller and texturally more massive fault pearls have fabric and chemical compositions that are in part different from those of the larger pearls. Indeed, similar to large fault pearls, small pearls show a central core having concentrations of Al_2O_3, FeO, K_2O, MnO, and W, and alternations of thin bands with distinct Ni, Ba, and Sr compositions. However, the small fault pearls are in general massive and lack the compositional banding generated by the thin, metal-rich layers (especially, they lack bands with higher Co, Mn, U, and Y concentrations).

Although the level of chalcedony of sample LLM* is made for the most part by silica, it hosts a large number of minor and trace components (Figs. 95, 96). Such components are in general disseminated within chalcedony, rather than locally concentrated, demonstrating that these elements are diadochical within the SiO_2 structure and do not constitute separate phases. Important minor elements are Na_2O (0.1-1.2 wt%, Fig. 94e), K_2O (0.2-0.6 wt%, Fig. 94g), and Al_2O_3 (0.2-0.3 wt%, Fig. 94f) and important trace components are Ni (100-500 μg/g, Fig. 95a) and Cr (100-450 μg/g, Fig. 95b). A number of other additional components are present with a lower range of concentrations (Figs. 95c, i) ranging between hundreds to few μg/g (Ti: 200-800 μg/g; Co: 10-50 μg/g; Sc: 20-70 μg/g; Mo: 10-35 μg/g; Pb: 4-9 μg/g; Sb: 4-18 μg/g; Nb: 2-6 μg/g; Ta: 0.2-0.6 μg/g; Th: 0.2-0.6 μg/g; U: 0.4-1 μg/g; Sn: 10-30 μg/g; Zr: 4-12 μg/g; In: 1-3 μg/g). Peculiar trace elements to

highlight within chalcedony are Ag (4-12 μg/g, Fig. 95g) and a set of other elements that occur exclusively within this phase. These are As (50-80 μg/g, Fig. 96a), Cd (30-50 μg/g, Fig. 96b), Ga (20-25 μg/g, Fig. 96c), REEs (e.g., Gd, Nd, and Dy, Figs. 96d, e, f), Re (1.5-2 μg/g, Fig. 96g), Hf (1.4-2 μg/g, Fig. 96h) and Ce (1.5-2 μg/g, Fig. 96i).

The micro-breccia at the contact between the chalcedony shear vein and the fault pearls contains ferroan-dolomite. Single spot SEM-EDS and LA-ICP-TOFMS analyses show that, in addition to CaO (15-30 wt.%, Fig. 94b) and MgO (15-25 wt.%, Fig. 94c), this dolomite hosts 1-2 wt.% of FeO (Fig. 94d) with relatively high concentrations of Mn (600-1000 μg/g, Fig. 94h). Important minor components are Na_2O (0.2-0.4 wt.%, Fig. 94e), K_2O (0.2-0.3 wt.%, Fig. 94g), Al_2O_3 (0.1-0.2 wt.%, Fig. 94f), and Sr (400-700 μg/g, Fig. 94i). Documented trace components are Ni (150-250 μg/g), Ba (20-50 μg/g), Pb (2-4 μg/g), Sn (5-10 μg/g), Sb (2-8 μg/g), and U (0.2-0.6 μg/g).

The chemical composition of the matrix of the LMM* fault rock reflects strictly the fabric of its fine-grained dolomite and chalcedony. Thus, the spatial distribution of the major components CaO, MgO, and SiO_2 identify the 2-3 mm thick dolomite layer formed at the contact with the shear band (central area of Fig. 94b, c) and the anhedral enclaves of silica formed between fault pearls (Fig. 94a). The most important minor/trace components of the matrix are FeO (1-2 wt.%, Fig. 94d), Al_2O_3 (0.4-0.5 wt.%, Fig. 94f), K_2O (<0.4 wt.%, Fig. 94g), Na_2O (<0.4 wt.%, Fig. 94e), Sr (600-700 μg/g, most abundant within dolomite band, Fig. 14i), Cr (100-150 μg/g, Fig. 95b), Zn (100-150 μg/g), Cu (40-80 μg/g, Fig. 95c), Sc (10-20 μg/g), Sb (6-8 μg/g, Fig. 95e), Sn (5-10 μg/g), Cs (2-4 μg/g), Pb (2-3 μg/g), and U (ca. 0.5 μg/g). A number of these elements (Cu, Na, Pb, Sb, Sn, U) is poorly present within the fault pearls, and is mostly found within matrix and chalcedony.

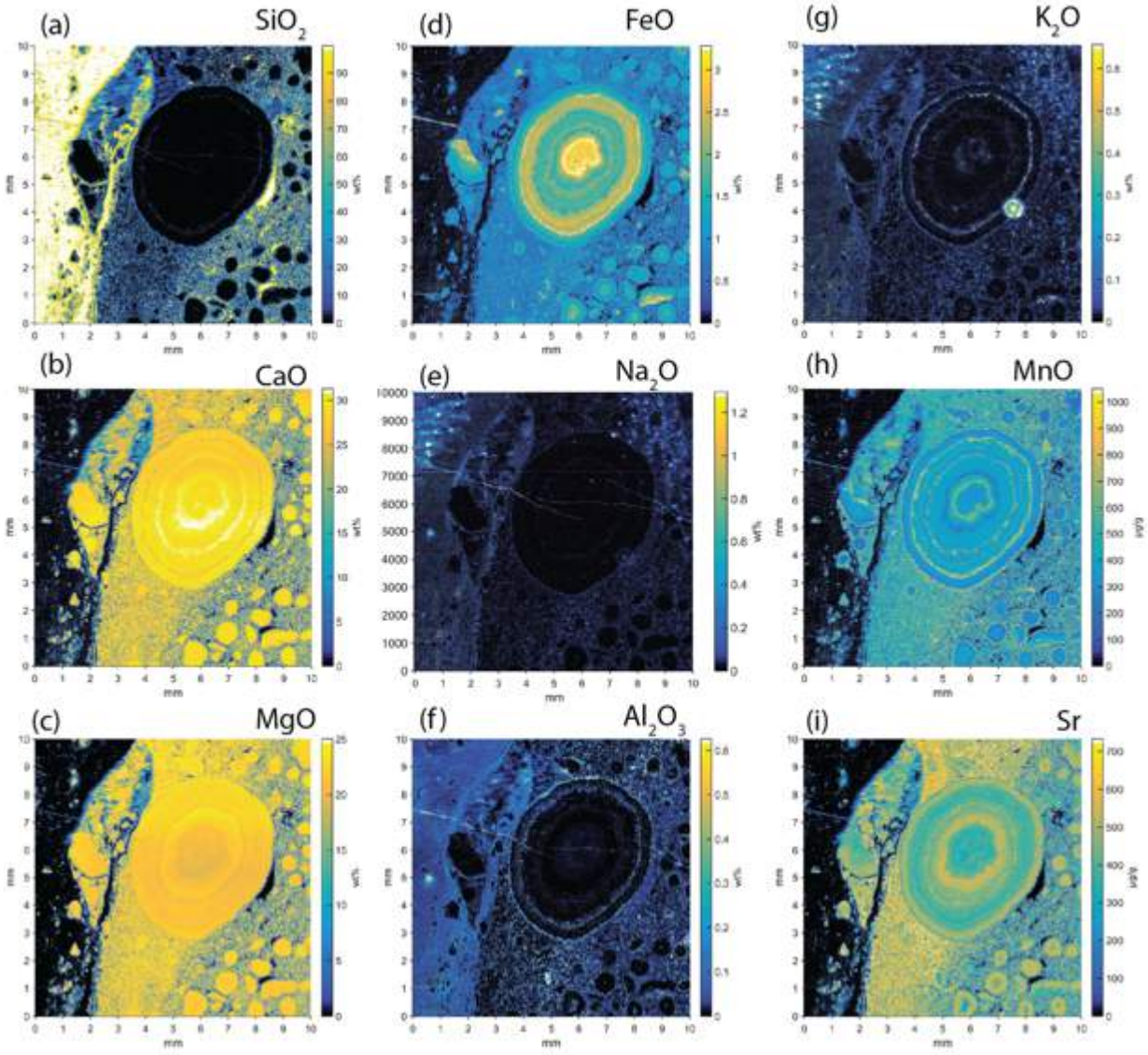

Figure 93: High resolution, large-format LA-ICP-TOFMS compositional maps of representative major components and Sr of sample LLM*. The colour codes of the maps correspond to concentration units of the components (in wt% oxide or µg/g).

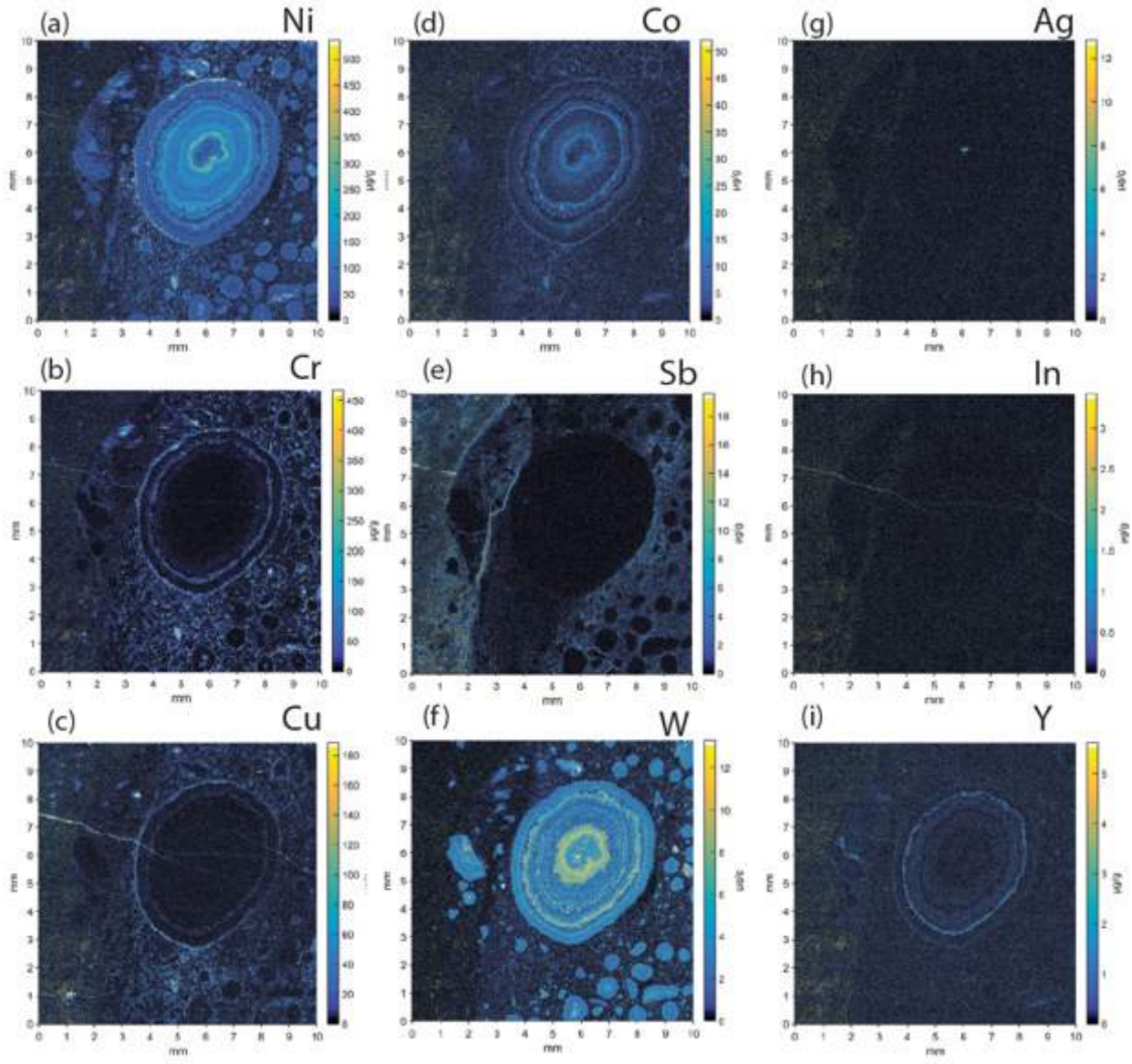

Figure 94: High resolution, large-format LA-ICP-TOFMS compositional maps of representative minor and trace components of sample LLM*. The colour codes of the maps correspond to concentration units of the components (in wt% oxide or µg/g).

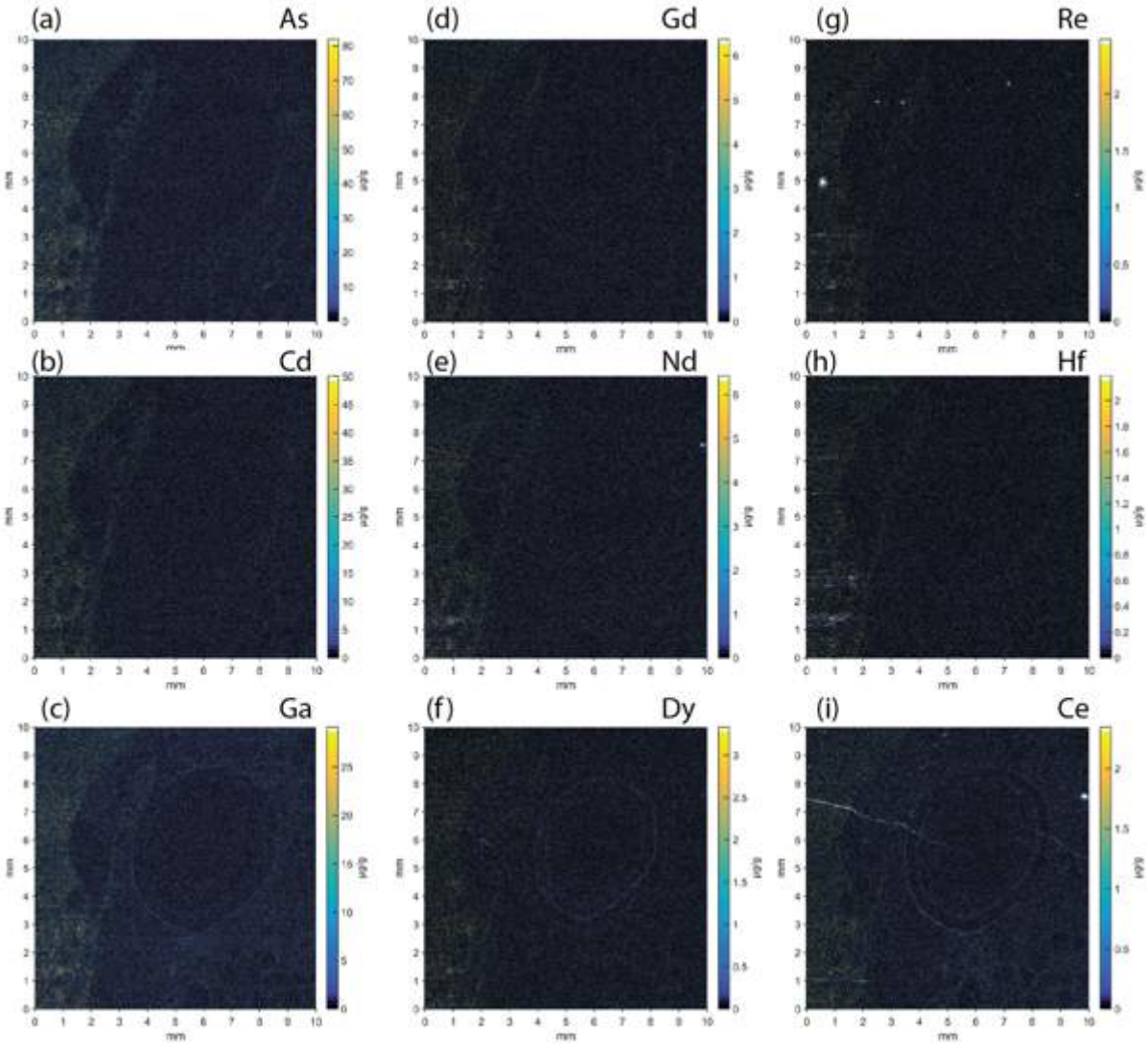

Figure 95: High resolution, large-format LA-ICP-TOFMS compositional maps of representative trace components of sample LLM*. The colour codes of the maps correspond to concentration units of the components (in wt% oxide or µg/g).

9 – Discussion

9.1 – Introduction

The discussion will be divided into two main parts. The first part deals with the geology and the structural evolution of the Lavagnina Lakes area (paragraph 9.2, 9.3, 9.4), with a focus on: *i*) the fluid-rock interaction in ductile to brittle-ductile structures (paragraph 9.5) and *ii*) gold/chalcedony occurrences in the area (paragraph 9.6, 9.7, 9.8, 9.9).

In the second part I will discuss the structural evolution of the Bisciarelle Creek Thrust Fault (paragraph 9.11.1), highlighting the role of fluid-rock interaction in the development of fault pearls (paragraph 9.11.2-9.11.7).

9.2– Geology of the study area – main remarks

The Lavagnina Lakes area (about 32 km^2, Fig. 96; geological map in the supplementary materials) is located along the Gorzente River, with an average altitude of about 400 m a.s.l., and most of the study area is part of the *"Parco Naturale delle Capanne di Marcarolo"*. Here the outcrops in the represent about the 15-20% of the entire area.

The analysed area, shown in the geological map in Figure 1, is mainly characterised by outcrops of peridotites, (lherzolites, dunites, pyroxenites), serpentinites, metabasites (metabasalts), metagabbros, lenses of metasediments, and listvenites (in decreasing order of volumetric extension).

At the northern edge of the area, continental breccias and conglomerates belonging to the Tertiary Piedmont Basin (TPB) occur. The continental breccias, cropping out in this area, are related to the "Brecce della Crosazza", instead the conglomerates are related to the "Conglomerati di Molare".

At Case Ferrere locality (Fig. 96), a carbonatic klippe, bordered by thrust faults with a W-SW sense of shear (Capponi et al., 1998) occurs. The carbonatic klippe is made up by dolomite, dolomitic limestone, and grey crystalline selciferous limestone; related to the "Dolomie del monte Gazzo" and to the "Calcari di Gallaneto" (Capponi et al., 1998).

In the geological map four different types of contact have been distinguished:

- lithological contacts (e.g. for the metasediment, metabasites, and metagabbro lenses),
- fault contacts,
- stratigraphic contacts (e.g. between the conglomerates and the breccias),
- transgressive contacts (between the Tertiary Piedmont Basin deposits and the metamorphic bedrock).

In the geological map drawn using QGIS, I added the new data from this work (Fig. 96; geological map in the supplementary materials) including: the track for the outcrops, the lithotypes, the attitude of structural elements (fault surfaces, lineations, veins, composite fabrics, tectonite foliations, stratifications), the photographs of the outcrops and their related structures, the samples positions, and the location of closed mine entrance. In the geological map, the Quaternary covers are not represented for the sake of clarity.

The structures analysed in the area, and reported in the geological map, has been divided in different systems (see below) on the base of:

- metamorphism,
- direction of tectonic transport, and
- rheological behaviour.

The geological cross-section (A-A'-A", Fig. 96; with geological map in the supplementary materials) is oriented W-SW-NE. This orientation is approximately perpendicular to the strike of the main structures (RSZ), in order to show their trend.

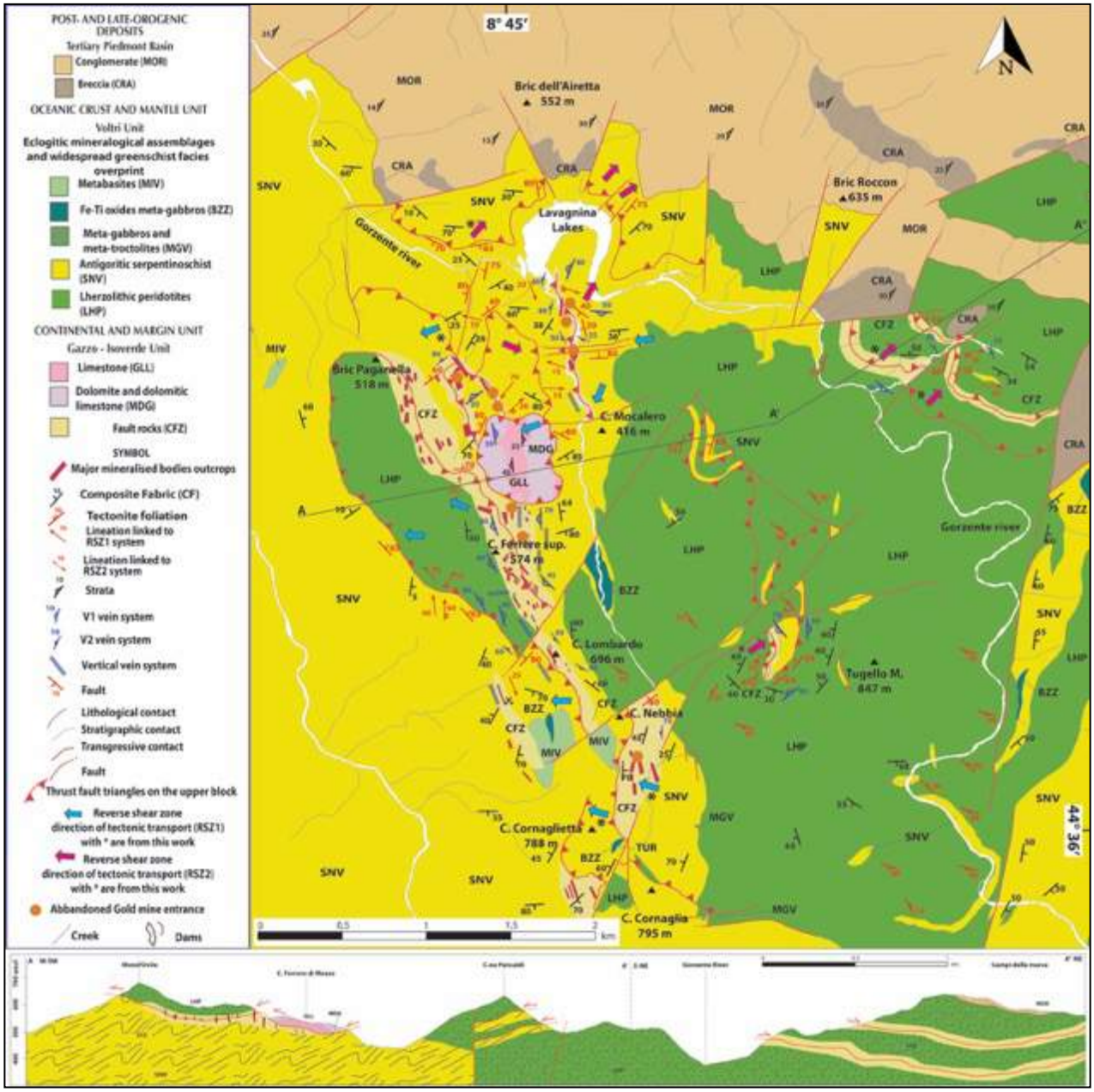

Figure 96: Structural sketch of the Lavagnina Lake area, redrawn with updates and georeferenced with QGIS open source software (after Spagnolo, 2004, see chapter 5 of this work).

9.3 – Structural evolution of the Lavagnina Lakes area

On the basis of the geological survey and the field data presented in this work, the area of the Lavagnina Lakes, during late- to post-orogenic evolution, underwent a complex polyphasic tectonic history parable to one described for other areas of the Voltri Massif (Capponi and Crispini, 2002; Spagnolo et al., 2007; Federico et al., 2009; Federico et al., 2014; Capponi et al., 2016).

The structures of the study area show evidences of multiple reactivations with different deformation mechanism, pointing to a long period of tectonic activity.

These structures show superposition of ductile, brittle-ductile and brittle deformations, developed in the upper crustal levels, strongly dependent on the lithology of the host rocks.

The ductile structures are characterised by D1-D2 structures (Capponi and Crispini, 2002) represented by similar folds characterised by Na-amphibole greenschist to greenschist facies s.s. overprint (Tab. 7).

On the other hand, the upper crustal levels deformation (UCD) are characterised by the brittle-ductile to brittle structures and are mainly represented by three main tectonic phase (D3, D4, and D5 Tab. 7).

	Structures-system	Rehological behaviour	Description	Orientation	Association	Depth - T estimate
	D1/D2	Ductile	D1 and D2 similar folds and composite fabric (CF)	D1/D2 hinge lines show scattered orientation on the axial plane, mostly plunging to N		
UPPER CRUSTAL DEFORMATION	D3	Ductile to brittle-ductile	Dragged folds with chevron style	Axes: NE trend moderate plunge	Shear zones (RSZ1)	ALT-1 4 - 11 km ca. 270 - 300 °C
	RSZ1		Shear zones (RSZ1), gold-bearing veins	WNW-ESE striking Top to S-SW with minor Top to N-NW	V1: Fe-Mg carbonates, chalcedony-quartz gold-bearing veins	
	D4	Brittle-ductile to brittle	Open parallel folds (km scale)	Axes: NE-SW trend	Shear zones (RSZ2)	ALT-2 3 - 9 km ca. 250 °C
	RSZ2		Shear zones (RSZ2), hydraulic breccias, gold-bearing veins	Top to NW with minor Top to SW-NE	V2: Fe-Mg carbonates, chalcedony and quartz gold-bearing veins; V3: chalcedony and quartz Sepiolite duplex structures	
	D5	Brittle	Strike-slip and normal faults	N-S strike-slip, minor Riedel NNE-SSW and NNW-SSE; E-W normal faults	Narrow carbonate alteration, Riedel shear planes	

Table 7: Summary of the three main tectonic phases of the upper crustal levels deformation.

The oldest UCD event (D3 event) is characterised by the coexistence of dragged folds with chevron style, and the oldest system of reverse shear zone (RSZ1, Moncalero Creek Fault, Fig. 96, Tab. 7), that are developed under greenschist to low greenschist metamorphic conditions. Commonly, RSZ1 structures develop in the reverse limbs of the D3 folds or cut them; locally the RSZ1 may be folded by the

D3 deformation. This testify to an early development of the RSZ1, under ductile regime and their subsequent evolution from the ductile to brittle-ductile regime.

The RSZ1 structures show a main sense of shear with top to S-SW, with a minor top to N-NW (e.g. Moncalero Creek Fault, see paragraph 5.3.1).

The RSZ1 structures, are mainly developed in serpentinites and lherzolites (Fig. 96). They show a symmetric damage zone with development of damage zones up to 1 m thick. The symmetric development of the damage zones is the product of ruptures along faults separating bodies with the same elastic characteristics. This limited damage zones implies small variations in terms of porosity and permeability conditions with respect to the characteristics of the host rocks.

This system shows the occurrence of a former intense carbonation (ALT-1) with the development of listvenites and are related to the oldest gold-bearing mineralisations of the area. This ALT-1 event is volumetrically limited since the alteration occurs only near the main faults or near P and R fractures and joints. This evidence points out the importance of such system in influencing the fluid circulation, and the limited development of the carbonation implies that this process leads to a reduction of the porosity and permeability turning the structures from a preferential pathway to a potential seal for the fluid circulation.

The temperatures constrained by Giorza (2010), for the ALT-1 using fluid inclusion in magnesite and Fe-dolomite, are of ca. 270-300 C°. Considering a possible range of geothermal gradients the ALT-1 has been developed at about 4-11 km.

Reverse shear zones similar to the RSZ1 system with the same sense of shear, and the same metamorphic conditions are described for the western sector of the Voltri Massif, and have been dated to the Eocene–early Oligocene (Seno et al., 2003; 2005; Molli et al., 2010; Federico et al., 2009; 2014; Maino and Seno, 2016).

The D4 event is characterised by the coexistence of open parallel folds, and the younger set of reverse shear zones (RSZ2-A, RSZ2-B) that are developed under zeolite facies to non-metamorphic conditions.

The RSZ2 system is widespread in the study area (e.g. Tugello Creek Thrust Fault and Bisciarelle Creek Thrust Fault, Fig. 96, Tab. 7). This system in place locally reactivates pre-existent RSZ1 structures. The RSZ2 structures show scattered slickenlines, and a variable sense of shear, with at least two different stages of tectonic movements. The older stage (RSZ2-A) is characterised by a main

top to NW, instead the younger stage (RSZ2-B) is characterised by top to -SW and -NE.

With respect to the oldest RSZ1 system, the younger RSZ2 system shows a volumetrically more developed carbonation (ALT-2) and completely different structural and textural characteristics.

The RSZ2 reverse faults, developed quartz-carbonate faults hosting orogenic Au deposits. They are developed near the lithological transition between serpentinized lherzolites, at the hanging wall, and the serpentinites that make up the footwall.

These faults show an asymmetric damage zone, more developed in the footwall with respect to the hanging wall, with several meters of different fault rock types (Chapter 5). The asymmetric development of the damage zones is the cumulative product of earthquakes ruptures on bimaterial faults separating different elastic bodies (Ben-Zion, 2001; MacGuire et al., 2002; Ben-Zion and Shi, 2005; Shi and Ben-Zion 2006; Mitchell et al., 2011). Hence, the asymmetry that characterises the damage zone of the RSZ2 fault system should be the result of cumulative seismic ruptures along the bimaterial interface represented by the serpentinized lherzolites and the serpentinites.

The core of the analysed structures, that I ascribe to the RSZ2 system (the Tugello Creek thrust fault and the Bisciarelle Creek thrust fault) host levels of carbonates (up to two levels) characterised by carbonate-coated grains, cockade or hydrothermal breccias and by the fault pearls (only in the Bisciarelle Creek thrust fault) coeval with sub-micron carbonates coating of slip surfaces, chalcedony shear veins and shear surfaces, injection veins, syn-kinematic filamentous phase, and sepiolite duplex structures.

The presence of sepiolite, as the presence of chalcedony crystallized over a previous deposition of amorphous silica gel (described in paragraph 9.11.4), along fault slip surfaces have been found to play a significant role in controlling fault strength leading to an almost complete loss of strength facilitating shear localization (Shimamoto and Logan, 1981; Tembe et al., 2010; Sànchez-Roa et al., 2017; 2018). At local scale, the presence of these “soft” layers along the fault surfaces may have localised the shear deformation along the faults of the RSZ2, reactivating them, as highlighted by the development of different fault rock types along the same structure in the study area.

Moreover the presence of syn-kinematic sepiolite gives limits about the P-T development conditions of the structures, since the stability field of sepiolite is ultimately limited by the reaction sepiolite = talc + quartz + H_2O, which is located at about 1-500 MPa at 325 °C (Frank-Kamenetskiy et al., 1969; Sànchez-Roa et al., 2017; 2018).

Hence the coupled presence of sepiolite and chalcedony may produce a profound dynamic strength reduction, which is fundamental for earthquake propagation (Di Toro et al., 2004; Rice, 2006; Kirkpatrick et al., 2013).

The temperatures constrained by Giorza (2010), for the ALT-2 using fluid inclusions in magnesite and Fe-dolomite, are of ca. 250 °C for the carbonation linked to the ALT-2. Considering a possible range of geothermal gradients ALT-2 has been developed at about 3-9 km. Therefore, based on the depth estimates, these structures developed at or above the brittle ductile transition.

The age constraints for the RSZ2 system come from biostratigraphic data of Oligocene deposits belonging to the Tertiary Piedmont Basin. These deposits, in fact, are locally folded and tilted by the D4 folds (Capponi and Crispini 2002; Carrapa and Garcia-Castellanos, 2005; Mosca et al., 2010; Maino et al., 2013; Federico et al., 2014) and involved in the RSZ2: the D4 event can therefore be reasonably referred to the late Oligocene - early Miocene.

The youngest D5 (Tab. 7) tectonic event developed in brittle regime. It is characterised mainly by a system of E-W strike slip faults and by normal reactivation of previous fault (e.g. Paganella Creek Fault), developed under non-metamorphic conditions. This event is related to the youngest stage of the upper crustal levels deformations.

Brittle structures similar to the D5 tectonic event, are described for the western sector of the Voltri Massif, and have been dated to the Miocene to Present (Seno et al., 2003; 2005; Molli et al., 2010; Federico et al., 2009; 2014; Maino and Seno, 2016).

Generally, the association of folds, reverse shear zones and fault duplexes, as observed in the analysed area, is a common feature of transpressive domains and resulted by kinematic partitioning of strain (e.g. Gosh et al., 2016 and references therein). Deformation in transpressive zones is often compartmentalised, so that individual constituent of bulk strain are segregates and localised into separate

deformational domains (Jones et al. 2004; Sarkarinejad and Azizi, 2008; Zhang et al., 2010).

According to literature, the meso- and microstructures (sub-micron carbonates coating of slip surfaces, chalcedony shear veins and shear surfaces, injection veins, and syn-kinematic filamentous phase) studied in the fault core of the RSZ2 structures, as described for the Bisciarelle Creek thrust fault, seismic-related. Therefore, the association of the faults belonging to the RSZ2 systems with all these seismic related structures supports the hypothesis that these faults developed during shear events at seismic rates. Thus, on the basis of all these evidences, the entire RSZ2 faults system could be considered as a local paleo-seismic faults system or at least may have registered paleo-seismic events.

9.4 – Geodynamic evolution of the Lavagnina Lakes area in the frame of the Western Alps

Comparing the upper crustal levels deformations (D3-D4-D5) that affect the Lavagnina Lakes area with the broader geodynamic context of the evolution of the Western Alps (Tab.8), and the up-to-date geological and geodynamical interpretations (Hinsbergen et al., 2014; Schmid et al., 2017 and reference therein) they could represent the transition between the last stages of the Alpine evolution and the first events of the Apennine tectonics (Mosca et al., 2010; Carminati and Doglioni, 2012).

	Structures-system	Rehological behaviour	Description	Orientation	Age	Geodynamic event in the W-Alps
UPPER CRUSTAL DEFORMATION	D3 / RSZ1	Ductile to brittle-ductile	RSZ1	WNW-ESE striking Top to S-SW with minor Top to N-NW	Stage 1: pre-35 Ma Schmidt et al., 2017	Nappe stacking
	D4	Brittle-ductile to brittle	RSZ2	RSZ2-A Top to NW	Stage 2: 35-25 Ma Schmidt et al., 2017	Thrusting of the Penninic Front
	RSZ2			RSZ2-B Top to SW-NE	Stage 3: 25 Ma to Present Schmidt et al., 2017	Oroclinal bending in the southernmost Western Alps
	D5	Brittle	Strike-slip and normal faults	N-S strike-slip, minor Riedel NNE-SSW and NNW-SSE; E-W normal faults	23 Ma to Present Sue et al., 2009	Post collisional evolution

Table 8: Summary of the three main tectonic phases of the upper crustal levels deformation in the frame of the Western Alps

Therefore, comparing the sense of tectonic transport, the metamorphism and the constrained age of the D3 event, the RSZ1 structures of the analysed area can be related to the first early stage described by Schmid et al. (2017) for the Western Alps orogenic evolution (Stage 1: pre-35 Ma; Fig. 97d).

In the Western Alps stage 1 is characterised by top to NNW thrusting and it has been preserved only in some parts of the Piedmont-Ligurian units (Philippot, 1990) and in some parts of the External Western Alps (Dumont et al., 2011). These events were associated with nappe stacking and early stages of exhumation of parts of nappes buried to high-P (e.g. Schmid et al., 1996).

Comparing the metamorphism, the constrained age of the D4 event and the sense of tectonic transport for the RSZ2-A structures, they can be related to the second stage described by Schmid et al. (2017) for the Western Alps orogenic evolution (Stage 2: 35-25 Ma; Fig. 97c; Dumont et al., 2012).

In the Western Alps stage 2 is characterised by top to W-NW thrusting and it can reliably be directly linked to thrusting along the Penninic Front (Schmid et al., 2017). The end of stage 2 at around 25 Ma ago is compatible with the onset of the Paleo-Apenninic phase (Schumacher and Laubscher 1996) at about this time.

Stage 2 certainly pre-dates the onset of rapid counterclockwise rotation of the Corsica-Sardinia block at 21 Ma ago (Gattacceca et al. 2007).

The RSZ2-B structures may have been affected by the beginning of the third stage described by Schmid et al. (2017) for the Western Alps orogenic evolution (Stage 3: 25-0 Ma; Fig. 97b, a).

This event actually post-dates the stage 2 (Trullenque et al., 2005), and it is associated the oroclinal bending in the southernmost Western Alps; this idea is supported by three main lines of evidence:

- Collombet et al. (2002) reported counterclockwise rotations about a sub-vertical axis in respect to stable Europe that increase from 68° in the Ubaye region to 117° in the Ligurian Alps;
- all the major tectonic elements of the internal Alps derived from the Briançonnais and Piedmont-Liguria paleogeographical domains can be followed into western Liguria (Hinsbergen et al., 2014);
- a 50° counterclockwise rotation phase of the Corsica-Sardinia block occurred between 20.5 and 16 Ma ago (Gattacceca et al. 2007; Massonne et al., 2017) around a pivot near the N tip of Corsica, as Corsica and Sardinia drifted away from their pre-Miocene location south of southern France (Advokaat et al., 2014); this virtually demands substantial counterclockwise rotation in Liguria associated with oroclinal bending. Note that such counterclockwise rotation is directly demonstrated by the same counterclockwise rotation of mostly Oligocene sediments of the Tertiary Piedmont Basin sealing pre-Oligocene Alpine structures evidenced by paleomagnetic data (Maffione et al. 2008).

Oroclinal bending in the southernmost Western Alps during stage 3 is evidently associated with orogeny in the Apennines (Schmid et al., 2017 and reference therein). Slab rollback (Rosenbaum and Lister, 2004, Hinsbergen et al., 2014) of the Adria plate towards N in the northernmost Apennines is the underlying driving force for both oroclinal bending and the rotation of Corsica and Sardinia (Schmid et al., 2017 and reference therein).

Comparing the constrained age of the D5 event structures can be related to a late extensional / transtensional reactivation phase of the pre-existing discontinuities, developed during the post collisional evolution, described for the Western Alps orogenic evolution (Sue et al., 2007).

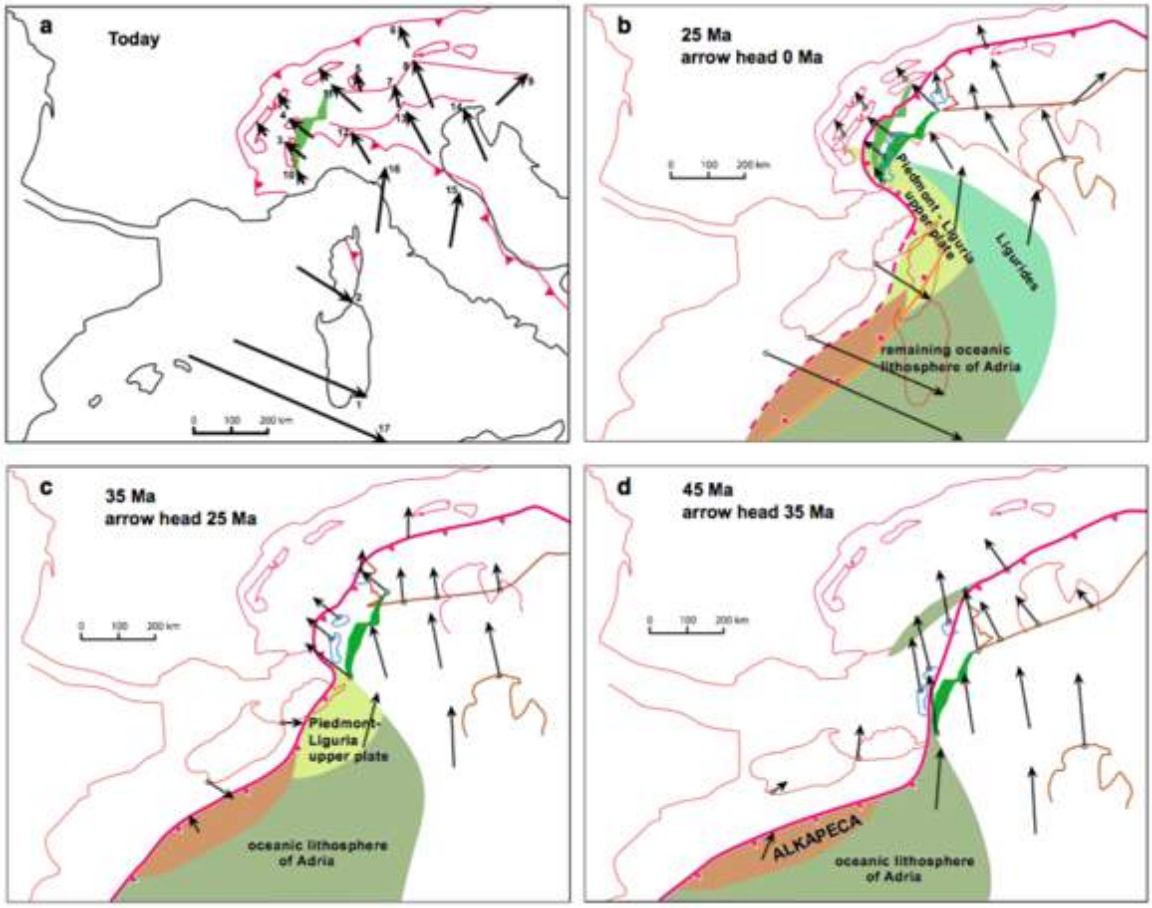

Figure 97: Kinematic restoration of the Alps–Apennines orogenic system reconstructed by Schmidt et al. (2017) from Eocene to the present day.

9.5 – Fluid rock interactions in the RSZs systems

Fault zones in the upper crust are typically composed of complex fracture networks and discrete zones of comminuted and geochemically altered fault rocks.

Faults deeply affect the patterns of fluid flow in both modern and paleo-flow found in the upper crust (Sibson, 2001; Bense et al., 2013). Deformation along faults in the shallow crust (<1 km) introduces permeability heterogeneity and anisotropy, which has an important impact on processes such as regional groundwater flow, hydrocarbon migration, and hydrothermal fluid circulation. Fault zones have the capacity to act as hydraulic conduits connecting shallow and deep geological environments, but simultaneously the fault cores of many faults often act as effective barriers to flow. This affects local fluid-pressure gradients, mechanical failure, propagation of pressure transients, fluid infiltration into and out of a fault zone via fault-valve mechanisms (e.g., Sibson, 1992; Faleiros et al.,

2014; Shelly et al., 2015; Japas et al., 2016), and fault-zone sealing and healing (e.g., Faulkner and Rutter, 2003; Faulkner et al., 2008; Boulton et al., 2017).

On the other hand the presence and flow of fluids in the upper crust has a major impact on the mechanics of faulting (Caine et al., 1999; Caine et al., 2010 and reference therein). The presence or absence of syntectonic fluids and their fluid-rock interactions have important effects on deformation and they strongly influence the transition between ductile and brittle behaviour of the host rocks (Caine et al., 1999; Caine et al., 2010; Bense et al., 2013; Maerten et al., 2017 and reference therein). Fluid expulsion and localized mineralisations along faults can lead to the formation of economic mineral deposits (Micklethwaite, 2009), and may also impact onto the locations and magnitudes of foreshock, earthquake and aftershock distributions (Ross et al., 2017).

Most economic mesothermal deposits are formed near to the brittle – ductile transition (Sibson et al., 1988; Craw and Campbell, 2004; Holdsworth et al., 2015), similarly to what observed in the analysed area (see below).

The occurrence of syn-tectonic fluid flow and consequent fluid-rock interaction (carbonation or listvenitization) along the two systems of Reverse Shear Zones (RSZ1-RSZ2), is testified by metasomatic alteration (ALT-1, ALT-2, and ALT-3), by at least three systems of veins (V1, V2, and V3), and by the development of hydraulic and cockade breccias.

The evidence that the carbonation took place along these structures, in particular along the RSZs systems, and within their damage zones, highlights how these structures acted as important fluid pathways and played a major control in the distribution of the ore deposits.

This fluid-rock interaction develops various degrees of carbonated fault rocks, passing through listvenites, until their total substitution with carbonate levels (e.g. Bisciarelle Creek thrust fault). In the area the listvenitization took place over lherzolites and serpentinites. The carbonation of these rocks release SiO_2 into the fluids (Boschi et al., 2009; Ulrich et al., 2014), as described in the chapter 2, that subsequently develop silica gel or chalcedony deposition.

The process of carbonation, developed along the Bisciarelle Creek thrust fault (Chapter 8, and paragraph 9.11.5) is comparable with the listvenitization process described by Akbulut et al. (2006), that proposed a high pH fluid bearing As, Ba, Sb, Sr and rich in SiO_2, Ca and CO_2, flushes trough the fault, the damage zone or is

strained up to the fractures. Carbonation of the host rock took place due to the fluid-rock interaction and particularly magnesite ($MgCO_3$) and dolomite ($(Ca,Mg)(CO_3)_2$) precipitated. Fluids are the source for the Ca and CO_2 (Hansen et al., 2005; Akbulut al., 2006) as observed for the mass transfer profiles (Chapter 7) of the Bisciarelle thrust fault. The host rock (lherzolite or serpentinite), instead, is the source of Mg, and in minor proportion of Ca, for the presence of pyroxenes, during the metasomatic process. Dolomite precipitated either as cement of the brecciated main ore bodies, or as late infill in cavities of veinlet networks, due to an increase of the Ca/Mg ratio in the fluid. This can be explained either by magnesite precipitation in a Ca–Mg-rich fluid or by a late supply of Ca^{2+} ions, after the early magnesite deposition (Herrero et al., 2011). The first hypothesis appears improbable since at low pressure/low temperature magnesite is more soluble than Ca-carbonates (Boschi et al., 2009). Moreover, the presence of Ca^{2+} into the fluid decreases the stability field of magnesite and enhances the precipitation of dolomite or calcite (Herrero et al., 2011). For the analysed area the second hypothesis seems more plausible: the presence of the metasediments (mainly calcschists and micaschists), of the carbonatic klippen at "Case Ferrere" locality, and the Tertiary Piedmont Basin deposits and their local interaction with mineralising fluids can explain the late supply of Ca^{2+} and the switch from magnesite to dolomite precipitation. The depletion of Mg content in the environment due to the precipitation of dolomite and limited Ca solubility create small amounts of calcite ($CaCO_3$) together with silica gel (Akbulut et al., 2006).

A small amount of As and Sb (Chapter 8, and paragraph 9.11.5) is added to the newly formed alteration assemblage due to high pH environment (Herrero et al., 2011).

As described above, the carbonation process release SiO_2 into the fluids (Boschi et al., 2009). Consequently at later stages, silica supersaturation takes place in the fluid due to the carbonate precipitation and introduction of additional silica from the host rock (Akbulut et al., 2006 and reference therein).

For the entire area, assuming as model the Bisciarelle Creek Fault, in both the two models proposed above as mechanism responsible for the development of the fault pearls, the transition between the carbonates precipitation and silica supersaturation, may be considered instantaneously and cyclic. Generally for the entire study area, a secondary silica supersaturation of the fluids with later silica

gel deposition could explain why the chalcedony (with consequent recrystallization to quartz) is always the last phase of crystallization, both in the shear veins that cut the newly developed carbonates levels (e.g. Tugello Creek Fault), and in the V1 and V2 vein systems.

In some instances the conversion of peridotite to listvenite is nearly isochemical except for the addition of volatiles (H_2O and CO_2) similarly to what described for the Bisciarelle creek thrust fault (chapter 7), while other samples show have also seen significant calcium addition and/or variable, minor addition of K and Mn (Russel et al., 2010). However, carbonation, often with silica cavity fillings and pronounced chalcedony, opal and/or quartz hanging walls (silica caps) are a feature of low to moderate temperature hydrothermal deposits in the Alpine and other serpentinite complex (Ilich and Toshovich, 2002; Russel et al., 2010).

Many studies about ultramafic rock carbonation have proposed different temperature conditions for listvenite bodies worldwide: about 210–280 °C in Canada (Schandl and Gorton, 2012), about 80–130 °C in Oman (Falk and Kelemen, 2015), temperatures up to 150 °C in Norway (Van Noort et al., 2013), and temperatures lower than 300 °C in Italy (Boschi et al., 2009).

The value estimated by Boschi et al. (2009) for the carbonation over serpentinites is coherent with the data presented by Giorza (2010) for this area (see below).

These peculiar rocks are interesting since they are located along the major fault systems where metamorphic and hydrothermal fluids are channelled (Halls and Zhao, 1995; Bistacchi et al., 2001; Akbulut et al., 2006; Zoheir and Lehmann, 2011; Power et al., 2013), and they are worldwide associated with gold mineralisations (Ash and Arksey, 1990; Halls and Zhao, 1995; Bistacchi et al., 2001; Béziat et al., 2008; Escayola et al., 2009; Zoheir and Lehmann; 2011; Ananyev et al., 2015; Falk and Kelemen, 2015; Qiu and Zhu, 2015; Belogub et al., 2017).

9.6 – Gold deposits in the Lavagnina Lakes area

Major mineralised body outcrops in the Lavagnina Lake – Gorzente River area (Fig. 98) occur in serpentinites, particularly in the serpentinite schists or at the lithological transition with lherzolites. In particular these mineralisations are mainly associated with the carbonation and listvenitization of the host rocks into a

narrow NNW-SSE oriented belt (Fig. 98). The carbonation and the listvenitization, mainly developed in the serpentinites, or at the lithological transition with the lherzolites, may be due to a preferential fluid circulation inside these rocks, and it is due to their schistosity, that act as a pathway for the fluid circulation and hence causes a greater permeability. On the contrary, at the lithological transition, the lherzolites may act as seal with respect to the serpentinites or the serpentinite schists, confining the fluid flow.

The temperatures constrained by Giorza (2010), using fluid inclusion in magnesite and Fe-dolomite, are of ca. 270-300 C° for the carbonation linked to the ALT-1, and temperature of ca. 250 °C for the carbonation linked to the ALT-2. Considering a possible range of geothermal gradients the ALT-1 has been developed at about 4-11 km, instead the ALT-2 has been developed at about 3-9 km. Therefore, based on the depth estimates, these mineralisations developed at or above the brittle ductile transition.

Gold-bearing V1 and V2 veins show similar mineralogical associations (Fe- Mg-carbonates + quartz + native gold + sulphides) and they normally occur in the footwall of RSZs structures as Riedel shear veins or as extensional veins. They developed at crustal depth, and are mainly related to the upper crustal deformation tectonic events. Their comparable features testify to similar genetic mechanisms acting in two different stages during major emplacement of late-orogenic gold deposits.

Main lode gold deposits in the area are linked to V2 veins and occurred during D4 tectonic event; RSZ2 can be referred to as secondary structures that are linked to major dextral transpressive systems instead V2 veins mainly acquire R or P Riedel shear orientation. As a result the emplacement of V2 gold-bearing veins can be referred to the development of the regional-scale dextral transpressive system mainly acting during D4 event. The similarities between V1 and V2 veins support the hypothesis of comparable genetic mechanisms; accordingly the occurrence of V1 gold-bearing veins related to RSZ1 structures is one of the points that testify to an earlier development of the transpressive systems that may acted both during D3 and D4 events.

The Lavagnina Lakes mineralisations show several characteristics similar to what described in literature for the mesothermal gold deposits or for the so called

orogenic gold type deposits (e.g. Craw et al., 1999, 2001; Goldfarb et al., 2001; Craw et al., 2004; Wyman et al., 2016) i.e.:

- they typically occur in structural traps (e.g. along faults, in fault intersection zones, and in damage zones),
- they are generally small and either mined on a small-scale historically,
- they developed at depth from 11 to 3 km,
- the gold vein systems are hosted primarily in greenschist facies rocks of widely varying protoliths,
- fill extensional fractures or dilatational sites in shear fractures, and
- generally they are located at or near major topographic divides in the various mountain belts.

So, on the base of all these similar characteristics, the Lavagnina Lakes deposit may be ascribed to the orogenic gold type deposits.

These deposits consist of abundant quartz and carbonate veins and show evidence for deposition from fluids at moderate temperatures (250-400 °C, Craw et al., 1999, 2001; Goldfarb et al., 2001; Craw et al., 2004).

These deposits are related to late-orogenic evolution of main collisional belts, (Goldfarb and Grooves, 2015). The association with regional-scale transpressive systems is a common features described for mesothermal gold deposits (Craw et al., 2002). Structurally hosted gold-bearing vein systems in metamorphic terranes display, in fact, many similar characteristics and they are found throughout the world in orogenic belts of Archean to Cenozoic age (Goldfarb et al. 2001; Goldfarb and Grooves, 2015). They constitute a single class of precious metal deposit that is characteristically associated with deformed and metamorphosed mid-crustal blocks, particularly in spatial association with major crustal structures (Goldfarb et al., 2001). The majority of lode gold deposits formed proximal to regional trans-lithospheric terrane-boundary structures that acted as vertically extensive hydrothermal plumbing systems; these structures record variably thrust and transpressional - transtensional displacements (Goldfarb and Grooves, 2015).

Recent works on mesothermal gold system testify to a close relationship between seismic events that causes fluid redistribution and consequent gold mineralisations. In particular the transfer of low-salinity fluids, similar to those described for the area (see below), to the sites of gold deposition is controlled by earthquake events (Sibson et al., 1988; Cox, 2005; Tomkins, 2013; Weatherley and

Henley, 2013; Goldfarb and Groves, 2015), allowing fluids to rapidly traverse large thicknesses of crust. This rapid rise takes the fluids out of equilibrium with their surroundings, promoting destabilization of the gold-carrying complexes. In addition to the rapid rise of fluids, cavity expansion, linked to seismic slip, generates extreme reductions in pressure that cause the fluid that is trapped in the jog to expand to a very low-density vapour (Wheatherley and Henley, 2013). This process, called flash vaporization (Moncada et al., 2012; Wheatherley and Henley, 2013; Chen et al., 2017), is directly related to the slip volume and, as a function of earthquake magnitude, the strike length of the rupture zone on the parent fault (Lovett, 2013; Wheatherley and Henley, 2013). Such flash vaporization of the fluid results in the rapid co-deposition of silica with a range of trace elements to form gold-enriched quartz veins (Lovett, 2013; Wheatherley and Henley, 2013).

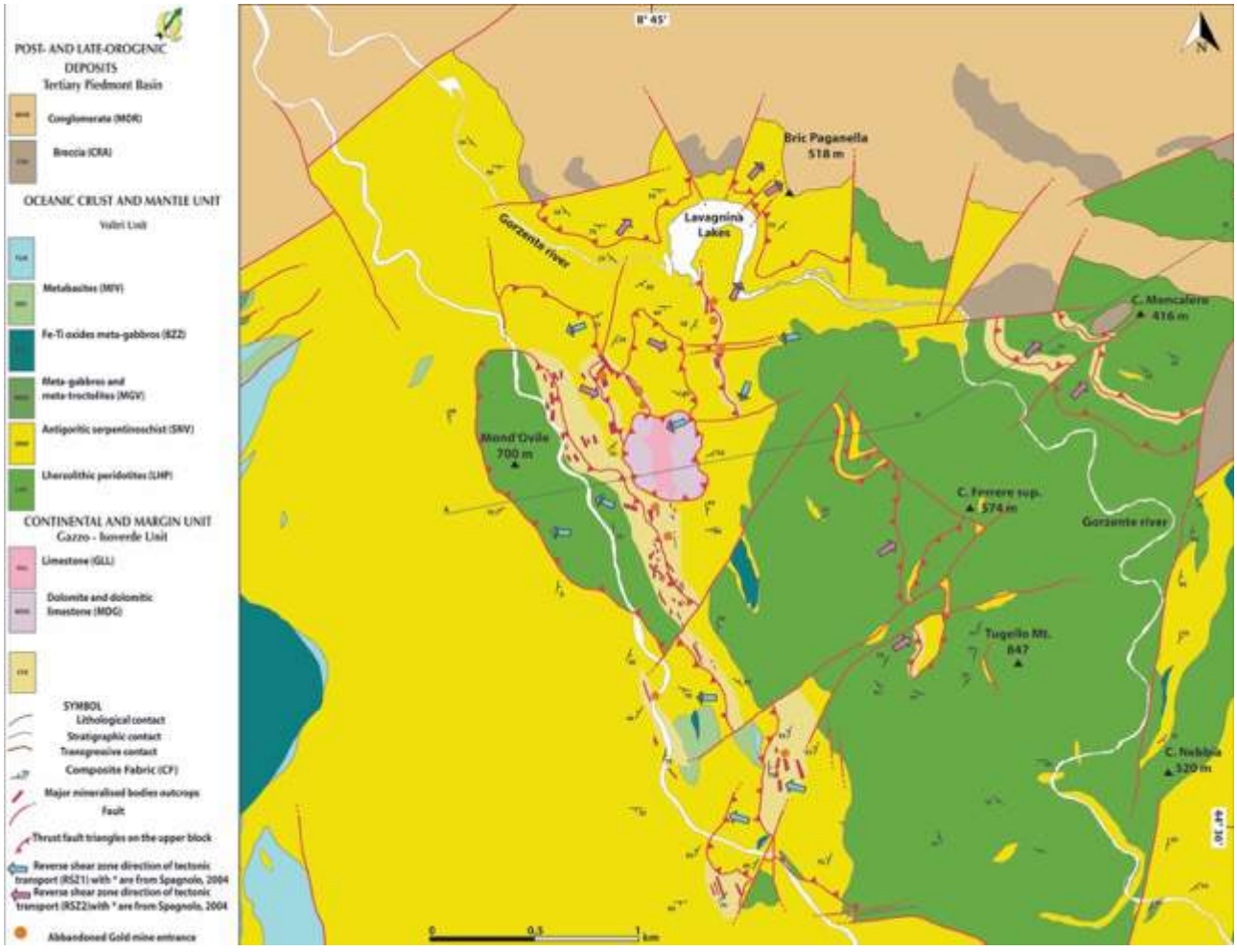

Figure 98: Simplified structural sketch of the Lavagnina Lakes area.

9.7 – Chalcedony in the Lavagnina Lakes area

Chalcedony is widespread in the analysed area, it has been observed as filling of extensional veins, and in syn-kinematic shear veins along fault slip surfaces (e.g. Tugello Creek thrust fault and Bisciarelle Creek thrust fault; chapter 5). The presence of chalcedony is interesting both in the extensional veins both, as above described, and in the shear veins. It is common in the hydrothermal systems, and it is related to gold-quartz veins (Herrington and Wilkinson, 1993; Moncada et al., 2012).

Generally, after the initial precipitation of amorphous silica gel (colloid), it subsequently crystallizes to chalcedony. The amorphous silica gel deposition can occur in brittle-ductile shear zones during seismic slip where a significant fluid-pressure drop occurs (Herrington and Wilkinson, 1993; Kirckpartik et al., 2013).

Such process rapidly supersaturates the hydrothermal fluid with respect to amorphous silica, which precipitates instead of quartz, owing to favourable kinetics. Depressurization commonly leads to fluid unmixing and destabilization of soluble gold complexes (Moncada et al., 2012; Wheatherley and Henley, 2013). However, the presence of colloidal silica can stabilize gold colloid, allowing further transport of particulate gold in suspension in the hydrothermal fluid (Hannington et al., 2016). Silica gel would be highly unstable under mesothermal conditions and would undergo rapid crystallization to form quartz (Herrington and Wilkinson, 1993). The crystallization would tend to expel solid impurities toward grain boundaries, and to obliterate the primary fluid inclusions. This can explain the reason why all the quartz samples taken in the area are devoid of fluid inclusions.

9.8 – Gold and chalcedony distribution in the Voltri Massif

Gold deposits are described in many units, e.g. in the Sestri-Voltaggio Zone (Agostinetti et al., 1995) and in the ophiolitic rocks belonging to the Internal Ligurian Units (Garuti et al., 2008), but they are widely developed only in the Voltri Massif (Fig. 99) and specially in the Val Gorzente ores (Fig. 98).

Gold exploitation in the Voltri Massif is very ancient and it dates back to the Roman Age (Pipino 2003). The most ancient documents that testify to gold-digger

activity and to gold exploitation date from the 13th century, but the most important works were carried out during the last century, when placers, eluvial soils and gold- bearing veins were actively exploited (Pipino 1976, 1977). Most important abandoned gold mine entrance and gold-bearing quartz veins, founded in literature are reported in Fig. 99.

The most interesting mineralisations are linked to the development of: matasomatic carbonation, listvenitization, and hydrothermal quartz veins and stockwork type deposits; moreover, recent studies have shown that gold is unevenly distributed in the ultramafic rocks, where the average gold content ranges from 0.1 to 2.0 g/ton. In veins the average content is normally low, ranging from 2.0 to 20.0 g/ton, but sometimes is exceptionally high, exceeding 200.0 g/ton (Pipino 2000).

Moreover, some of the gold occurrences in the Voltri Massif are associated with the presence of chalcedony (Fig. 99), as the widespread chalcedony vein system related to fault damage zone near Sassello village, and along the Roboaro River (GPS coordinates N44.544686°, E8.436038°; Scarsi, 2014). Thus, could be hypothesized a relation at regional scale between the presence of gold linked to chalcedony-quartz veins. A future study on this relationship may provide important information on regional scale.

All the gold-occurrences in the Voltri Massif, i.e. location of the abandoned gold mine entrance and the evidences of gold-bearing veins from literature, are prevalently oriented along a NNW-SSE (Fig. 99) belt similarly to what observed in the Lavagnina Lakes area.

Hence, also at regional scale, the main lode gold deposits can be effectively referred to as secondary structures that are linked to major dextral transpressive system. As a result the emplacement of the Voltri Massif gold-bearing veins can be referred to the development of the regional-scale dextral transpressive system mainly acting during D4 event.

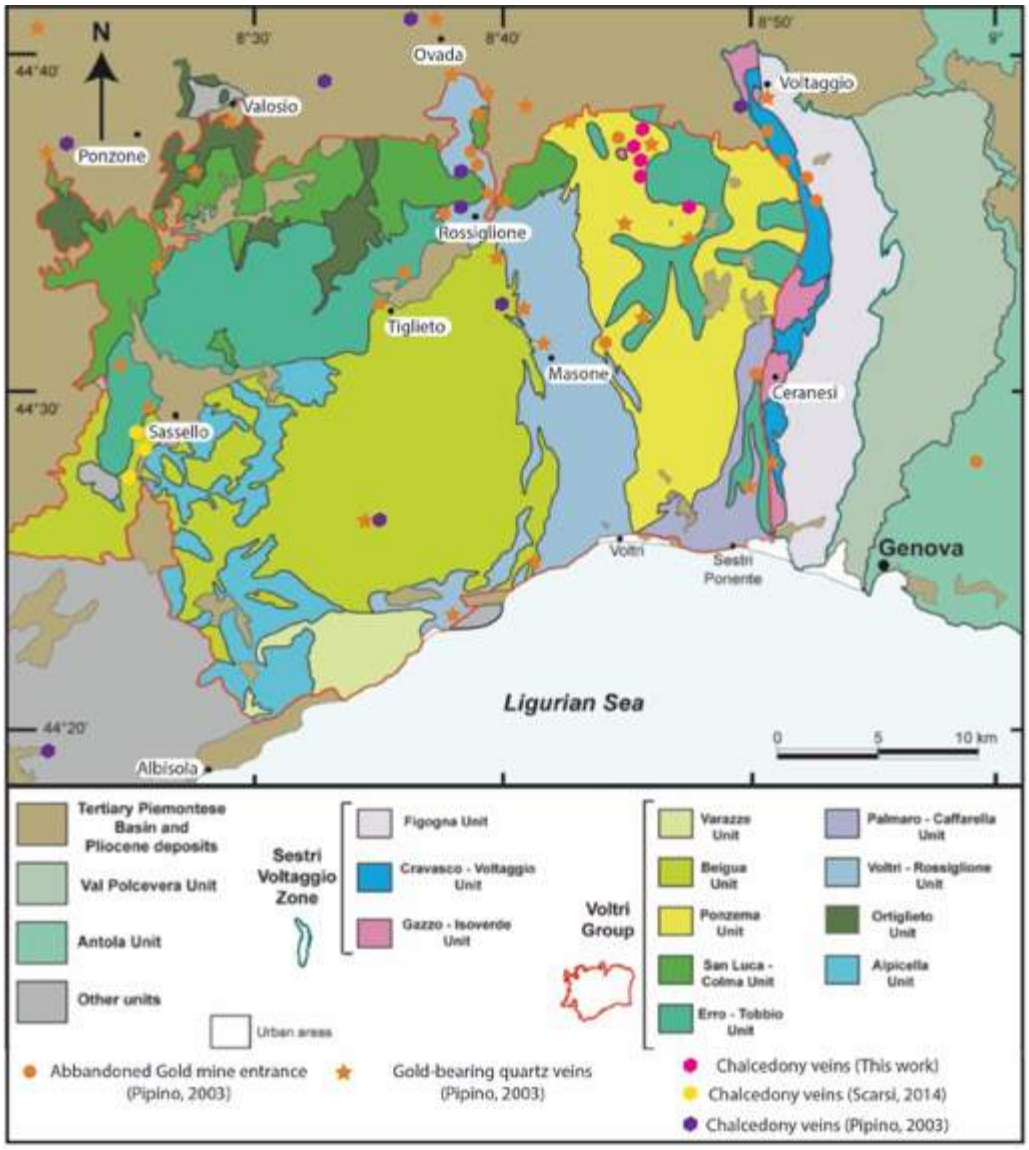

Figure 99: Sketch map of the eastern Ligurian Alps (modified by Capponi et al., 2016) showing the location of abandoned gold mine entrance (Pipino, 2003), The gold-bearing quartz veins (Pipino, 2003), and the chalcedony veins (Pipino, 2003; Scarsi, 2014; This Work).

9.9 – Genesis and transport of gold-bearing mineralizing fluids

The so-called "mesothermal" gold deposits are associated with regionally metamorphosed terranes of all ages, developed during compressional to transpressional deformation in accretionary and collisional orogens (Groves et al., 2000, 2016). On their depth formation, these deposits are best subdivided into epizonal (< 6km), mesozonal (6-12 km) and hypozonal (> 12 km).

The greenstone-hosted quartz-carbonate vein deposits correspond to structurally controlled complex epigenetic deposits characterised by simple to complex networks of gold-bearing, laminated quartz-carbonate fault-fill veins.

These veins are hosted by moderately to steeply dipping, compressional brittle-ductile shear zones and faults with locally associated shallow-dipping extensional veins and hydrothermal breccias (Dubè and Gosselin, 2007; Ugarkar et al., 2016). The deposits are generally hosted by greenschist metamorphic rocks of dominantly mafic composition and formed at intermediate depth (5- 15 km depth), at or above the brittle-ductile transition (Goldfarb et al., 2005; Tomkins, 2013). The mineralisations is syn- to late-deformation and typically post-peak greenschist-facies metamorphism (Diamond, 1990). Gold is largely confined to the quartz-carbonate vein network.

The fluids, which carried gold and which developed veining and metasomatic alterations such as listvenites in ALT-1 or carbonate-bearing rock levels in ALT-2, can be constrained using the fluid inclusion data provided by Giorza (2010) that contain low saline (7-9%) aqueous liquid with CO_2-CH_4-N_2 vapour bubble; with the salt components mainly represented by Na, K, with a significant amount of Li, B, Rb and Ba. The gold-bearing mineralisations of the Lavagnina Lakes area, on the basis of their depths estimates (3 to 11 km), and following the classification of Groves et al. (2000), could be classified as epizonal to mesozonal deposits following the

The origin of these fluids is an open question about Lavagnina Lake – Gorzente River area gold-bearing system. Possible origins of fluids debated in literature for lode-gold deposits in orogenic belts are:

- a magmatic origin with fluids related to late-orogenic plutonic intrusions (Goldfarb et al., 2001; Large et al., 2016)
- a metamorphic origin with fluids generated during prograde metamorphism and ascended along steep faults and fractures (Dubè and Gosselin, 2007; Phillips and Powell, 2009, 2010)
- a meteoric origin where fluids are tectonically driven to depth and then rise up channelled into fractures and faults (Craw et al., 2015).

In the Lavagnina Lake- Gorzente River area the magmatic origin can be excluded since there are no evidences of late-orogenic plutonic intrusion in the Voltri Massif.

The metamorphic or meteoric origin of fluids can be discussed for the study area:

- the metamorphic origin of fluid can be hypothesised on the basis of similarity between late-orogenic gold deposits and according to fluid origin

detected in other sectors of the NW Alps (Rauchenstein-Martinek et al., 2014). Gold and sulphur dissolve in fluids under greenschist facies conditions and near to the brittle-ductile transition. Gold is subsequently deposited from these fluids in fracture systems between the brittle-ductile transition and near-surface region, forming mesothermal mineral deposits (Craw et al., 2015). Current knowledge on Au deposits indicates that these mineralized fault networks form due to the flux of volumes of chemically uniform hydrothermal fluids (Garofalo et al., 2014). These fluids are aqueous-carbonic in composition (5-20 mol% CO_2), had a T in the 200-400 °C range at the time of mineralisations, were at, or close to, their boiling point, and were enriched in As, Sb, B, and Au (Garofalo et al., 2014). In particular, the conditions under which listvenites are formed correspond in pressure and temperatures to the field of these gold deposits (Schandl and Gorton, 2012; Boschi et al., 2009).

The metamorphic fluid model suggested that heating caused by crustal thickening during the collisional event produces devolatilisation of the Mesozoic metasediments in the Piedmont ophiolite nappe, under upper-greenschist or higher metamorphic conditions. The deep-seated, Au-transporting metamorphic fluid has been channelled to higher crustal levels through major crustal faults or deformation zones. Along its pathway, the fluid has dissolved various components, including a potential gold-rich precursor. The fluid then precipitated as vein material or wall-rock replacement in second and third order structures at higher crustal levels through fluid-pressure cycling processes and temperature, pH and other physico-chemical variations (Dubè and Gosselin, 2007; Ugarkar et al., 2016).

- a meteoric origin of fluid can be referred to tectonically driven hydrothermal systems. Tectonic processes associated with continental collision causes regional fluid flow, which may involve meteoric, basinal and crustal fluids (Craw et al., 2015). Mesothermal mineralisations occurs in part of this complex flow system. Fluids are brought to depth and subsequently are channelled up into main fractures and faults.

  Tectonically driven systems are described for the Acqui Terme – Visone thermal spring system that develop ca. 20 km far from the Lavagnina Lake –

Gorzente River area (Bruni et al., 2002; Piana et al., 2006; Pasquale et al., 2011). Hydrothermal waters referred to the Acqui Terme – Visone geochemical system derive by infiltrations of meteoric waters that are brought to depth of about 3.5 Km. Consequently these fluids ascend along high vertical permeability zones produced by the main fault systems belonging to the Bagni-Visone transtensive system (Piana et al., 2006).

The RSZs systems show similarities with the worldwide orogenic gold type deposits as:

- the uniformity of fluid composition (Diamond, 1990; 1993; Wang et al., 2015; Yang et al., 2016),
- the development in second or third order structures (Groves et al., 2000 Qiu et al., 2002; Dubè and Gosselin, 2007; Zeng et al., 2014; Ugarkar et al., 2016),
- the development of the mineralisations near or above the brittle ductile transition (Sibson et al., 1988; Herrington and Wilkinson, 1993; Craw et al., 1999, Groves et al., 2000; Philips and Powell, 2009; 2010), and
- the mineralisations are developed in greenschist facies conditions (Craw et al., 1999; Craw and Campbell, 2004; Groves et al., 2016),

On the basis of all these similarities, the fluid involved in the development of the gold mineralisations of the Lavagnina Lakes area can be related to a tectonically driven hydrothermal system and/or orogenic system gold deposits.

B and Li are light elements, which are potentially tracer of fluid origin because they are released in the fluid phase during metamorphic devolatilisation (Harvey et al., 2014) and are present in very low concentration in mantle reservoirs. Even if the fluid-rock interaction occurred with a host-rock, like serpentinite, considered a source of boron, it seems highly unlikely that serpentinite can provide such a quantity of boron (Giorza, 2010). It is more reasonable to suppose that the fluid was originally enriched in this element, which can derive from other sources, like metasediments.

Moreover the metamorphic origin of fluid referred to tectonically driven hydrothermal systems is best evaluated by comparing the concentration ranges of the key trace elements As, Sb, In, Ga, Ag, Zn, and Cu of pearl levels and

chalcedony (Chapter 8) with those of the same elements in the average upper crust (Rudnick and Gao, 2003). Such comparison clearly shows that the peak concentrations of these elements are 5 (Cu, Zn) to 50 (Sb, In) times higher than those of the upper crust, demonstrating that the fluid involved in the Lavagnina Lakes area was capable to transport and deposit a suite of ore elements.

Finally the fluid composition, described by Giorza (2010) is compatible with the metamorphic fluids that were generated during Alpine metamorphism of Mesozoic calcschists (Pettke et al., 2000). These carbonate-bearing metasediments are abundant in the Piemontese Zone and may be present at considerable depth below the Voltri Unit (Fig. 100).

Despite all these features an influence, or a mixing with meteoric fluids cannot be totally excluded, and future isotopic study on the vein systems of the area may provide fundamental information to better constrain this hypothesis.

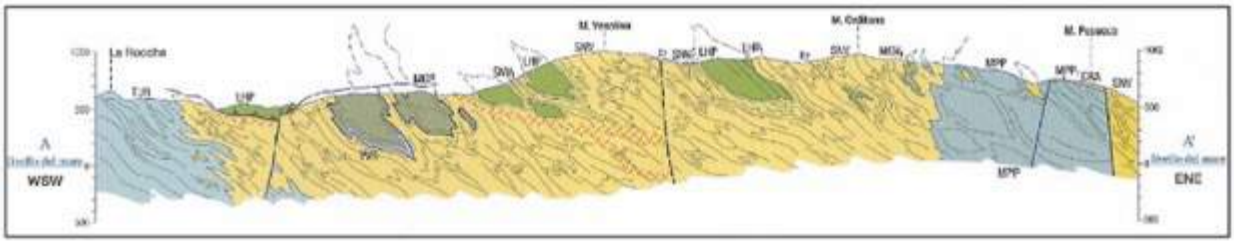

Figure 100: Geological cross-section of the Voltri Massif drawn by Capponi and Crispini (2008) at ca. 10 km far from the Lavagnina Lakes area.

Taking into account the age of the structures related to the gold mineralisations in the Lavagnina Lakes area, as well as the age of the structures of the Voltri Massif, the older structures, the RSZ1, can be dated to the Eocene–early Oligocene and are developed from 4 to 11 km depth, instead the younger structures can be reasonably referred to the late Oligocene early Miocene and developed from 3 to 9 km depth.

Hence, considering the age of these structures and the geological setting of the Lavagnina Lakes area (Fig. 96, 98), and of the entire Voltri Massif (Fig. 99), can be assumed that the gold-bearing fluids, related to the RSZ1 and RSZ2 mineralisations, have permeated and interacted substantially with the same lithotypes belonging to the Gazzo Isoverde Unit (e.g. limestone and dolomite and dolomitic limestone) and to the Voltri Unit (e.g. metasediment, metabasite,

metagabbro, serpentinites, and lherzolitic peridotites). However, the lithotypes belonging to the Tertiary Piedmont Basin are different; in fact it is assumed that the RSZ1 structures may have mainly interacted with the formation of "Brecce di Costa Cravara" and minimally with the formation of "Conglomerati di Molare", as the latter is dated to Oligocene; instead the RSZ2, and hence the fluid that have interested these structures, have interacted with both these formations, supported by the local deformation of the "Conglomerati di Molare" deposits by the D4 folds (Capponi and Crispini 2002; Carrapa and Garcia-Castellanos, 2005; Mosca et al., 2010; Maino et al., 2013; Federico et al., 2014). The geochemical data obtained by Giorza (2010) on the fluid inclusion related to the metasomatic alteration ALT-1 and ALT-2, support this hypothesis, showing only a slightly compositional variation between the two different alterations.

Furthermore, since the gold mineralisations in the area, and at more large-scale in the Voltri Massif, are mostly located nearby the TPB deposits, hence the transgressive contact between the TPB deposits and the underlying units may have played an important role in the fluid circulation. In fact it is also a lithological contact with on one side sedimentary rocks characterised by diffuse primary porosity, linked to the heterometric dimension of the clasts, and on the other side metamorphic rocks characterised mainly by a secondary porosity, linked to the fault zones. The circulation of the rising up fluids would pass from a canalized flow, driven from the damage zone of the faults to a diffused flow. The results of this change of flow could be a deceleration of the circulation of the fluids, and a concentration of the fluids near this contact, with a consequent major fluid-rock interaction and consequently and increase mineralisations.

On the other hand, taking into account the structural setting of the Lavangina Lakes area within the Voltri Massif, the structures that at local and regional scales may have played a greater role are of two types:

- high-angle to sub-vertical faults, observed both in the analysed area (Fig. 96, 98, 101), and identified on aerial photographs and described by Crispini et al. (2009) in the whole Voltri Massif (Fig. 100, 102). These structures can be considered the main pathway for fluid infiltration to

depth or as preferential pathway for fluids ascend along high vertical permeability zones produced by the main fault systems;

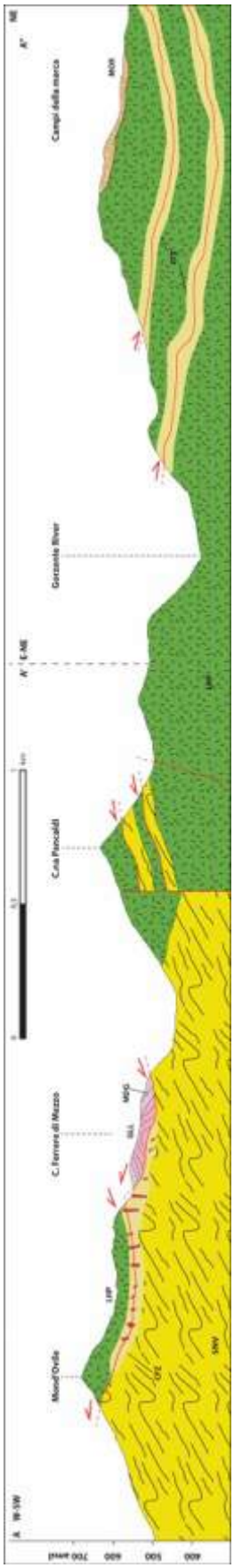

Figure 101: Geological cross-section of the Lavagnina Lakes area, the location of the trace of the cross-section, and the legend of the colours and symbols are reported in Fig. 96.

Figure 102: Map of the tectonic lineament interpreted from aerial photographs, from Crispini et al., 2009.

- reverse shear zones, as the RSZ1 and RSZ2 in the analysed area (Fig. 96, 98, 101), and comparable structures described in the Voltri Massif (Spagnolo et al., 2007; Crispini et al., 2009; Federico et al., 2009). These structures may have intercepted the fluid, at different depth, and take them back to the surface.

Finally, the different depths of the RSZ1 (4-11 km) and the RSZ2 (3-9 km) may have influenced the fluid canalization and consequently fluid-rock interaction (e.g. carbonation):

- firstly the two systems of reverse shear zones show different brittle-ductile behaviour; in fact the RSZ2 shows a more brittle behaviour with the development of more abundant fault gouges, with respect to the RSZ1. Then the RSZ2 may have represented a preferential pathway for the fluid circulation channelling huge volume of fluids, resulting in a major volume of carbonate metasomatism.
- secondly, the major depth of the RSZ1, also linked with their more ductile behaviour, can lead to suppose that this structures were not always able to bring the fluids up to the surface, and hence, on the field, probably they do not show their real volumetric interaction with the bedrock, with a buried portion.

9.10 – Comparison with the gold mineralisations of the Western Alps

Mesothermal gold lodes are widespread in orogenic belts of all ages; the chemistry of ore-forming fluids and the late orogenic timing of the deposits are remarkably similar through time and space (Pettke et al., 2000). So, for the peculiar geographical and the geological location of the analysed area, and the Voltri Massif in general, could be interesting a comparison with the gold-mineralisations described in the Western Alps.

Gold-bearing quartz veins occur sporadically over a 140 km length of the Western Alps, from Simplon (near the Swiss border) in the north, to Gran Paradiso (Italy), in the south (Diamond and Wiedenbeck; 1986). The similarities of all these mineralisations in their mineral parageneses, the epigenetic structural conditions unify these occurrences in a unique metallogenic district firstly named by Huttenlocker (1934) as the "Monte Rosa Gold District".

In the past, many authors (e.g. Dal Piaz et al., 1979; Dal Piaz and Venturelli, 1983; Diamond and Wiedenbeck, 1986) studied this district, and highlighted that the age of the gold-bearing veins (mid-Oligocene, ca. 32 Ma) coincide with the late-Alpine magmatic intrusions, supporting the hypothesis that these deposits of the western Alps may be genetically related to the late-Alpine phase of intrusive magmatism.

Soon after, Curti (1987) through the analysis of the oxygen isotopes accordingly to the Pb isotopic data in the same area, assumed that the fluids were generated by metamorphic devolatilization within the metasediments. Pettke et al. (2000), studied particularly the Brusson area, in the southwest of the district; they constrained temperatures between the 250-340 C°, estimating 5 to 12 km depth development. The veins emplacement was markedly diachronous dated from 10 Ma years for the veins from Crodo to ca. 31-32 Ma in the Brusson area (Pettke et al., 2000). The new age data demonstrate that only the deposits in the southwest of the district are coeval with magmatism, instead the remaining deposits are as much as 20 m.y. younger.

Accordingly to chemical and Sr and Pb isotopic fluid signatures that match those of the hydrothermal fluids, Pettke et al. (2000) supported the metamorphic origin of the gold-bearing fluids firstly proposed by Curti (1987) at least for the younger set of mineralisations (10 Ma). They linked the origin of the gold bearing fluids to the metamorphic devolatilization of Mesozoic calcschist below the Brusson district, assuming a fundamental role of the structures in the rise of the fluids.

The gold-bearing mineralisations described for the Lavagnina Lakes area, and for the whole Voltri Massif, show several similarities with the mineralisations described in literature (Dal Piaz et al., 1979; Dal Piaz and Venturelli, 1983; Diamond and Wiedenbeck, 1986; Curti, 1987; Pettke et al., 2000) for the "Monte Rosa Gold District":

- are both related to the late-Alpine orogenic tectonics;
- similar ages from 35 to ca. 20 Ma estimated for the mineralisations in the study area and from 35 to 10 Ma for the Brusson-Crodo mineralisations;
- similar depths from 3 to 11 km for the RSZ systems in the Voltri Massif, and between 5 to 12 km depth for the Brusson area veins;
- the mineralisations are related to second or third order tectonic structures;
- gold-mineralisations are both linked to quartz-carbonate veins;
- Similar estimated temperatures from 250 to 300 C° for the veins of the study area and 240 to 300 C° for the veins of the Brusson area.

9.11 – The Bisciarelle Creek Thrust Fault

9.11.1 – Structural evolution

The Bisciarelle fault is a late-orogenic, brittle reverse fault cutting the lherzolite of the Voltri Massif, Ligurian Alps, Italy. This fault is co-genetic with quartz-carbonate faults hosting orogenic Au deposits. For its attitude, the tectonic direction of movement and for the deformational events can be related to the younger system of regional reverse shear zones (RSZ2), also compared to what described for the Voltri Massif by Capponi and Crispini, 2002 and Federico et al., 2005. This set of reverse faults is linked to a dextral transpressive zone, which affected the Lavagnina Lake area active during Oligo-Miocene time (Spagnolo et al., 2007).

The analysed structure is developed near the lithological transition between serpentinized lherzolites, at the hanging wall, and the serpentinites that make up the footwall. Two hypothesis may be proposed for the presence of the serpentinites along the Bisciarelle Creek thrust fault:

- the serpentinites are coeval with the development of the thrust fault, and the serpentinization of the wall rock could be related and could have be enhanced by the syn-kinematic fluid flow channelized by the fault, or
- the serpentinites were pre-existent to the development of the fault.

If the serpentinization of the wall rock was related to the fault, the serpentinites should be more developed near the fault core, probably without relicts of the pristine rock, and with a decreasing degree of serpentinization moving away from the core.

Instead, if the serpentinites were pre-existent to the development of the fault, mineralogical relicts of the pristine rock should be found, as observed in the Bisciarelle Creek thrust fault. Especially, as support of this second hypothesis, in the damage zone of the Bisciarelle fault there are different kind fault rocks made up of serpentinite clasts as: serpentinite schist foliated fault gouge, the carbonated fault gouge with serpentinite clasts, cataclasites over the serpentinites and the

hydraulic breccias made up of serpentinite clasts surrounded by carbonates (described in detail in chapter 5.3.4.1).

Hence, the most sustainable hypothesis seem to be that the serpentinites were pre-existent to the fault development.

The Bisciarelle Creek thrust fault shows an asymmetric damage zone, more developed in the footwall with respect to the hanging wall, with several meters of different fault rock types as described in chapter 5.3.4.1. This asymmetry should be enhanced by the syn-kinematic carbonation that has led to a further variation of the lithological contrast: the syn-kinematic carbonation predominantly took place along the fault core producing the metric dolomite level, which shows evidence for successive shear localization, and along the footwall with several meters of carbonated fault rock.

How can this asymmetry in this fault damage zone be explained? In literature asymmetric rupture propagation has been observed, in all fault types (normal, reverse and strike-slip fault) in most large earthquakes (Bhat et al., 2010), and McGuire et al. (2002) show that about 80% of the shallow earthquakes, which have occurred since 1994, were characterised by asymmetric propagation over the fault plane.

On the base of simulations of dynamic ruptures with off-fault plastic yielding Ben-Zion and Shi (2005) suggested that strongly asymmetric damage zones are the cumulative product of earthquakes rupture. Repeating occurrences of such ruptures is expected to produce strongly asymmetric rock damage zone (Ben-Zion, 2001; Shi and Ben-Zion, 2006; Mitchell et al., 2011), as described for the Bisciarelle fault. When subsonic ruptures propagates in the direction of the slip on the compliant side of the wall (in the case of a thrust the compliant side is the hanging wall), there is a dynamic reduction of normal stress across the fault, instead for rupture propagation in the opposite direction there is a dynamic increase of normal stress (Shi and Ben-Zion, 2006) that lead to the asymmetric development of the damage zone. The magnitudes of these effects increase with the propagation velocity, the degree of material contrast across the fault, and the propagation distance along the fault (Ranjith and Rice, 2001).

Hence, the asymmetry that characterises the damage zone of the Bisciarelle zone should be the result of cumulative seismic ruptures.

9.11.2 – Mass transfer of the fluid-rock interactions

Through the mass transfer profiles was possible to identify and quantify the elements transferred from the fluid to the wall rock, that generate the intense carbonation along the Bisciarelle fault, and *vice versa* .

In the RB10-RB1 dataset, the volatiles (H_2O and CO_2) and Sb are the only components that show profiles which indicate transfer, of these components, from the fluid to the wall rock. As discussed in chapter 7, a combination of diffusional transport and precipitation in microfractures took place close to the fault, and this does not allow an evaluation of the true mass transfer adjacent to the fault. Therefore, the mass transfer values calculated close to the fault contact should be taken as semi-quantitative. Although in the field the carbonation of the Bisciarelle Creek thrust fault was progressive and homogeneous, so these profiles highlight that it could be much more complex and extremely linked to the development of microstructures not visible in the field.

With regard to the other components (i.e. L.O.I. and CaO) that were systematically transferred from the fluid to the rock, Sb shows additions that vary between 0.2 and 5 g per ton of protolith. The vast majority of all other components (i.e. Cr, Co, Fe_2O_3) show profiles with mixed mass transfers corresponding to both additions and subtractions with respect to the protolith (i.e., positive and negative excursions of the profiles across the zero-mass-change line). Within the considered distance from the fault core, the coupled peaks mark the transfer from the fluid to the rock of SiO_2, MgO, Fe_2O_3, Ba, Nb, Ta, Sn, and U, which are associated with the precipitation of carbonates and chalcedony micro veins within the damage zone of the fault.

Both small veins and short-range mobilisation with consequent re-precipitation are not homogeneously distributed and hence are not strictly related to the distance from the fault core.

Mass transfer data show unequivocally that at Bisciarelle the dolomite and smectite alteration occurred during intense carbonation and hydration of the host lherzolite, but without a substantial transfer of other chemical elements. This evidence is typical for the carbonation of ultramafic rocks, where mineralogical transformations are achieved isochemically with the exception for the volatiles (Hansen et al., 2005). This implies that the precipitation of the hydrothermal suite

of metals, described in chapter 8, within the fault pearls (Pb, W, Cu) and chalcedony (Sb, Ag, Au, In) was entirely a fault-controlled process, and that the host rock took a poor record of this hydrothermal circulation. Interestingly, the evidence for transfer of Si, Fe, Co, and Cr from the lherzolite to the fault provides a strong indication that the enrichment of these elements in fault pearls and chalcedony was actually possible due to this transfer. Therefore, the composition of the fault fluid was actually modified by the transfer of some wall rock components, and such transfer played a fundamental role in determining the physical properties of key structural features of the fault.

Since the precipitation of the hydrothermal suite of metals, above described, was entirely a fault-controlled process, this is an evidence that support that the development of the fault pearls and the chalcedony shear veins is also fault-controlled and related to this syn-kinematic hydrothermal process.

9.11.3 – Morphometric image analysis of fault pearls

The morphometric image analysis results (described in chapter 5.3.5) show that the fault pearls have circular shape irrespective to the direction of observation (parallel and orthogonal to the slickenlines), with values that indicate a nearly perfect circular shape. These values are in line with the roundness values, hence the fault pearls in three-dimensions can be considered as nearly perfect spheres or as very spherical textures.

Therefore as well sorted spherical objects, they seem to be related only to mineral precipitation syn-kinematic to the fault movement. This hypothesis is also witnessed by the orientation data, that show a weak peak at 101° on the face parallel to the slickenlines, which show that the orientation of some of the fault pearls is linked to the fault movement.

Moreover there is no close packing, no indentation or pressure solution evidences between different grains of the smallest fault pearls in the sample because carbonates and in part chalcedony matrix occupy the volume between distinct grains.

9.11.4 – Meso- and microtextures

Fault meso-structures with textural and compositional characteristics that are somewhat similar to those described here are the clast cortex aggregates (Rempe et al., 2014; Smith et al., 2011). These are composite grains that form at the slipping zones of faults and are made of a central clast and an outer fine-grained cortex. In contrast with the fault pearls, the shape of these aggregates is poorly rounded and their textures is cataclastic and lacks banding. Moreover, the fault pearls are texturally and genetically different from clast-cortex grains described in literature in other fault contexts, because the clasts-cortex grains consist of core grains (quartz, lithic clasts, or clasts of older cemented gouge) with concentric coating of smaller clasts in a fine-grained matrix; differently, our fault pearls only rarely show a core clast of different nature and the coating is made of newly crystallized carbonates and not of smaller existing clasts, sticked together. Thus, their genetic mechanism must be distinct from that of the fault pearls.

However, our pearls are really similar to pisolite or cave pearls (e.g. Nader, 2007), related to vadose groundwater circulation or to oolite/pisolite deposits related to hydrothermal circulation (Sant'Anna et al., 2004; Wu et al., 2014).

Moreover, I can exclude the possibility of a pre-existent pisolite-rich limestone cut by the fault because: *i)* its movement would have resulted in a pervasive cataclasis of the carbonatic horizon. *ii)* The growth of pisolites did not occur after the end of the fault activity because evidence of truncation of the grains by both shear surfaces and chalcedony shear veins locally exist; *iii)* if these grains formed during a period of inactivity of the fault they would again been damaged by the following slip as in *i*).

Key genetic constraints are *i)* the essentially syn-deformational and epitaxial growth of the fault pearls; *ii)* the growth of chalcedony in the vuggs between distinct fault pearls and in the chalcedony shear veins. These are uncommon constraints for a fault zone, but exclude fault pearls growth during post-deformation fault filling.

The chalcedony described in the chalcedony shear veins and in the fault pearls matrix, shows dispersed moss, jigsaw, flamboyant textures, and fibrous chalcedony with epitaxial growth. All these textures, suggest a rapid precipitation of silica gel and subsequent recrystallization.

The deposition of silica gel and amorphous silica has been related to the boiling of the fluids in response to fast fault slip linked to seismic activity (Moncada et al., 2012); this gel produces lubrication along the fault surface with consequent dynamic strength reduction, which is fundamental for earthquake propagation (Di Toro et al., 2004; Rice, 2006; Kirkpatrick et al., 2013).

The boiling of the fluids may be due to two aspects of fast fault slip: *i*) the rapid increase in temperature of the fluid, which in the case of a fault would be related to the shear heating, *ii*) the rapid decrease of pressure as a consequence of the fracture opening, or *iii*) the concomitance of both shear heating and decrease of pressure. The boiling of the fluids is the instantaneous vaporization of the liquid phase (Moncada et al., 2012), and the exact proportion of the fluids that will vaporize depends on the P-T conditions of the system as well as on the ability of the fluid to extract "excess heat" from the surrounding wallrock (Henley and Huges, 2000). In case of boiling, amorphous silica with colloform textures will precipitate (Moncada et al., 2012). This peculiar genesis process would be responsible for the lack of fluid inclusions, as observed in all the quartz samples of the analysed area. In fact as described by Herrington and Wilkinson (1993) the dynamic recrystallization over silica gel or amorphous silica is responsible for the obliteration of primary fluid inclusions.

The fast fault slip is testified by several textures: quartz surrounded by filamentous silica matrix at the top of the chalcedony shear veins, injection veins along slip surfaces, mirror-like slip surfaces and vesicular porosity.

Filamentous silica, observed on the top of the chalcedony shear surfaces, is similar to the glass filaments related to the mechanical amorphization developed in experiments of quartz sand deformation at high slip velocities (V>10 cm s-1: Hayward et al., 2016), and this filamentous matrix is similar in appearance to the gels reported during high-velocity sliding experiments on quartz interfaces (Di Toro et al., 2004).

Moreover, as described by Kirkpatrick et al. (2013) the dynamic reduction of fault strength, as a function of slip or slip rate is fundamental to earthquake propagation, and the silica gel lubrication is one of the variety of mechanisms proposed to cause coseismic weakening based on theoretical and experimental work. They described a shiny layer of 0.5 to 3.0 mm thick layer of translucent silica that cover the slip surfaces of the Corona Heights fault in San Francisco.

Kirkpatrick et al. (2013) interpreted this silica layer as syn-kinematic; acting as a dynamic weakening mechanism during coseismic slip at shallow crustal levels. Hence the development of syn-kinematic chalcedony shear veins (ca. 10 cm thick) at the top of the fault core could have acted as a weakening process during coseismic slips, causing a shear localization inside the shear veins, preventing the comminution and the cataclastic deformation of the fault pearls. Injection veins have been observed to be linked to the chalcedony shear veins. These kinds of veins have been interpreted as injection of fluidized gouge into off-fault cracks (Rowe et al., 2012 a, b and reference therein). These injection veins, as described in chapter 8, are up to 10 mm long and 2 mm wide, with an aspect ratio (width/length) of 0.2 similar to those described for the pseudotachylites by Rowe et al. (2012b).

For the opening of similar structures, is required a net internal pressure (ΔP), which has been estimated from the following equation (Rubin, 1995):

$$\Delta P = M \frac{w_0}{2l}$$

where w_0 is the maximum crack width, l is the crack length, and M is the stiffness (μ/(1-ν) where μ is the shear modulus and ν is the Poisson's ratio). For estimate the net internal pressure, has been used the shear modulus and the Poisson's ratio of the dolostone (Tab. 9), since the observed injection veins are host inside the dolomitic level of the fault core.

The ΔP estimated for the injection veins produce a ΔP= 5.8 x 10^9 Pa; this number would be reduced by up to one order of magnitude if the wall rock is sufficiently damaged. Moreover, this value is almost the same for the Asbestos Mountain fault zone pseudotachylites (Fig. 103) obtained by Rowe et al. (2012b).

Hence, the observed injection veins have the same aspect ratio and the same ΔP of pseudotachylites suggesting, as described by Rowe et al. (2012b), that both form coseismically.

Rock type	Poisson's ratio (ν)	Shear modulus (μ; Pa)
Dolostone	0.28 (Kulhawy, 1975)	2.8 x 10^8 (Agosta et al., 2007)

Table 9: Value used in injection vein pressure calculations.

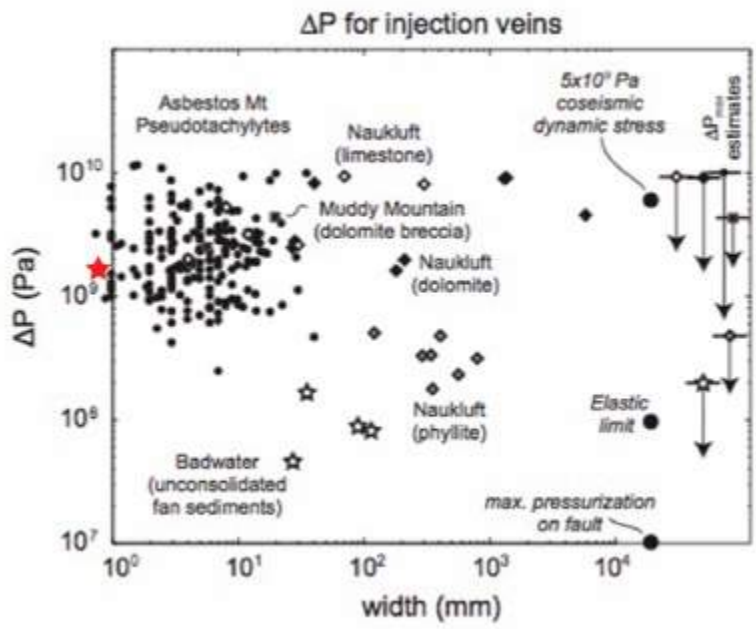

Figure 103: Calculated overpressure limits (ΔP) from pseudotachylites and granular injection veins (Rowe et al., 2012b). The red star represent the data obtained for the calculated overpressure of the Bisciarelle fault.

Along slip surfaces in carbonates there are clear evidences for friction marked by intense comminution and vesicular porosity, which can be linked to thermal dissociation of carbonates due to fast slip (Rowe and Griffith, 2015 and reference therein) and consequent shear heating. The top of these slip surfaces shows characteristics similar to the mirror-like slip surface, as described in chapter 8. The genesis of these mirror-like surfaces has been documented in experimental work and is linked to extreme shear localization during high velocity fault slip, and the available data generally suggest that these surfaces do not form without elevated temperature on the slip surfaces, with thermal breakdown of the carbonates (Rowe and Griffith, 2015 and reference therein).

9.11.5 – LA-ICP-TOFMS data of the fault pearls

Another key genetic constraint for the fault pearls levels is the precipitation from a hydrothermal fluid. Current knowledge on orogenic Au deposits indicates that these mineralized fault networks form due to the flux of volumes of chemically uniform hydrothermal fluids (Garofalo et al., 2014). These fluids were:

- aqueous-carbonic in composition (5-20 mol% CO_2),
- had a T in the 200-400 °C range at the time of mineralisation,
- were at (or close to) their boiling point, and
- were enriched in As, Sb, B, and Au (Garofalo et al., 2014).

A similar fluid must have been involved in the formation of the Bisciarelle fault.

Mineral paragenesis and elemental imaging by LA-ICP-TOFMS confirm the hypothesis of hydrothermal derivation of the fault rock. This is best evaluated by comparing the concentration ranges of the key trace elements As, Sb, In, Ga, Ag, Zn, and Cu of fault pearls levels and chalcedony with those of the same elements in the average upper crust (Rudnick and Gao, 2003). Such comparison clearly shows that the peak concentrations of these elements are 5 (Cu, Zn) to 50 (Sb, In) times higher than those of the upper crust, demonstrating that the Bisciarelle fault fluid was capable to transport and deposit a suite of ore elements.

These evidences are fundamental to discuss the possible origin of the fluids that developed the carbonation and the fluid-rock interactions along the Bisciarelle thrust fault and along the main fault of the Lavagnina Lakes area (see paragraph 9.3).

9.11.6 – Genesis of the fault pearls

On the basis of all the constraints above described, I proposed two models for the development of such peculiar textures.

The first mechanism proposed for the development of such peculiar textures is the process known as *transient* boiling in microfluidic industry (Zhao et al., 2000; Visentini et al., 2013), which is also described as “nucleate” boiling (Dhir, 1991). Transient boiling is reported in many micromechanical devices (e.g., cladding tubes of nuclear reactors) as a process whereby liquids flowing in thin cavities are

instantaneously overheated (by 10-30 °C) to generate a vapour phase that expands up to explosive boiling. Experimental (Lida et al., 1993; Visentini et al., 2013) and numerical (Wang et al., 2017) studies show that this process is transient because the overheating conditions are met for tens of μs, and that during this time a myriad of expanding vapour bubbles fill the volume initially occupied by the liquid. If the Bisciarelle fault core developed according to this mechanism, fault pearls and matrix formed together and instantaneously and their texture would reflect stages of mineral deposition during bubble growth. Thus, the closely packed fault pearls would represent the mineralized products of vapour generated by the transient boiling of the hydrothermal fluid at ~250 °C and the porous fault pearls matrix would represent the co-existing liquid phase. The concentric bands of the large fault pearls would be a product of boiling events during which some fault pearls expand at the expenses of the small ones with a sequence of stops and onsets (pulses) that were probably governed by variations of T and P_{vap} at the fracture wall. Competitive bubble growth and cyclic variations of P_{vap} were described by experimental (Visentini et al., 2013; Zhao et al., 2000) and numerical (Dhir, 1991) studies of transient boiling.

According to this model, a fault pearls level could result from an initial shear heating event, testified by the several shear surfaces with textures linkable to high velocity slip, followed by precipitation of dolomite from the expanding vapour at the vapour-liquid interface. This is documented for dolomite in vapour precipitation processes in which vapour bubbles represent heterogeneous nucleation sites (e.g., Babu et al., 2016; Tsuchiya et al., 2017). Such mechanism is characterised by epitaxial growth (Sunagawa, 1978), which is observed in the fault pearls. Dolomite deposition took place at about 250 °C, i.e., a temperature at which carbonates are known to be part of boiling assemblages in mineral deposits (Drummond and Ohmoto, 1985).

Transient boiling is consistent with the chemical compositions of fault pearls, matrix, and chalcedony. The fault pearls composition would reflect that of the vapour phase, i.e., essentially CO_2 precipitating dolomite. In contrast, the compositions of the thin/massive fault pearls bands and of the porous fault pearls matrix – which are both fine grained and enriched in a large number of poorly volatile elements (e.g., Fe, Al, K, Sr, Cr, Zn, etc.) – would reflect the composition of the liquid phase of the boiling fluid, in agreement with experimental data (cf.

Pokrovski et al., 2005). Thin bands and fault pearls matrix have similar compositions because they both represent the liquid phase of the transiently boiling hydrothermal fluid.

Finally, the chalcedony shear veins would represent the precipitation product of an Ag-As-Ga-Sb-In-rich ore fluid that lost CO_2 due to boiling.

The second model proposed for the development of the fault pearls is related to a development during several cycle of hydrothermal fluid flows (T around 250°C), coeval with a stick-slip movement, with cycles of fluid pressure build-ups, fault opening, fluid flushing, and mineral precipitation during the seismic failure of the fault, according to what proposed by Sibson et al. (1988).

In Figure 104 I sketched the inferred stages, which led to the development of the above described meso- and microstructures. At T1 (Fig. 104) incipient first slipping events, linked to the fluid pressure raise. Between T1 and T2, thanks to fluid pressure, the fault opens.

At T2a (Fig. 104) the co-seismic slipping, due to over-pressured fluids, leads to brecciation of the wall rock, recorded by the hydraulic breccia. Impurities within the fluid, consisting both of micro-clasts or crystallites, act as growth center for the fault pearls, particularly the serpentinite micro-clasts produce the minor fault pearls with carbonated serpentinite core. The fluid flushing along the structure and the resulting fluid-rock interaction also leads to clast and fault walls carbonation. The carbonation of serpentinite leads to the formation of Ca+Mg±Fe carbonates, with the release of SiO_2 into the fluids. The almost total lack of silica, associated with carbonates, indicates a high pH, that holds the silica in solution and enhances the precipitation of carbonates (Akbulut et al., 2006). Even if small quantities of chalcedony is present in the vuggs between the pearls, it may be due to the fluctuation in the pH conditions linked to the cyclic precipitation of carbonates.

At T2b (Fig. 104), during the initial phase of rapid pressure drop linked to the seismic rupture, the radial texture of the pearls develops similarly to the growth of sferulites (Beck and Andreassen, 2010); this stage is comparable to grain-inertial flow (Rowe and Griffith, 2015 and reference therein). Then, during the new stage of fluid pressure build up, the fluid flushing stage, comparable to the laminar flow (Rowe and Griffith, 2015), the fault pearls develop their laminated texture (T3, Fig. 104). These events (T2a-T3) of static

and dynamic overpressure are repeated cyclically during a stick-slip movement, as witnessed by the several sets of concentric layers, recognized in the fault pearls.

Once the fluids precipitated the carbonate component, developing the carbonate matrix filling the vuggs between distinct grains, the fault core become a high-strength level. Then, after the total carbonates precipitation, a relatively silica enrichment occurs into the fluids until its saturation.

At T4 stage (Fig. 104) the fast fault slip, testified by the mirror-like slip surfaces, injection veins and chalcedony shear veins, causes the flashing of fluid in response to seismic activity producing a rise in fluid pressure and consequent fault opening. The rapid opening, also witnessed by fault pearls microbreccia, can induce the fluid pressure drop causing the liquid phase to instantly vaporize. In this case amorphous silica gel with widespread gold particles will precipitate. Microstructural quartz assemblages and chalcedony non-oriented porosity witness fast slips and flash vaporization of fluids. These textures compared with those described by Moncada et al., (2012), can be explained by evolution from silica gel, which solidified as hydrous silica then recrystallized to anhydrous quartz (Faber et al., 2014). The presence of amorphous silica gel leads to an almost complete loss of strength along slip surfaces (Faber et al., 2014), preventing the fault pearls from being fully brecciated during this stage. The occurrence of two types of chalcedony veins (VA-VB described in chapter 8) testify the cyclicity of vaporization; their filamentous surfaces are related to the mechanical amorphization and constitute a low-strenght level that possibly acted as further preventer of brecciation of fault pearls.

The close association of fault pearls with seismic-related structures such as sub-micron carbonate coating of slip surfaces, quartz microtexture related to silica gel deposition, and syn-kinematic filamentous phase along slip zone support the hypothesis that also the fault pearls are paleo-seismic events indicators. On the whole, the association of all these structures record paleo-seismic events. Nanograins cause weakening mostly at high slip rates, coinciding with the development of fault mirror surfaces, which are due to extreme localization of slip only at high-velocity and not at sub-seismic slip velocities (Rowe and Griffith, 2015 and reference therein). Several co-seismic

processes can produce amorphous materials, e.g. precipitation from fluid, related to fluid flashing (Moncada et al., 2012), or mechanical processes, related to loss of structure (Hayward et al., 2016).

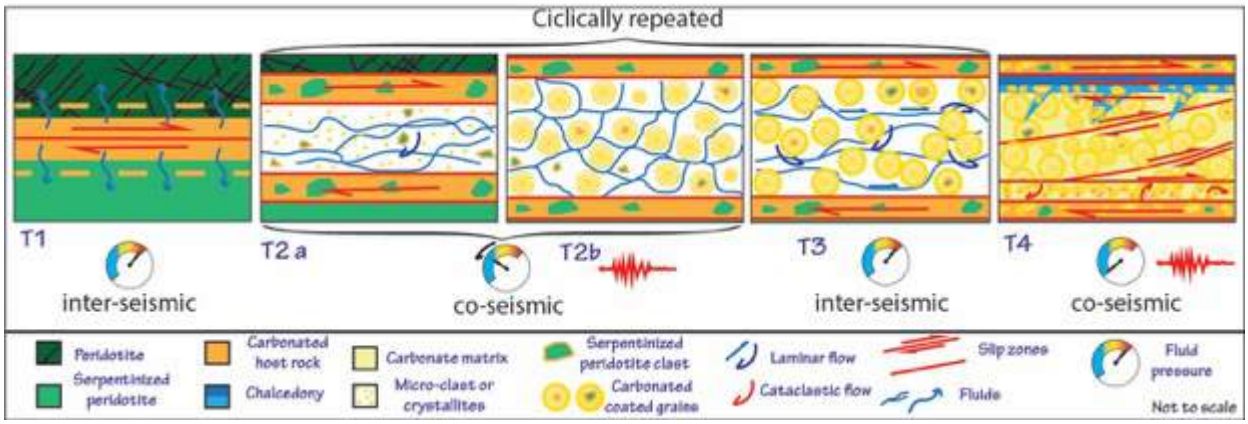

Figure 104: Structural evolution of fault pearls simplified scheme (not to scale).

Although both the two models proposed fit the presented and described data with similar degree of reliability, to decide which of the two effectively led to the development of the fault pearls, are necessary further analysis as 3D tomography to effectively demonstrate that the fault pearls did not grow in contact. Moreover, for the first time Prokofiev et al. (2017) described the natural occurrence of colloidal silica inclusions in chalcedony-hosted vacuoles similar to the moss-textures described in the chalcedony shear veins of the Bisciarelle Creek thrust fault; so another possibility is to look for and analyse similar colloidal silica inclusions in the samples of the area to better constrain the P-T conditions and chemical composition of the fluids and therefore provide a direct evidence for the boiling.

9.11.7 – Concluding remarks about the fault pearls

The close association of fault pearls with seismic-related structures such as sub-micron carbonates coating of slip surfaces, quartz microtexture related to silica gel deposition, syn-kinematic filamentous phase, injection veins with similar characteristics and overpressure with respect to seismic pseudotachylites along slip zone supports the hypothesis that fault pearls developed during shear events at seismic rates, and hence are considerable as paleo-seismic events indicators.

On the whole, the association of all these structures record paleo-seismic events. Nanograins cause weakening mostly at high slip rates, coinciding with the development of fault mirror surfaces, which are due to extreme localization of slip only at high-velocity and not at sub-seismic slip velocities (Rowe and Griffith, 2015 and reference therein). Several co-seismic processes can produce amorphous materials, e.g. precipitation from fluid, related to fluid boiling (Moncada et al., 2012), or mechanical processes, related to loss of structure (Hayward et al., 2016).

Fault pearls described along this fault are new in the geological record, and so is the possibility that boiling hydrothermal fluids within faults may generate undeformed, static structures at seismic velocity. The Bisciarelle fault could represent a good example of such case; however, the poor documentation of fault pearls in field studies suggests that they are either rare, or alternatively overlooked.

10 – Concluding remarks

The Lavagnina Lakes area revealed interesting information about the ductile, brittle-ductile to pure brittle structures in ultramafic rocks and the consequences of fluid-rock interaction processes in these structures; moreover this study furnished new hints on the formation of gold and chalcedony hydrothermal mineralization along faults.

The Lavagnina Lakes area is mainly characterized by the occurrence of high-pressure metaophiolite of the Voltri Massif in contact in the North-Eastern sector with sedimentary rocks of the Tertiary Piedmont Basin. The area of the Lavagnina Lakes is known since the Roman age for its gold deposits along the Gorzente River (Pipino, 2001); the most interesting gold mineralisations of the Lavagnina Lakes area could be divided into two types: *i*) quartz vein systems, or *ii*) lode mineralization related to fault-linked listvenites.

On the basis of the geological survey and the field data presented in this work, the study area, during late- to post-orogenic evolution, underwent a complex polyphasic tectonic history comparable to the one described for other areas of the Voltri Massif.

The mesoscale structural data suggest that in the Lavagnina Lakes area the late-orogenic evolution went from late-Eocene to Present and recorded both the last stages of the Alpine history and the first events of the Apennine tectonics. In the analysed domains, the interaction between the two orogenic phases resulted in a complex superposition of upper crustal deformations (UCD) that are linked to different structural levels.

The upper crustal levels deformation (UCD) are characterised by brittle-ductile to brittle structures and are mainly represented by three main tectonic phases (i.e. D3, D4, and D5).

The older D3 event caused the development of dragged fold with chevron style and of reverse shear zones (RSZ1) and has been related to the first early orogenic stage described for the Western Alps evolution (pre-35 Ma), associated with nappe stacking and early stages of exhumation of parts of nappes buried to high-P.

The D4 event caused the development of open parallel folds and of reverse shear zones (RSZ2-A, RSZ2-B); RSZ2-A have been related to the second orogenic stage of the Western Alps evolution (35-25 Ma), that can reliably be linked to

thrusting along the Penninic Front; RSZ2-B are possibly linked to the beginning of the third orogenic stage of the Western Alps evolution (25 Ma to present), associated to the oroclinal bending in the southernmost Alpine chain.

The younger event (D5 event) has been related to a late extensional / transtensional reactivation phase of the pre-existing discontinuities, developed during the post collisional evolution.

The detailed study of RSZs structures in the Lavagnina Lakes area showed that, though they are similar in attitude to other RSZs widespread throughout the Voltri Massif, they contain particular mineralisations (e.g. gold and chalcedony) and structures that have been described for the first time in this work.

Analysing general RSZ2 structures and in particular the Bisciarelle Creek Fault, it appears clear that the fluid involved in the development of gold mineralization of the Lavagnina Lakes area can be related to a tectonically driven hydrothermal system and/or orogenic system gold deposits.

The mapping of gold mineralization and of chalcedony occurrences in the Voltri Massif allowed to highlight that, at a km-scale, they occur along a lineation of mineralization associated with chalcedony and quartz veins. At regional scale this lineation is oriented mainly NNW-SSE, similarly to the axes trend of D4 folds. Hence the RSZ2 in the Voltri Massif could effectively represent a regional tectonically driven hydrothermal systems.

A detailed outcrop-scale investigation highlighted that the Bisciarelle Creek Thrust fault, that I related to the RSZ2 system, shows peculiar fault textures, organized in bands, called fault pearls.

This fault (exposed for ca. 100 m) shows a complex core characterised by parallel to sub-parallel multiphase slip surfaces that are mainly sub-horizontal or gently dipping to W-SW with top to NE; it is coeval with syntectonic Au-bearing quartz and chalcedony shear veins.

Fault activity was accompanied by fluid infiltration that caused an almost complete replacement of the original host rock mineralogy, now characterised mainly by dolomite and ferroan-dolomite and smectite alteration. Fluid infiltration and related mineral by mineral replacement were enhanced by schistosity and veins.

Micro-structural investigations revealed that fault pearls, which characterise the Bisciarelle fault core, are novel and unique textures never reported in

literature. The most similar fault meso-structures, in term of textural and compositional characteristics, to those described here, are the clast cortex aggregates. The clasts-cortex grains however consist of core grains (quartz, lithic clasts, or clasts of older cemented gouge) with concentric coating of smaller clasts in a fine-grained matrix; on the other hand, our fault pearls rarely show a core clast of different nature and the coating is made of newly crystallized carbonates and not of smaller existing clasts, sticked together. Thus, the genetic mechanism of clasts-cortex grains must be distinct from that of the fault pearls.

The fault pearls are moreover associated with injection veins, carbonate shear surface with characteristic similar to mirror-like surface, vescicular porosity, chalcedony shear veins with textures testifying crystallization over silica gel, chalcedony shear surface characterised by quartz surrounded by filamentous silica matrix; in literature all these textures are related to fast slip and possible paleo-seismic events.

The morphometric image analysis showed that the fault pearls are well-sorted spherical objects and they seem to be related only to mineral precipitation syn-kinematic to the fault movement. This hypothesis is also supported by the orientation data of the fault pearls, that show a weak peak at 101° on the face parallel to the slickenlines. Single-spot SEM-EDS analyses revealed that ferroan dolomite makes the pearl bands (CaO: 29.13±2.33 wt%; MgO: 19.03±4.86 wt%; FeO: 1.77±0.87 wt%) and that minor compositional variations across large and thin bands exist.

In general, mass transfer data show unequivocally that at the Bisciarelle Creek Thrust fault the dolomite and smectite alteration occurred during intense carbonation and hydration of the host lherzolite, but without a substantial transfer of other chemical elements. This evidence is typical for the carbonation of ultramafic rocks, where mineralogical transformations are achieved isochemically with the exception for the volatiles. This implies that the precipitation of the hydrothermal suite of metals within the fault pearls (Pb, W, Cu) and chalcedony (Sb, Ag, Au, In) was entirely a fault-controlled process, and that the host-rock took a poor record of this hydrothermal circulation.

Elemental imaging by LA-ICPTOFMS provides a detailed account of the distribution of chemical elements within pearls, matrix, and chalcedony shear veins, confirming the hypothesis of hydrothermal derivation of the fault rock.

Hence, considering all these constraints, I propose two models for the genesis of such peculiar textures:

i) the first proposed mechanism is the process known as *transient* boiling in microfluidic industry, which is also described as "nucleate" boiling. Thus, the closely packed pearls would represent the mineralized products of vapor generated by the transient boiling of the hydrothermal fluid at ~250 °C and the porous pearl matrix would represent the co-existing liquid phase;

ii) the second model envisages the development of the fault pearls during several cycle of hydrothermal fluid flows (T around 250°C), coeval with a stick-slip movement, with cycles of fluid pressure build-up, fault opening, fluid flushing, and mineral precipitation during the seismic failure of the fault, according to what proposed by Sibson et al. (1988).

In conclusion, the analysed reverse shear zones, that I related to the RSZ2 system, are characterised by several textures (e.g. carbonate shear surface with characteristic similar to mirror-like surface, vescicular porosity, chalcedony shear veins with textures testifying crystallization over silica gel), and by gold mineralisations that in literature are both related to fast fault slip and possible paleo-seismic events (Lovett, 2013; Wheatherley and Henley, 2013). This evidence could support the hypothesis that at local and probably at regional scale the RSZ2 system can be considered a system of paleo-seismic structures. Further investigation may provide important information about this possibility.

References

Abbate, E., Bortolotti, V., Passerini, P., 1970, Olistostromes and olistoliths: Sedim. Geol., 4 (3/4) , 521-528.

Abbate, E., Bortolotti, V., Principi, G., 1980, Apennines ophiolites: a peculiar oceanic crust: In: G. Ricci (eds), Special issue on Tethyan Ophiolites, Ofioliti, 1 , 59-96.

Abbate, E., and Sagri, M., 1984, Le unità torbiditiche cretacee dell'appennino settentrionale ed i margini continentali della Tetide: Memorie Società Geologica Italiana, v. 24, p. 359-375.

Abbate, E., Bortolotti, V., Marcucci, M., Passerini, P., and Principi, G., 1992a, Le successioni ofiolitiche dell'Appennino Settentrionale Atti Convegno Minerogenesi Appenninica: Soc. It. Min. Petr., p. 43-46.

Abbate, E., Bortolotti, V., Passerini, P., Principi, G., and Treves B., 1992b, Origine ed evoluzione delle ofioliti appenniniche: ipotesi a confronto. Atti Convegno Minerogenesi Appenninica. Soc. It. Min. Petr., p. 47-49.

Advokaat, E., L., van Hinsbergen, D., J., J., Maffione, M., Langereis, Cor G., Vissers, R., L., M., Cherchi, A., and Columbu, S., 2014, Eocene rotation of Sardinia, and the paleogeography of the western Mediterranean region: Earth and Planetary Science Letters, v. 401, p. 183–195.

Agosta, F., Prasad, M., Aydin, A., 2007, Physical properties of carbonates fault rocks, fucino basin (Central Italy): implications for fault seal in platform carbonates: Geofluids, v.7, p. 19-32.

Agostinetti, P. P., Bergonzi, G., Cattin, M., Del Soldato, M., Gambari, F. M., and Tizzoni, M., 1995, Gold in the Alps: a view from the south. In: Prehistoric Gold in Europe, in Springer Netherlands, pp. 199-218.

Ague, J.J., 1994, Mass transfer during Barrovian metamorphism of pelites, south-central Connecticut; I, Evidence for changes in composition and volume: American Journal of Science, v. 294, p. 989–1057.

Ague, J.J., 1997, Crustal mass transfer and index mineral growth in Barrow's garnet zone, northeast Scotland: Geology, v. 25, p. 73–76.

Akbulut, M., Pişkin, Ö., and Karayiğit, A. İ., 2006, The genesis of the carbonatized and silicified ultramafics known as listvenites: a case study from the Mihalıççık region (Eskişehir), NW Turkey: Geological Journal, v. 41(5), p. 557-580.

Allasinaz, A., Gelati, R., Gnaccolini, M., Martinis, B., Orombelli, G., Pasquarè, G., and Rossi, P.M., 1971, Note illustrative della Carta Geologica d'Italia alla scala 1/100000 – Foglio 82 Genova, Servizio Geologico d'Italia, p. 134, Roma.

Aydin, A., 2000, Fractures, faults and hydrocarbon entrapment, migration and flow: Mar. Pet. Geol., v. 17, p. 797–814.

Ananyev, Y., S., Maskov, A., A., and Abramova, R., N. 2015, Raisa Nikolaevna. Hydrothermal alteration mapping of Siberian gold-ore fields based on satellite spectroscopy data:IOP Conference Series: Earth and Environmental Science. p. 012001.

Ash, C., H., and Arksey, R., L., 1990, The listwanite-lode gold association in British Columbia: Geological fieldwork, Paper 1990-1, p. 359-364.

Babu, E. S., Kim, S., Song, J.-H., and Hong, S.-K., 2016, Effects of growth pressure on morphology of ZnO nanostructures by chemical vapor transport: Chemical Physics Letters, v. 658, p. 182-187.

Barnes, H.L., 1997, Geochemistry of hydrothermal ore deposits: John Wiley & Sons, v. 1.

Baumgartner, L.P., and Olsen, S.N., 1995, A least-squares approach to mass transport calculations using the isocon method: Economic Geology, v. 90, p. 1261–1270.

Beck, R., Andreassen, J. P., 2010, The onset sperulitic growth in crystallization of calcium carbonate: Journal of Crystal Growth, v. 312, p. 2226-2238.

Belogub, E. V., Melekestseva, I. Y., Novoselov, K. A., Zabotina, M. V., Tret'yakov, G. A., Zaykov, V. V., and Yuminov, A. M., 2017, Listvenite-related gold deposits of the South Urals (Russia): A review: Ore Geology Reviews, v. 85, p. 247-270.

Beltrando, M., Compagnoni, R., and Lombardo, B., 2010, (Ultra-) High pressure metamorphism and orogenesis: An Alpine perspective: Gondwana Research, v. 18, p. 147-166.

Bense, V. F., Gleeson, T., Loveless, S. E., Bour, O., and Scibek, J., 2013, Fault zone hydrogeology: Earth-Science Reviews, v. 127, p. 171-192.

Bense, V., Person, M., Chaudhary, K., You, Y., Cremer, N., Simon, S., 2008, Thermal anomalies indicate preferential flow along faults in unconsolidated sedimentary aquifers: Geophys. Res. Lett. 35. http://dx.doi.org/10.1029/2008GL036017.

Ben-Zion, Y., 2001, Dynamic ruptures in recent models of earthquake faults, Journal of the Mechanics and Physics of Solids: v. 16, p. 795-815.

Ben-Zion, Y., and Shi, Z., 2005, Dynamic rupture on a material interface with spontaneous generation of plastic strain in the bulk: Earth and Planetary Science Letters, v. 236 (1), p. 486-496.

Bernini M. and Zecca M. , 1990, Le deformazioni nelle formazioni di Molare e di Rocchetta (Oligocene-Miocene inferiore) della regione di Mioglia (SV) (Margine Sud del Bacino Terziario Piemontese: Atti Tic. Sc. Terra, 33, 1–10.

Bertrand, A., and Sue, C., 2017, Reconciling late faulting over the whole Alpine belt: from structural analysis to geochronological constrains: Swiss Journal of Geosciences, p. 1-16.

Béziat, D., Dubois, M., Debat, P., Nikiéma, S., Salvi, S., & Tollon, F., 2008, Gold metallogeny in the Birimian craton of Burkina Faso (West Africa): Journal of African Earth Sciences, v. 50(2), p. 215-233.

Bhat, H.S., Biegel, R.L., Rosakis, A.J., Sammis, C.G., 2010, The effect of asymmetric damage on dynamic shear rupture propagation II: With mismatch in bulk elasticity: Tectonophysics, v. 493, p. 163-271.

Billi, A., Di Toro, G., Landowe, S. J., and Hammlerp, G. M., 2008, Fault-related carbonate rocks and earthquake indicators: recent advances and future trends: Structural Geology: New Research, 63-86.

Bistacchi, N., Bistacchi, A., Massironi, M., Dal Piaz, G., and Omenetto, P., 2001, Post-nappe hydrothermal activity in the north-western Alps: relationships between gold-quartz lodes, listvenites and extensional fault systems: Geologisch-Paläontologische Mitteilungen Innsbruck, v. 25, p. 45-46.

Bistacchi, A., Eva, E., Massironi, M., and Solarino, S., 2000, Miocene to Present kinematics of the NW-Alps: evidences from remote sensing, structural analysis, seismotectonics and thermochronology: Journ. of Geodyn., v. 30, p. 205-228.

Bistacchi, A., and Massaroni, M., 2000: Post-nappe brittle tectonics and kinematic evolution of the north-western Alps: an integrated approach: Tectonophysics, v. 327, p. 267-292.

Bohlke, J.K., 1989, Comparison of metasomatic reactions between a common CO 2-rich vein fluid and diverse wall rocks; intensive variables, mass transfers, and Au mineralization at Alleghany, California: Economic Geology, v. 84, p. 291–327.

Borghini, G., Rampone, E., Crispini, L., De Ferrari, R., and Godard, M., 2007, Origin and emplacement of ultramafic–mafic intrusions in the Erro-Tobbio mantle peridotite (Ligurian Alps, Italy): *Lithos*, *94*(1-4), 210-229.

Boschi C., Dini A., Dallai L., Ruggieri G., Gianelli G., 2009: Enhanced CO2-mineral sequestration by cyclic hydraulic fracturing and Si-rich fluid infiltration into serpentinites at Malentrata (Tuscany, Italy): Chemical Geology 265, p. 209-226; doi:10.1016/j.chemgeo.2009.03.016

Boullier, A.-M., Yeh, E.-C., Boutareaud, S., Song, S.-R., Tsai, C.-H., 2009: Microscale anatomy of the 1999 Chi-Chi earthquake fault zone: Geochem. Geophys. Geo- syst. v. 10 (3) http://dx.doi.org/10.1029/2008GC002252.

Boulton, C., Menzies, C. D., Toy, V. G., Townend, J., and Sutherland, R., 2017, Geochemical and microstructural evidence for interseismic changes in fault zone

permeability and strength, Alpine Fault, New Zealand: Geochemistry, Geophysics, Geosystems, v. 18(1), p. 238-265.

Boutareaud, S., Boullier, A.-M., Andre ani, M., Calugaru, D.-G., Beck, P., Song, S.-R., and Shimamoto, T., 2010, Clay clast aggregates in gouges: new textural evidence for seismic faulting: J. Geophys. Res. v. 115 (B02408), p. 15.

Boutareaud, S., Calugaru, D.-G., Han, R., Fabbri, O., Mizoguchi, K., Tsutsumi, A., Shimamoto, T., 2008, Clay-clast aggregates: a new textural evidence for seismic fault sliding?: Geophys. Res. Lett. v. 35, p. 5.

Brodsky, E.E., Rowe, C.D., Meneghini, F., and Moore, J.C., 2009: A geological fingerprint of extremely low viscosity fault fluids mobilized during an earthquake. J. Geophys. Res. 114 (B01303), 14. http://dx.doi.org/10.1029/2008JB005633.

Brogi, A., 2011, Bowl-shaped basin related to low-angle detachment during continental extension: the case of the controversial Neogene Siena Basin (central Italy, Northern Apennines): Tectonophysics, v. 499, p. 131–148.

Bruni J., Canepa M., Chiodini G., Cioni R., Cipolli F., Longinelli A., Marini L., Ottonello G., Vetuschi Zuccolini M., 2002, Irreversibile water-mass transfer accompanying the generation of the neutral Mg-HCO3 and high pH, Ca-OH spring water of the Genova province, Italy: Applied Geochemistry, v. 17, p. 455-474.

Bucher, S., Schmidt, S.M., Bousquet, R., Fugenschuh, B., 2003: Late-stage deformation in a collisional orogen (Western Alps): nappe refolding, back-thrusting or normal faulting?: Terra Nova, v. 15, p. 109-117.

Buisson, G., and Leblanc, M., 1985a: Gold-bearing listwaenites (carbonatized ultramafic rocks) from ophiolite complexes, In: Gallagher J.M., Ixer R.A., Neary C.R., (eds): Metallogeny of basic ond ultrabasic rocks. Inst. Min. Metall. London, p. 121 - 132.

Buisson, G., and Leblanc, M., 1985b: Gold in carbonatized ultramafic rocks from ophiolite complexes, Econ. Geology, v. 80, p. 2028-2029.

Burger, M., Gundlach-Graham, A., Allner, S., Schwarz, G., Wang, H. A. O., Gyr, L., Burgener, S., Hattendorf, B., Grolimund, D., and Günther, D., 2015, High-Speed, High-Resolution, Multielemental LA-ICP-TOFMS Imaging: Part II. Critical Evaluation of Quantitative Three-Dimensional Imaging of Major, Minor, and Trace Elements in Geological Samples: Analytical Chemistry, v. 87, p. 8259-8267.

Cabella, R., Cortesogno, L., and Gaggero, L., 1991, Il basamento cristallino del Torrente Visone: Rend. Soc. Geol. It., v. 14, p. 29-33.

Cabella, R., Cortesogno, L., Gaggero, L., and Lucchetti, G., 1994, Clinopyroxenes through the blueschist facies metamorphism of the Liguria Alps: compositional variability and miscibility gaps: Atti Tic. Sc. Terra, Ser. Spec., v. 1, p. 55-63.

Caine, J. S., Bruhn, R.L., and Forster, C. B., 2010, Internal structure, fault rocks, and inferences regarding deformation, fluid flow, and mineralization in the seismogenic Stillwater normal fault, Dixie Valley, Nevada: Journal of Structural Geology, v. 32, p. 1576-1589.

Caine, J. S., and Forster, C. B., 1999, Fault zone architecture and fluid flow: Insights from field data and numerical modeling: Faults and Subsurface Fluid Flow in the Shallow Crust, p. 101-127.

Capponi, G., 1991, Megastructure of the south-eastern part of the Voltri Group (Ligurian Alps); a tentative interpretation: Bollettino della Societa Geologica Italiana, v. 110, p. 391–403.

Capponi, G., 1987, Alcune considerazioni sul massiccio di Voltri (Alpi Liguri): Bollettino della Societa Geologica Italiana, v. 106, p. 633–645.

Capponi, G., and Crispini, L., 2002, Structural and metamorphic signature of alpine tectonics in the Voltri Massif (Ligurian Alps, North-Western Italy): Eclogae Geologicae Helvetiae, v. 95, p. 31–42.

Capponi, G., and Crispini, L., 1997, Progressive shear deformation in the metasediments of the Voltri Group (Ligurian Alps, Italy): occurrence of structures recording extension parallel to the regional foliation: Boll. Soc. Geol. It., v. 116, p. 267 - 277.

Capponi, G., and Crispini, L., 1990, Chloritoid bearing assemblages in metagabbros from the Erro-Tobbio Unit (Voltri Massif, Ligurian Alps): preliminary data: Ofioliti, v. 15 (2), p. 327-332.

Capponi, G., Crispini, L. & Federico, L. (with contributions by Cabella, R., Faccini, F., Ferraris, F., Firpo, M., Roccati, A., Marescotti, P., Piazza, M. & Scambelluri, M. and collaboration by Dabove, G. M., Poggi, E., Torchio, S., Vigo, A. & Vetuschi Zuccolini, M.), 2013, Note illustrative al Foglio 212 'Spigno Monferrato' della Carta Geologica Regionale della Liguria. Retrieved from http://www.cartografia. regione.liguria.it/.

Capponi, G., Crispini, L., Federico, L., and Malatesta, C., 2016, Geology of the Eastern Ligurian Alps: a review of the tectonic units: Ital. J. Geosci., V. 135, p,. 157-169. doi: 10.3301/IJG.2015.06.

Capponi, G., Crispini, L., and Ferrarazzo, I., 1998, New field data on the Case Ferrere area (Voltri Massif, Ligurian Alps): Bollettino della Società geologica italiana, v. 117, p. 87–92.

Capponi, G., Crispini, L., and others, 2008, Foglio 213–230 «Genova» della Carta Geologica d'Italia alla scala 1: 50.000: Apat-Regione Liguria, Selca, Firenze.

Capponi, G., Crispini, L., Federico, L., Piazza, M., and Fabbri, B., 2009, Late Alpine tectonics in the Ligurian Alps: constraints from the Tertiary Piedmont Basin conglomerates: Geological Journal, 44(2), 211-224.

Capponi, G., Crispini, L., Piazza, M., Amandola, L., 2001, Field constraints to the Mid-tertiary kinematics of the Ligurian Alps: Ofioliti, 26 (2b), 409-416.

Capponi, G., Crispini, L., Silvestri, R., and Vigo, E., 1999, The role of Early Miocene thrust tectonics in the structural arrangement of the Voltri Group (Ligurian Alps, Italy): evidence from the Bandita area: Ofioliti, v. 24, p. 13–19.

Capponi, G., Gosso, G., Scambelluri, M., Siletto, G.B., and Tallone, S., 1994, Carta geologico-strutturale del settore centro-meridionale del Gruppo di Voltri (Alpi liguri) e note illustrative: Bollettino della Società Geologica Italiana, v. 113, p. 383–394.

Carminati, E., and Doglioni, C., 2012, Alps vs. Apennines: the paradigm of a tectonically asymmetric Earth: Earth-Science Reviews, v. 112(1), p. 67-96.

Carrapa, B., Di Giulio, A., Mancin, N., Stockli, D., Fantoni, R., Hughes, A., and Gupta, S., 2016, Tectonic significance of Cenozoic exhumation and foreland basin evolution in the Western Alps: Tectonics, v. 35(8), p. 1892-1912.

Carrapa, B., Bertotti, G., Krijgsman, W., 2003, Subsidence, stress regime and rotation(s) of a tectonically active sedimentary basin within the western Alpine Orogen: the Tertiary Piedmont Basin (Alpine domain, NW Italy), In: Mc Cann T. & Saintot A. (eds): Tracing tectonic deformation using the sedimentary record. Geol. Soc, London, Special Pub., 208, 205-227.

Carrapa, B. and Garcia – Castellanos, D., 2005, Western Alpine back-thrusting as subsidence mechanism in the Tertiary Piedmont Basin (Western Po Plain, NW Italy): Tectonophisics, 406, 197-212.

Castellarin, A., 2001, Alps-Apennine and Po plain-frontal Apennines relations., In: Vai B., Martini I. (eds.). Anatomy of an orogen: the Apennines and adjacent Mediterranean Basins. Kluwer.

Castellarin, A., 1994, Strutturazione eo- e meso-alpina dell'Appennino Settentrionale attorno al "nodo ligure": Studi Geologici Camerti, Vol. Spec. Crop 1-1a, 99 - 108.

Cerrina, Feroni, A., Martelli, L., Martinelli, P., and Ottria, G., Catanzariti, R., 2002, Carta Geologico-Strutturale dell'Appennino Emiliano-Romagnolo-Note Illustrative. Regione Emilia-Romagna, Selca Firenze.

Chen, J., Niemeijer, A., and Fokker, P., A., 2017, Vaporization of fault water during seismic slip: Journal of Geophysical Research: Solid Earth.

Chester, F.M., Evans, J.P., Biegel, R.L., 1993, Internal structure and weakening mechanisms of the San-Andreas fault: J. Geophys. Res., v. 98 (B1), p. 771–786.

Chiesa, S., Cortesogno, L., Forcella, F., Galli, M., Messiga, B., Pasquare, G., Pedemonte, G.M., Piccardo, G.B., and Rossi, P.M., 1975, Assetto strutturale ed interpretazione geodinamica del Gruppo di Voltri: Bollettino della Societa Geologica Italiana, v. 94,

p. 555–581.

Choi, J.-H., Jin, K., Enkhbayar, D., Davvasambuu, B., Bayasgalan, A., Kim, Y.-S., 2012, Rupture propagation based on damage patterns, slip distribution, and fault segmentation of the 1957 MW 8.1 Gobi–Altay earthquake rupture along the Bogd fault, Mongolia: J. Geophys. Res. 117. http://dx.doi.org/10.1029/2011JB008676.

Choi, J.-H., Jin, Edwards, P., Ko, K., Kim, Y-S., 2016, Definition and classification of fault damage zones: A review and a new methodological approach: Earth-Sciences Reviews, v. 152, p. 70-87.

Cilona, A., Aydin, A., Johnson, N.M., 2015, Permeability of a fault zone crosscutting a sequence of sandstones and shales and its influence on hydraulic head distribution in the Chatsworth Formation, California, USA: Hydrogeol. J., v. 23, p. 405–419.

Cimmino, F., and Messiga B., 1979, I calcescisti del Gruppo di Voltri (Liguria Occidentale): le variazioni composizionali delle miche bianche in rapporto alla evoluzione tettonico – metamorfica Alpina: Ofioliti , v. 4 (3), p. 269 – 294.

Collettini, C., Viti, C., Tesei, T., and Mollo, S., 2013, Thermal decomposition along natural carbonate faults during earthquakes: Geology, 41(8), 927-930.

Collombet, M., Thomas, J. C., Chauvin, Y., Tricart, P., Bouillin, J. P., and Gratier J. P., 2002, Counterclockwise rotation of the western Alps since the Oligocene: new insights from paleomagnetic data: Tectonics, v. 21(4), p. 1032.

Corsi, B., Elter, F., M., Giammarino, S., 2001, Structural fabric of the Antola Unit (Riviera di Levante, Italy) and implication for its Alpine versus Appennine origin: Ofioliti, 26(1), 1-8.

Cortesogno, L., Di Battistini, G., Lucchetti, G. , and Venturelli, G., 1979, Metamorphic assemblages of two high pressure low temperature ophiolitic units of central western Liguria: mineralogical and chemical features and tectonic significance: Ofioliti, v. 4 (2), pp. 121-156.

Cortesogno, L., and Forcella, F., 1978, Il massiccio cristallino di Arenzano, frammento di crosta continentale Brianzonese al margine meridionale del Gruppo di Voltri: Rend. Simp., v. 34(2), p. 307-350.

Cortesogno, L., Galbiati, B., and Principi, G., 1987: Note alla Carta geologica delle ofioliti del Bracco e ricostruzione della paleogeografia giurassico-cretacica: Ofioliti v. 12, p. 261-342.

Cortesogno, L., and Haccard, D., 1984, Note illustrative alla carta geologica della zona Sestri-Voltaggio: Mem. Soc. Geol. It., v. 28, p. 115-150.

Cortesogno, L., and Haccard, D., 1979, Présentation des principales unités constitutives de la zone de Sestri Voltaggio et de leurs relations structurales: Bull. Soc. Géol. France, v. 21, p. 379-388

Cortesogno, L., Lucchetti, G., and Penco, A.M., 1977, Le attuali conoscenze sulle zeoliti in Liguria: distribuzione, significato genetico e minerali associati, Rend. SIMP, v. 33 (1), p. 15 - 33.

Cox, S.F., 2005, Coupling between deformation, fluid pressures, and fluid flow in ore-producing hydrothermal systems at depth in the crust. In: Hedenquist, J.W., Thompson, J.F.H., Goldfarb, R.J., Richards, J.P. (Eds.), Economic Geology One Hundredth Anniversary Volume. Society of Economic Geologists, p. 39-76.

Cox, S.F., Knackstedt, M.A., Braun, J., 2001, Principles of structural control on permeability and fluid flow in hydrothermal systems: Reviews in Economic Geology, v. 14, p. 1-24.

Craw, D., MacKenzie, D., and Grieve, P., 2015, Supergene gold mobility in orogenic gold deposits, Otago Schist, New Zealand: New Zealand Journal of Geology and Geophysics, v. 58(2), p. 123-136.

Craw, D., and Campbell, J. R., 2004, Tectonic and structural setting for active mesothermal gold vein systems, Southern Alps, New Zealand: Journal of structural geology, v. 26(6), p. 995-1005.

Craw, D., 2001, Tectonic controls on gold deposits and their environmental impact: New Zealan., Journ. of Geoch. Explor. v. 73, p. 43-56.

Craw, D., Windle, S., J., and Angus, P., V., 1999, Gold mineralization without quartz veins in a ductile-brittle shear zone, Macraes Mine, Otago Schist, New Zealand: Mineralium Deposita, v. 34(4), p. 382-394.

Crispini, L., 1996, Evoluzione strutturale dei metasedimenti del Gruppo di Voltri e della Zona Sestri-Voltaggio: implicazioni nell'evoluzione tettonica e geodinamica Alpina. Tesi di Dottorato, Univ. di Genova, VI ciclo.

Crispini, L., and Capponi, G., 2001, Tectonic evolution of the Voltri Group and Sestri Voltaggio Zone (southern limit of the NW Alps): a review: Ofioliti, v. 26 (2a), p. 161-164.

Crispini, L., Federico, L., Capponi, G., and Spagnolo C., 2009, Late orogenic transpressional tectonics in the "Ligurian Knot": Boll. Soc. Geol. It., v. 128 (2), p. 433-441.

Curti, E., 1987, Lead and oxygen isotope evidence for the origin of the Monte Rosa gold lode deposits (Western Alps, Italy); a comparison with Archean lode deposits: Economic Geology, v. 82(8), p. 2115-2140.

D'atri, A., Piana, F., Tallone, S., Bodrato, G. and Roz Gastaldi, M., 1997, Tettonica Oligo-Miocenica nell'alto Monferrato (Bacino Terziario Piemontese) e nel settore nord-occidentale del Gruppo di Voltri (Acqui Terme - Cassinelle, AL): Atti Tic. Sc. Terra, (Serie Speciale), 5, 85 - 100.

Dal Piaz, G.V., 2001, History of tectonic interpretations of the Alps: J. Geo- dynamics, v. 32, p. 99-114.

Dal Piaz, G.V., 1999, The Austroalpine–Piedmont nappe stack and the puzzle of Alpine Tethys: Memorie di Scienze Geologiche, Padova, v. 51, p. 155–176.

Dal Piaz, G.V., Bistacchi, A., and Massironi, M., 2003, Geological outline of the Alps: Episodes v. 26, p. 175–180.

Dal Piaz, G. V. and Gosso, G., 1994, Some remarks on evolution of the Alpine lithosphere: Quad. Geodin. Alp. Quatern., v. 2, p. 91-99.

Dal Piaz, G., V., & Venturelli, G., 1983, Brevi riflessioni sul magmatismo post-ofiolitico nel quadro dell'evoluzione spazio-temporale delle Alpi: Mem. Soc. Geol. It, v. 26, p. 5-19.

Dal Piaz, G. V., Venturelli, G., Scolari, A., 1979, Calc-alcaline to ultrapotassic post-collisional volcanic activity in the internal northwestern Alps: Mem. Sci. Geol. Padova, v. 32, p. 16.

Decandia, F.A., and Elter, P., 1972, La zona ofiolitifera del Bracco nel settore compreso tra Levanto e la Val Graveglia (Appennino Ligure): Mem. Soc. Geol. It. v. 11, p. 503-530.

Decarlis, A., Dallagiovanna, G., Lualdi, A., Maino, M., and Seno, S., 2013, Stratigraphic evolution in the Ligurian Alps between Variscan heritages and the Alpine Tethys opening: A review: Earth-Science Reviews, v. 125, p. 43-68.

Decarlis, A., Maino, M., Dallagiovanna, G., Lualdi, A., Masini, E., Seno, S., and Toscani, G., 2014, Salt tectonics in the SW Alps (Italy-France): From rifting to the inversion of the European con- tinental margin in a context of oblique convergence: Tectonophysics, v. 636, p. 293-314. doi: 10.1016/j.tecto.2014.09.003.

Dela Pierre, F., Mikhailov, V., Polino, R., 1995, The tectonosedimentary evolution of the tertiary basin in the Western Po plain: kinematics inferred from subsidence curves: Atti Convegno " Rapporti Alpi - Appennino" . Acc. Naz. Sci. Scritti & Documenti.

Desmons, J., Compagnoni, R., and Cortesogno, L., 1999, Alpine metamorphism of the Western Alps: II. High P/T and related pre-greenschist metamorphism: Schweiz. Mineral. Petrogr. Mitt., v. 79, p. 111 - 134.

Dewey, J.F., Helman, M.L., Turco, E., Hutton, D.H.W., Knott, S.D., 1989, Kinematics of the western Mediterranean. In: Coward, M.P., Dietrich, D., Park, R.G. (Eds.), Alpine tectonics: Geological Society, London, Special Publications, vol. 45, p. 265–283.

Dhir, V., K., 1991, Nucleate and transition boiling heat transfer under pool and external flow conditions: International Journal of Heat and Fluid Flow, v. 12, no. 4, p. 290-314.

Di Biase, D., Marroni, M., Pandolfi, L., 1997, Age of the deformation phases in the Internal Liguride Units: evidences from lower Oligocene Val Borbera conglomerate of Tertiary Piedmont Basin (Northern Italy): Ofioliti, 22 (2), 231-238.

Diamond, L., W., 1993, Post-metamorphic gold-quartz veins from NW Italy: the composition and origin of the ore fluid: Mineralogical Magazine, v. 57, p. 407-422.

Diamond, L., W, 1990, Fluid inclusion evidence for P-V-T-X evolution of hydrotermal solutions in late-Alpine gold-quartz veins at Brusson, Val D'Ayas, NW Italian Alps: American Journ. of Science, v. 290, October 1990, p. 912-958

Diamond, L., W., and Wiedenbeck, M., 1986, K-Ar radiometric ages of the gold-quartz veins at Brusson, Val d'Ayas, NW Italy: Evidence of mid-Oligocene hydrothermal activity in the northwestern Alps: Schweiz. mineral. petrogr. Mitt, v. 66, p. 385-393.

Dilles, J.H., and Einaudi, M.T., 1992, Wall-rock alteration and hydrothermal flow paths about the Ann-Mason porphyry copper deposit, Nevada; a 6-km vertical reconstruction: Economic Geology, v. 87, p. 1963–2001.

Di Toro, G., Goldsby, D.L., Tullis, T.E., 2004, Friction falls toward zero in quartz rock as slip velocity approaches seismic rates: Nature, v. 427, p. 436-439.

Dockrill, B., Shipton, Z.K., 2010, Structural controls on leakage from a natural CO_2 geologic storage site: Central Utah, U.S.A.: J. Struct. Geol., v. 32, p. 1768–1782.

Doglioni, C., Mongelli, F., and Pialli, G., 1998, Boudinage of the Alpine belt in the Apenninic back-arc: Mem. Soc. Geol. It, 52, 457-468.

Drummond, S. E., and Ohmoto, H., 1985, Chemical evolution and mineral deposition in boiling hydrothermal systems: Economic Geology, v. 80, p. 126-147.

Drury, M.R., Hoogerduijn, Strating, E.H., and Vissers, R.L.M., 1990, Shear zone structures and microstructures in mantle peridotites from the Voltri massif, Liguria Alps, N.W. Italy: Geologie en Mijnbouw, v. 69, p. 3-17.

Dubé, B., & Gosselin, P., 2007, Greenstone-hosted quartz-carbonate vein deposits. Mineral Deposits of Canada: A synthesis of major deposit-types, district metallogeny, the evolution of geological provinces, and exploration methods: Geological Association of Canada, Mineral Deposits Division, Special Publication, v. 5, p. 49-73.

Dumont, T., Schwartz, S., Guillot, S., Simon-Labric, T., Tricart, P., and Jourdan, S., 2012, Structural and sedimentary records of the Oligocene revolution in the Western Alpine arc: Journal of Godynamics, v. 56–57, p. 18–28.

Dumont, T., Simon-Labric, T., Authemayou, C., and Heymes, T., 2011, Lateral termination of the north-directed Alpine orogeny and onset of westward escape in the Western Alpine arc: Structural and sedimentary evidence from the external zone: Tectonics, doi:10.1029/2010TC002836.

Eichhubl, P., Davatzes, N.C., Becker, S.P., 2009, Structural and diagenetic control of fluid migration and cementation along the Moab fault, Utah: AAPG Bulletin, v. 93 (5), p. 653-681.

Eichhubl, P., D'Onfro, P.S., Aydin, A., Waters, A., McCarty, D.K., 2005, Structure, petro- physics, and diagenesis of shale entrained along a normal fault at Black Diamond Mines, California e implications for fault seal: AAPG Bulletin, v. 89 (9), p. 1113-1137.

Ellero, A., Leoni, L., Marroni, M., Sartori, F., 2001, Internal Liguride Units from Central Liguria, Italy: new constraints to the tectonic setting from white mica and chlorite studies: Schweiz. Mineral. Petrogr. Mitt., 81, 399-53.

Elter, P., 1994, "Introduzione alla geologia dell'Appennino Ligure-Emilia- no" in Guide Geologiche Regionali – 10 itinerari – Appennino Ligure-Emiliano: Società Geologica Italiana (Roma), Be-Ma Editrice, p. 17-24.

Elter, P., and Pertusati, P.C. 1973, Considerazioni sul limite Alpi- Appennino e sulle sue relazioni con l'arco delle Alpi Occidentali: Memorie della Società Geologica Italiana, v. 12, p. 359-375.

Escayola, M. P., Proenza, J. A., Van Staal, C., Rogers, N., and Skulski, T., 2009, The Point Rousse listvenites, Baie Verte, Newfoundland: altered ultramafic rocks with potential for gold mineralization: Current research. Newfoundland and Labrador Department of Natural Resources, Geological Survey, Report, 09-1.

Eva, E. and Solarino, S., 1998, Variations of stress directions in the western Alpine arc: Geophysical Journ. Int., v. 135, p. 438-448.

Evans, J.P., Prante, M.R., Janecke, S.U., Ault, A.K., and Newell, D.L., 2014, Hot faults: Iridescent slip surfaces with metallic luster document high-temperature ancient seismicity in the Wasatch fault zone, Utah, USA: Geology, v. 42, p. 623–626.

Evans, J.P., Forster, C.B., Goddard, J.V., 1997, Permeability of fault-related rocks, implications for hydraulic structure of fault zones: Journal of Structural Geology, v. 19, p. 1393-1404.

Faber, C., Rowe, C.D., Miller, J.A., Fagereng, Å., and Neethling, J.H., 2014, Silica gel in a fault slip surface: Field evidence for palaeo-earthquakes? Journal of Structural Geology, v. 69, p. 108–121, doi: 10.1016/j.jsg.2014.09.021.

Faccenna, C., Piromallo, C., Crespo-Blanc, A., Jolivet, L., and Rossetti, F., 2004, Lateral slab deformation and the origin of the western Mediterranean arcs: Tectonics, 23(1).

Faleiros, A., M., da Cruz Campanha, G., A., Faleiros, F., M., and da Silveira Bello, R. M., 2014, Fluid regimes, fault-valve behavior and formation of gold-quartz veins—The Morro do Ouro mine, Ribeira Belt, Brazil: Ore Geology Reviews, v. 56, p. 442-456.

Falk, E., S., and Kelemen, P., B., 2015, Geochemistry and petrology of listvenite in the Samail ophiolite, Sultanate of Oman: complete carbonation of peridotite during ophiolite emplacement: Geochimica et Cosmochimica Acta, 160, 70-90.

Farough, A., Moore, D.E., Lockner, D.A., and Lowell, R.P., 2016, Evolution of fracture permeability of ultramafic rocks undergoing serpentinization at hydrothermal conditions: An experimental study: Geochem. Geophys. Geosyst., v. 17, p. 44–55, doi:10.1002/2015GC005973.

Faulkner, D.R., Jackson, C.A.L., Lunn, R.J., Schlische, R.W., Shipton, Z.K., Wibberley, C. A.J., Withjack, M.O., 2010, A review of recent developments concerning the structure, mechanics and fluid flow properties of fault zones: Journal of Structural Geology, V. 31, p. 1557-1575.

Faulkner, D.R., Mitchell, T.M., Rutter, E.H., and Cembrano, J., 2008, On the structure and mechanical properties of large strike-slip faults. In: Wibberley, C.A.J., Kurz, W., Imber, J., Holdsworth, R.E., Collettini, C. (Eds.), The Internal Structure of Fault Zones: Implications for Mechanical and Fluid Flow Properties: Geological Society, London, Special Publications, v. 299, p. 139-150.

Faulkner, D.R., Rutter, E.H., 2003, The effect of temperature, the nature of the pore fluid, and sub-yield differential stress on the permeability of phyllosilicate-rich fault gouge: Journal of Geophysical Research e Solid Earth, v. 108 (B5).

Favaro, S., Handy, M. R., Scharf, A., & Schuster, R., 2017, Changing patterns of exhumation and denudation in front of an advancing crustal indenter, Tauern Window (Eastern Alps): Tectonics, v. 36, p. 1053-1071, 10.1002/2016TC004448.

Federico, L., Capponi, G., Crispini, L., and Scambelluri, M., 2004, Exhumation of alpine high-pressure rocks: insights from petrology of eclogite clasts in the Tertiary Piedmontese Basin (Ligurian Alps, Italy): Lithos, v. 74, p. 21-40.

Federico, L., Capponi, G., Crispini, L., Scambelluri, M., and Villa, I.M., 2005, $^{39}Ar/^{40}Ar$ dating of high-pressure rocks from the Ligurian Alps: evidence for a continuous subduction-exhumation cycle: EPSL, v. 240, p. 668-680.

Federico, L., Crispini, L., Scambelluri, M., and Capponi, G., 2007, Ophiolite mélange zone records exhumation in a fossil subduction channel: Geology, v. 35, p. 499–502.

Federico, L., Crispini, L., Vigo, A., and Capponi, G., 2014, Unravelling polyphase brittle tectonics through multi-software fault-slip analysis: The case of the Voltri Unit, Western Alps (Italy): J. Struct. Geol.,v. 68, p. 175-193.

Federico, L., Spagnolo, C., Crispini, L., and Capponi, G., 2009, Fault- slip analysis in the metaophiolites of the Voltri Massif: constraints for the tectonic evolution at the Alps/Apennine boundary: Geological Journal, v. 44 (2), p. 225-240.

Federico, L., Spagnolo, C., Crispini, L., and Capponi, G., 2005, Multiple reactivation of reverse shear zones in a transpressional regime during late-alpine to early-

apennine tectonics (Voltri massif, Ligurian Alps): Geoitalia 2005, Epitome v.1, p. 311-312.

Fondriest, M., Smith, S.A.F., Di Toro, G., Zampieri, D., and Mittempergher, S., 2012: Fault zone structure and seismic slip location in dolostones, an example from the Southern Alps, Italy: J. Struct. Geol. v. 45, p. 52-67.

Forcella, F., Mottana, A., Pasquaré, G., and 1973, Il massiccio cristallino interno di Valosio (Gruppo di Voltri, Provincia di Al): Mem. Soc. Geol. It., v. 12,(4), p. 485- 528.

Frank-Kamenetskiy, V. A., Kotov, N., V., and Klochkova, G. N., 1969, Phase transformations in sepiolite and palygorskite at different pressures under hydrothermal conditions: Geokhimiya, v. 1, p. 14–21.

Frey, M., Desmons, J. and Neubauer, F., 1999, The new metamorphic map of the Alps: Schweiz. mineral. petrogr. Mitt., v. 79, p. 1-230.

Galli, M., Bezzi A., Piccardo, G.B., Cortesogno, L., and Pedemonte, G.M., 1972, Le ofioliti dell'Appennino ligure: un frammento di crosta-mantello "oceanici" dell'antica Tetide: Mem. Soc. Geol. It. v. 11, p. 467-502.

Garofalo, P.S., 2004a, Mass transfer during gold precipitation within a vertically extensive vein network (Sigma deposit – Abitibi greenstone belt – Canada). Part I. Patterns of hydrothermal alteration haloes: European Journal of Mineralogy, v. 16, p. 753–760, doi: 10.1127/0935-1221/2004/0016-0753.

Garofalo, P.S., 2004b, Mass transfer during gold precipitation within a vertically extensive vein network (Sigma deposit – Abitibi greenstone belt – Canada). Part II. Mass transfer calculations: European Journal of Mineralogy, v. 16, p. 761–776, doi: 10.1127/0935-1221/2004/0016-0761.

Garofalo, P.S., 2012, The composition of Alpine marine sediments (Bündnerschiefer Formation, W Alps) and the mobility of their chemical components during orogenic metamorphism: Lithos, v. 128, p. 55–72.

Garofalo, P. S., Fricker, M. B., Guenther, D., Bersani, D., and Lottici, P. P., 2014, Physical-chemical properties and metal budget of Au-transporting hydrothermal fluids in orogenic deposits, in Garofalo, P. S., and Ridley, J. R., eds., Gold-transporting hydrothermal fluids in the Earth's crust. Special Publication 402, Volume 402: London, The Geological Society of London, p. 71-102.

Garuti, G., Bartoli, O., Scacchetti, M., & Zaccarini, F., 2008, Geological setting and structural styles of Volcanic Massive Sulfide deposits in the northern Apennines (Italy): evidence for seafloor and sub-seafloor hydrothermal activity in unconventional ophiolites of the Mesozoic Tethys: Boletin de la Sociedad Geologica Mexicana, 60(1).

Gattacceca, J., Deino, A., Rizzo, R., Jones, D. S., Henry, B., Beaudoin, B., and Vadeboin, F., 2007, Miocene rotation of Sardinia: New paleomagnetic and geochronological

constraints and geody- namic implications: Earth and Planetary Science Letters, v. 258, p. 359–377.

Gelati, R., and Gnaccolini, M., 1998, Synsedimentary tectonics and sedimentation in the Tertiary Piedmont Basin, Northwestern Italy: Riv. It. Paleont. Strat., v. 104, p. 193-214.

Gelati, R., and Gnaccolini M., 1988, Sequenze deposizionali in un bacino episuturale, nella zona di raccordo tra Alpi ed Appennino settentrionale: Atti Tic. Sc. Terra, v. 31, p. 340-350.

Genna, A., Jébrak, M., Marcoux, E., and Milési, J.P., 1996, Genesis of cockade breccias in the tectonic evolution of the Cirotan epithermal gold system, West Java: Canadian Journal of Earth Sciences, v. 33, p. 93–102.

Giglia, G., Capponi, G., Crispini, L., and Piazza, M., 1996, Dynamics and seismotectonics of the West-Alpine arc: Tectonophysics, v. 267, p. 143-175.

Giorza, A., 2010, Late to post-metamorphic hydrothermalism in the Voltri Unit (Lavagnina Lakes Area, NW Alps). Structural-Petrological-Geochemical Approach [PhD Thesys]: Università degli Studi di Torino.

Goldfarb, R. J., and Groves, D. I., 2015, Orogenic gold: Common or evolving fluid and metal sources through time: Lithos, v. 233, p. 2-26.

Goldfarb, R. J., Groves, D. I., and Gardoll, S., 2001, Orogenic gold and geologic time: a global synthesis: Ore geology reviews, v. 18(1), p. 1-75.

Goldsby, D. L., and Tullis, T. E., 2011, Flash heating leads to low frictional strength of crustal rocks at earthquake slip rates: Science, 334(6053), 216-218.

Görler, K., 1962, Stratigraphie und Tektonik des nördlichen Abschnitts der Zone Sestri-Voltaggio einschliesslich der angrenzenden Gebiete (Prov. Alessandria und Genua). Diss. Freie. Univ. Berlin.

Görler, K., and Ibbeken, H., 1964, Die Bedeutung der Zone Sestri-Voltaggio als Grenze zwischen Alpen und Apennin: Geol. Rund., v. 53 (1), p. 73-84.

Ghosh, G., Bose, S., Das, K., Dasgupta, A., Yamamoto, T., Hayasaka, Y., and Mukhopadhyay, J., 2016, Transpression and juxtaposition of middle crust over upper crust forming a crustal scale flower structure: Insight from structural, fabric, and kinematic studies from the Rengali Province, eastern India. Journal of Structural Geology, v. 83, p. 156-179.

Grant J. A., 1986. The isocon diagram- a simple solution to Gresens' equation for metasomatic alteration. Economic Geology 81, pp. 1976-1982.

Grant, J.A., 2005, Isocon analysis: a brief review of the method and applications: Physics and Chemistry of the Earth, Parts A/B/C, v. 30, p. 997–1004.

Gresens R. L., 1967. Composition-volume relationships of metasomatism. Chem. Geology 2, pp. 47-55.

Groves, D., I., and Santosh, M., 2016, The giant Jiaodong gold province: The key to a unified model for orogenic gold deposits?: Geoscience Frontiers, v. 7(3), p. 409-417.

Groves, D., I., Goldfarb, R., J., Knox-Robinson, C., M., Ojala, J., Gardoll, S., Yun, G., Y., and Holyland, P., 2000, Late-kinematic timing of orogenic gold deposits and significance for computer-based exploration techniques with emphasis on the Yilgarn Block, Western Australia: Ore Geology Reviews, v. 17(1), p. 1-38.

Gudmundsson, A., Simmenes, T. H., Larsen, B., and Philipp, S. L., 2010, Effects of internal structure and local stresses on fracture propagation, deflection, and arrest in fault zones: Journal of Structural Geology, v. 32(11), p. 1643-1655.

Gueguen, E., Doglioni, C., Fernandez, M., 1998, On the post-25 Ma geodynamic evolution of the western Mediterranean: Tectonophysics, 298, 259-269.

Gundlach-Graham, A., Burger, M., Allner, S., Schwarz, G., Wang, H.A.O., Gyr, L., Grolimund, D., Hattendorf, B., and Günther, D., 2015. High-Speed, High-Resolution, Multielemental Laser Ablation-Inductively Coupled Plasma-Time-of-Flight Mass Spectrometry Imaging: Part I. Instrumentation and Two-Dimensional Imaging of Geological Samples. Analytical Chemistry 87, 8250-8258.

Gundlach-Graham, A., and Günther, D., 2016. Toward faster and higher resolution LA–ICPMS imaging: on the co-evolution of LA cell design and ICPMS instrumentation. Analytical and Bioanalytical Chemistry 408, 2687-2695.

Gunther, D., Frischknecht, R., Heinrich, C. A., and Kahlert, H. J., 1997, Capabilities of an argon fluoride 193 nm excimer laser for laser ablation inductively coupled plasma mass spectometry microanalysis of geological materials: Journal of Analytical Atomic Spectrometry, v. 12, p. 939-944.

Gratuze, B., 1999, Obsidian Characterization by Laser Ablation ICP-MS and its Application to Prehistoric Trade in the Mediterranean and the Near East: Sources and Distribution of Obsidian within the Aegean and Anatolia: Journal of Archaeological Science, v. 26, p. 869-881.

Haccard D., and Lorentz C., 1979, Les déformations de l'Eocène supérieur au Stampien de la terminaison septentrionale de la zone de Sestri-Voltaggio: Bull. Soc. Géol. France, 7, T.XXI, n.4, 401-413

Halls, C. and Zhao, R., 1995, Listvenite and related rocks: perspectives on terminology and mineralogy with reference to an occurrence at Cregganbaun: Co.Mayo, Republic of Ireland, Mineral. Deposita, v. 30, p. 303-313.

Han, R., Shimamoto, T., Hirose, T., Ree, J.-H., and Ando, J. -I, 2007, Ultralow friction of carbonate faults caused by thermal decomposition: Science, v. 316. http:// dx.doi.org/10.1126/science.1139763.

Handy, M. R., Schmid, S. M., Bousquet, R., Kissling, E., and Bernoulli, D., 2010, Reconciling plate-tectonic reconstructions of Alpine Tethys with the geological–geophysical record of spreading and subduction in the Alps: Earth-Science Reviews, 102(3-4), 121-158.

Hannington, M., Harðardóttir, V., Garbe-Schönberg, D., and Brown, K. L., 2016, Gold enrichment in active geothermal systems by accumulating colloidal suspensions: Nature Geoscience, v. 9(4), p. 299-302.

Hansen, L.D., Dipple, G.M., Gordon, T.M., and Kellett, D.A., 2005, Carbonated Serpentinite (listwanite) at Atlin, British Columbia: A Geological Analogue to Carbon Dioxide Sequestration: The Canadian Mineralogist, v. 43, p. 225–239, doi: 10.2113/gscanmin.43.1.225.

Harvey, J., Garrido, C. J., Savov, I., Agostini, S., Padrón-Navarta, J. A., Marchesi, C., and Gómez-Pugnaire, M., T., 2014, 11 B-rich fluids in subduction zones: the role of antigorite dehydration in subducting slabs and boron isotope heterogeneity in the mantle: Chemical Geology, v. 376, p. 20-30.

Hayward, K.S., Cox, S.F., Fitz Gerald, J.D., Slagmolen, B.J.J., Shaddock, D.A., Forsyth, P.W.F., Salmon, M.L., and Hawkins, R.P., 2016, Mechanical amorphization, flash heating, and frictional melting: Dramatic changes to fault surfaces during the first millisecond of earthquake slip: Geology, v. 44, p. 1043–1046, doi: 10.1130/G38242.1.

Hendriks, L., Gundlach-Graham, A., Hattendorf, B., and Gunther, D., 2017, Characterization of a new ICP-TOFMS instrument with continuous and discrete introduction of solutions: Journal of Analytical Atomic Spectrometry, v. 32, p. 548 - 561.

Henley, R.W., Huges, G.O., 2000, Underground fumaroles: "Excess heat" effects in vein formation: Economic Geology, v. 95 (3), p. 453-466.

Herrero, M. J., Martín-Pérez, A., Alonso-Zarza, A. M., Gil-Peña, I., Meléndez, A., and Martín-García, R., 2011, Petrography and geochemistry of the magnesites and dolostones of the Ediacaran Ibor Group (635 to 542Ma), Western Spain: Evidences of their hydrothermal origin: Sedimentary Geology, v. 240(3), p. 71-84.

Herrington, R.J., and Wilkinson, J.J., 1993, Colloidal gold and silica in mesothermal vein systems, Geology, v. 21, p. 539-542.

Hinsbergen, D., J., Vissers, R. L., & Spakman, W., 2014, Origin and consequences of western Mediterranean subduction, rollback, and slab segmentation: Tectonics, v. 33(4), p. 393-419.

Holdsworth, R., E., Dempsey, E., Selby, D., Darling, J., R., Feely, M., Costanzo, A., and Porter, S., J., 2015, Silurian–Devonian magmatism, mineralization, regional exhumation and brittle strike-slip deformation along the Loch Shin Line, NW Scotland: Journal of the Geological Society, v. 172(6), p. 748-762.

Holyoke, C.W., Tullis, J., 2006, The interaction between reaction and deformation: an experimental study using a biotite plus plagioclase plus quartz gneiss: Journal of Metamorphic Geology, v. 24 (8), p. 743-762.

Hoogerduijn Strating, E.H., 1990, Folding of lithosphere in the Piemonte-Ligurian ocean: Geol. Mijnbouw, v. 69, p. 31-41.

Hoogerduijn Strating, E.H., 1991, The Evolution of the Piemonte- Ligurian ocean. A structural study of ophiolite complexes in Liguria (NW Italy): Geol. Ultraiectina, v. 74, 145 pp.

Hoogerdujn Strating, E. H., 1994, Extensional faulting in an intraoceanic subduction complex-working hypothesis for the Paleogene of the Alps- Appennine system: Tectonophysics, 238, 255-273.

Hoogerduijn Strating, E.H., Rampone, E., Piccardo, G.B., Drury, M. R., Vissers, R.L.M., 1993: Subsolidus emplacement of mantle peridotites during incipient oceanic rifting and opening of the Mesozoic Tethys (Voltri Massif, NW Italy): J. Petrol. v. 34, p. 901–927.

Hunziker, J. C., Desmonds, J., Hurford, A. J., 1992, Thirty-two years of geochronological work in the Central and Western Alps: a review of seven maps: Mem.De Geol., Lausanne, v. 13, p. 59.

Hurford, A. J., Hunziker, J. C., Stockert, B., 1991, Constraints on the late-thermotectonic evolution of the western Alps: evidence for episodic rapid uplift: Tectonics, v. 10, p. 758-769.

Huttenlocher, H., F., 1934, Die Erzlagerstattenzone der Westalpen: Schweiz. mineral. petrogr. Mitt., v. 14, p. 22-149.

Ibbeken, H., 1962, Stratigraphie und Tektonik des nördlichen Absch- nitts der Zone Sestri-Voltaggio und des angrenzenden Gebietes bis zum oberen Scriviatal (Prov. Alessandria und Genua). Diss. Freie. Univ. Berlin.

Ilich, M., and Toshovich, R., 2002, Geology and origin of the Golesh vein magnesite deposit: a brief survey: Guide to Geological Excursions, Proceedings of XVII, Congress of Carpathian-Balkan Geological Association, Bratislava.

Japas, M. S., Urbina, N. E., Sruoga, P., Garro, J. M., and Ibañes, O., 2016, A transient fault-valve mechanism operating in upper crustal level, Sierras Pampeanas, Argentina: Journal of Geodynamics, v. 101, p. 142-154.

Jébrak, M., 1997, Hydrothermal breccias in vein-type ore deposits: a review of mechanisms, morphology and size distribution: Ore geology reviews, v. 12, p. 111–134.

Jefferies, S.P., Holdsworth, R.E., Shimamoto, T., Takagi, H., Lloyd, G.E., Spiers, C.J., 2006, Origin and mechanical significance of foliated cataclastic rocks in the cores of crustal-scale faults: examples from the Median Tectonic Line, Japan:

Journal of Geophysical Research e Solid Earth, v. 111 (B12).

Jones, R. R., Holdsworth, R. E., Clegg, P., McCaffrey, K., and Tavarnelli, E., 2004, Inclined transpression: Journal of Structural Geology, v. 26(8), p. 1531-1548.

Kaneko, Y., Takeshita, T., Watanabe, Y., Schigematsu, N., and Fujimoto, K., 2017: Alteration Reaction and Mass Transfer via Fluids with Progress of Fracturing along the Median Tectonic Line, Mie Prefecture, Southwest Japan, Earth and Planetary Sciences, DOI: 10.5772/68112.

Kelemen, P.B., Matter, J., Streit, E.E., Rudge, J.F., Curry, W.B., Blusztajn, J., 2011: Rates and Mechanisms of Mineral Carbonation in Peridotite: Natural Processes and Recipes for Enhanced, in situ CO2 Capture and Storage, Annual Review of Earth and Planetary Sciences, v. 39, p. 545-576.

Kelemen, P. B., and Matter, J., 2008, In situ carbonation of peridotite for CO2 storage: Proceedings of the National Academy of Sciences, v. 105(45), p. 17295-17300.

Keulen, N., Heilbronner, R., Stunitz, H., Boullier, A.-M., Ito, H., 2007, Grain size distributions of fault rocks: a comparison between experimetally and naturally deformed granitoids, v. 29, p. 1128-1300.

Kim, Y.-S., Sanderson, D.J., 2008, Earthquake and fault propagation, displacement and damage zones. In: Landowe, S.J., Hammler, G.M. (Eds.), Structural Geology: New Research. Nova Science Publishers, Hauppauge, New York, pp. 99–117.

Kirkpatrick, J.D., Rowe, C.D., White, J.C., Brosky, E.E., 2013: Silica gel formation during fault slip: Evidence from the rock record: Geology, v. 41; no. 9; p. 1015-1018.

Kirkpatrick, J.D., and Rowe, C.D., 2013, Disappearing ink: How pseudotachylytes are lost from the rock record: Journal of Structural Geology, v. 52, p. 183–198.

Kirkpatrick, J.D., Shipton, Z.K., Evans, J.P., Micklethwaite, S., Lim, S.J., McKillop, P., 2008, Strike-slip fault terminations at seismogenic depths: the structure and kinematics of the Glacier Lakes fault, Sierra Nevada United States: Journal of Geophysical Research e Solid Earth, v. 113, B04304, doi:10.1029/2007JB005311.

Kulhawy, F.H., 1975, Stress deformation properties of rock and rock discontinuites: Engineering Geology, v. 9, p. 327-350.

Kretz, R. 1983, Symbols for rock-forming minerals: American Mineralogist, v. 68, p. 277–9.

Large, S. J., Bakker, E. Y., Weis, P., Wälle, M., Ressel, M., and Heinrich, C. A., 2016, Trace elements in fluid inclusions of sediment-hosted gold deposits indicate a magmatic-hydrothermal origin of the Carlin ore trend: Geology, v. 44(12), p. 1015-1018.

Laubscher H., 1996, Shallow and deep rotations in the Miocene Alps, Tectonics, v.

15/5, p. 1022-1035.

Laubscher, H., 1992, The arc of the Western Alps today: Eclogae. Geol. Helv., v. 84/3, p. 631-659.

Leach, A.M., and Hieftje, G.M., 2002. Factors Affecting the Production of Fast Transient Signals in Single Shot Laser Ablation Inductively Coupled Plasma Mass Spectrometry. Applied Spectroscopy 56, 62-69.
Leach, A. M., and Hieftje, G. M., 2005: Applied Spectroscopy, v. 56, p. 62-69.

Leoni, L., Marroni, M., Sartori, F., Tamponi, M., 1996, The grade of metamorphism in the metapelites of the Internal Liguride units (Northern Apennines, Italy): Eur. Journ. of Miner., 8, 35-50.

Levi, N., Ellero, A., Pandolfi, L., and Ottria, G., 2006, Polyorogenic deformation history recognized at shallow structural levels: the case of the Antola unit (Northern Apennine, Italy): Journal of Structural Geology, v. 28, p. 1694-1709.

Lida, Y., Okuyama, K., and Sakurai, K., 1993, Peculiar bubble generation on a film heater submerged in ethyl alcohol and imposed a high heating rate over 10^7 K s^{-1}: International Journal of Heat and Mass Transfer, v. 36, no. 10, p. 2699-2701.

Longerich, H. P., Jackson, S. E., and D. Gunther, 1996: Inter-laboratory note. Laser ablation inductively coupled plasma mass spectrometric transient signal data acquisition and analyte concentration calculation**:** Journal of Analytical Atomic Spectrometry, v. 11, p. 899-904.

Lopez, D.L., Smith, L., 1995: Fluid flow in fault zones: Analysis of the interplay of convective circulation and topographically driven groundwater flow, Water Resources Research, v. 31, p. 1489-1503.

Lorenz, C., 1968, Contribution a l'étude stratigraphique de l'oligocene e du miocene inferieur des confins ligure-piemontais (Italie): Atti Ist. Geol. Univ. Genova, v. 6 (2), p. 273-889.

Lovett, R.A., 2013, Earthquakes make gold veins in an istant; Nature, doi:10.1038/nature.2013.12615.

Lucchetti, G., Cabella, R., Cortesogno, L. , 1990, Pumpellytes and coexisting minerals in low-grade metamorphic facies of Liguria, Italy: J. Metam. Geol., 8, 539-550.

Lunn, R.J., Willson, J.P., Shipton, Z.K., Moir, H., 2008, Simulating brittle fault growth from linkage of preexisting structures: Journal of Geophysical Research e Solid Earth, V. 113 (B7).

MacLean W. H. and Kranidiotis P., 1987. Immobile elements as monitors of mass transfer in hydrothermal alteration: Phelps Dodge massif sulphide deposit, Matagami, Quebec. Economic Geology 81, pp. 951-962.

Maerten, L., Maerten, F., and Lejri, M., 2017, Along fault friction and fluid pressure effects on the spatial distribution of fault-related fractures: Journal of Structural Geology.

Maffione, M., Speranza, F., Faccenna, C., Cascella, A., Vignaroli, G., and Sagnotti, L., 2008, A synchronous Alpine and Corsica-Sardinia rotation: J. Geophys. Res., v. 113, B03104. doi: 10.1029/2007 JB005214.

Maino, M., Dallagiovanna, G., Dobson, K. J., Gaggero, L., Persano, C., Seno, S., and Stuart, F. M., 2012, Testing models of orogen exhumation using zircon (U–Th)/He thermochronology: Insight from the Ligurian Alps, Northern Italy: Tectonophysics, v. 560, p. 84-93.

Maino, M., Decarlis, A., Felletti, F., and Seno, S., 2013, Tectono- sedimentary evolution of the Tertiary Piedmont Basin (NW Italy) within the Oligo-Miocene central Mediterranean geodynamics: Tectonics, v. 32, p. 1-27. http://dx.doi.org/10.1002/tect.20047.

Maino, M., and Seno, S., 2016, The thrust zone of the Ligurian Penninic basal contact (Monte Fronté, Ligurian Alps, Italy): Journal of Maps, v. 12(sup1), p. 341-351.

Malatesta, C., Crispini, L., Federico, L., Capponi, G., and Scambelluri, M., 2012, The exhumation of high pressure ophiolites (Voltri Massif, Western Alps): Insights from structural and petrologic data on metagabbro bodies: Tectonophysics, v. 568-569, p. 102-123.

Malatesta, C., Federico, L., Crispini, L., and Capponi, G., 2017, Fluid-controlled deformation in blueschist-facies conditions: plastic vs brittle behaviour in a brecciated mylonite (Voltri Massif, Western Alps, Italy): Geol. Mag., p. 1-21. doi:10.1017/S0016756816001163.

Malusà, M. G., Danišík, M., and Kuhlemann, J., 2016, Tracking the Adriatic-slab travel beneath the Tethyan margin of Corsica–Sardinia by low-temperature thermochronometry: Gondwana Research, v. 31, p. 135-149.

Malusà, M.G., Polino, R., Zattin, M., Bigazzi, G., Martin, S., Piana, F., 2005, Miocene to present differential exhumation in the Western Alps: insights from fission track thermochronology: Tectonics, v. 24, p. 1–23.

Mancktelow, N. S., 1985, The Simplon Line: a major displacement zone in the western Lepontine Alps: Eclogae. Geol. Helv., v. 84, p. 73-96.

Mancktelow, N. S., 1997, Neogene orogen-parallel extension in the Alps: the Simplon and Brenner fault zones: Quad. Geodin. Alp. Quatern., v. 4, p. 74.

Marrett, R., Allmendinger, R.W., 1992, Amount of extension on “small” faults: an example from the Viking graben: Geology, v. 20, p. 47–50.

Marroni, M., Feroni, A., C., Di Biase, D., Ottria, G., Pandolfi, L., Taini A., 2002, Polyphase folding at upper structural levels in the Borbera Valley (Northern Apennines, Italy): implications for the tectonic evolution of the linkage area between Alps and Apennines: C. R. Geoscience, 334, 565-572.

Marroni, M., Monechi, S., Perilli, N., Principi, G., and Treves, B., 1992, Late Cretaceous flysch deposits of the Northern Apennines, Italy: age of inception of orogenesis-controlled sedimentation, Cretaceous Research, v. 13, p. 487-504.

Marroni, M., Pandolfi, L., 2007, The architecture of an incipient oceanic basin: a tentative reconstruction of the Jurassic Liguria-Piemonte basin along the Northern Apennines–Alpine Corsica transect", Int J Earth Sci (Geol Rundsch).

Massonne, H. J., Cruciani, G., Franceschelli, M., and Musumeci, G., 2017, Anticlockwise pressure–temperature paths record Variscan upper-plate exhumation: Example from micaschists of the Porto Vecchio region, Corsica: Journal of Metamorphic Geology.

Matter, J.M., and Kelemen, P.B., 2009, Permanent storage of carbon dioxide in geological reservoirs by mineral carbonation: Nature geosciences, doi: 10.1038/ngeo683.

McGuire, J.J., Zhao, L., Jordan, T.H., 2002, Predominance of unilateral rupture for a global catalog of large earthquakes: Bull. Seismol. Soc. Am., v. 8, p. 3309-3317.

Messiga, B., 1987, Alpine metamorphic evolution of Ligurian Alps (North-West Italy): chemography and petrological constraints inferred from metamorphic climax assemblages: Contrib. Mineral. Petrol., v. 95, p. 269-277.

Messiga, B., Piccardo, G.B., and Ernst, W.G., 1983, High pressure Eo-Alpine parageneses developed in magnesian metagabbros, Gruppo di Voltri, Western Liguria, Italy: Contrib. Mineral. Petrol., v. 83, p. 1-15.

Messiga, B., and Scambelluri, M., 1991, Retrograde P-T-t path for the Voltri Massif eclogites (Ligurian Alps, Italy): some tectonic implications: Journ. of Metam. Geol., v. 9, p. 93-109.

Messiga, B., Tribuzio, R., and Scambelluri, M., 1992, Mafic eclogites from the Valosio crystalline massif (Ligurian Alps, Italy): Schweiz. Mineralog. Petrog. Mittel., v. 72, p. 365-377.

Micklethwaite, S., 2009, Mechanisms of faulting and permeability enhancement during epithermal mineralisation; Cracow gold field, Australia: Journal of Structural Geology, v. 31 (3), p. 288-300.

Miletto, M. and Polino, R., 1992, A gravity model of the crust beneath the Tertiary Piedmonte Basin (northwestern Italy): Tectonophysics, 212, 243-256.

Mitchell, T.M., Ben-Zion, Y., Shimamoto, T., 2011: Pulverized fault rocks and damage asymmetry along the Arima-Takatsuki Tectonic Line, Japan: Earth and Planetary Sciences Letters, v. 308, p. 284-297.

Molli, G., 2008, Northern Apennine–Corsica orogenic system: an updated overview. In: Siegesmund, S., Fugenschuh, B., Froitzheim, N. (Eds.), Tectonic Aspects of the Alpine–Dinaride–Carpathian System: Geological Society of London, Special Publications, v. 298, p. 413–442.

Molli, G., Crispini, L., Malusà, M.G., Mosca, P., Piana, F., and Federico, L., 2010, Geology of the Western Alps-Northern Apennine junction area: a regional review: Journal of the Virtual Explorer, v. 36, p. 1-49.

Moncada, D., Mutchler, S., Nieto, A., Reynolds, T.J., Rimstidt, J.D., and Bodnar, R.J., 2012, Mineral textures and fluid inclusion petrography of the epithermal Ag–Au deposits at Guanajuato, Mexico: Application to exploration: Journal of Geochemical Exploration, v. 114, p. 20–35, doi: 10.1016/j.gexplo.2011.12.001.

Monzawa, N., and Otsuki, K., 2003: Comminution and fluidization of granular fault materials: implications for fault slip behavior: Tectonophysics v. 367, p. 127-143.

Mosca, P., R. Polino, S. Rogledi, and M. Rossi, 2010, New data for the kinematic interpretation of the Alps-Apennines junction (Northwestern Italy): Int. J. Earth Sci., v. 99, p. 833–849.

Mountain, B.W., and Williams-Jones, A.E., 1996, Mass transfer and the path of metasomatic reactions in mesothermal gold deposits; an example from Flambeau Lake, Ontario: Economic Geology, v. 91, p. 302–321.

Mutti, E., Papani, L., Di Biase, D., Davoli, G., Mora, S., Segadelli, S., and Tinterri, R., 1995, Il Bacino Terziario Epimesoalpino e le sue implicazioni sui rapporti tra Alpi e Appennino: Mem. Sci. Geol., v. 47, p. 217-244.

Nader, F., 2007, Petrographic and geochemical study on cave pearls from Kanaan Cave (Lebanon): International Journal of Speleology, v. 36, p. 39–50, doi: 10.5038/1827-806X.36.1.4.

Nicolas, A., Bouchez, J.-L., and Boudier, F., 1972, Kinematic inter- pretation of plastic deformations in the lherzolite Massif of Lanzo (Piedmont Alps); comparison with other massifs. Tectonophysics, v. 14, p. 143-171.

Novellino, R., Prosser, G., Spiess, R., Viti, C., Agosta, F., Tavarnelli, E., and Bucci, F. 2015, Dynamic weakening along incipient low-angle normal faults in pelagic limestones (Southern Apennines, Italy): Journal of the Geological Society of London, v. 172, p. 283-286.

Otsuki, K., Monzawa, N., and Nagase, T., 2003: Fluidization and melting of fault gouge during seismic slip: Identification in the Nojima fault zone and implications for focal earthquake mechanisms: J. Geophys. Res. 108 (B42192), 18. http:// dx.doi.org/10.1029/2001JB001711.

Pasquale, V., Verdoya, M., and Chiozzi, P., 2011, Groundwater flow analysis using different geothermal constraints: The case study of Acqui Terme area, northwestern Italy: Journal of Volcanology and Geothermal Research, v. 199, p. 38–46, doi: 10.1016/j.jvolgeores.2010.10.003.

Patacca, E. and Scandone, P., 1989, Post-Tortonian mountain building in the Apennines. The role of the passive sinking of a relic lithospheric slab, In: Boriano A., Bonafede M., Piccardo G. B., Vai G. B. (eds): The lithosphere in Italy. Atti Conv. Lincei, 80, 157-176.

Pavoni, N., 1991, Bipolarity in structure and dynamics of the Earth's mantle: Eclogae. Geol. Helv., v. 84, p. 327-343.

Perrello, P., Delle Piane, L., Piana, F., Stella, F., Damiano, A., 2004, Brittle post-metamorphic tectonics in the Gran Paradiso Massif (north-western Italian Alps): Geodin. Acta, v. 17, p. 69-88.

Pettke, T., L.W. Diamond and J.D. Kramers, 2000, "Mesothermal gold lodes in the north-western Alps: A review of genetic constraints from radiogenic isotopes.": European Journal of Mineralogy v. 12, p. 213-230.

Peuble, S., Andreani, M., Gouze, P., Pollet-Villard, M., Reynard, B., & Van de Moortele, B., 2017, Multi-scale characterization of the incipient carbonation of peridotite: Chemical Geology.

Pfiffner, O. A., Ellis, S., and Beaumont, C., 2000, Collision tectonics in the Swiss Alps: insight from geodynamic modelling: Tectonics, v. 19, p. 1065-1094.

Pfiffner, O. A., 2016, Basement-involved thin-skinned and thick-skinned tectonics in the Alps: Geological Magazine, v. 153(5-6), p. 1085-1109.

Philippot, P., 1990, Opposite vergence of nappes and crustal extension in the French-Italian Western Alps: Tectonics, v. 9, p. 1143–1164.

Phillips, G. N., and Powell, R., 2010, Formation of gold deposits: a metamorphic devolatilization model: Journal of Metamorphic Geology, v. 28(6), p. 689-718.

Phillips, G. N., and Powell, R., 2009, Formation of gold deposits: Review and evaluation of the continuum model: Earth-Science Reviews, v. 94(1), p. 1-21.

Piana, F., D'atri, A., and Orione, P., 1997, The Visone Formation, a marker of the Early Miocene tectonics in the Alto Monferrato Domain (Tertiary Piemonte Basin, NW Italy): Mem. Sci. Geol., v. 49, p. 145 – 162.

Piana F, Tallone S, Cavagna S, Conti A., 2006, Thrusting and faulting in metamorphic and sedimentary units of Ligurian Alps: an example of integrated field work and geochemical analyses: International Journal of Earth Science, v. 95, p. 413–430.

Piccardo, G.B., Rampone, E., and Scambelluri, M., 1988, The alpine evolution of the Erro - Tobbio peridotites (Voltri Massif-Ligurian Alps): some field and petrographic constraints. Ofioliti, v. 13 (2/3), p. 169-174.

Pipino, G., 1976, Le manifestazioni aurifere del gruppo di Voltri con particolare riguardo ai giacimenti della Val Gorzente, L'Industria Mineraria, Novembre, p. 452-468.

Pipino, G., 1978, Alcune considerazioni sui giacimenti delle ofioliti liguri, L'Industria Mineraria, Marzo-Aprile, p. 97-107.

Pipino, G., 1980, Gold in ligurian ophiolites (Italy), Int. Oph. Symp. Geol. Survey Dep., Cyprus, 756-773

Pipino, G., 1982, I giacimenti metalliferi del Piemonte Genovese.

Pipino, G., 2000, Le Valli dell'Oro - Miscellanea di geologia, archeologia e storia dell'Ovadese e della bassa Val d'Orba, Museo Storico Dell' Oro Italiano - Tipografia Pesce, Ovada, p. 237.

Pipino, G., 2001, Le miniere d'oro delle Valli Gorzente e Piota, Ente Di Gestione Parco Naturale Capanne Di Marcarolo.

Pipino, G., 2003, Oro, miniere, storia. Miscellanea di giacimentologia e storia mineraria italiana, Museo Storico Dell' Oro Italiano - Tipografia Pesce, Ovada, p. 510.

Pittarello, L., Koeberl C., 2013, Clast size distribution and quantitative petrography of shocked and unshocked rocks from El'gygytgyn impact structure: Meteoritics & Planetary Science, v. 48, p. 1325-1338.

Platt, J. P., and Vissers, R. L. M., 1980, Extensional structures in anisotropic rocks. Journal of Structural Geology, v. 2(4), p. 397-410.

Pokrovski, G. S., Roux, J., and Harrichoury, J.-C., 2005, Fluid density control on vapor-liquid partitioning of metals in hydrothermal systems: Geology, v. 33, no. 8, p. 657-660.

Polino, R., Clari P., Crispini, L. D' Atri, A., Dela Pierre, F., Novaretti, A., Piana, F., Ruffini, R., and Timpanelli, M., 1995, Relazioni tra le zone di taglio crostali e bacini sedimentari: l'esempio della giunzione alpino-appenninica durante il Terziario. Guida all'escursione in Monferrato e nella Zona Sestri-Voltaggio, Atti Convegno " Rapporti Alpi - Appennino" & Guide alle Escursioni: Acc. Naz. Sci. Scritti & Documenti, v. 14, p. 531-539.

Polino, R., Dal Piaz, G.V., and Gosso, G., 1990, Tectonic erosion at the Adria margin and accretionary processes for the Cretaceous orogeny of the Alps: Mémoires de la Société géologique de France, v. 156, p. 345–367.

Power, I. M., Harrison, A. L., Dipple, G. M., Wilson, S. A., Kelemen, P. B., Hitch, M., and Southam, G., 2013, Carbon mineralization: from natural analogues to engineered systems: Reviews in Mineralogy and Geochemistry, v. 77(1), p. 305-360.

Principi, G., Cortesogno, L., Cellai, D., Gaggero, L., Garuti, G., Gazzotti, M., Passerini, P., and Treves, B., 1992, "Le ofioliti dell'Appennino Settentrio- nale". Atti Convegno SIMP (Firenze 21-23/9/1992): Guida all'escursione: p. 1-76.

Principi, G., and Treves, B., 1985, "Le unità ofiolitiche giurassico-cretacee nell'area della media Val di Vara. Accrezione di un segmento trasforme.": Mem. Soc. Geol. It. v. 30, p. 205-212.

Prokofiev, V., Y., Kamenetsky, V., S., Selektor, S., L., Rodemann, T., Kovalenker, V., A., and Vatsadze, S., Z., 2017, First direct evidence for natural occurrence of colloidal silica in chalcedony-hosted vacuoles and implications for ore-forming processes. Geology, v. 45(1), p. 71-74.

Qiu, T., and Zhu, Y., 2015, Geology and geochemistry of listwaenite-related gold mineralization in the Sayi gold deposit, Xinjiang, NW China: Ore Geology Reviews, v. 70, p. 61-79.

Qiu, Y., Groves, D., I., McNaughton, N., J., Wang, L. ,G., and Zhou, T., 2002, Nature, age, and tectonic setting of granitoid-hosted, orogenic gold deposits of the Jiaodong Peninsula, eastern North China craton, China: Mineralium Deposita, v. 37(3), p. 283-305.

Rampone, E. and Piccardo, G., 2000, The ophiolite-oceanic lithosphere analogue: new insights from the northern Apennines (Italy)., In: Y. Dilek, E.M. Moores, D. Elthon And A. Nicolas (eds.): Ophiolites and oceanic crust: new insights from field studies and the Ocean Drilling Project. Geol. Soc. America Spec. Paper 349, 21-34.

Rampone, E., Romairone, A., Abouchami, W., Piccardo, G.B., Hofmann, A.W., 2005, Chronology, petrology and isotope geochemistry of the Erro-Tobbio peridotites (Ligurian Alps, Italy): records of late Paleozoic lithospheric extension: J. Petrol. v. 46, p. 799–827.

Ramsay, J. G., and Huber, M. I., 1987, The techniques of modern structural geology. Vol.2: Folds and fractures, Academic Press, p. 700.

Rawling, G.C., Goodwin, L.B., Wilson, J.L., 2001, Internal architecture, permeability structure, and hydrologic significance of contrasting fault-zone types: Geology v. 29 (1), p. 43-46.

Ranjith, k., Rice, J.R., 2001, Slip dynamics at an interface between dissimilar materials: J. Mech. Phys. Solids, v. 49, p. 341-361.

Rauchenstein-Martinek, K., Wagner, T., Wälle, M., and Heinrich, C. A., 2014, Gold concentrations in metamorphic fluids: a LA-ICPMS study of fluid inclusions from the Alpine orogenic belt: Chemical Geology, v. 385, p. 70-83.

Reed, M. H., 1997: Hydrothermal alteration and its relationships to ore fluid composition. in Geochemistry of Hydrothermal Ore Deposits“, H. L. Barnes, ed. Third ed. John Wiley & Sons, Inc., p. 303-365.

Rempe, M., Smith, S.A.F., Ferri, F., Mitchell, T.M., and Di Toro, G., 2014, Clast-cortex aggregates in experimental and natural calcite-bearing fault zones: Journal of Structural Geology, v. 68, p. 142–157, doi: 10.1016/j.jsg.2014.09.007.

Rice, J.R., 2006, Heating and weakening of faults during earthquake slip: Journal of Geophysical Research, v. 111, B05311, doi:10.1029/2005JB004006.

Rollet, N., Déverchère, J., Beslier, M., Guennoc, P., Réhault, J., Sosson, M., Truffert, C., 2002, Back arc extension, tectonic inheritance and volcanism in the Ligurian Sea, Western Mediterranean: Tectonics, Vol.21, N. 3, 1-23

Rosenbaum, G., and Lister, G. S., 2004, Neogene and Quaternary rollback evolution of the Tyrrhenian Sea, the Apennines, and the Sicilian Maghrebides: Tectonics, v. 23(1).

Rosenbaum, G., Lister, G.S., and Duboz, C., 2002. Relative motions of Africa, Iberia and Europe during Alpine orogeny: Tectonophysics 359, 117–129.

Ross, Z. E., Rollins, C., Cochran, E. S., Hauksson, E., Avouac, J. P., and Ben-Zion, Y., 2017, Aftershocks driven by afterslip and fluid pressure sweeping through a fault-fracture mesh: Geophysical Research Letters.

Rossi M., Mosca, P., Polino, R., Rogledi, S., and Biffi, U., 2009, New outcrop and subsurface data in the Tertiary Piedmont Basin (NW-Italy): unconformity-bounded stratigraphic units and their relationships with basin-modification phases: Rivista Italiana Paleontologia Stratigrafica, v. 115 (3), p. 305-335.

Rotevatn, A., Fossen, H., 2011, Simulating the effect of subseismic fault tails and process zones in a siliciclastic reservoir analogue: implications for aquifer support and trap definition: Mar. Pet. Geol., v. 28, p. 1648–1662.

Rovereto, G., 1939, Liguria Geologica: Mem. Soc. Geol. It., v. 2, p. 743.

Rowe, C.D., Fagereng, r., Miller, J.A., and Mapani, B., 2012a, Signature of coseismic decarbonation in dolomite fault rocks of the Naukluft Thrust, Namibia: Earth Planet. Sci. Lett. 333-334, p. 200-210.

Rowe, C.D., Kirkpatrick, J.D., Brodsky, E.E., 2012b, Fault rock injections record paleo-eartquakes, Earth and Planetary Sciences Letters, v. 335-336, p. 154-166.

Rowe, C.D., and Griffith, W.A., 2015, Do faults preserve a record of seismic slip: A second opinion: Journal of Structural Geology, v. 78, p. 1–26.

Rubin, A.M., 1995, Propagation of magma-filled cracks: Annual Review of Earth and Planetary Sciences, v.23, p.287-336.

Rudnick, R. L., and Gao, S., 2003, The Composition of the Continental Crust, in Holland, H. D., and Turekian, K. K., eds., Treatise on Geochemistry. Volume 3. The Crust, Elsevier, p. 1-64.

Russell, M. J., Hall, A. J., and Martin, W., 2010, Serpentinization as a source of energy at the origin of life: Geobiology, v. 8(5), p. 355-371.

Salvi, S., and Williams-Jones, A.E., 1996, The role of hydrothermal processes in concentrating high-field strength elements in the Strange Lake peralkaline complex, northeastern Canada: Geochimica et Cosmochimica Acta, v. 60, p. 1917–1932.

Sánchez-Roa, C., Faulkner, D., R., Boulton, C., Jimenez-Millan, J., and Nieto, F. 2017, How phyllosilicate mineral structure affects fault strength in Mg-rich fault systems. Geophysical Research Letters.

Sánchez-Roa, C., Vidal, O., Jiménez-Millán, J., Nieto, F., and Faulkner, D., R., 2018, Implications of sepiolite dehydration for earthquake nucleation in the Galera Fault Zone: A thermodynamic approach: Applied Geochemistry, v. 89, p. 219-228.

Sant'Anna, L.G., Riccomini, C., Rodrigues-Francisco, B.H., Sial, A.N., Carvalho, M.D., and Moura, C.A.V., 2004, The Paleocene travertine system of the Itabora basin, Southeastern Brazil: Journal of South American Earth Sciences, v. 18, p. 11–25, doi: 10.1016/j.jsames.2004.08.005.

Sarkarinejad, K., and Azizi, A., 2008, Slip partitioning and inclined dextral transpression along the Zagros Thrust System, Iran: Journal of Structural Geology, v. 30(1), p. 116-136.

Scambelluri, M., Rampone, E., and Piccardo, G. B., 2001, Fluid and element cycling in subducted serpentinite: a trace-element study of the Erro-Tobbio High pressure ultramafites (Western Alps, NW Italy): Journal of Petrology, v. 42, p. 56-67.

Scambelluri, M., Müntener, O., Hermann, J., Piccardo, G.B. and Trommsdorff, V., 1995, - Subduction of water into the mantle: history of an Alpine peridotite: Geology, V. 23 (5), p. 459-462.

Scambelluri, M., Hoogerduijn Strating, E.H., Piccardo, G.B., Vissers, R.L.M. and Rampone, E., 1991, Alpine olivine- and tita- nian clinohumite-bearing assemblages in the Erro-Tobbio peridotite (Voltri Massif, NW Italy): J. Metamor. Geol., v. 9, p. 79-91.

Scarsi, M., 2014, Tectonic evolution of the western sector of the Voltri Massif, structural analysis of carbonate metaophiolites and garnet marbles of the Erro River (Location La Pesca): unpublished Master Thesis.

Scarsi, M., Malatesta, C., and Fornasaro, S., 2017, Lawsonite-bearing eclogite from a tectonic mélange in the Ligurian Alps: new constraints for the subduction plate-interface evolution: Geol. Mag., p. 1-18. doi:10.1017/S0016756817000395.

Schandl, E. S., and Gorton, M. P., 2012, Hydrothermal alteration and CO_2 metasomatism (natural carbon sequestration) of komatiites in the south-western Abitibi greenstone belt: The Canadian Mineralogist, v. 50(1), p. 129-146.

Schleicher, A. M., van der Pluijm, B. A., and Warr, L. N., 2010, Nanocoatings of clay and creep of the San Andreas fault at Parkfield, California: Geology, 38(7), 667-670.

Schmid, S., Aebli, H. R., Heller, F., and Zingg, A., 1989, The role of the Periadriatic Line in the tectonic evolution of the Alps, In: Coward M., Dietrich D., Park R. G. (eds), Alpine Tectonics: Geol. Soc. London, Spec. Pub., v. 45, p. 153-171.

Schmid, S., M., and Kissling, E., 2000, The arc of the western Alps in the light of geophysical data on deep crustal structure: Tectonics, 19, N.1, 62-85.

Schmid, S. M., Kissling, E., Diehl, T., van Hinsbergen, D., J., and Molli, G., 2017, Ivrea mantle wedge, arc of the Western Alps, and kinematic evolution of the Alps–Apennines orogenic system: Swiss Journal of Geosciences, p. 1-32, DOI: 10.1007/s00015-016-0237-0.

Schmid, S. M., Pfiffner, O. A., Froitzheim, N., Scho¨nborn, G., and Kissling, E., 1996, Geophysical-geological transect and tectonic evolution of the Swiss-Italian Alps: Tectonics, v. 15, p. 1036–1064.

Scholz, C.H., Cowie, P.A., 1990, Determination of total strain from faulting using slip measurements: Nature, v. 346, p. 837–839.

Schulz, S.E., Evans, J.P., 1998, Spatial variability in microscopic deformation and composition of the Punchbowl fault, southern California: implications for mechanisms, fluid–rock interaction, and fault morphology: Tectonophysics, v. 295, p. 223–244.

Schulz, S.E., Evans, J.P., 2000, Mesoscopic structure of the Punchbowl Fault, Southern California and the geologic and geophysical structure of active strike- slip faults: Journal of Structural Geology, v. 22 (7), p. 913-930.

Seifritz, W., 1990; CO_2 disposal by means of silicates: Nature 345, p. 486.

Schumacher, M., E., and Laubscher, H., 1996, 3D crustal architecture of the Alps–Apennines join—a new view on seismic data: Tectonophysics, v. 260, p. 349–363.

Schwartz, S., Gautheron, C., Audin, L., Dumont, T., Nomade, J., Barbarand, J., and van der Beek, P., 2017, Foreland exhumation controlled by crustal thickening in the Western Alps: Geology, v. 45(2), p. 139-142.

Scrocca, D., Doglioni, C., and Innocenti, F., 2003, Constraints for an interpretation of the Italian geodynamics: a review: Memorie Descrittive della Carta Geologica d'Italia, v. 62, p. 15-46.

Seno, S., Dallagiovanna, G., and Vanossi, M., 2003, Palaeogeography and thrust development in the Penninic domain of the Western Alpine chain: examples from the Ligurian Alps: Bollettino della Società Geologica Italiana, v. 122(2), p. 223-232.

Seno, S., Dallagiovanna, G., and Vanossi, M., 2005, Pre-Piedmont and Piedmont–Ligurian nappes in the central sector of the Ligurian Alps: a possible pathway for their superposition on to the inner Briançonnais units: Bollettino della Società Geologica Italiana, v. 124 (2), p. 455–464.

Shelly, D. R., Taira, T. A., Prejean, S. G., Hill, D. P., and Dreger, D. S., 2015, Fluid-faulting interactions: Fracture-mesh and fault-valve behavior in the February 2014 Mammoth Mountain, California, earthquake swarm: Geophysical Research Letters, v. 42(14), p. 5803-5812.

Shi, Z.Q., Ben-Zion, Y., 2006, Dynamic rupture on a bimaterial interface governed by slip-weakening friction: Geophysical Journal International: v. 165, p. 469-484.

Shimamoto, T., and Logan, J., M., 1981, Effects of simulated clay gouges on the sliding behavior of Tennessee sandstone: Tectonophysics, v. 75, p. 243–255.

Shipton, Z.K., Cowie, P.A., 2001, Damage zone and slip-surface evolution over mm to km scales in high-porosity Navajo sandstone, Utah: Journal of Structural Geology: v. 23 (12), p. 1825-1844.

Shipton, Z., Evans, J., Kirchner, D., Kolesar, P., Williams, A., Heath, J., 2004, Analysis of CO2 leakage through low-permeability faults from natural reservoirs in the Colorado Plateau, southern Utah. In: Baines, S., Worden, R. (Eds.), Geological Storage of Carbon Dioxide: Geological Society of London, Special Publications, v. 233, p. 43–58.

Sibson, R.H., 2001, Seismogenic framework for hydrothermal transport and ore deposition: Reviews in Economic Geology, v. 14, p. 25-50.

Sibson, R.H., 2000, Fluid involvement in normal faulting: Journal of Geodynamics, v. 29, p. 469-499.

Sibson, R.H, 1992, Implications of fault-valve behaviour for rupture nucleation and recurrence: Tectonophysics, v. 211, p. 283-289.

Sibson, R.H., Robert, F., and Poulsen, K.H., 1988, High-angle reverse faults, fluid-pressure cycling, and mesothermal gold – quartz deposits: Geology v. 16, p. 551–555.

Sibson, R.H., 1977, Fault rocks and fault mechanisms: Journal of the Geological Society, v. 133, p. 191–213.

Siman-Tov, S., Aharonov, E., Sagy, A., and Emmanuel, S., 2013, Nanograins form carbonate fault mirrors: Geology, 41(6), 703-706.

Smith, S.A., Billi, A., Di Toro, G., and Spiess, R., 2011, Principal slip zones in

limestone: microstructural characterization and implications for the seismic cycle (Tre Monti Fault, Central Apennines, Italy): Pure and Applied Geophysics, v. 168, p. 2365–2393.

Spagnolo, C., 2004, Late-Orogenic tectonics in the Eastern sector of the Ligurian Alps [Unpublished PhD Thesys]: Università degli Studi di Genova.

Spagnolo, C., Crispini, L., and Capponi, G., 2007, Late structural evolution in an accretionary wedge: insights from the Voltri Massif (Ligurian Alps, Italy): Geodinamica Acta, v. 20, p. 21–35.

Stampfli, G.M., 1993, Le Briançonnais, terrain exotique dans les Alpes?: Eclogae Geologicae Helvetiae, v. 86 (1), p. 1–45.

Stampfli, F.M., Mosar, J., Marquer, D., Marchant, R., Baudin, T., and Borel, G., 1998, Subduction and obduction processes in the Swiss Alps: Tectonophysics, v. 296, p. 159-204.

Steck, A., and Hunziker, J. C., 1994, The Tertiary structural and thermal evolution of the Central Alps - compressional and extensional structures in an orogenic belt: Tectonophysics, v. 238, p. 229-254.

Sue, C., Delacou, B., Champagnac, J. D., Allanic, C., Tricart, P., and Burkhard, M., 2007, Extensional neotectonics around the bend of the Western/Central Alps: an overview: International Journal of Earth Sciences, v. 96(6), p. 1101-1129.

Sue, C. and Tricart, P., 2003, Neogene to ongoing normal faulting in the inner western Alps: a major evolution of the late alpine tectonics: Tectonics, v. 22, n. 5, p. 1050.

Sulem, J., and Famin, V., 2009, Thermal decomposition of carbonates in fault zones: Slip-weakening and temperature-limiting effects. Journal of Geophysical Research: Solid Earth, 114(B3).

Sunagawa, I., 1978, Vapour growth and epitaxy of minerals and synthetic crystals: Journal of Crystal Growth, v. 45, p. 3-12.

Tavarnelli, E., 1997, Structural evolution of a foreland fold-and-thrust belt: the Umbria-Marche Apennines, Italy: Journal of Structural Geology, v. 19, p. 523-534.

Tembe, S., Lockner, D., A., and Wong, T., F., 2010, Effect of clay content and mineralogy on frictional sliding behavior of simulated gouges: Binary and ternary mixtures of quartz, illite, and montmorillonite: J. Geophys. Res., v. 115, B03416, doi:10.1029/2009JB006383.

Tomkins, A., G., 2013, On the source of orogenic gold: Geology, v. 41(12), p. 1255-1256.

Treves B., 1984, Orogenic belts as accretionary prism: the example of the Northern Apennines: Ofioliti, 9, 577-618.

Triglav, J. T., van Elteren and Šelih, V. S., Analytical Chemistry, 2010, Basic modelling approach to optimize elemental imaging by laser ablation ICPMS: American Chemical Society, v. 82, p. 8153-8160.

Trullenque, G., 2005, Tectonic and microfabric studies along the Penninic Front between Pelvoux and Argentera massifs (Western Alps) (293 pp). University of Basel, Ph.D. thesis. Pdf available at http://edoc.unibas.ch/353/.

Turco, E., Duranti, D., Iaccarino, S., and Villa, G., 1994, Relationships between foraminiferal biofacies and lithofacies in the Oligocene Molare Formation and Rigoroso Marl: preliminary results from the Piota River section (Tertiary Piedmont Basin, NW Italy): Giornale di Geologia, 56(2), 101-117.

Tsuchiya, Y., Wada, Y., Hiaki, T., Onoe, K., and Matsumoto, M., 2017, Effects of CO2 fine bubble injection on reactive crystallization of dolomite from concentrated brine: Journal of Crystal Growth, v. 469, p. 36-41.

Ugarkar, A. G., Malapur, M. A., and Kumar, B. C., 2016, Archean turbidite hosted orogenic gold mineralization in the Gadag greenstone belt, Western Dharwar Craton, Peninsular India: Ore Geology Reviews, v. 72, p. 1224-1242.

Ulrich, M., Muñoz, M., Guillot, S., Cathelineau, M., Picard, C., Quesnel, B., and Couteau, C., 2014, Dissolution–precipitation processes governing the carbonation and silicification of the serpentinite sole of the New Caledonia ophiolite: Contributions to Mineralogy and Petrology, v. 167(1), p. 952.

Vanossi, M., 1984, Geologia delle Alpi liguri: Memorie/Soc. geol. Italiana, v. 28.
Vanossi, M., Cortesogno, L., Galbiati, B., Messiga, B., Piccardo, G., and Vannucci, R., 1986, Geologia delle Alpi liguri: dati, problemi, ipotesi: Memorie della Società Geoligica Italiana, v. 28, p. 5–75.

Van Elteren, J.T., Izmer, A., Sala, M., Orsega, E.F., Selih, V.S., Panighello, S., and Vanhaecke, F., 2013. 3D laser ablation-ICP-mass spectrometry mapping for the study of surface layer phenomena - a case study for weathered glass. Journal of Analytical Atomic Spectrometry 28, 994-1004.

Van Elteren, J. T., and Vanhaecke, F., 2016, Angular resolution dependency in 2D LA-ICP-MS mapping–the case for low-dispersion laser ablation cells: J. Anal. At. Spectrom., v. 31, P. 1998-2004.

Van Malderen, S.J., van Elteren J.T., and F. Vanhaecke, 2015 Submicrometer imaging by laser ablation-inductively coupled plasma mass spectrometry via signal and image deconvolution approaches, Anal Chem, v. 87, p. 6125-6132.

Van Malderen, S. J. M., Managh, A. J., Sharp, B. L., and Vanhaecke, F., 2016, Recent developments in the design of rapid response cells for laser ablation-inductively coupled plasma-mass spectrometry and their impact on bioimaging applications: Journal of Analytical Atomic Spectrometry, v. 31, p. 423-439.

Van Noort, R., Spiers, C. J., Drury, M. R., and Kandianis, M. T., 2013, Peridotite dissolution and carbonation rates at fracture surfaces under conditions relevant for in situ mineralization of CO^2: Geochimica et Cosmochimica Acta, v. 106, p. 1-24.
Venturelli, G., Thorphe, R. S., Dal Piaz, G. V., Del Moro, A., Potts, P. J., 1984, Petrogenesis of calcalcaline, shoshonitic and associated ultrapotassic Oligocene volcanic rocks from the North-Western Alps, Italy: Contrib. Mineral. Petrol, v. 86, p. 209-220.
Verberne, B.A., Plümper, O., de Winter, D.M., and Spiers, C.J., 2014, Superplastic nanofibrous slip zones control seismogenic fault friction: Science, v. 346, p. 1342–1344.

Vialon, P., Rochette, P., and Menard, G., 1989, Indentation and rotation in the western Alpine arc, In: Coward M., Dietrich D., Park R. G. (eds), Alpine Tectonics: Geol. Soc. London, Spec. Pub., v. 45, p. 329-338.

Viganò, A., Tumiati, S., Recchia, S., Martin, S., Marelli, M., and Rigon, R., 2011, Carbonate pseudotachylytes: evidence for seismic faulting along carbonate faults: Terra Nova, v. 23(3), p. 187-194.

Vignaroli, G., Faccenna, C., Jolivet, L., Piromallo, C., and Rossetti, F., 2008, Subduction polarity reversal at the junction between the Western Alps and the Northern Apennines, Italy. Tectonophysics, 450(1), 34-50.

Visentini, R., Ruyer, P., and Colin, C., Experimental study of transient boiling, in Proceedings 8th International Conference on Multiphase Flow ICMF 2013, Jeju Island Republic of Korea, 2013, p. 1-8.

Viti, C., Brogi, A., Liotta, D., Mugnaioli, E., Spiess, R., Dini, A., Zucchi, M., and Vannuccini, G., 2016, Seismic slip recorded in tourmaline fault mirrors from Elba Island (Italy): Journal of Structural Geology, v. 86, p. 1–12.

Vissers, R.L.M., Drury, M.R., Hoogerduijn Strating, E.H., Van der Wal, D., 1991, Shear zones in the upper mantle: a case study in an Alpine lherzolite massif: Geology, v. 19, p. 990–993.
Walsh, J.J., Watterson, J., Yielding, G., 1991, The importance of small-scale faulting in regional extension; Nature, v. 351, p. 391–393.

Wang, H. A., Grolimund, D., Giesen, C., Borca, C. N., Shaw-Stewart, J. R., Bodenmiller B., and Günther D., 2013: Fast chemical Imaging at high spatial resolution by laser ablation coupled plasma mass spectrometry: Analytical chemistry, v. 85, p. 10107-10116.

Wang, Q., Gu, J., Li, Z., and Yao, W., 2017, Dynamic modeling of bubble growth in vapor-liquid phase change covering a wide range of superheats and pressures: Chemical Engineering Science, v. 172, p. 169-181.

Wang, Z., L., Yang, L., Q., Guo, L., N., Marsh, E., Wang, J. P., Liu, Y., and Zhao, R., X., 2015, Fluid immiscibility and gold deposition in the Xincheng deposit, Jiaodong Peninsula, China: A fluid inclusion study: Ore Geology Reviews, v. 65, p. 701-717.

Wyman, D. A., Cassidy, K. F., and Hollings, P., 2016, Orogenic gold and the mineral systems approach: resolving fact, fiction and fantasy: Ore Geology Reviews, v. 78, p. 322-335.

Welch, L. A., and Allen, D. M., 2014, Hydraulic conductivity characteristics in mountains and implications for conceptualizing bedrock groundwater flow: Hydrogeology Journal, v. 22(5), p. 1003-1026.

Weatherley, D. K., and Henley, R. W., 2013, Flash vaporization during earthquakes evidenced by gold deposits: Nature Geoscience, v. 6(4), p. 294-298.

Wibberley, C.A.J., Shimamoto, T., 2003, Internal structure and permeability of major strike-slip fault zones: the Median Tectonic Line in Mie Prefecture, Southwest Japan; Journal of Structural Geology, v. 24, p. 59-78.

Wilson, J.E., Chester, J.S., Chester, F.M., 2003, Microfracture analysis of fault growth and wear processes, Punchbowl fault, San Andreas system, California: J. Struct. Geol., v. 25, p. 1855–1873.

Woodhead, J.D., Hellstrom, J., Hergt, J.M., Greig, A., and Maas, R., 2007. Isotopic and Elemental Imaging of Geological Materials by Laser Ablation Inductively Coupled Plasma-Mass Spectrometry. Geostandards and Geoanalytical Research 31, 331-343.

Wu, C., Yi, H., Hui, B., Xia, G., and Ma, X., 2014, A new sediment type of coated grain: Oolitic sinter: Science China Earth Sciences, v. 57, p. 2013–2024, doi: 10.1007/s11430-014-4921-5.

Yang, L., Q., Guo, L., N., Wang, Z., L., Zhao, R., X., Song, M., C., and Zheng, X., L., 2016, Timing and mechanism of gold mineralization at the Wang'ershan gold deposit, Jiaodong Peninsula, eastern China: Ore Geology Reviews.

Zanzucchi, G., 1978, Tectonics of the Parma Province Apennines: I.U.G.S. Scient. Rep., 83, 276-279.

Zeng, Q., Wang, Z., He, H., Wang, Y., Zhang, S., and Liu, J., 2014, Multiple isotope composition (S, Pb, H, O, He, and Ar) and genetic implications for gold deposits in the Jiapigou gold belt, Northeast China: Mineralium Deposita, v. 49(1), p. 145-164.

Zhang, B., Zhang, J., and Zhong, D., 2010, Structure, kinematics and ages of transpression during strain-partitioning in the Chongshan shear zone, western Yunnan, China: Journal of Structural Geology, v. 32(4), p. 445-463.

Zhao, Z., Glod, S., and Poulikakos, D., 2000, Pressure and power generation during explosive vaporization on a thin-film microheater: International Journal of Heat and Mass Transfer, v. 43, no. 2, p. 281-296.

Zoheir, B., and Lehmann, B., 2011, Listvenite–lode association at the Barramiya gold mine, Eastern Desert, Egypt: Ore Geology Reviews, v. 39(1), p. 101-11.

Ringraziamenti

I miei più sentiti ringraziamenti vanno alla **Prof.ssa Laura Crispini**, al **Prof. Paolo Garofalo** e al **Prof. Giovanni Capponi** , per tutto il tempo dedicatomi, per il supporto scientifico, per tutti gli insegnamenti che mi hanno fornito, per la grandissima pazienza che hanno avuto nei miei confronti e per avermi fatto amare profondamente la geologia, specie quella strutturale.

Ringrazio il **Prof. Luca Pandolfi** e il **Prof. Enrico Tavarnelli** per il tempo dedicato alla revisione e alla valutazione di questa tesi di dottorato.

Ringrazio la **Prof.ssa Laura Federico**, non presente nella prima pagina della tesi, ma anche a lei devo grandi ringraziamenti, per le lunghe discussioni, per il supporto scientifico e per i numerosi insegnamenti.
Ringrazio il **Prof. Cabella**, il **Prof. Zuccolini** e la **Prof.ssa Cristina Carbone** per la stima che mi hanno sempre dimostrato.
Ringrazio **Alex**, **Gunner**, **Marcel** e **Lorenzo** per la loro simpatia e amicizia dimostratami durante il periodo a Zurigo.
Ringrazio il **Dott. Geol. Giuseppe Pipino** per aver condiviso le sue conoscenze e la sua esperienza riguardanti la zona di studio e per il tempo dedicatomi.

E ora qui dovrei aprire un elenco lunghissimo di ringraziamenti…

In ambito universitario ringrazio le mie colleghe la Dott.ssa **Cristina Malatesta (MammaCri)** e la Dott.ssa **Silvia (Sissi) Fornasaro** in primis per avermi sopportato e poi anche supportato in questa avventura, per il lavoro svolto insieme, sia di ricerca che con gli studenti; per il parchetto contest, il bomber e le girls, dovrei scrivere una tesina solo per ringraziarle a sufficienza.
Ringrazio il mio amico e collega il Dott. **Guido Bonello** per le pause caffè di questi anni, i pranzi, per tutte le schiodate fatte insieme, e per la collaborazione futura (incrociamo le dita).
Ringrazio **Nicholas Vaiarini** e **Marco Puddu**, beh perché non potevo non ringraziarvi, continuate così!!

Ringrazio la mia famiglia che mi ha sempre sostenuto nonostante le numerose cadute di questi tre anni, in moto e non solo. Ringrazio la **Mamma** perché veramente mi ha aiutato in tutto quello che si possa pensare nonostante tutti i capelli bianchi che le ho fatto venire con la moto; ringrazio **Gianni** per aver sopportato il mio caratteraccio e per avermi insegnato ad impegnarmi sempre e comunque a testa bassa; ringrazio **GianZio** per avermi spronato a dare sempre il massimo e cercare di essere sorridente nel farlo; ringrazio la **Zia** per il supporto, i giri in moto e per le bevute di straforo; ringrazio la mia **Sorellina Giorgia**, forse una delle persone più importanti e speciali della mia vita, per essermi sempre stata vicina, nei momenti felici e soprattutto per avermi sopportato e supportato nei momenti più bui del 2016, ti voglio bene.

Ringrazio **Elisa (Popi)**, la mia fidanzata, per tutto quello che mi dimostra ogni giorno, per la sua presenza e per avermi spronato a non mollare mai e a dare sempre il meglio di me… Sei arrivata quasi alla fine di questo mio percorso, ma sarà anche l'inizio di qualcosa di nuovo!!! Sei arrivata nel momento in cui avevo perso ogni speranza, e sei riuscita a ridarmi un sorriso inaspettato, GRAZIE, GRAZIE, GRAZIE! Ti Voglio Bene!!!

Ringrazio gli **amici di una vita e quelli nuovi**:
Gli **Ovada-Genovesi**: la mia miglior amica **Chiara** mi ripeterò con i ringraziamenti della Tesi Magistrale, ma la ringrazio per dirmi in faccia sempre quello che pensa, anche se a volte quello che dice sembrano mattonate nei denti, **Luana** perché si trattiene un pelo di più di sua sorella, e per le sue fantastiche torte, sono le amiche che ognuno vorrebbe avere; **Davide (Lo Sbirro)** per tutta la sua filosofia filosofeggiante che manco lui segue; **Manuela** per le risate, le serate passate e per le prese per i fondelli il troglodita.
Matteo (Piede), merita un paragrafo a se stante, in quanto credo sia l'amico più sincero e leale che abbia mai avuto.
Marcello, per il Tiglieto in tenuta tecnica maglietta e pantaloncini, e per la sua amicizia; **Chichi** per avermi fatto ridere anche quando sarebbe stato meglio piangere, **Booster** per tutti i commenti riguardanti… beh… riguardanti le ragazze; **Claudione** per le "sciuptoie" al piattello, **Bumbix** per i giri in moto a cannone;

Il gruppo "folkloristico" Gressoney: Silvia (la mia mogliettina, ormai ex) con la quale non si riesce a star seri per più di cinque minuti di fila, per tutte le chiacchierate e i programmi fatti; **Sara** che forse più di tutti/e si piega alle mie cavolate; **Stefania** per tutte le volte che ci siamo piegati dal ridere; **Lucia** per gli spritz alle tre del pomeriggio; **Cesidia (infiltrata)** per i suoi fantastici Long Island; **Edoardo** beh sappiamo tutti e due i motivi di questi ringraziamenti, ne abbiamo già discusso e non volevi neanche essere inserito in questa lista…
Vi ringrazio tutti per le GRASSE risate e soprattutto per le ci---he fotoniche in qualsiasi momento dell'anno e a qualsiasi ora del giorno.

Il gruppo **KSA**: **Luca**, **Erika, Bledi, Freibs, Cunningham, Robert** e **Massimo** per le botte in palestra e le risate tutti insieme.
Tony ed Eliana, parte del KSA e non solo, per le serate passate con l'altoparlante nella giacca e per una quantità infinita di altri motivi;

Ringrazio i nuovi amici del **Tavolo VIPs**: **Pillalla, Michele e Doris,** per le Focus, le attività e le bellissime serate insieme, siete dei grandi!

Ringrazio **Caterina** (la mia fantastica Ducati Streetfighter) per tutte le tirate, le impennate, le sfiammate dallo scarico e le saponette tritate insieme dalla caramagna… Sei veramente una grande compagna, e mi hai aiutato molto a superare i momenti difficili… Grazie per avermi sempre riportato a casa intero e senza un graffio… Ti chiedo scusa per le due sdraiate in questi ultimi anni, ma ci siamo rialzati insieme.

E infine ringrazio un po' anche me, perché non ho mai mollato…

"…as a symbol I can be incorruptible, I can be everlasting…"

Marco

Supplementary materials

X-Ray Powder Diffraction Spectra

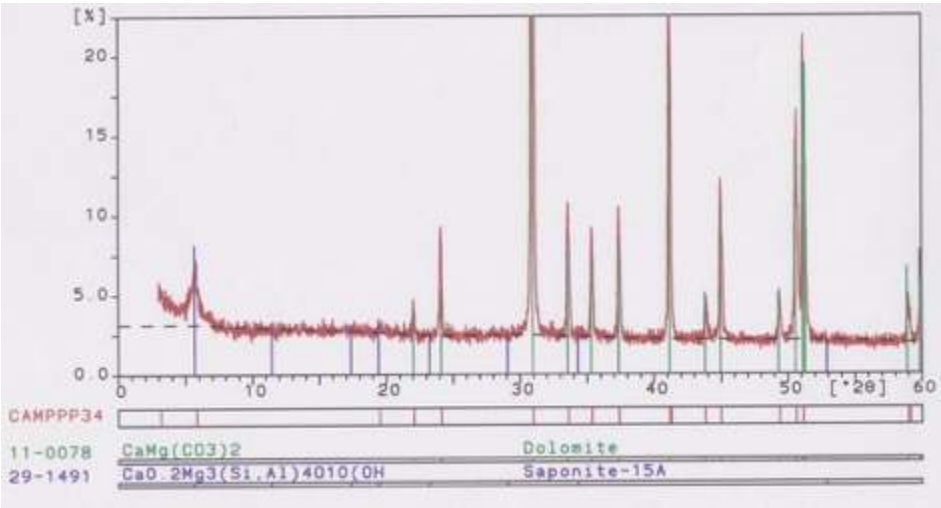

S1: Serpentinite fault gouge, characterised by the crystallization of clay minerals from the Tugello Creek Thrust (Chapter 5.3.2).

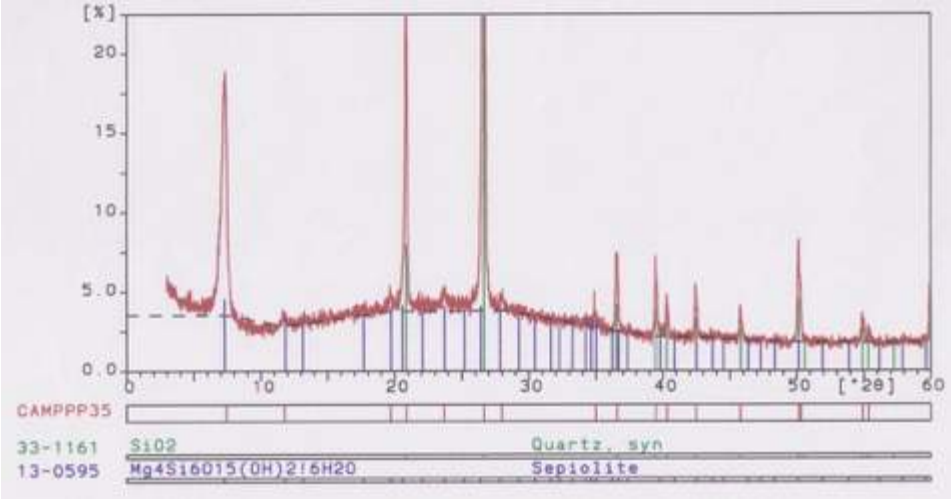

S2: PP35 sample of sepiolite duplex structures from the Tugello Creek Thrust (Chapter 5.3.2).

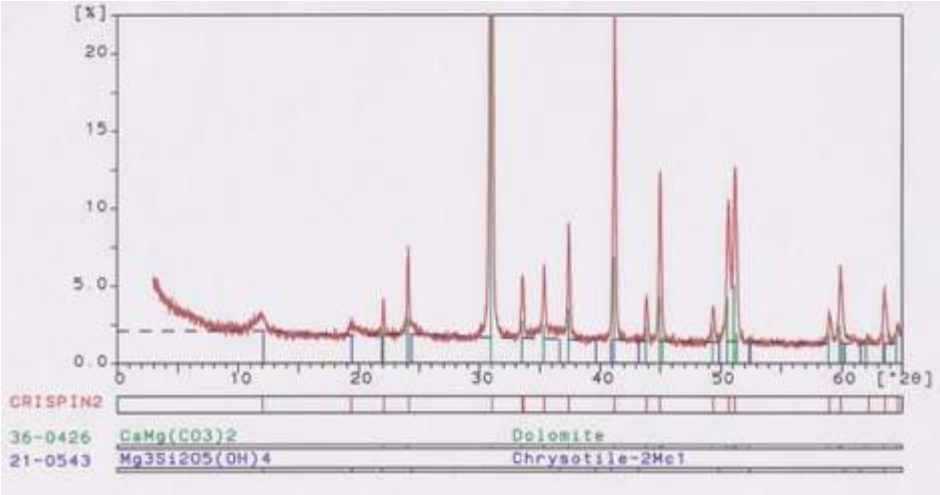

S3: Sample PP37, dolomite level of the central part of the fault core of the Tugello Creek Thrust (Chapter 5.3.2).

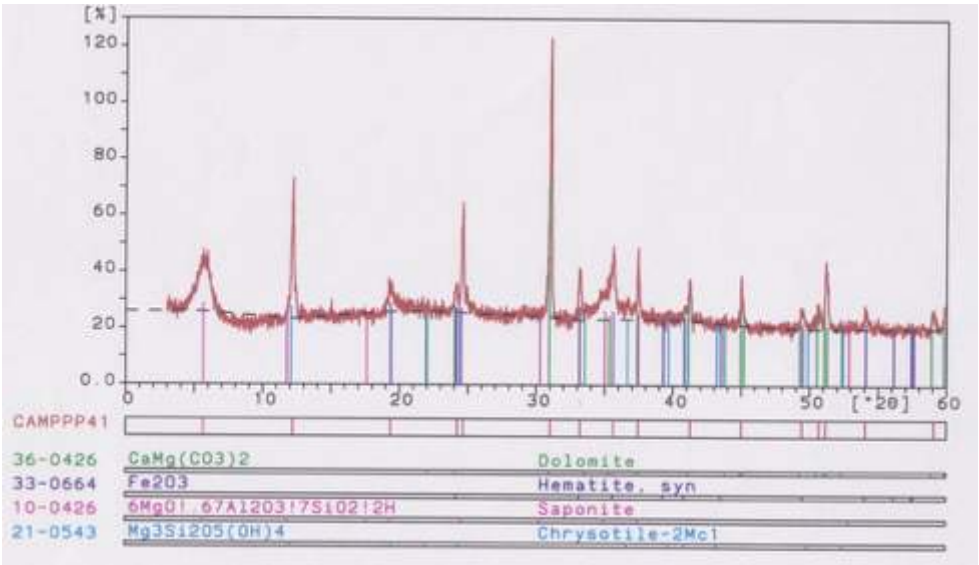

S4: Sample PP41, serpentinite fault gouge, from the footwall of the Tugello Creek Thrust (Chapter 5.3.2

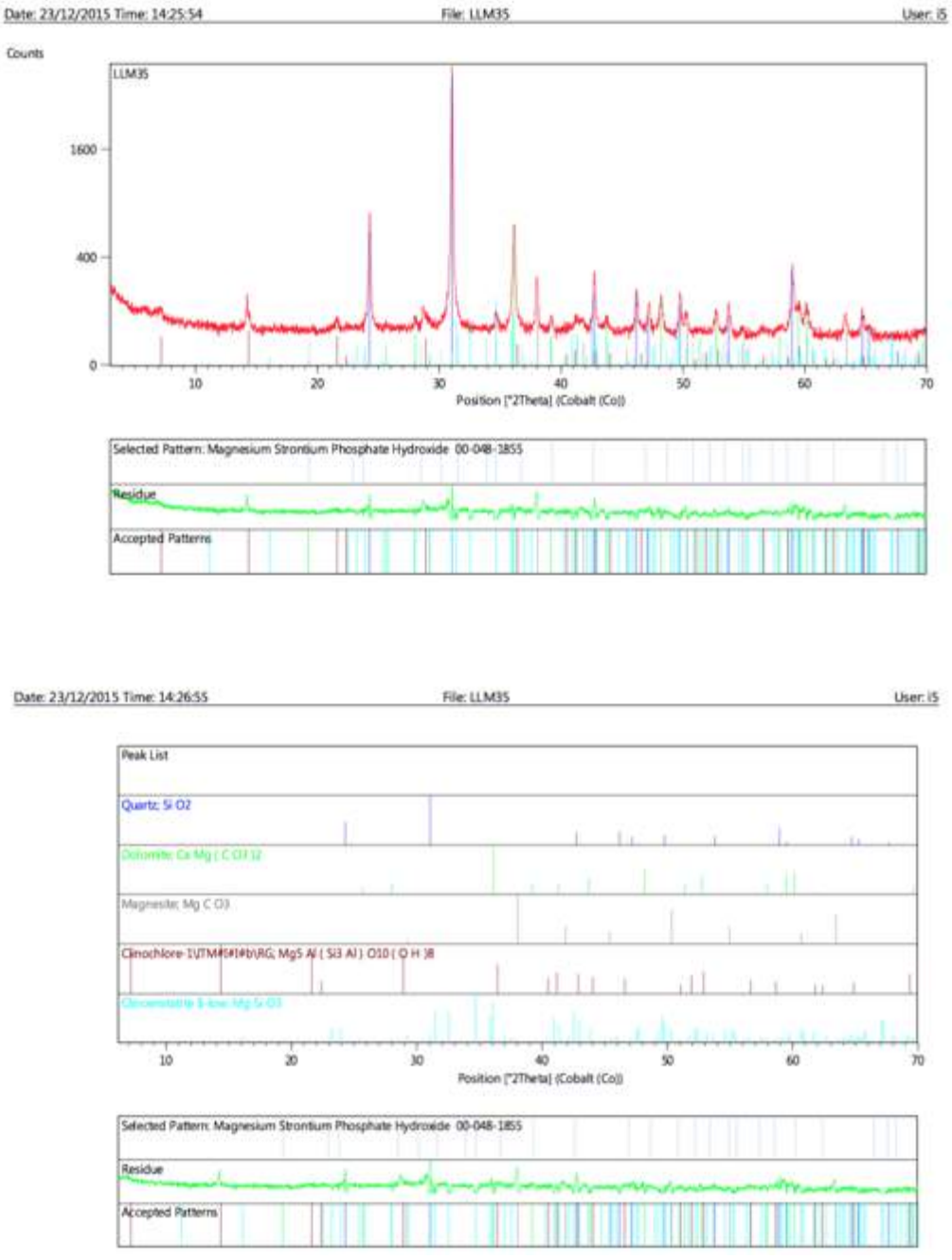

S5a: Sample LLM35, black Chatter marks from the Paganella Creek fault surface (Chapter 5.3.3).

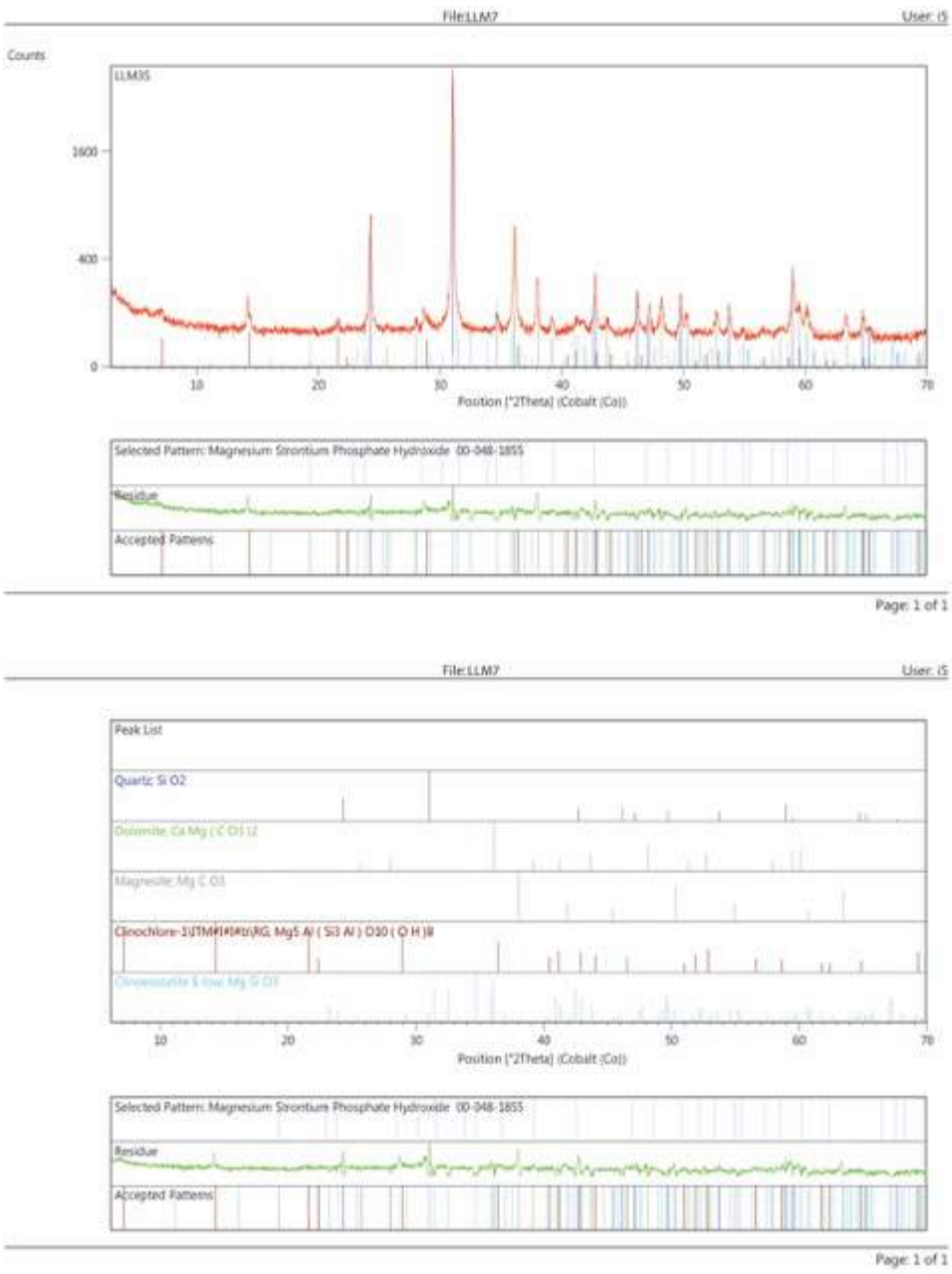

S6: sample LLM7 incohesive black level with sigmoidal bodies Paganella Creek fault (Chapter 5.3.3).

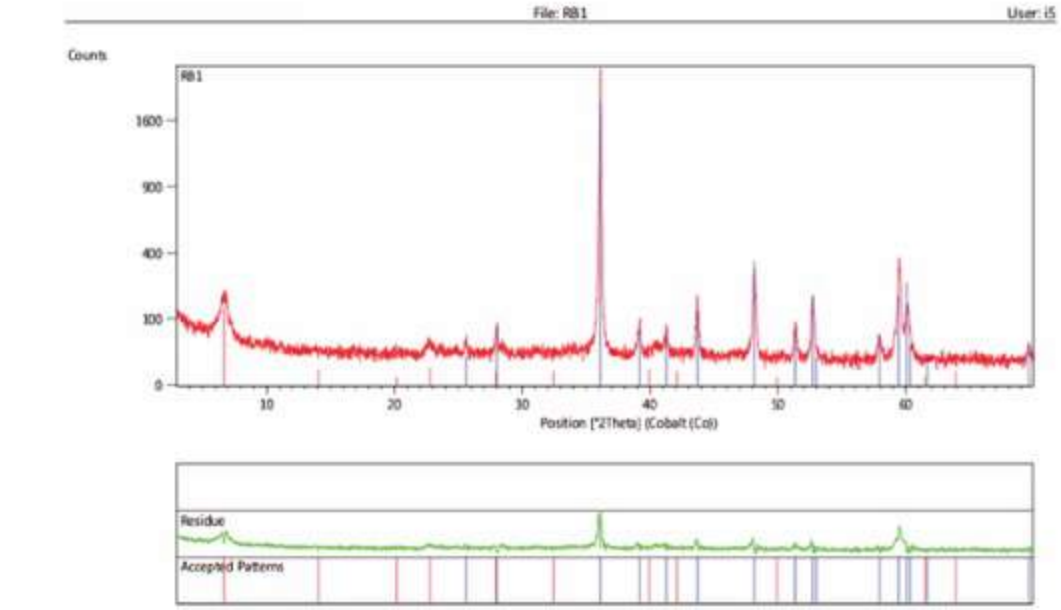

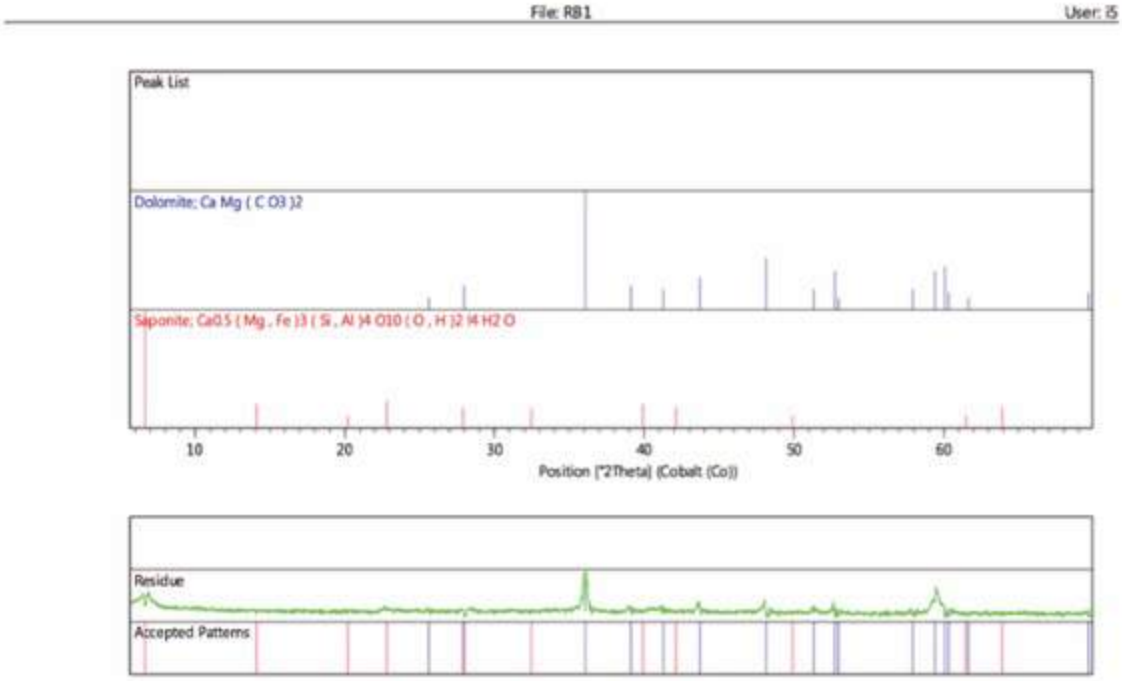

S7: Sample RB1, cataclastic dolomite and emerald green saponite fault gouge from the Bisciarelle Creek Thrust fault (Chapter 5.3.4).

Analyte Symbol	Detection Limit	Analysis Method	RB1	RB2	RB3	RB4	RB5	RB6	RB7	RB8	RB9	RB10
Mass		INAA	34,3	30,9	26	26,9	24,9	29,7	28,7	28,2	25,4	36,8
Weight percent												
SiO2	0,01	FUS-ICP	11,13	34,5	35,78	36,91	37,04	39,24	35,57	40,13	38,15	41,37
Al2O3	0,01	FUS-ICP	1,08	2,16	3,33	2,55	0,95	1,41	0,59	2,36	2,43	2,5
Fe2O3(T)	0,01	FUS-ICP	3,24	7,79	7,32	6,66	6,98	6,98	8,11	5,08	8,3	7,97
MnO	0,001	FUS-ICP	0,161	0,102	0,07	0,092	0,091	0,084	0,119	0,101	0,104	0,118
MgO	0,01	FUS-ICP	21	32,67	36,35	36,4	37,31	37,85	35,52	38,78	35,15	37,29
CaO	0,01	FUS-ICP	22,92	4,95	2,25	2,13	2,54	0,77	4,84	0,86	1,98	2,37
Na2O	0,01	FUS-ICP	0,03	0,02	0,01	0,01	0,01	0,01	0,01	0,02	0,03	0,18
K2O	0,01	FUS-ICP	0,7	0,08	0,08	< 0.01	< 0.01	< 0.01	< 0.01	< 0.01	< 0.01	0,07
TiO2	0,001	FUS-ICP	0,034	0,058	0,015	0,077	0,028	0,043	0,018	0,13	0,065	0,069
P2O5	0,01	FUS-ICP	< 0.01	< 0.01	< 0.01	< 0.01	< 0.01	0,01	0,01	< 0.01	< 0.01	< 0.01
LOI		FUS-ICP	39,07	17,17	14,76	14,8	14,92	12,75	15,01	12,69	12,85	8,27
Total	0,01	FUS-ICP	99,36	99,5	99,96	99,64	99,86	99,16	99,81	100,2	99,07	100,2
Parts per million												
Sc	1	FUS-ICP	4	11	3	13	6	9	5	13	13	13
Be	1	FUS-ICP	< 1	< 1	< 1	< 1	< 1	< 1	< 1	< 1	< 1	< 1
V	5	FUS-ICP	16	57	39	54	32	49	21	53	60	63
Cr	20	FUS-MS	680	2060	2700	2430	2290	1110	2390	2360	2380	2710
Co	1	FUS-MS	34	91	87	87	89	93	118	89	89	93
Ni	20	FUS-MS	820	1730	1840	1620	1890	1820	2370	1800	1680	1960
Cu	10	FUS-MS	10	10	20	< 10	< 10	20	20	< 10	20	30
Zn	30	FUS-MS	< 30	40	30	40	50	30	60	40	40	40
Ga	1	FUS-MS	1	2	3	2	1	2	1	2	2	2
Ge	0,5	FUS-MS	< 0.5	0,6	0,9	0,8	0,9	1	0,8	1	1	0,9
As	5	FUS-MS	< 5	< 5	< 5	< 5	< 5	< 5	< 5	< 5	< 5	< 5
Rb	1	FUS-MS	21	2	3	< 1	< 1	< 1	< 1	< 1	< 1	2
Sr	2	FUS-ICP	331	33	38	30	362	14	201	10	26	4
Y	0,5	FUS-MS	2	1,6	0,9	1,9	0,8	1	0,5	1,4	1,8	2,3
Zr	1	FUS-ICP	29	81	20	11	35	7	17	18	16	85
Nb	0,2	FUS-MS	< 0.2	< 0.2	< 0.2	< 0.2	< 0.2	< 0.2	< 0.2	< 0.2	< 0.2	< 0.2
Mo	2	FUS-MS	< 2	< 2	< 2	< 2	< 2	< 2	< 2	< 2	< 2	< 2
Ag	0,5	FUS-MS	< 0.5	< 0.5	< 0.5	< 0.5	< 0.5	< 0.5	< 0.5	< 0.5	< 0.5	< 0.5
In	0,1	FUS-MS	< 0.1	< 0.1	< 0.1	< 0.1	< 0.1	< 0.1	< 0.1	< 0.1	< 0.1	< 0.1
Sn	1	FUS-MS	< 1	< 1	< 1	< 1	< 1	< 1	< 1	< 1	< 1	< 1
Sb	0,2	FUS-MS	0,2	1,3	1,1	0,8	0,5	0,5	1,3	1,8	0,4	< 0.2
Cs	0,1	FUS-MS	3,3	0,3	0,5	0,3	< 0.1	0,2	< 0.1	0,3	0,2	1,4
Ba	2	FUS-ICP	26	35	14	15	58	11	249	17	9	15
La	0,05	FUS-MS	1,4	< 0.05	0,07	0,06	0,38	< 0.05	2	< 0.05	0,11	0,07
Ce	0,05	FUS-MS	3,5	0,2	0,21	0,14	< 0.05	< 0.05	1,81	0,1	0,06	0,18
Pr	0,01	FUS-MS	0,44	0,03	0,04	0,03	0,01	< 0.01	0,21	0,03	0,02	0,03
Nd	0,05	FUS-MS	1,76	0,22	0,19	0,15	0,09	0,07	0,65	0,22	0,16	0,22
Sm	0,01	FUS-MS	0,26	0,05	0,08	0,06	< 0.01	0,04	0,09	0,1	0,12	0,13
Eu	0,005	FUS-MS	0,077	0,039	0,029	0,045	0,017	0,023	0,023	0,067	0,039	0,044
Gd	0,01	FUS-MS	0,23	0,18	0,12	0,19	0,09	0,08	0,09	0,18	0,2	0,18
Tb	0,01	FUS-MS	0,05	0,04	0,02	0,04	0,02	0,02	0,02	0,04	0,04	0,04
Dy	0,01	FUS-MS	0,29	0,27	0,13	0,28	0,1	0,13	0,11	0,27	0,29	0,33
Ho	0,01	FUS-MS	0,07	0,06	0,03	0,07	0,03	0,03	0,02	0,06	0,07	0,08
Er	0,01	FUS-MS	0,18	0,21	0,08	0,21	0,1	0,12	0,06	0,17	0,19	0,23
Tm	0,005	FUS-MS	0,031	0,035	0,014	0,034	0,019	0,02	0,01	0,027	0,028	0,043
Yb	0,01	FUS-MS	0,22	0,25	0,09	0,22	0,15	0,15	0,07	0,21	0,23	0,34
Lu	0,002	FUS-MS	0,037	0,042	0,016	0,034	0,026	0,025	0,012	0,035	0,037	0,053
Hf	0,1	FUS-MS	0,7	1,7	0,4	0,2	0,8	0,1	0,3	0,3	0,3	2
Ta	0,01	FUS-MS	0,02	< 0.01	< 0.01	< 0.01	< 0.01	< 0.01	< 0.01	< 0.01	< 0.01	0,02
W	0,5	FUS-MS	0,7	0,7	< 0.5	1,1	0,5	0,8	< 0.5	0,6	< 0.5	< 0.5
Tl	0,05	FUS-MS	< 0.05	0,09	< 0.05	< 0.05	< 0.05	< 0.05	< 0.05	< 0.05	< 0.05	< 0.05
Pb	5	FUS-MS	< 5	< 5	< 5	< 5	< 5	< 5	< 5	< 5	< 5	< 5
Bi	0,1	FUS-MS	< 0.1	< 0.1	< 0.1	< 0.1	< 0.1	< 0.1	0,1	< 0.1	< 0.1	< 0.1
Th	0,05	FUS-MS	0,05	< 0.05	0,1	< 0.05	< 0.05	< 0.05	0,17	< 0.05	< 0.05	< 0.05
U	0,01	FUS-MS	< 0.01	0,07	0,13	< 0.01	0,01	< 0.01	< 0.01	0,17	< 0.01	0,05
As	0,5	INAA	< 0.5	1,2	0,8	1,2	1,2	1,3	1,7	4,8	1,9	1,2
Br	0,5	INAA	< 0.5	< 0.5	< 0.5	< 0.5	< 0.5	< 0.5	< 0.5	< 0.5	< 0.5	< 0.5
Cr	5	INAA	612	1910	2480	2110	2070	1010	2040	2020	2170	2330
Sc	0,1	INAA	4,1	11,1	2,8	12,3	6,3	8,8	4,6	12,3	12,5	12,4
Se	3	INAA	< 3	< 3	< 3	< 3	< 3	< 3	< 3	< 3	< 3	< 3
Sb	0,2	INAA	0,4	1,9	1,4	0,9	0,4	0,7	1,3	2	0,6	< 0.2
Parts per billion												
Au	2	INAA	< 2	< 2	< 2	< 2	< 2	< 2	< 2	< 2	< 2	< 2
Ir	5	INAA	< 5	< 5	< 5	< 5	< 5	< 5	< 5	< 5	< 5	< 5
Distance (m)			0,5	1,7	2,7	3,5	4,9	6,1	7,5	8,9	10,6	15,6

S8: Bulk rock chemical analysis of the transect RB1-RB10 (Chapter 7).

Sample	LLM31BC1A1	LLM31B	LLM31B	LLM31C	LLM31D	LLM31D	LLM31D	LLM31D	LLM31D	LLM31D	LLM31D	LLM31D	LLM31D	LLM32B	LLM31F	LLM31F
Point	C1area1	C1area1	C2area1	c2area1	C1area1	C1area1	C1area1	C1area1	C3area1	C6area1	C7area1	C7area1	C8area1	C8area1	C1area1	C4area1
	Spot 1	Spot 2	Spot 1	Spot2	Spot1	Spot2	Spot3	Spot4	Spot 2	Spot 1	Spot 1	Spot 2	Spot 1	Spot 2	Spot1	Spot1
									CCGs							
MgO	20,03	18,60	19,38	21,89	19,53	20,38	20,45	20,35	20,71	20,28	20,55	20,60	20,10	20,09	21,67	21,00
CaO	29,70	29,54	28,33	29,81	29,68	29,83	30,08	30,45	29,31	29,92	29,45	30,27	28,56	30,26	29,67	29,54
MnO	0,00	0,00	0,00	0,00	0,00	0,00	0,00	0,00	0,00	0,00	0,00	0,00	0,00	0,00	0,00	0,00
FeO	0,92	1,28	3,45	0,65	3,35	1,99	0,75	1,29	2,11	1,18	1,33	1,42	3,09	1,95	0,00	2,15
ZnO	0,00	0,00	0,00	0,00	0,00	0,00	0,00	0,00	0,00	0,00	0,00	0,00	0,00	0,00	0,00	0,00
SrO	0,00	0,00	0,00	0,00	0,00	0,00	0,00	0,00	0,00	0,00	0,00	0,00	0,00	0,00	0,00	0,00
BaO	0,00	0,00	0,00	0,00	0,00	0,00	0,00	0,00	0,00	0,00	0,00	0,00	0,00	0,00	0,00	0,00
PbO	0,00	0,00	0,00	0,00	0,00	0,00	0,00	0,00	0,00	0,00	0,00	0,00	0,00	0,00	0,00	0,00
Totale	50,65	49,42	51,16	52,35	52,56	52,20	51,28	52,09	52,13	51,38	51,33	52,29	51,75	52,30	51,34	52,69

Sample	LLM31F	LLM31F	LLM31F	LLM32A	LLM32A	LLM32A	LLM32A	LLM32A	LLM32A	LLM32A	LLM32B	LLM32B	LLM32B	LLM32B	LLM32B	LLM32B
Point	C7area1	C7area1	C7area1	C1area1	C1area1	C1area2	C2area1	C2area2	C2area2	C2area2	C5area1	C1area1	C1area1	C2area1p1	C2area1	C2area1
	Spot1	Spot2	Spot3	Spot1	Spot2	Spot1	Spot1	Spot2	Spot3	Spot4	Spot1	Spot1	Spot2	Spot1	Spot2	Spot3
									CCGs							
MgO	21,80	21,71	22,93	20,69	21,60	21,03	21,16	21,07	21,43	21,25	21,94	21,67	20,43	21,08	20,23	20,88	19,99
CaO	29,90	30,69	30,55	29,69	29,64	29,56	30,11	29,77	29,07	29,71	29,03	29,67	29,61	29,84	29,70	30,58	29,36
MnO	0,00	0,00	0,00	0,00	0,00	0,00	0,00	0,00	0,00	0,00	0,00	0,00	0,00	0,00	0,00	0,00	0,00
FeO	1,63	0,70	0,46	1,16	0,33	0,55	0,63	0,93	0,88	1,08	0,82	0,00	1,19	0,84	1,77	0,62	2,40
ZnO	0,00	0,00	0,00	0,00	0,00	0,00	0,00	0,00	0,00	0,00	0,00	0,00	0,00	0,00	0,00	0,00	0,00
SrO	0,00	0,00	0,00	0,00	0,00	0,00	0,00	0,00	0,00	0,00	0,00	0,00	0,00	0,00	0,00	0,00	0,00
BaO	0,00	0,00	0,00	0,00	0,00	0,00	0,00	0,00	0,00	0,00	0,00	0,00	0,00	0,00	0,00	0,00	0,00
PbO	0,00	0,00	0,00	0,00	0,00	0,00	0,00	0,00	0,00	0,00	0,00	0,00	0,00	0,00	0,00	0,00	0,00
Totale	53,33	53,10	53,94	51,54	51,57	51,14	51,90	51,77	51,38	52,04	51,79	51,34	51,23	51,76	51,70	52,08	51,75

Sample	LLM31C	LLM31C	LLM31C	LLM32A	LLM32A	LLM32B	LLM32B	LLM32A								
Point	c2area1	c3area1	c3area1	C2area1	C2area1	C2area2	C2area2	C1area2								
	Spot3	Spot1	Spot2	Spot5	Spot6	Spot1	Spot3	Spot3								
						Chalcedony										
Al2o3	0	0	0	0,29	0,17	0,82	0,39	0,28								
SiO2	100,41	99,87	99,98	99,85	99,85	99,4	96,17	90,69								
Total	100,41	99,87	99,98	100,14	100,02	100,22	96,56	90,96								

Sample	LLM32B	LLM32A	LLM32A	LLM32B												
Point	C1area1	C2area2	C2area2	C1area1												
	Spot2	Spot5	Spot6	Spot4												
					MATRIX											
MgO	21,67	21,07	21,43	21,67												
CaO	29,67	29,77	29,07	29,67												
MnO	0,42	0,18	0,21	0,42												
FeO	0,00	0,93	0,88	0,00												
ZnO	0,00	0,00	0,00	0,00												
SrO	0,00	0,00	0,00	0,00												
BaO	0,00	0,00	0,00	0,00												
PbO	0,00	0,00	0,00	0,00												
Totale	51,76	51,95	51,59	51,76												

S9: SEM-EDS analysis of the fault pearls, chalcedony, and dolomite matrix from the Bisciarelle Creek Thrust fault (Chapter 8).